Development of Bulk-Type All-Solid-State Batteries Using Lithium-Ion Conducting Solid Electrolyte Films

Development of Bulk-Type All-Solid-State Batteries Using Lithium-Ion Conducting Solid Electrolyte Films

Atsushi Sakuda

January 2011

Doctoral Thesis at Osaka Prefecture University

Development of Bulk-Type All-Solid-State Batteries Using Lithium-Ion Conducting Solid Electrolyte Films

Contents

1. General introduction

There has been increasing interest in hybrid electric vehicles (HEVs), plug-in hybrid electric vehicles (PHEVs) and electric vehicles (EVs) using rechargeable batteries because environmental problems and energy problems such as global warming and finite fossil-fuel supplies have become aggravated. The key to the deployment of PHEVs and EVs is the development of next generation rechargeable batteries because the vehicles need more energy than HEVs to increase the mileage per charge [1].

Among the various available energy storage technologies, lithium-ion secondary batteries have become the prime candidate for power sources of large machines. The lithium-ion secondary batteries have been used as power sources of various portable electronic devices such as cell phones, laptop computers, digital cameras, etc. In recent years, their applications have started to towards use as a power source for larger machines [2].

Lithium-ion secondary batteries are composed of positive and negative electrodes connected with a lithium-ion conducting electrolyte. Commercially produced lithium-ion secondary batteries usually use layered lithium metal oxide ($LiMO_2$, where M is usually cobalt, nickel or manganese) as a positive electrode, carbon as a negative electrode, and an organic electrolyte solution. The average voltage for single cell is normally 3.5 to 4.0 V. Lithium-ion secondary batteries have about five times larger energy density per mass than lead-acid batteries [1, 3].

There are fundamental safety concerns in lithium-ion secondary batteries because of the co-presence of a flammable organic electrolyte solution and charged electrode materials with high energy, which carries a risk of runaway reactions resulting in fires or explosions. In addition, the increase in the battery size needed for high power devices raises further safety concerns. To improve the safety of the batteries, lithium-ion secondary batteries used in

current EVs have lower energy density than those used in portable electronic devices [4]. The development of large-scale lithium-ion secondary batteries combining high safety and high energy density has thus been strongly desired for increasing mileage per charge of EVs.

Next generation lithium-ion secondary batteries using nonflammable electrolytes such as ionic liquid electrolytes [5-8] and solid electrolytes using organic polymers [9, 10], inorganic crystals [11-14], glasses [15, 16], and glass-ceramics [17-19] have been studied because the batteries are expected to be safer and more reliable than conventional lithium-ion secondary batteries using organic electrolyte solutions. In particular, all-solid-state lithium secondary batteries using inorganic solid electrolytes have been studied as promising next generation batteries. Because of the use of inorganic solid electrolytes instead of organic electrolyte solution, the batteries have many advantages, such as high safety, no leakage, a long charge-discharge life [18, 20], a wide operation temperature range, and the potential application of new electrode materials that are difficult to use in conventional batteries.

The key material for all-solid-state batteries is a solid electrolyte. To construct all-solid-state batteries, a solid electrolyte with excellent properties is needed [21]. The requirements which should be satisfied as a solid electrolyte for a battery are listed here:

(a) high lithium-ion conductivity over the temperature range of battery operation (not the bulk conductivity but total conductivity including grain boundary conduction should be high)

(b) negligible electronic conductivity

(c) transference number $\sigma_{Li}/\sigma_{total}$ close to 1, where σ_{total} includes conductivity contributions from other ions in the electrolyte as well as lithium ions and electrons

(d) wide electrochemical window

(e) high chemical stability with the positive and negative electrode materials

(f) high chemical stability with the positive and negative current collectors

(g) good press formability to construct all-solid-state batteries

(h) low flammability, toxicity, and cost

In general, sulfide-based solid electrolytes show higher lithium-ion conductivity compared with oxide-based solid electrolytes because of high polarizability of sulfide ions. The conductivity of sulfide-based solid electrolytes is usually more than 10^{-4} S cm^{-1} [22-26]; the conductivity of oxide-based solid electrolytes is usually less than that of sulfide-based ones. Among many sulfide-based solid electrolytes, $Li_{3.25}Ge_{0.25}P_{0.75}S_4$ (thio-LISICON) [23], and Li_2S–P_2S_5 glasses and glass-ceramics [24-26] show significantly high lithium-ion conductivity of more than 10^{-3} S cm^{-1} at room temperature. The conductivities of the Li_2S–P_2S_5 glasses increase with an increase in the Li_2S content up to 80 mol% Li_2S. Furthermore, the conductivities of the Li_2S–P_2S_5 glasses are increased by heat treatment, which comes from the formation of super lithium-ion conductive glass-ceramics. The lithium-ion conductivities at room temperature are almost comparable to that of liquid electrolytes. In addition, the formability of sulfide-based solid electrolytes is superior to that of oxide-based solid electrolytes. As a result, relatively smooth contacts of interface between electrode and electrolyte are able to be formed in all-solid-state batteries using sulfide-based solid electrolytes. They have a wide electrochemical window and negligible electron conductivity. The lithium-ion transference number is close to 1. The flammability is negligible compared with organic electrolytes. The sulfide-based solid electrolytes satisfy important requirements as solid electrolytes; they are thus a strong candidate as a solid electrolyte for all-solid-state lithium secondary batteries.

Oxide-based solid electrolytes usually show lower lithium-ion conductivity than sulfide-based solid electrolytes. Therefore, the oxide-based solid electrolytes have been used as a solid electrolyte for thin film batteries. The most common oxide-based solid electrolyte for all-solid-state batteries is amorphous lithium phosphorous oxynitride (LiPON)

[27-29]. In general, the amorphous thin films which have high lithium-ion concentration have high conductivity. LiPON is usually prepared by a RF sputtering of lithium orthophosphate (Li_3PO_4) target under N_2 gas atmosphere to introduce nitrogen into lithium phosphate to increase the lithium-ion conductivity. The conductivity at room temperature is reported to be 2×10^{-6} S cm^{-1} [27-29]. The glasses in the systems with two lithium ortho-oxosalts such as Li_3BO_3–Li_4GeO_4 and Li_4SiO_4–Li_3BO_3 have also been reported to show high lithium-ion conductivity in oxide-based glassy solid electrolytes [30]. In the Li_4SiO_4–Li_3BO_3 system, at the middle composition of two ortho-oxosalts, the glasses showed the highest conductivity of 6×10^{-6} S cm^{-1} at 300 K [31]. This phenomenon is called the "mixed anion effect" [31, 32]. The glasses were prepared by rapid quenching of melts with a twin-roller quenching apparatus [30]. Amorphous thin films in the system Li_4SiO_4–Li_3PO_4 have been prepared by RF-sputtering and the thin films showed the high lithium-ion conductivity of 10^{-6} S cm^{-1} at room temperature [33].

Two types of all-solid-state batteries have been studied to date. One is thin-film batteries and the other is bulk-type batteries. Thin-film batteries, which are composed of electrode and solid electrolyte thin films, are anticipated for application as power sources of microdevices. Bulk-type batteries, which are composed of composite electrodes of active material and electrolyte powders, are anticipated as power sources with high-energy density for use in PHEVs and EVs.

In order to construct a thin film battery, it is necessary to fabricate a multi-layer film of negative electrode, solid electrolyte, and positive electrode films sandwiched with current collector films using appropriate techniques. The films for thin film batteries have been prepared using vacuum thermal vapor deposition (VD), various sputtering, chemical vapor deposition (CVD) and electrostatic spray deposition (ESD), pulsed laser deposition (PLD), and sol-gel techniques. The thin-film batteries reported so far exhibit excellent long-cycling

performance at room temperature [34-36].

PLD can prepare thin films with high quality. The important characteristics in PLD are the ability to transfer almost stoichiometrically a bulk target to the deposited films, control many parameters such as ambient gas pressure and laser fluence, and easily prepare thin films with high melting point. This technique has been mainly used for the preparation of crystalline electrode thin films such as $LiCoO_2$ [37], $LiMn_2O_4$ [38], and $LiFePO_4$ [39] in the field of lithium-ion secondary battery. Recently, some research groups have reported the preparation of amorphous oxide-based solid electrolyte thin films, such as $Li_xLa_{(2-x)/3}TiO_3$ [40], $Li_{3.4}V_{0.6}Si_{0.4}O_4$ [41-43], Li_2SiO_3 [44, 45], Li_3PO_4 [46] and LiPON [47] by PLD. Only a couple of papers have described sulfide-based solid electrolyte thin films prepared by PLD, amorphous $Li_{3.25}Ge_{0.25}P_{0.75}S_4$ (thio-LISICON) [48] and Li_2S–P_2S_5 [49] thin films. The sulfide-based solid electrolyte films prepared using PLD exhibited a high conductivity of more than 10^{-4} S cm^{-1}.

The use of solid electrolytes with high conductivity is indispensable in the fabrication of bulk-type batteries. Therefore, sulfide-based solid electrolytes have been mainly used as solid electrolytes for bulk type all-solid-state batteries [11-19]. The bulk-type all-solid-state batteries exhibit long cycle performance. The batteries In / $LiCoO_2$ using Li_2S–P_2S_5 glass-ceramic solid electrolytes were reversibly charged and discharged for more than 700 cycles at the current density of 0.064 mA cm^{-2} [20].

Secondary batteries with large scale are required to show excellent performances such as high energy density, high power operation, high voltage, wide temperature range operation, long cycle life, high safety, and low cost. There are some issues to be resolved in bulk-type all-solid-state batteries. For example, the operation under a high current density of more than several milliamperes per square centimeters is difficult; the cycle performance at a high current density is needed to be improved [50]. The increase of energy density is also

desired.

The satisfaction of the requirement shown below should lead to better performance in all-solid-state batteries:

(i) use of solid electrolytes with high performance

(ii) selection of electrode materials which are suitable for all-solid-state batteries

(iii) formation of favorable lithium-ion and electron conducting path to the electrode materials

(iv) formation of low resistance solid/solid interfaces between electrodes and electrolytes over the temperature range of battery operation

(v) use of composite electrode with high packing density of electrode materials.

(vi) decrease of the thickness of solid electrolyte layer

(vii) retention of the contact between electrodes and electrolytes during cycling when the electrode particles are changing their volume

(viii) decrease of the damage to electrode caused by volume change during charge and discharge

(ix) suppression of the decomposition of the interface between electrodes and electrolytes

In general, all-solid-state batteries show higher internal resistance than conventional batteries. As a result, all-solid-state batteries are affected by large current-resistance drop (IR drop) in the operation at a high current density. In order to improve a rate capability of all-solid-state batteries, decreasing the internal resistances is very important. Highly conductive solid electrolytes such as Li_2S–P_2S_5 glass-ceramics have been applied to decrease the resistance of the solid electrolyte layer of all-solid-state batteries [17-19]. The design of composite electrodes composed of electrode active materials and solid electrolytes is also important. The use of suitable conductive additives and the optimization of the composite ratio of active materials and solid electrolytes have been carried out; the charge and discharge

under a high current density more than 1 mA cm^{-2} were achieved in the bulk type all-solid-state batteries [50, 51].

Oxide coatings on positive active materials had been reported to improve cycle performance and rate capability of conventional batteries [52, 53]. $LiCoO_2$ is typically used at the voltage up to 4.2 V vs. Li; the available capacity is about 140 mAh g^{-1}, which is only a half of the theoretical capacity of about 280 mAh g^{-1}. In order to increase the available capacity of the $LiCoO_2$, it needs to be charged at above 4.2 V. However, a significant capacity fading is observed at such a high voltage region. Oxide coatings such as SnO_2, Al_2O_3, ZrO_2, MgO, $AlPO_4$, Li_3PO_4, and $Li_{1.5}Al_{0.5}Ge_{1.5}(PO_4)_3$ and other coatings such as Li_2CO_3 and AlF_3 on $LiCoO_2$ have been reported as an effective approach to improve cycle performance at a high voltage above 4.2 V in the batteries with organic liquid [54-65], polymer [10, 66], and ionic liquid electrolytes [67]. The effects of the modification are reported as (i) suppression of structural change caused by phase transition of $LiCoO_2$, (ii) decrease of cobalt dissolution from $LiCoO_2$ to liquid electrolyte, and (iii) suppression of side reactions between the electrode and electrolyte. The coatings are also effective in improving rate capability. The batteries using coated $LiCoO_2$ show a higher voltage and a larger capacity on discharge process than those using uncoated $LiCoO_2$.

Modification of interface between $LiCoO_2$ electrode and the sulfide electrolyte by the coatings of oxide thin films has been reported to improve rate capability of all-solid-state batteries. Ohta *et al.* have reported that the coatings of $Li_4Ti_5O_{12}$, $LiNbO_3$, and $LiTaO_3$ on $LiCoO_2$ particles by spray coating brought about an excellent rate capability in the all-solid-state batteries using crystalline $Li_{3.25}Ge_{0.25}P_{0.75}S_4$ (thio-LISICON) as a solid electrolyte [12, 13, 68]. Figure 1-1 shows the impedance profiles of all-solid-state batteries Li–In /$Li_{3.25}Ge_{0.25}P_{0.75}S_4$/$LiCoO_2$ with various thicknesses of $Li_4Ti_5O_{12}$ coating [From Ref. 12]. A semicircle in the high-frequency region (> 0.5 Hz) is assigned to the interfacial resistance.

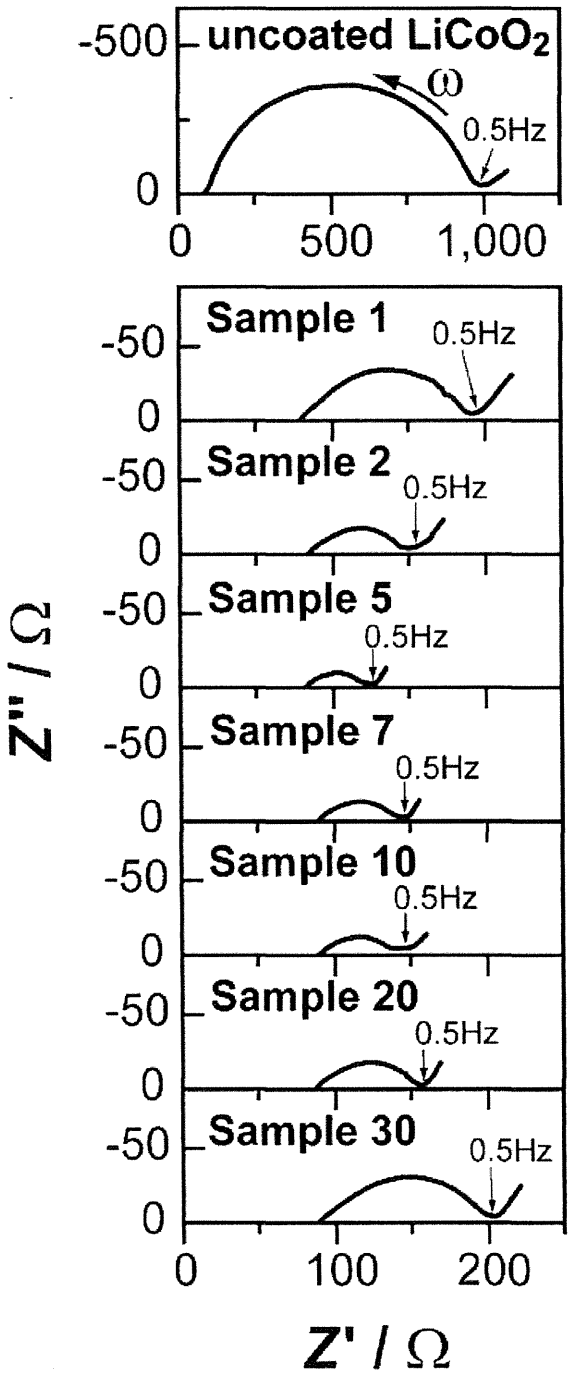

Figure 1-1 Complex impedance (Z) plots of the In–Li/$LiCoO_2$ cells. The sample number shows the calculated thickness (nm) of $Li_4Ti_5O_{12}$ coating [Ref. 12].

The impedance profiles clearly demonstrated the reduction of the interfacial resistance by the interposition of $Li_4Ti_5O_{12}$. The coating layers suppressed the formation of a high-resistive layer between the $LiCoO_2$ positive electrode material and the sulfide solid electrolyte. As a result, the batteries using the coated $LiCoO_2$ were discharged even at a high current density of 10 mA cm^{-2}. Ohta *et al.* have proposed a "space charge model" to explain the decrease of interfacial resistance. However, the cause of the large resistance at the interface between $LiCoO_2$ and sulfide-based solid electrolytes has not been clarified yet. The requirements of coating materials to decrease the interfacial resistance have not been studied. Clarification of these points will lead to a breakthrough in the development of all-solid-state batteries.

Information about the interface between electrode and electrolyte particles is necessary to construct an ideal electrode-electrolyte interface in all-solid-state batteries. Electrochemical impedance spectroscopy (EIS) is a useful measurement used to analyze the internal resistance of the all-solid-state batteries. There are some components which may have a large resistance; EIS offers the ability to separate different resistance components. This allows us to clarify large resistance components which should be reduced. Transmission electron microscopy (TEM) is also a powerful tool to obtain information of the electrode-electrolyte interface. The morphology, structure, and elemental distribution at the interfacial region directly affect the electrochemical performance of the all-solid-state batteries; their investigation enables us to obtain guidelines for the development of all-solid-state batteries with high performance. As an example of the research on all-solid-state batteries using TEM observation, Brazier *et al.* reported TEM observation of the electrode-electrolyte interface on the thin film batteries using oxide-based solid electrolyte (amorphous Li_2O–V_2O_5–SiO_2). Their TEM observations suggested that the deterioration of the interface upon cycling was caused by the migration of the chemical elements between stacked layers [69].

The aim of this thesis is the improvement of electrochemical performance such as rate capability, energy density and cycle life of bulk-type all-solid-state lithium secondary batteries.

In this thesis, the focus is on lithium-ion conductive solid electrolyte films. Solid electrolyte thin films will be anticipated for use not only for thin-film batteries but also for bulk-type battery applications. There is a strong possibility that an ideal interface between electrode and solid electrolyte is constructed.

New all-solid-state batteries using solid electrolyte films have been designed in this study. Figure 1-2 shows schematic diagrams of (a) bulk-type all-solid-state batteries usually studied, (b) all-solid-state batteries using a Solid-Electrolyte-coated $LiCoO_2$ (SE-coated $LiCoO_2$), (c) all-solid-state batteries with a thin solid electrolyte layer, and (d) all-solid-state batteries with the SE-coated $LiCoO_2$ and the thin solid electrolyte layer. In all-solid-state batteries usually studied as shown in Fig. 1-2 (a), a composite electrode composed of $LiCoO_2$ electrode particles and Li_2S–P_2S_5 solid electrolyte particles is used as a positive electrode to provide lithium-ion conducting path to $LiCoO_2$. The amounts of the solid electrolyte particles needed in the composite electrode are about 20-30 wt% at the present stage [51]. In addition, electron conducting additives such as acetylene black (AB) and vapor grown carbon fiber (VGCF) are required in the case using electrode active materials with low electronic conductivity [51]. The decrease in contents of the solid electrolyte and the conducting additive is effective in increasing energy density of composite electrode. In the all-solid-state batteries using the SE-coated $LiCoO_2$ shown in Fig. 1-2 (b), a favorable contact between $LiCoO_2$ electrode and Li_2S–P_2S_5 solid electrolytes can be formed. In addition, the contents of solid electrolyte in the positive electrode would be considerably reduced. This will lead to a dramatic improvement of energy density of all-solid-state batteries. In the all-solid-state batteries with the thin solid electrolyte layer shown in Fig. 1-2 (c), the positive

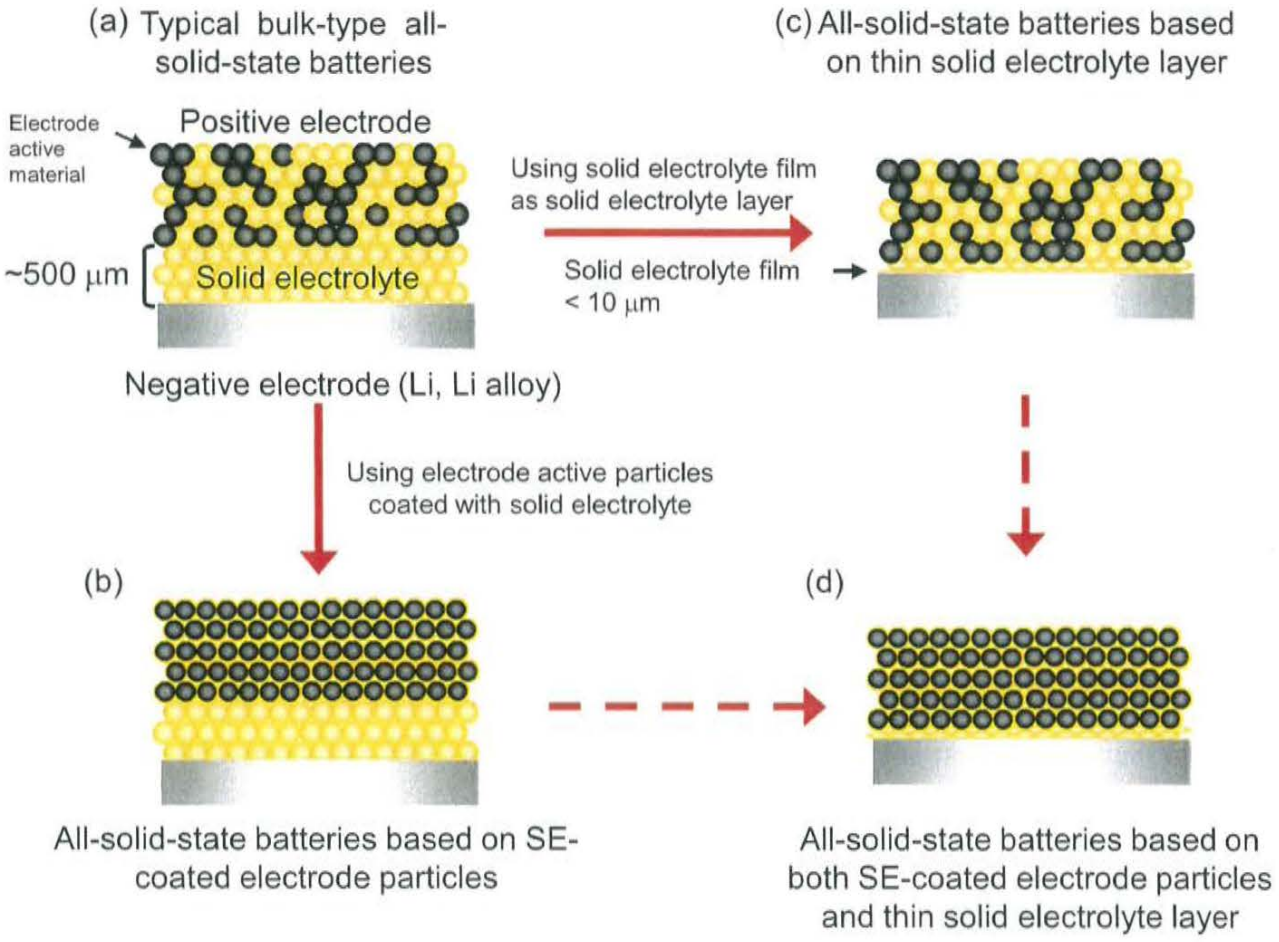

Figure 1-2 Schematic diagrams of (a) typical all-solid-state batteries, (b) all-solid-state batteries based on SE-coated electrode particles, (c) all-solid-state batteries based on thin solid electrolyte layer, and (d) all-solid-state batteries based on both SE-coated electrode and thin solid electrolyte layer.

composite electrode and the negative electrode were separated using the thin solid electrolyte layer. High energy density and high rate capability are expected by using the solid electrolyte thin film because of decreasing thickness and resistance of solid electrolyte. The construction of all-solid-state batteries with both the SE-coated $LiCoO_2$ and the thin solid electrolyte layer shown in Fig. 1-2 (d) is an ultimate goal in the all-solid-state batteries.

The solid electrolyte thin films for SE-coated $LiCoO_2$ particles require high lithium-ion conductivity to form lithium-ion conducting path in the composite electrolyte. The highly conducting thin films are also preferred to be used for the thin solid electrolyte layer for the improvement of rate performance. In this thesis, sulfide-based solid electrolyte films in the system Li_2S–P_2S_5 with high lithium-ion conductivity were prepared using a PLD technique. As described above, only a couple of articles have reported sulfide-based solid electrolyte thin films prepared by PLD. Although it is important to clarify the effects of preparation conditions on the structure, composition, and ionic conductivity of the sulfide films, such effects have not been reported so far in detail [48, 49]. The influence of preparation conditions such as chemical composition of target, gas pressure during deposition, and laser power on the film properties such as chemical composition, local structure and ionic conductivity of thin films was investigated to develop solid electrolyte thin films with high performance.

In order to reduce the ratio of the amount of solid electrolyte in the composite electrode layer, the improvement of the electrode-electrolyte interface is essential. Therefore, this thesis focuses on the interface between electrode and solid electrolyte. Characterization of the interface between electrode and solid electrolyte was carried out. Although a few studies on the investigation of the interface between electrode and electrolyte in all-solid-state batteries have been reported so far, more detail investigations are required for the enhancement of battery performance. Electrochemical impedance spectroscopy and TEM

observation for the electrode-electrolyte interface were conducted in this thesis. There are few reports for TEM observation of the interface between electrode and solid electrolyte. The TEM observation of the interface gives us useful information to develop the study of all-solid-state batteries.

One of the approaches for the improvement of the property of the interface is the interfacial modification using coatings of various materials on electrode particles. By inserting coating layer at the interface, the interfacial properties were changed; the effects of the coatings on the properties were investigated. Oxide films with various lithium-ion conductivities and metal sulfide materials with electronic conductivities were used as coating materials.

This doctoral thesis consists of five chapters indicated below:

Chapter 1

This chapter describes the background, the objectives and the contents of this thesis.

Chapter 2

This chapter describes electrochemical performance of all-solid-state cells improved by interfacial modification between $LiCoO_2$ electrode and Li_2S–P_2S_5 solid electrolyte. First, the rate capability of all-solid-state cells using bare $LiCoO_2$ and Li_2S–P_2S_5 solid electrolyte was investigated; the resistance components of all-solid-state cells were analyzed by electrochemical impedance spectroscopy. An interfacial modification between layered metal oxide electrodes of $LiCoO_2$ and Li_2S–P_2S_5 solid electrolytes was carried out to improve the electrochemical performance of all-solid-state cells. Coatings of oxide and sulfide films such as Li_2O–SiO_2, Li_2O–TiO_2, Li_4SiO_4–Li_3PO_4, CoS, and NiS were formed on the oxide electrode particles using sol-gel, PLD, and thermal decomposition techniques as a way to

Chapter 5

This chapter summarizes all the conclusions in this thesis.

modify the interface between the electrode and the solid electrolyte. The effects of the coatings on electrochemical performance of the all-solid-state cells are discussed.

Chapter 3

This chapter reports interfacial observation between $LiCoO_2$ electrodes and Li_2S–P_2S_5 solid electrolytes using transmission electron microscopy. The interface between the $LiCoO_2$ electrode and the $80Li_2S \cdot 20P_2S_5$ glass-ceramic solid electrolyte of all-solid-state cells was studied using TEM. In addition, the electrode-electrolyte interfaces of the cell using the coated $LiCoO_2$ were compared with that using uncoated $LiCoO_2$ to clarify the coating effect from the perspective of structural changes.

Chapter 4

This chapter reports preparation and application of sulfide-based solid electrolyte (SE) thin films by PLD. Thin films of Li_2S–P_2S_5 and Li_2S–GeS_2 system were selected because these sulfide-based glass systems exhibited high conductivity of lithium ion. The chemical composition, local structure, and ionic conductivity of the films prepared under various Ar gas pressure were studied to clarify the effect of ambient gas pressure on sulfide-film properties. Using the sulfide-based solid electrolyte films, two kinds of new all-solid-state batteries were designed and constructed. One is the all-solid-state batteries using SE-coated electrode particles shown in Fig. 1-2 (b) and the other is bulk-type all-solid-state batteries with solid electrolyte thin layer shown in Fig. 1-2 (c). The structure of all-solid-state batteries was characterized using SEM and TEM observations; the electrochemical performance of the cells was investigated.

References

[1] M. Armand and J.M. Tarascon, *Nature*, **451** (2008) 652.

[2] K. Sanderson, *Nature News* (2009) doi:10.1038/news.2009.948 News

[3] J.-M. Tarascon and M. Armand, *Nature*, **414** (2001) 359.

[4] Denchi Handbook (2010) pp. 619. (Written in Japanese)

[5] H. Sakaebe and H. Matsumoto, *Electrochem. Commun.*, **5** (2003) 594.

[6] H. Nakagawa, S. Izuchi, K. Kuwana, T. Nukuda and Y. Aihara, *J. Electrochem. Soc.*, **150** (2003) A695.

[7] B. Garcia, S. Lavall´ee, G. Perron, C. Michot, and M. Armand, *Electrochem. Acta*, **49** (2004) 4583.

[8] P.C. Howlett, D.R. MacFarlane, and A.F. Hollenkamp, *Electrochem. Solid-State Lett.*, **7** (2004) A97.

[9] K. Zaghib, M. Simoneau, M. Armand and M. Gauthier, *J. Power Sources*, **81–82** (1999) 300.

[10] S. Seki, Y. Kobayashi, H. Miyashiro, Y. Mita and T. Iwahori, *Chem. Mater.*, **17** (2005) 2041.

[11] R. Kanno, M. Murayama, T. Inada, T. Kobayashi, K. Sakamoto, N. Sonoyama, A. Yamada, and S. Kondo, *Electrochem. Solid-State Lett.*, **7** (2004) A455.

[12] N. Ohta, K. Takada, L. Zhang, R. Ma, M. Osada, and T. Sasaki, *Adv. Mater.*, **18** (2006) 2226.

[13] N. Ohta, K. Takada, I. Sakaguchi, L. Zhang, R. Ma, K. Fukuda, M. Osada, and T. Sasaki, *Electrochem. Commun.*, **9** (2007) 1486.

[14] T. Kobayashi, A. Yamada, and R. Kanno, *Electrochim. Acta,* **53** (2008) 5045.

[15] K. Takada, N. Aotani, K. Iwaomto, and S. Kondo, *Solid State Ionics*, **86-88** (1996) 877.

[16] N. Machida, H. Yamamoto, S. Asano, and T. Shigematsu, *Solid State Ionics*, **176** (2005)

473.

[17] F. Mizuno, S. Hama, A. Hayashi, K. Tadanaga, T. Minami, and M. Tatsumisago, *Chem. Lett.* (2002) 1244.

[18] A. Hayashi, T. Ohtomo, F. Mizuno, K. Tadanaga, and M. Tatsumisago, *Electrochem. Commun.*, **5** (2003) 701.

[19] Y. Seino, K. Takada, B.-C. Kim, L.-Q. Zhang, N. Ohta, H. Wada, M. Osada, and T. Sasaki, *Solid State Ionics*, **176** (2005) 2389.

[20] T. Minami, A. Hayashi, and M. Tatsumisago, *Solid State Ionics*, **177** (2006) 2715-2720.

[21] J.-B. Goodenough and Y. Kim, *Chem. Mater.*, **22** (2010) 587.

[22] N. Aotani, K. Iwamoto, K. Takada, and S. Kondo, *Solid State Ionics,* **68** [1-2] (1994) 35.

[23] R. Kanno and M. Murayama, *J. Electrochem. Soc.*, **148** [7] (2001) A742.

[24] A. Hayashi, S. Hama, T. Minami, and M. Tatsumisago, *Electrochem. Commun.*, **5** [2] (2003) 111.

[25] A. Hayashi, S. Hama, F. Mizuno, K. Tadanaga, T. Minami, and M. Tatsumisago, *Solid State Ionics*, **175** [1-4] (2004) 683.

[26] F. Mizuno, A. Hayashi, K. Tadanaga, and M. Tatsumisago, *Adv. Mater.*, **17** [7] (2005) 918.

[27] B. Wang, J.B. Bates, F.X. Hart, B.C. Sales, R.A. Zuhr, and J.D. Robertson, *J. Electrochem. Soc.*, **143** [10] (1996) 3203.

[28] J.B. Bates, N.J. Dudney, B. Neudecker, A. Ueda, and C.D. Evans, *Solid State Ionics*, **135** [1-4] (2000) 33.

[29] X.-H. Yu, J.B. Bates, G.E. Jellison Jr., and F.X. Hart, *J. Elcectrochem. Soc.*, **144** [2] (1997) 524.

[30] M. Tatsumisago, H. Narita, T. Minami, and M.Tanaka, *J. Am. Ceram. Soc.*, **66** (1983) C210.

[31] M. Tatsumisago, N. Machida, and T. Minami, *J. Ceram. Soc. Jpn.* **95** (1985) 197.

[32] B. Carette, M. Ribes, and J.L. Souquet, *Solid State Ionics*, **9-10** (1983) 735.

[33] K. Kanehori, K. Matsumoto, K. Miyauchi, and T. Kudo, *Solid State Ionics*, **9** (1983) 1445.

[34] S. D. Jones and J. R. Akiridge, *Solid State Ionics*, **53–56** [1] (1992) 628.

[35] S. D. Jones and J. R. Akridge, *J. Power Sources*, **44** [1–3] (1993) 505.

[36] B. Wang, J. B. Bates, F. X. Hart, B. C. Sales, R. A. Zuhr, and J. D. Robertson, *J. Electrochem. Soc.*, **143** [10] (1996) 3203.

[37] J.M. McGraw, C.S. Bahn, P.A. Parill, J.D. Perkins, D.W. Readey, and D.S. Ginley, *Electrochemica Acta*, **45** (1999) 187.

[38] C. Julien, E. Haro-Poniatowski, M.A. Camacho-Lopez, L. Escobar-Alarcon, and J. Jimenez-Jarquin, *Mater. Sci. Eng.* **B72** (2000) 36.

[39] F. Sauvage, E. Baudrin, M. Morcrette, and J.-M. Tarascon, *Solid-State Lett.*, **7** (2004) A15.

[40] S. Furusawa, H. Tabuchi, T. Sugiyama, S. Tao, and J.T.S. Irvine, *Solid State Ionics*, **176** (2005) 553.

[41] J. Kawamura, N. Kuwata, K. Toribami, N. Sata, O. Kamishima, and T. Hattori, *Solid State Ionics*, **175** (2004) 273.

[42] N. Kuwata, J. Kawamura, K. Toribami, T. Hattori, and N. Sata, *Electrochem. Commun.*, **6** (2004) 417.

[43] N. Kuwata, R. Kumar, K. Toribami, T. Suzuki, T. Hattori, and J. Kawamura, *Solid State Ionics*, **177** (2006) 2827.

[44] S. Furusawa, A. Kamiyama, and T. Tsurui, *Solid State Ionics*, **179** (2008) 536.

[45] N. Kuwata, N. Iwagami, and J. Kawamura, *Solid State Ionics*, **180** (2009) 644.

[46] N. Kuwata, N. Iwagami, Y. Tanji, Y. Matsuda, and J. Kawamura, *J. Electrochem. Soc.*,

157 (2010) A521.

[47] S. Zhao, Z. Fu, and Q. Qin, *Thin Solid Films*, **415** (2002) 108.

[48] N. Ohta, K. Takada, M. Osada, L. Zhang, T. Sasaki, and M. Watanabe, *J. Power Sources*, **146** [1-2] (2005) 707.

[49] N. Ota, N. Okuda, K. Emura, and A. Yamakawa, *SEI Technical Review*, **61** (2006) 41.

[50] F. Mizuno, A. Hayashi, K. Tadanaga, and M. Tatsumisago, *J. Electrochem. Soc.*, **152** (2005) A1499.

[51] F. Mizuno, A. Hayashi, K. Tadanaga, and M. Tatsumisago, *J. Power Sources*, **146** (2005) 711.

[52] L.-J. Fu, H. Liu, C. Li, Y.-P. Wu, E. Rahm, R. Holzeb, and H.-Q. Wu, *Solid State Sciences*, **8** (2006) 113.

[53] C. Li, H.-P. Zhang, L.-J. Fu, H. Liu, Y.-P. Wu, E. Rahmb, R. Holze, and H.-Q. Wu, *Electrochimica Acta*, **51** (2006) 3872.

[54] J. Cho, C.-S. Kim, and S. Yoo, *Electrochem. Solid-State Lett.* **3** (2000) 362.

[55] J. Cho, Y.J. Kim, and B. Park, *Chem. Mater.*, **12** (2000) 3788.

[56] J. Cho, Y.J. Kim, J.T. Kim, and B. Park, *Angew. Chem. Int. Ed.*, **40** (2001) 3367.

[57] J. Cho, B. Kim, J.-G. Lee, Y.-W. Kim, and B. Park, *J. Electrochem. Soc.*, **152** (2005) A32.

[58] M. Mladenov, R. Stoyanova, E. Zhecheva, and S. Vassilev, *Electrochem. Commun.*, **3** (2001) 410.

[59] Z. Wang, C. Wu, L. Liu, F. Wu, L. Chen, and X. Huang, *J. Electrochem. Soc.*, **149** (2002) A466.

[60] Z.X. Wang, X.J. Huang, L.Q. Chen, *J. Electrochem. Soc.*, **150** (2003) A199.

[61] Z. Chen and J.R. Dahn, *Electrochem. Solid-State Lett.*, **6** (2003) A221.

[62] Z. Chen and J.R. Dahn, *Electrochim. Acta*, **49** (2004) 1079.

[63] Y.-K. Sun, S.-W. Cho, S.-T. Myung, K. Amine, and J. Prakash, *Electrochim. Acta*, **53**

(2007) 1013.

[64] Y.-K. Sun, C.-S. Yoon, S.-Y. Myung, I. Belharouak, and K. Amine, *J. Electrochem. Soc.*, **156** (2009) A1005.

[65] J. Zhang, Y.-J. Xiang, Y. Yu, S. Xie, G.-S. Jiang, and C.-H. Chen, *J. Power Sources*, **132** (2004) 187.

[66] Y. Kobayashi, S. Seki, M. Tabuchi, H. Miyashiro, Y. Mita, and T. Iwahori, *J. Electrochem. Soc.*, **152** (2005) A1985.

[67] S. Seki, Y. Kobayashi, H. Miyashiro, Y. Ohno, A. Usami, Y. Mita, M. Watanabe, N. Terada, *Chem. Commun.* (2006) **544**.

[68] K. Takada, N. Ohta, L. Zhang, K. Fukuda, I. Sakaguchi, R. Ma, M. Osada, and T. Sasaki, *Solid State Ionics*, **179** (2008) 1333.

[69] A. Brazier, L. Dupont, L, Dantras–Laffont, N. Kuwata, J. Kawamura, and J.-M. Tarascon, *Chem. Mater.*, **20** (2008) 2352.

2. Improvement of Electrochemical Performance of All-Solid-State Cells by Interfacial Modification between Layered Metal Oxide Electrode and Li_2S–P_2S_5 Solid Electrolyte

2.1. Introduction

Lithium-ion secondary batteries have been widely used as power sources. Improved battery safety is necessary to realize advanced devices. Organic electrolytes have been used in commercial lithium-ion batteries. The lithium-ion secondary batteries have the safety concerns. For the improvement of safety and reliability of the batteries, the development of all-solid-state lithium secondary batteries using inorganic solid electrolytes is anticipated. Bulk-type all-solid-state batteries with the Li_2S–P_2S_5 glass-ceramic electrolytes exhibit long cycle performance [1]. Actually, the all-solid-state battery In/Li_2S–P_2S_5 glass-ceramics/$LiCoO_2$ was charged and discharged for more than 700 cycles with retaining high capacity of about 110 mAh g^{-1} at a current density of 0.064 mA cm^{-2} [1]. However, there are some challenges to be overcome in all-solid-state lithium secondary batteries. One is the enhancement of rate capability, which is one of the most important issues for the commercialization of bulk-type all-solid-state batteries. It is difficult for all-solid-state batteries to operate under a high current density of more than several milliamperes per square centimeter, despite the use of solid electrolytes with high lithium-ion conductivity. The second is the improvement of energy density. At the present stage, energy density of bulk-type all-solid-state batteries is less than that of conventional batteries. The third is the improvement of cycle performance. All-solid-state batteries show excellent cycle performance with a mild operation condition. The improvement of cycle performance of all-solid-state batteries under a severe condition, such as a large current density, high cut-off voltage, and high temperature, is anticipated.

One disadvantage of all-solid-state batteries is the difficulty of forming an effective electrode-electrolyte interfacial contact. In the batteries using a liquid electrolyte, a contact between electrode and electrolyte is effectively formed just by soaking an electrode active material into an electrolyte solution. In contrast, both electrode and electrolyte materials are solid in the all-solid-state batteries. It is necessary to form favorable interface between electrode and electrolyte to fabricate all-solid-state lithium secondary batteries with high performance.

A composite electrode which consists of electrode active materials, conductive additives and solid electrolytes has been used as an electrode layer to form lithium-ion and electron conducting path in an all-solid-state battery system. The design of composite electrodes is important. The use of suitable conductive additives and the optimization of the composite ratio of active materials and solid electrolytes were carried out to improve rate capability; the charge and discharge under a high current density more than 1 mA cm^{-2} were achieved in the bulk-type all-solid-state batteries [2, 3].

Modification of interface between $LiCoO_2$ electrode and the sulfide-based solid electrolyte by the coatings of oxide thin films has been reported to improve rate capability by decreasing interfacial resistance between electrode and solid electrolyte. Ohta *et al.* first reported that the coatings of $Li_4Ti_5O_{12}$, $LiNbO_3$, and $LiTaO_3$ on $LiCoO_2$ particles formed by spray coating brought about an excellent rate capability in the all-solid-state batteries using crystalline $Li_{3.25}Ge_{0.25}P_{0.75}S_4$ (thio-LISICON) as a solid electrolyte [4-6].

Oxide coatings on positive electrode materials were reported to improve cycle performance of the conventional batteries. So far, $LiCoO_2$ has been widely used as a positive electrode material for lithium-ion secondary batteries. $LiCoO_2$ has a layered structure and lithium ions deintercalate and intercalate during the charge-discharge process; $LiCoO_2$ shows excellent electrode performance as positive electrode. $LiCoO_2$ is typically

used at the potential up to 4.2 V vs. Li; the available capacity is about 140 mAh g^{-1}, which is only a half of the theoretical capacity of about 280 mAh g^{-1}. In order to increase the available capacity of the $LiCoO_2$, it needs to be charged above 4.2 V. However, a significant capacity fading is observed at such a high potential region. Oxide coatings such as SnO_2, Al_2O_3, ZrO_2, MgO, $AlPO_4$, Li_3PO_4, and $Li_{1.5}Al_{0.5}Ge_{1.5}(PO_4)_3$ and the other coatings such as Li_2CO_3 and AlF_3 on $LiCoO_2$ have been reported as an effective approach to improve cycle performance at a high potential above 4.2 V in the batteries with organic liquid [7-18], polymer [19, 20], and ionic liquid electrolytes [21]. The effects of the modification are reported as (i) suppression of structural change caused by phase transition of $LiCoO_2$, (ii) decrease of cobalt dissolution from $LiCoO_2$ to liquid electrolyte, and (iii) suppression of side reactions between the electrode and electrolyte. Okamoto *et al.*, have reported the performance at a high cutoff voltage of the all-solid-state batteries with $LiCoO_2$ electrode and the $0.01Li_3PO_4 \cdot 0.63Li_2S \cdot 0.36SiS_2$ glass electrolyte [22]. They investigated the charge-discharge performance at various charging cutoff potentials between 3.5 and 4.1 V vs. Li–In (4.1 and 4.7 V vs. Li) as shown in figure 2-1; initial capacities of the batteries increased with increasing the cutoff voltage as expected. However, the charge-discharge curves of the batteries which operated at a high cutoff potential above 3.9 V vs. Li–In were affected by large polarization, resulting in the capacity fading of the batteries. It is expected that the oxide coatings are effective in decreasing the interfacial resistance at the high potential.

In the present chapter, thin films of various materials were prepared and applied to all-solid-state batteries. The thin films are coated on a positive active material of $LiCoO_2$ to investigate the effects of the coatings on the electrochemical performance of all-solid-state cells. As the thin films, lithium-ion conducting solid electrolytes were mainly selected. The solid electrolyte films have been usually used in the research field of all-solid-state thin film lithium batteries. In this study, solid electrolyte films were used as coatings for

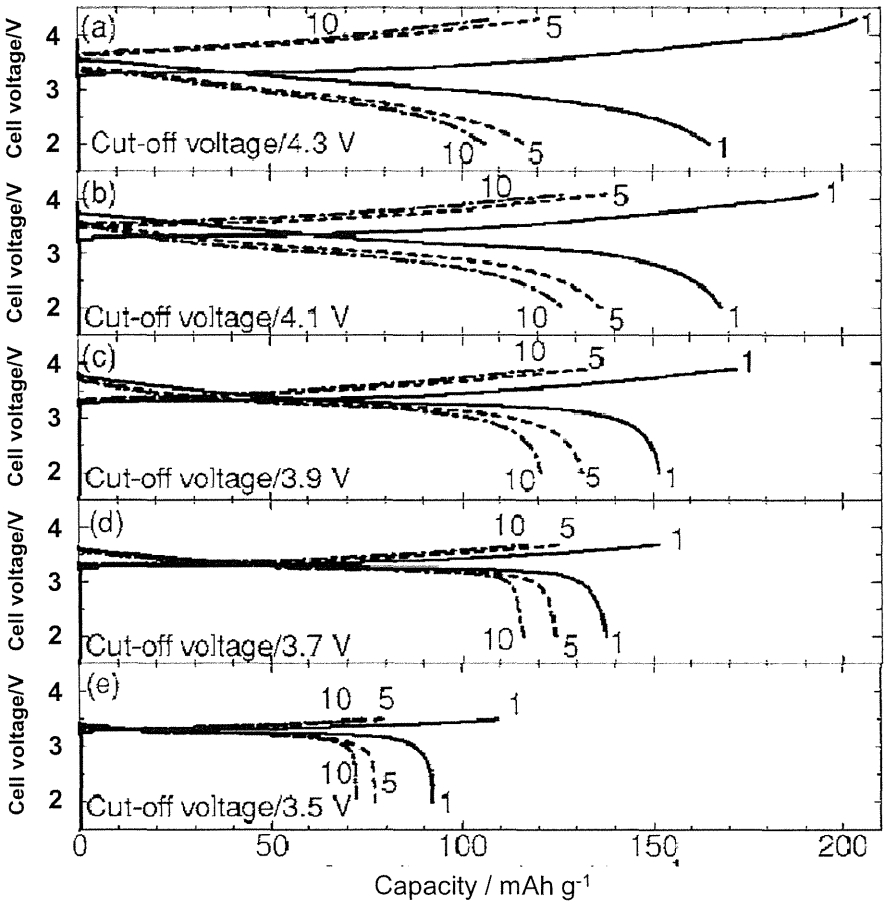

Figure 2-1 Dependence of the upper voltage limit: (a) 4.3, (b) 4.1, (c) 3.9, (d) 3.7, (e) 3.5 V, of first, fifth, and tenth charge and discharge curves for all-solid-state In/$LiCoO_2$ cells. [Ref. 22]

modification of the interfacial properties between positive electrode materials and sulfide-based solid electrolytes.

The electrochemical performance such as rate capability of all-solid-state batteries using uncoated $LiCoO_2$ and Li_2S–P_2S_5 solid electrolytes was studied to investigate the effects of the interfacial modifications on the electrochemical performance. Rate capability is strongly related with internal resistance in a battery. Impedance components of the all-solid-state cells with $LiCoO_2$ electrode and Li_2S–P_2S_5 solid electrolytes were identified using electrochemical impedance spectroscopy (EIS).

The interface between $LiCoO_2$ and Li_2S–P_2S_5 solid electrolyte was modified by coating oxide and sulfide materials on the $LiCoO_2$ particles. The coatings were introduced as a buffer layer between $LiCoO_2$ electrode and Li_2S–P_2S_5 solid electrolyte to improve interfacial properties. Although, the electrochemical performance of the batteries should be affected by the type of coating materials, the influence of coating materials has not been clarified yet. To investigate the importance of lithium-ion and electron conductivity of the coating materials, (i) inslative coatings such as SiO_2, (ii) low lithium-ion conductive coatings such as Li_2SiO_3, (iii) high lithium-ion conductive coatings such as amorphous Li_3PO_4, and (iv) electron conductive coatings such as CoS were coated on $LiCoO_2$ particles; their electrode performances in the all-solid-state cells using Li_2S–P_2S_5 solid electrolytes were evaluated.

The coatings were carried out using various techniques such as sol-gel, pulsed laser deposition (PLD), and thermal decomposition techniques to investigate coating effects on various types of materials. By using a sol-gel technique, lithium metal oxide such as amorphous Li_2O–SiO_2 and Li_2O–TiO_2 were coated on $LiCoO_2$ particles. PLD was used to prepare amorphous oxide films with high lithium-ion concentration, which are difficult to prepare using the sol-gel technique. To investigate the effect of coatings of sulfide materials, metal sulfide such as CoS and NiS were coated on $LiCoO_2$ particles; the electrochemical

performance of the all-solid-state cells using metal sulfide-coated $LiCoO_2$ was investigated. The coatings of the metal sulfide were formed using a thermal decomposition of dietyldithiocarbamates [$M(S_2CN(C_2H_5)_2)_2$] [23-26].

The coating amounts of the oxides and sulfides were varied to examine effects of thickness and coverage of the coating materials on electrochemical performance of all-solid-state cells. The effects of the interfacial modification are mainly investigated using electrochemical measurements such as EIS and charge-discharge measurements on the all-solid-state cells using coated $LiCoO_2$ particles.

2.2. Experimental

2.2.1. Preparation of Li_2S–P_2S_5 solid electrolytes

In this study, an $80Li_2S{\cdot}20P_2S_5$ (mol %) glass-ceramic among Li_2S–P_2S_5 solid electrolytes was mainly used as a solid electrolyte. The $80Li_2S{\cdot}20P_2S_5$ (mol %) glass-ceramic for solid electrolytes was prepared using mechanical milling and subsequent heat treatment [27]. For preparation of the $80Li_2S{\cdot}20P_2S_5$ glass, Li_2S (99.9%; Idemitsu Kosan Co. Ltd.) and P_2S_5 (99%; Aldrich Chemical Co. Inc.) were used as starting materials. These materials were mechanically milled at 510 rpm for 8-10 h at room temperature using a planetary ball mill (Pulverisette 7; Fritsch GmbH) with a zirconia pot (45 mL volume) and 160 zirconia balls of 5 mm diameter or 500 zirconia balls of 4 mm diameter. The obtained glassy powder was heated at 210 °C for 1-4 h to yield highly conductive $80Li_2S{\cdot}20P_2S_5$ glass-ceramic. The conductivity of the $80Li_2S{\cdot}20P_2S_5$ glass-ceramic was *ca.* 6×10^{-4} S cm^{-1}. The resistance for the pellet of 10 mm diameter and 500 μm thicknesses was *ca.* 100-200 Ω. The conductivity was measured using the pelletized $80Li_2S{\cdot}20P_2S_5$ glass-ceramic particles in a cell with stainless steel current collectors.

2.2.2. Preparation of oxide-coated $LiCoO_2$ by sol-gel technique

Amorphous SiO_2, TiO_2, Li_2O–SiO_2 with the Li_2O contents of 50 mol% (Li_2SiO_3), and Li_2O–TiO_2 with the Li_2O contents of 33 mol% ($Li_2Ti_2O_5$) films were coated on $LiCoO_2$ particles using a sol-gel technique. Scheme 2-1 shows the schematic diagram of the preparation procedure of oxide-coated $LiCoO_2$ particles using a sol-gel technique. The Li_2O–SiO_2 sols were prepared from lithium ethoxide (LiOEt) and tetraethoxysilane [$Si(OEt)_4$] under a N_2 gas atmosphere. Lithium metal (Li, 86 mmol) was added in dry ethanol (EtOH, 90 mL) and the mixture was refluxed until Li was dissolved to obtain LiOEt in ethanol (EtOH) solution. $Si(OEt)_4$ (43 mmol) was then added to the resultant solution and the solution was stirred at room temperature. SiO_2 sols were also prepared from EtOH (90 mL), $Si(OEt)_4$ (65 mmol), and 0.1 wt % hydrochloric acid aqueous solution [0.1 % (HCl)aq, 260 mmol]. The $Li_2Ti_2O_5$ sols were prepared from EtOH (10 mL, 99.5%), LiOEt (1 mmol, 1M solution in ethanol), titanium tetra-iso-propoxide [Ti(O-*i*-Pr)$_4$, 1 mmol, 95%], and acetyl acetone (AcAc, 1 mmol, 99%). The TiO_2 sols were also prepared from ethanol (10 mL), Ti(O-*i*-Pr)$_4$ (1 mmol), and AcAc (1 mmol).

The sols were diluted with dry ethanol. Then the diluted sols were mixed with $LiCoO_2$ particles (D10, Toda Kogyo Corp.). After drying at room temperature, the mixture was heated at 350°C for 30 min. The weight ratios of the coatings to $LiCoO_2$ particles were varied from 0.06/100 to 0.6/100.

2.2.3. Preparation of oxide-coated $LiCoO_2$ by pulsed laser deposition technique

The target at the composition $50Li_4SiO_4 \cdot 50Li_3PO_4$ (mol%) was prepared using lithium carbonate (Li_2CO_3, 99.997%), silica (SiO_2, 99.9%), and lithium orthophosphate (Li_3PO_4, 98%) as starting materials. The mixture of the starting materials was calcined at 750°C for 12 h and the obtained ceramics were milled with dehydrated EtOH using ball milling for 12 h

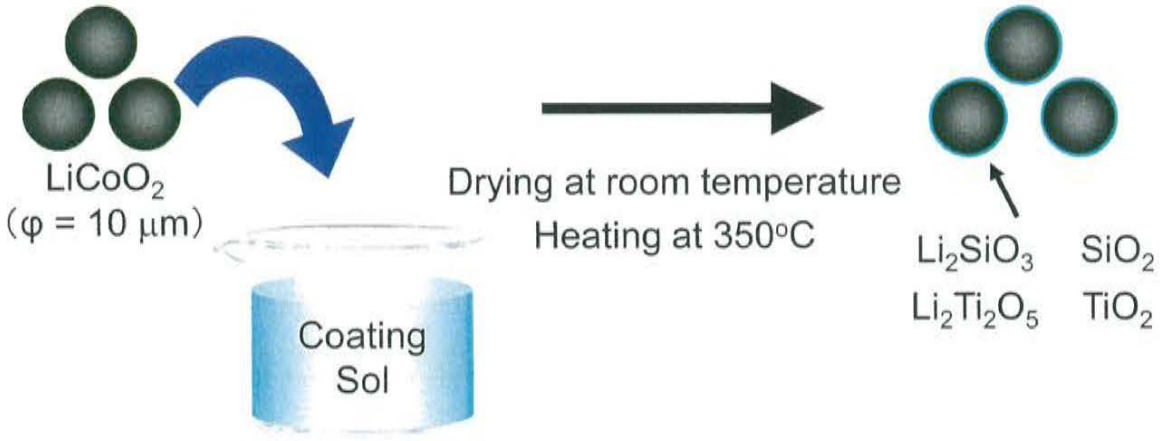

Scheme 2-1 Preparation procedure of oxide-coated $LiCoO_2$ particles using a sol-gel technique.

to obtain fine powder. After the ball milling, the obtained powder was dried at 80 °C for 24 hours. The powder was pressed into a pellet (20 or 23 mm in diameter), and the pellet was sintered with following steps of heating: at 400°C for 1 h, 800 °C for 1h, and at 1100 °C for 2 h. The lithium orthosilicate Li_4SiO_4 target was also prepared from Li_2CO_3 and SiO_2. The mixture was calcined at 750 °C for 12 h and then milled for 12 h with dehydrated EtOH. The obtained powder was pressed into a pellet and sintered at 750 °C for 6 h. The Li_3PO_4 target was prepared from Li_3PO_4 particles. The Li_3PO_4 powder milled for 12 h with dehydrate EtOH was pressed into a pellet and it was heated at 600 °C for 6 h [28]. The thin films were prepared by PLD with a KrF excimer laser (λ = 248 nm, LPXPro, Lambda Physik). The deposition condition is summarized in Table 2-1. Argon gas (99.99%) was used as an ambient gas. Laser fluence and argon gas pressure were changed; 2-6 J cm^{-2} of laser fluence and 0.01-5 Pa of Ar gas pressure were used. In a PLD vacuum chamber used in this study, a target holder was attached at an upper side and substrates were put at a bottom side in order to deposit thin films on particles in the later experiment. Silicon or quartz substrates were placed parallel to the target at a distance of 70 mm. The deposition was operated at room temperature. The $LiCoO_2$ particles modified with the Li_3PO_4, $50Li_4SiO_4 \cdot 50Li_3PO_4$, and Li_4SiO_4 thin film were prepared by coating the films on $LiCoO_2$ particles (D-10, Toda Kogyo Corp.). The $LiCoO_2$ particles were fluidized by a vibration system (VIB-FB, Nara Machinery Co., Ltd.) during the deposition.

2.2.4. Preparation of sulfide-coated $LiCoO_2$ by thermal decomposition technique

(i) Preparation of diethyldithiocarbamato metal complexes

Bis(diethyldithiocarbamato) cobalt (II) $[Co\{S_2CN(C_2H_5)_2\}_2]$ was prepared by the reaction between sodium diethyldithiocarbamate $[NaS_2CN(C_2H_5)_2]$ and cobalt (II) chloride ($CoCl_2$) in distilled water at room temperature. Obtained precipitate was washed with

Table 2-1 Deposition condition of amorphous Li_4SiO_4–Li_3PO_4 solid electrolyte thin films

Laser	**KrF excimer laser (248 nm)**
Target	**Li_3PO_4, Li_4SiO_4, Li_4SiO_4-Li_3PO_4**
Laser fluence	***ca.* 2-6 J cm^{-2} (200-600 mJ / pulse)**
Frequency	**10 Hz**
Temperature	**Room temperature**
Ambient gas	**Ar gas**
Gas pressure	**10^{-2} - 5 Pa**
T-S Distance (Target-substrate distance)	**7 cm**

distilled water to remove NaCl and water-soluble impurity and was recrystallized using CH_2Cl_2/*n*-hexane solvent. Similarly, Bis(diethyldithiocarbamato) nickel (II) [$Ni\{S_2CN(C_2H_5)_2\}_2$] was prepared by the reaction between sodium diethyldithiocarbamate [$NaS_2CN(C_2H_5)_2$] and nickel (II) chloride ($NiCl_2$) in distilled water at room temperature. Obtained precipitate was washed with distilled water to remove NaCl and water-soluble impurity and was recrystallized using CH_2Cl_2/*n*-hexane solvent.

(ii) Preparation of metal sulfides

Scheme 2-2 (a) shows the preparation procedure of cobalt sulfide (CoS) and nickel sulfide (NiS) by thermal decomposition of the respective dithiocarbamato complexes. The CoS was prepared by heat treatment of $Co[S_2CN(C_2H_5)_2]_2$ at 400°C for 2 h in an N_2 atmosphere. Similarly, the NiS was prepared by heat treatment of $Ni[S_2CN(C_2H_5)_2]_2$ at 400°C for 2 h in an N_2 atmosphere. The thermal decomposition behavior of the dithiocarbamato complexes was characterized with differential thermal analysis (DTA) / thermogravimetry (TG, Thermo plus 2 TG-8110, Rigaku). The X-ray diffraction (XRD) measurements were conducted to identify CoS and NiS prepared by thermal decomposition of $Co[S_2CN(C_2H_5)_2]_2$ and $Ni[S_2CN(C_2H_5)_2]_2$, respectively.

(iii) Preparation of metal-sulfide-coated $LiCoO_2$ particles

Scheme 2-2 (b) shows the preparation procedure of CoS-coated $LiCoO_2$ and NiS-coated $LiCoO_2$ particles. The $Co[S_2CN(C_2H_5)_2]_2$ was dissolved in CH_2Cl_2. Then the solution was mixed with $LiCoO_2$ particles (D10, Toda Kogyo Corp.) and dried at room temperature to obtain $LiCoO_2$ particles coated with $Co[S_2CN(C_2H_5)_2]_2$. The $LiCoO_2$ particles coated with $Co[S_2CN(C_2H_5)_2]_2$ were heated at 400°C for 2 hours in an N_2 atmosphere to obtain CoS-coated $LiCoO_2$ particles. NiS-coated $LiCoO_2$ particles were prepared with the same

(a)

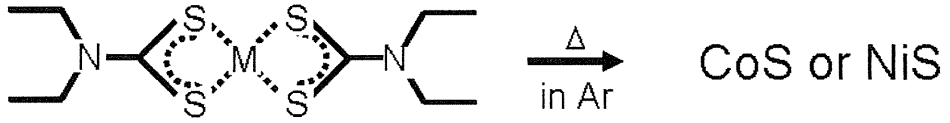

(M = Co or Ni)

(b)

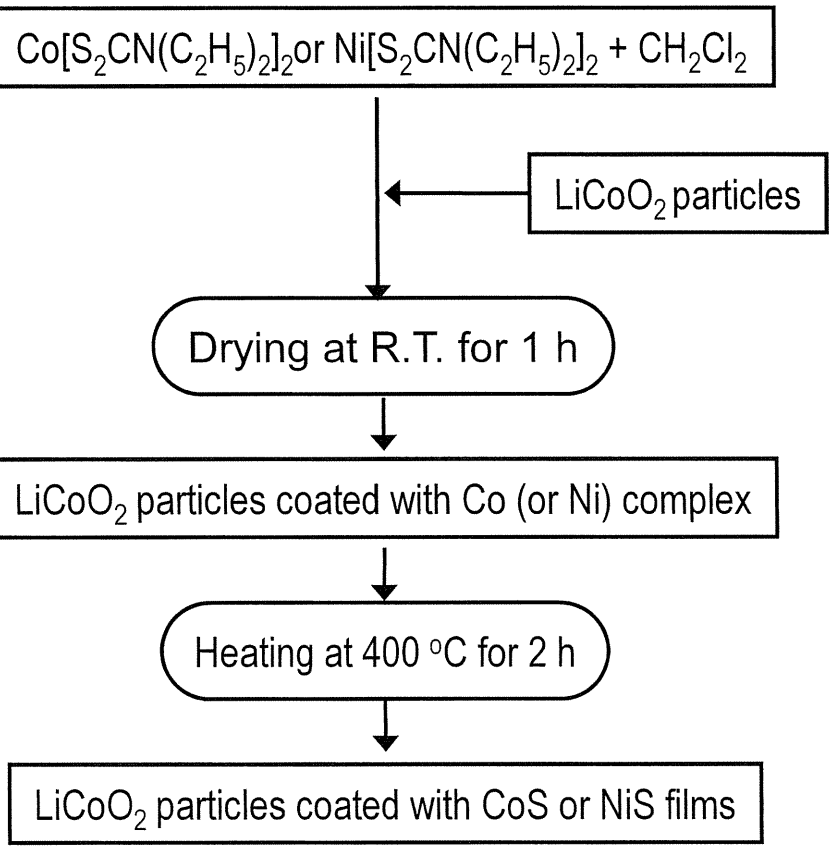

Scheme 2-2 Preparation procedure of (a) CoS and NiS and (b) metal sulfide-coated $LiCoO_2$ particles by a thermal decomposition technique.

procedure to CoS-coated $LiCoO_2$ using $Ni[S_2CN(C_2H_5)_2]_2$ as a precursor coating material.

2.2.5. Preparation of all-solid-state cells

All-solid-state cells were constructed as follows. The $LiCoO_2$ particles (D-10; Toda Kogyo Corp.) used for a positive electrode material were dried at 350°C before fabricating the all-solid-state cells. The $LiCoO_2$, Li_2S–P_2S_5 solid electrolytes, and conductive additive (vapor growth carbon fiber; VGCF) with a weight ratio of 70 : 30 : 0 or 40 : 60 : 4 were mixed using an agate mortar to prepare positive composite electrodes. Indium foil (99.999%; Furuuchi Chemical Corp.) was used as a negative electrode. A bilayer pellet consisting of the composite positive electrode (10 mg) and Li_2S–P_2S_5 solid electrolytes (80 mg) was obtained by pressing under 360 MPa (ϕ=10 mm); the indium foil was then attached to the bilayer pellet by pressing under 240 MPa. The pellet was pressed using two stainless steel rods; the stainless steel rods were used as current collectors for both positive and negative electrodes. All the processes for preparation of solid electrolytes and fabrication of all-solid-state batteries were performed in a dry Ar-filled glove box.

2.2.6. Characterization

Morphologies of prepared materials were observed using a field-emission (FE) scanning electron microscope (FE-SEM/S4500; Hitachi, Ltd.), SEM (JSM-5300; JEOL, or Tiny SEM Mighty-8; Technex Lab. Co., Ltd) equipped with an energy-dispersive X-ray spectroscopy (EDX) system, and a field-emission transmission electron microscope (FE-TEM, JEM-2010F; JEOL) operated at 200 kV. The cross section of the coated $LiCoO_2$ particle was obtained using a focused ion beam system (FB-2000A; Hitachi, Ltd.).

Electrochemical impedance spectroscopy measurements of the all-solid-state cells were performed using an impedance analyzer (SI 1260; Solartron) coupled with a

potentiostat/galvanostat (SI 1287; Solartron). The applied voltages used were 10-50 mV and the frequency range was from 10 mHz to 1 MHz. The cells were charged and discharged using a charge-discharge measuring device (BTS-2004; Nagano Co. Ltd.). The measurements were mainly conducted at 25°C.

2.3. Results and discussion

2.3.1. Rate capability of all-solid-state cells using uncoated $LiCoO_2$ and Li_2S–P_2S_5 solid electrolytes

Figure 2-2 (a) shows the discharge curves of all-solid-state cell In/$80Li_2S \cdot 20P_2S_5$ glass-ceramic/$LiCoO_2$ at various current densities of 0.13, 1.3, 2.6, and 6.4 mA cm^{-2} after charging to 3.6 V vs. Li–In, which corresponds to 4.2 V vs. Li, at a low current density of 0.13 mA cm^{-2}. On a discharge process at a large current density, a large polarization (a decrease in the discharging voltage) is observed. The resistance of the solid electrolyte layer used for the preparation of the cell was estimated as 150 Ω. The internal resistance, which is calculated from the potential drop and the current density, is about 300 to 400 Ω. The result shows that there is a large resistance except for the resistance of solid electrolyte layer. In addition to the decrease of the discharge voltage, the decrease of discharge capacities are observed with increasing the current density. The discharge capacities at 0.13, 1.3, 2.6, and 6.4 mA cm^{-2} are 64, 46, 36, and 10 mAh g^{-1}, respectively. Figure 2-2 (b) shows the cycle performance of all-solid-state cell at the current density of 1.3 mA cm^{-2}. The cutoff voltages for charging and discharging are 1.0 and 4.0 V vs. Li–In, respectively. The all-solid-state cell can be reversibly charged and discharged under a relatively high current density of 1.3 mA cm^{-2}. The decrease of capacity is observed during charge-discharge measurement. The rate capability of all-solid-state cells should be improved.

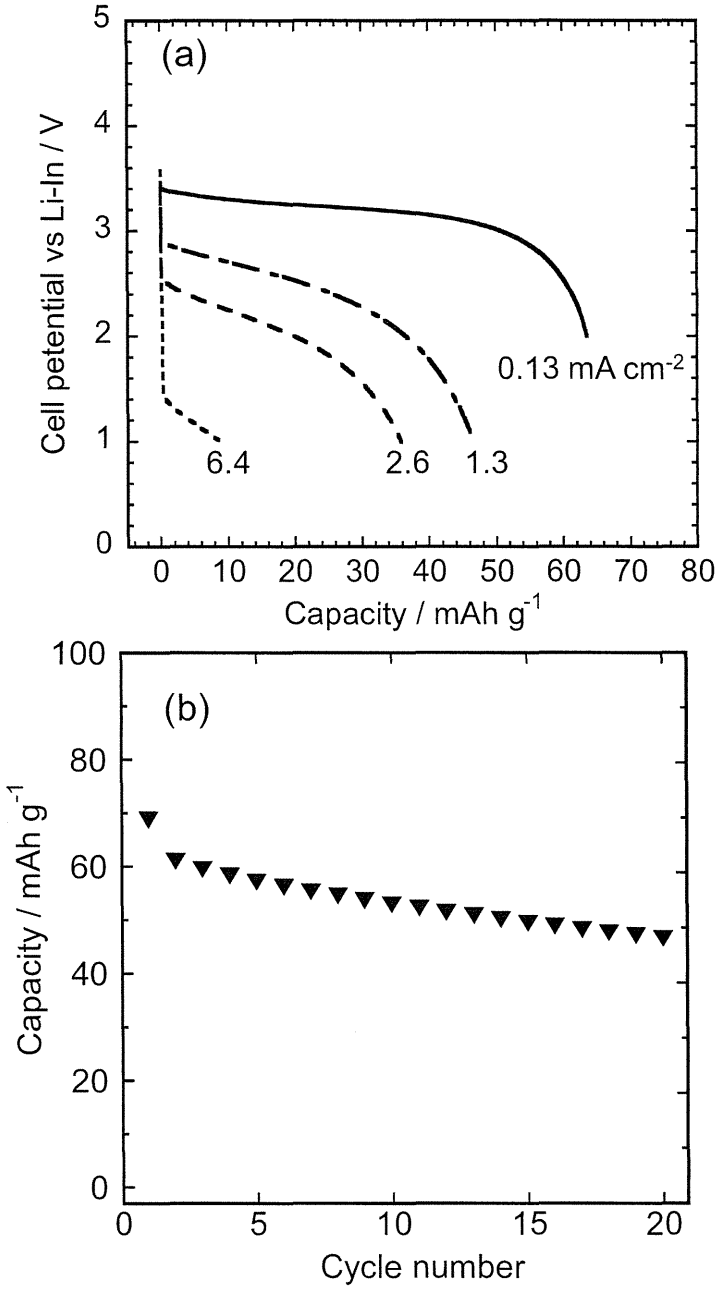

Figure 2-2

(a) Discharge curves of In / $80Li_2S{\cdot}20P_2S_5$ glass-ceramic / $LiCoO_2$ cells. The charging current density and cutoff voltage were 0.13 mA cm^{-2} and 3.6 V (vs Li-In), respectively.

(b) Cycle performance of all-solid-state cell In / $80Li_2S{\cdot}20P_2S_5$ glass-ceramic / $LiCoO_2$ at the current density of 1.3 mA cm^{-2} for charging and discharging. The cutoff voltage was 2.0-4.0 V vs. Li-In.

2.3.2. Impedance analysis on all-solid-state cells

As shown above, the rate capability of all-solid-state cells using $LiCoO_2$ as a positive electrode, indium (In) as a negative electrode, and $80Li_2S{\cdot}20P_2S_5$ glass-ceramic as a solid electrolyte is limited by the internal resistance. In order to improve rate capability of the all-solid-state cell, the decrease of the internal resistance is essential. Therefore, the resistance component of all-solid-state cell was identified to clarify which part of the all-solid-state cell was the cause of the large resistance. Ohta *et al.* has reported that there is a large resistance between $LiCoO_2$ and $Li_{3.25}Ge_{0.25}P_{0.75}S_4$ after charging [4, 5].

Figure 2-3 shows impedance profiles of the all-solid-state cells with various electrodes. Figure 2-3 (a) shows the impedance profile of the $In/80Li_2S{\cdot}20P_2S_5/LiCoO_2$ cell after charging to 3.6 V vs Li–In at the current density of 0.13 mA cm^{-2}. The impedance profiles are shown as connected dots. The impedance profile of panel (a) is separated into three resistance components: one is the resistance observed in the high-frequency region (>100 kHz), and the others correspond to two semicircles (the peak top frequencies of 500 and 1 Hz). Figure 2-3 (b) shows the impedance profile of pure solid electrolyte with stainless steel (SS) electrodes as an ion blocking electrode ($SS/80Li_2S{\cdot}20P_2S_5/SS$). In this impedance profile, the resistance in the high-frequency region (>100 kHz) and the straight line at the low-frequency region are observed. The impedance profile provides the resistance of solid electrolyte (R_{SE}). Therefore, the resistance at the high-frequency region (>100 kHz) is identified as the resistance of solid electrolyte. An $In/80Li_2S{\cdot}20P_2S_5/Li–In$ cell was fabricated to clarify the resistance related with the In electrode. The impedance measurement of the cell was carried out after charging. Figure 2-3 (c) shows the impedance profile of the $In/80Li_2S{\cdot}20P_2S_5/Li–In$ cell. The impedance measurements were carried out after charging at 0.64 mA cm^{-2} for 10 min. Two resistance components were observed in this profile. The resistance observed at the high frequency region (>100 kHz) is the R_{SE}. The

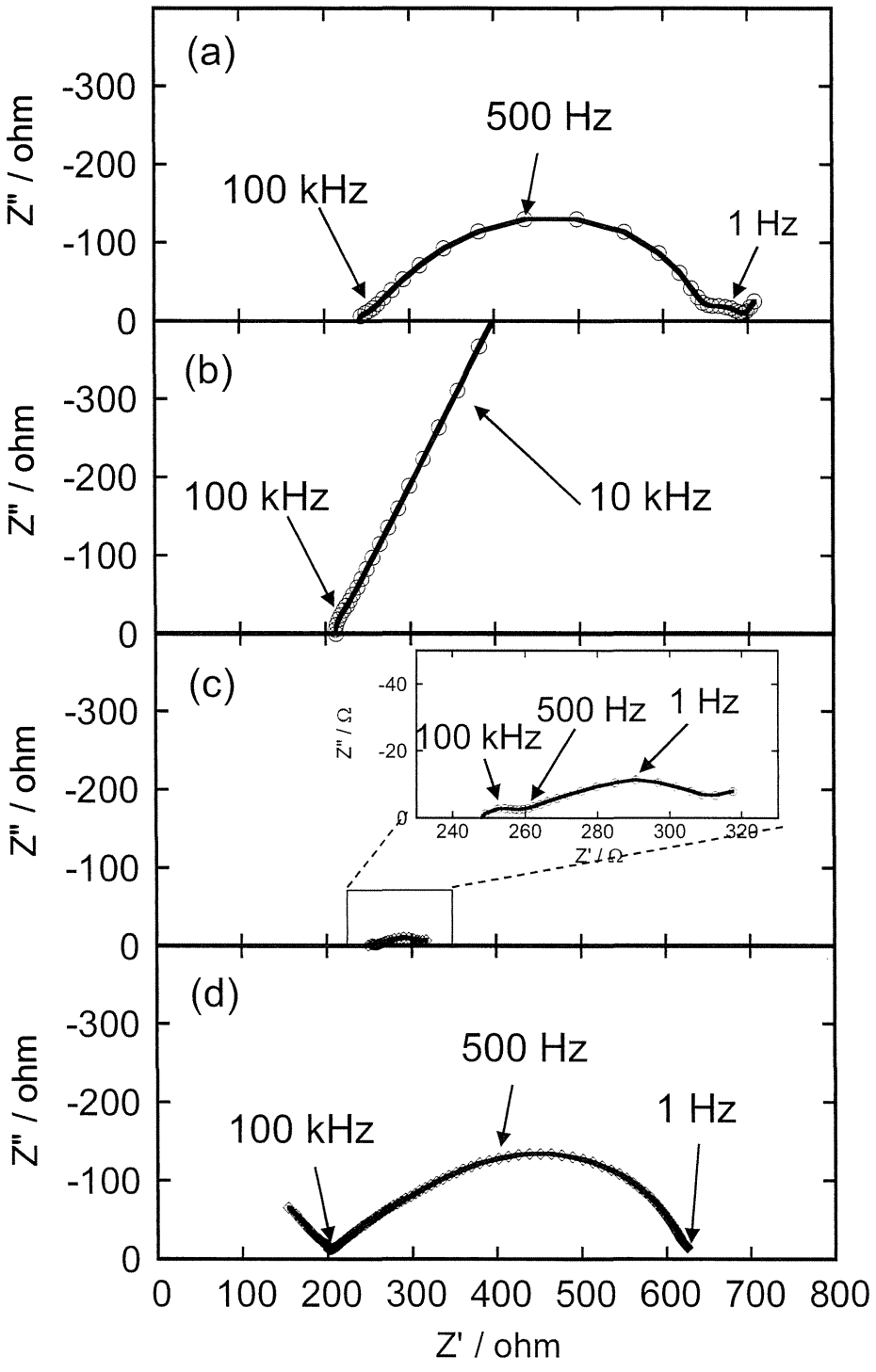

Figure 2-3 Impedance profiles of all-solid-state cells: (a) In/80Li_2S·20P_2S_5/$LiCoO_2$, (b) SS/80Li_2S·20P_2S_5/SS, (c) In/80Li_2S·20P_2S_5/Li–In, and (d) SS/80Li_2S·20P_2S_5/$LiCoO_2$.

resistance at the low frequency region (the peak top frequency of 1 Hz) is attributable to a resistance of the Li–In electrode, which is the negative electrode (R_{NE}). Figure 2-4 shows impedance profiles of In/$80Li_2S{\cdot}20P_2S_5$/Li–In cell for different charging states. The impedance profiles of the resistance observed at the low frequency region was dramatically changed by the charging state of the cells; consequently, R_{NE} relates to lithium-ion concentration in the indium negative electrode. R_{NE} would relate to the lithium diffusion in Li–In alloy. Figure 2-3 (d) shows the impedance profile of the SS/$80Li_2S{\cdot}20P_2S_5$/$LiCoO_2$ cell. The impedance measurement was carried out after charging to 4.2 V vs Li. During the charging process, metal lithium was deposited on the SS electrode surface. In this profile, the resistance at the high-frequency region (R_{SE}) and the resistance at the middle-frequency region (the peak top frequency of 500 Hz) were observed. The middle-frequency region resistance is observed only in the cells using the positive electrode. As a result, the middle-frequency region resistance is regarded as the resistance at the interface between $LiCoO_2$ and $80Li_2S{\cdot}20P_2S_5$ solid electrolyte (R_{PE}). Figure 2-5 shows identification of impedance components of all-solid-state cells In/$80Li_2S{\cdot}20P_2S_5$/$LiCoO_2$ after charging to 3.6 V vs. Li–In. All-solid-state cells have large resistances at the solid electrolyte layer and the interface between $LiCoO_2$ electrode and $80Li_2S{\cdot}20P_2S_5$ solid electrolyte. The resistance between $LiCoO_2$ and $80Li_2S{\cdot}20P_2S_5$ solid electrolyte would result from formation of a high-resistance layer between $LiCoO_2$ and $80Li_2S{\cdot}20P_2S_5$ solid electrolyte, which is discussed in Chapter 3. To improve the rate capability of the all-solid-state batteries, it is necessary to reduce the R_{PE}. In particular, improvement of the interface between electrodes and electrolytes engenders a low R_{PE} and high rate capability.

2.3.3. All-solid-state cells using coated $LiCoO_2$ electrode

2.3.3.1. Oxide-coated $LiCoO_2$ prepared by sol-gel technique

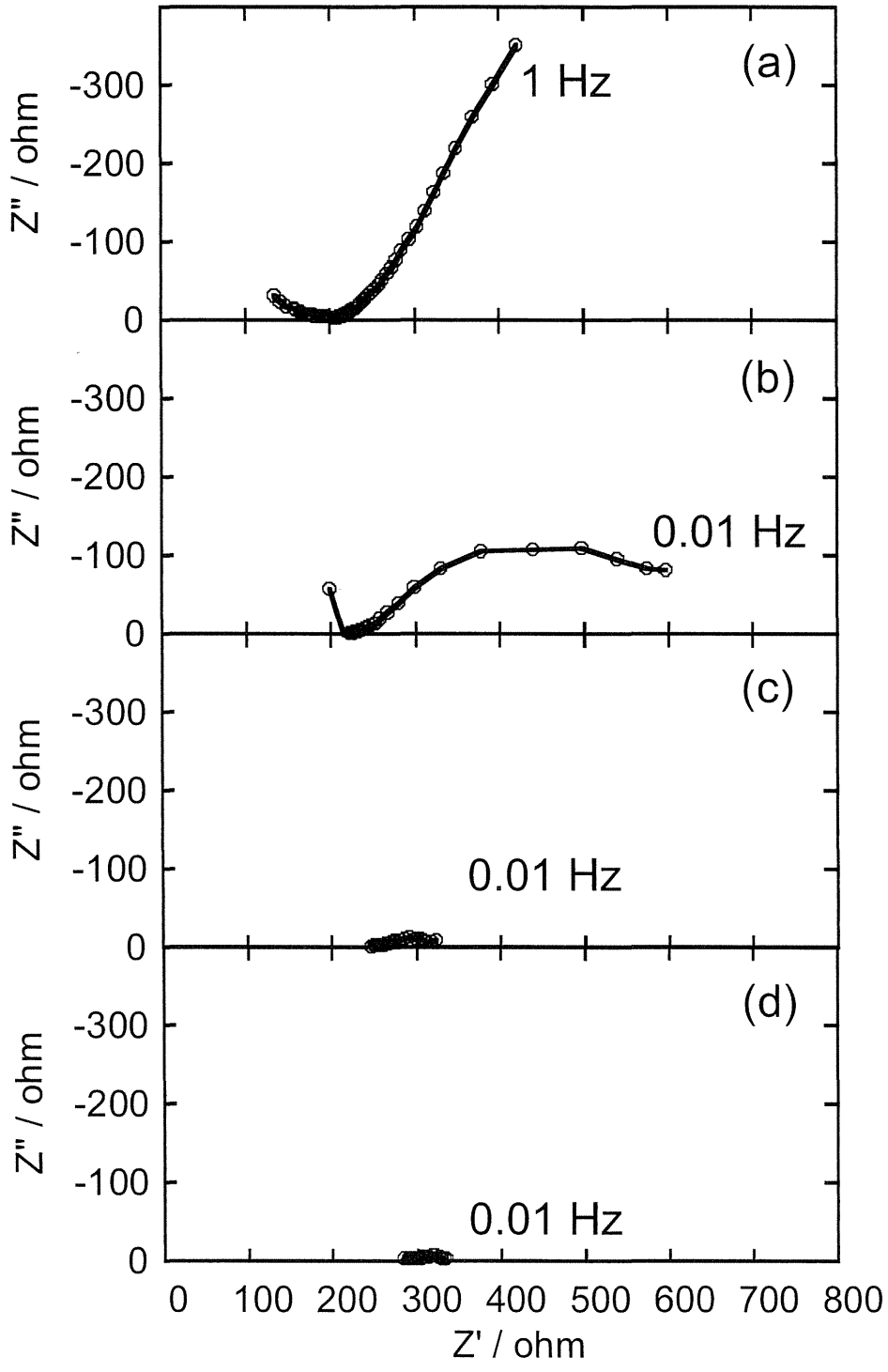

Figure 2-4 Complex impedance plot of In / $80Li_2S{\cdot}20P_2S_5$ glass-ceramic/ Li–In cell. (a) As prepared, (b) 0.1 mA 1 min charging, (c) 0.5 mA 10 min charging, and (d) 0.5 mA 2 h charging.

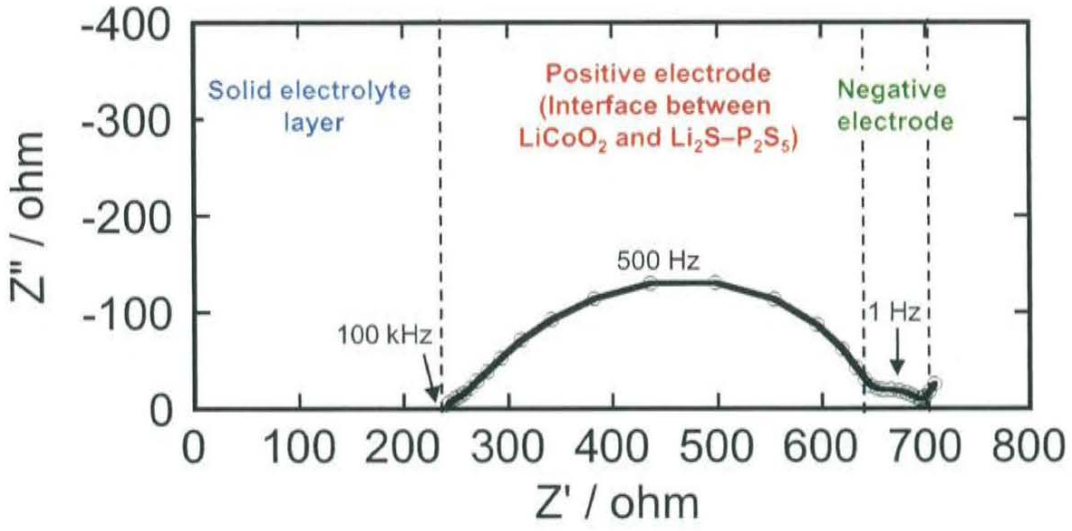

Figure 2-5 Identification of impedance components of all-solid-state cells In/ $80Li_2S{\cdot}20P_2S_5/LiCoO_2$ after charging to 3.6 V vs. Li–In.

(I) Li_2O–SiO_2 system

(i) Morphology of coated $LiCoO_2$

XRD measurements were carried out for Li_2SiO_3 powder prepared using the sol-gel method to determine the heat-treatment temperature of coating films. XRD patterns of the Li_2SiO_3 powder heated at (a) 350 and (b) 500°C for 30 min are shown in Fig. 2-6. The Li_2SiO_3 particles after heat-treatment at 350°C are amorphous. The diffraction patterns attributable to Li_2SiO_3 crystal are observed for the Li_2SiO_3 particles after heat-treatment at 500°C. Because amorphous Li_2SiO_3 exhibits higher lithium-ion conductivity than crystalline Li_2SiO_3 [29], the heat treatment temperature was determined as 350°C in this study.

The surface morphology of the coated $LiCoO_2$ was investigated using FE-SEM observations, TEM observations, and EDX measurements. Figure 2-7 shows the FE-SEM images of $LiCoO_2$ coated with SiO_2 (b-d) and Li_2SiO_3 (e-g). Uncoated $LiCoO_2$ is also shown in Fig. 2-7 (a). The surfaces of the uncoated and the SiO_2-coated $LiCoO_2$ are basically smooth. In the Li_2SiO_3-coated $LiCoO_2$, a somewhat rough surface caused by coating materials is observed. The SiO_2 sols were prepared in acidic conditions and Li_2SiO_3 sols were prepared in basic conditions. In basic conditions, a three-dimensional network of silica tends to grow to form nanosize particles [30]. Therefore, nanoparticles and films are preferentially formed in basic and acidic conditions, respectively. As a result, a rough surface is observed on the Li_2SiO_3-coated $LiCoO_2$ particle.

The EDX mappings of the 0.6 wt % Li_2SiO_3-coated $LiCoO_2$ are showed in Fig. 2-8. Both Si atoms of Li_2SiO_3 and Co atoms of $LiCoO_2$ are detected in the same area, indicating that the $LiCoO_2$ particles are covered with coating materials. Figure 2-9 shows a cross-sectional FE-TEM image of 0.6 wt % Li_2SiO_3-coated $LiCoO_2$ particles. The coating layer was confirmed on the $LiCoO_2$ particles; the coating layer thickness was *ca.* 10 nm.

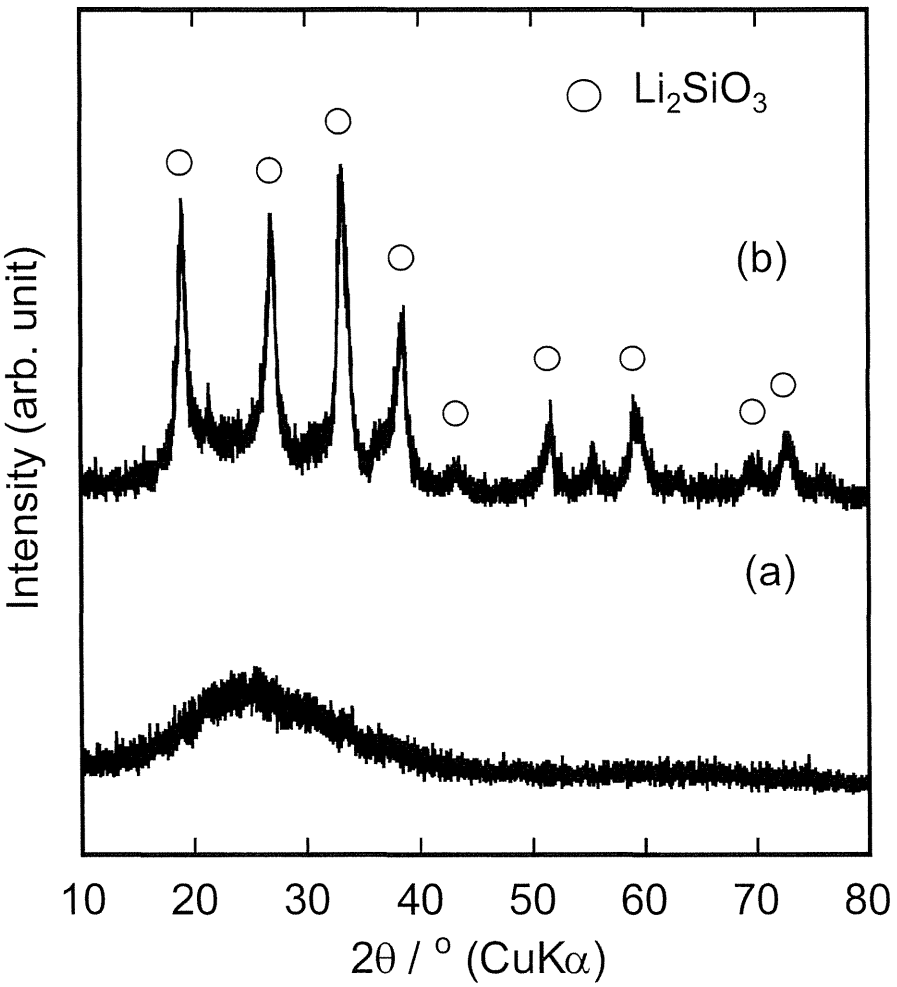

Figure 2-6 XRD patterns of Li_2SiO_3 powder heated at (a) 350 and (b) 500°C.

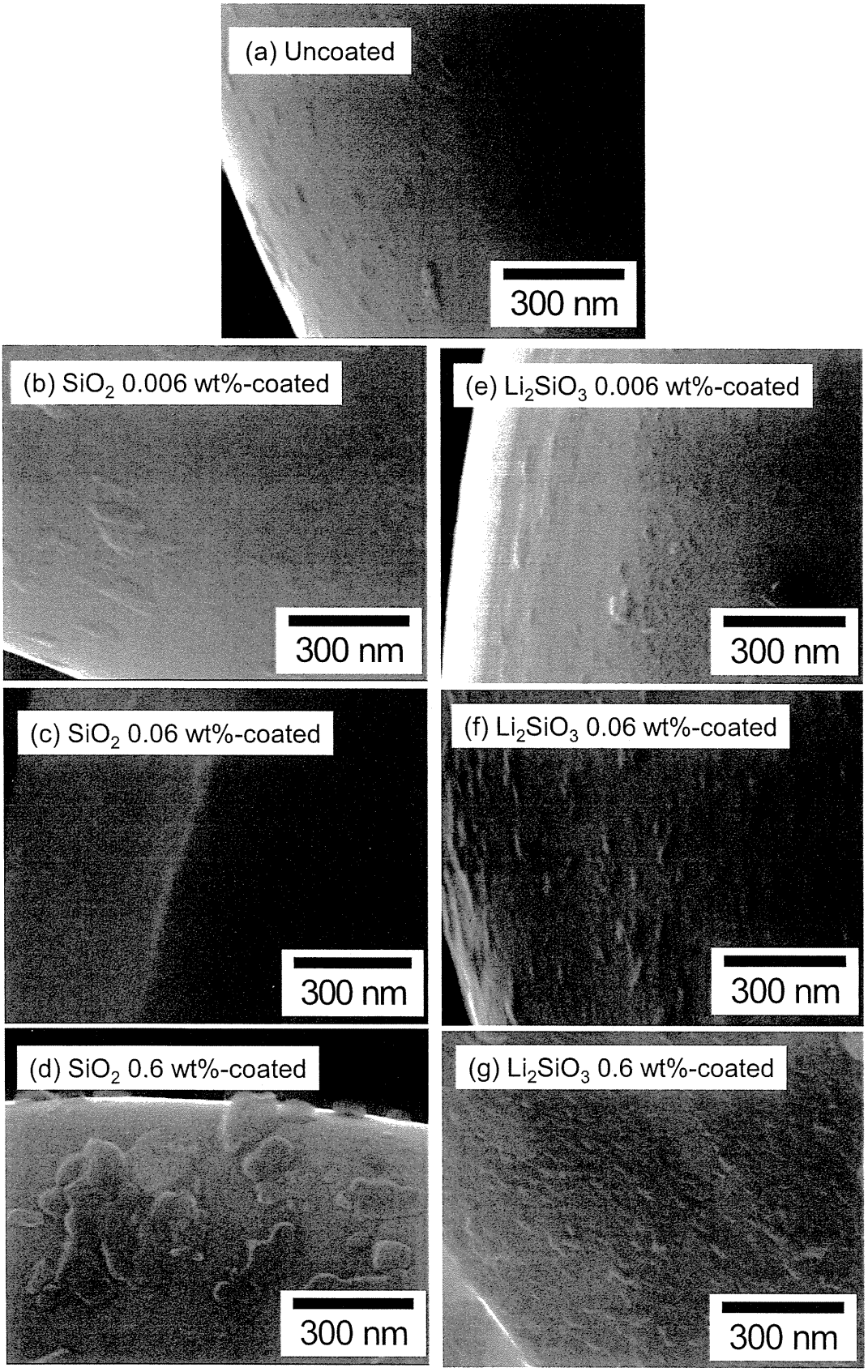

Figure 2-7 FE-SEM images of (a) uncoated, (b) 0.006 wt% SiO_2-coated, (c) 0.06 wt% SiO_2-coated, (d) 0.6 wt% SiO_2-coated, (e) 0.006 wt% Li_2SiO_3-coated, (f) 0.006 wt% Li_2SiO_3-coated, and (g) 0.6 wt % Li_2SiO_3-coated $LiCoO_2$ particles.

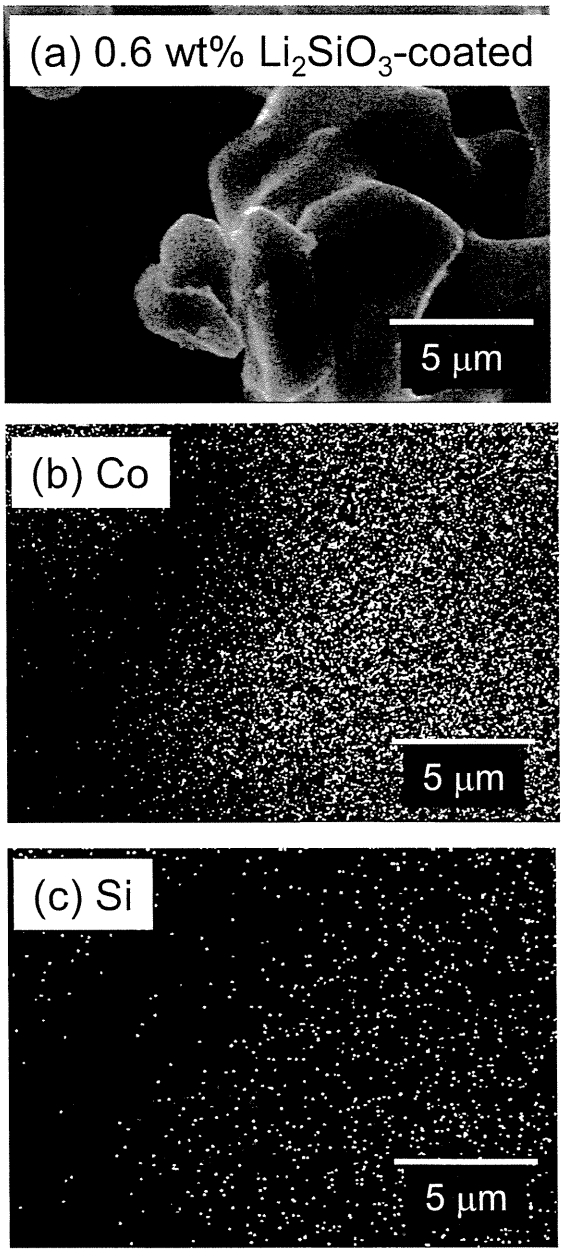

Figure 2-8 SEM image (a) and EDX mappings for (b) Co atom and (c) Si atom of Li_2SiO_3-coated $LiCoO_2$ particles.

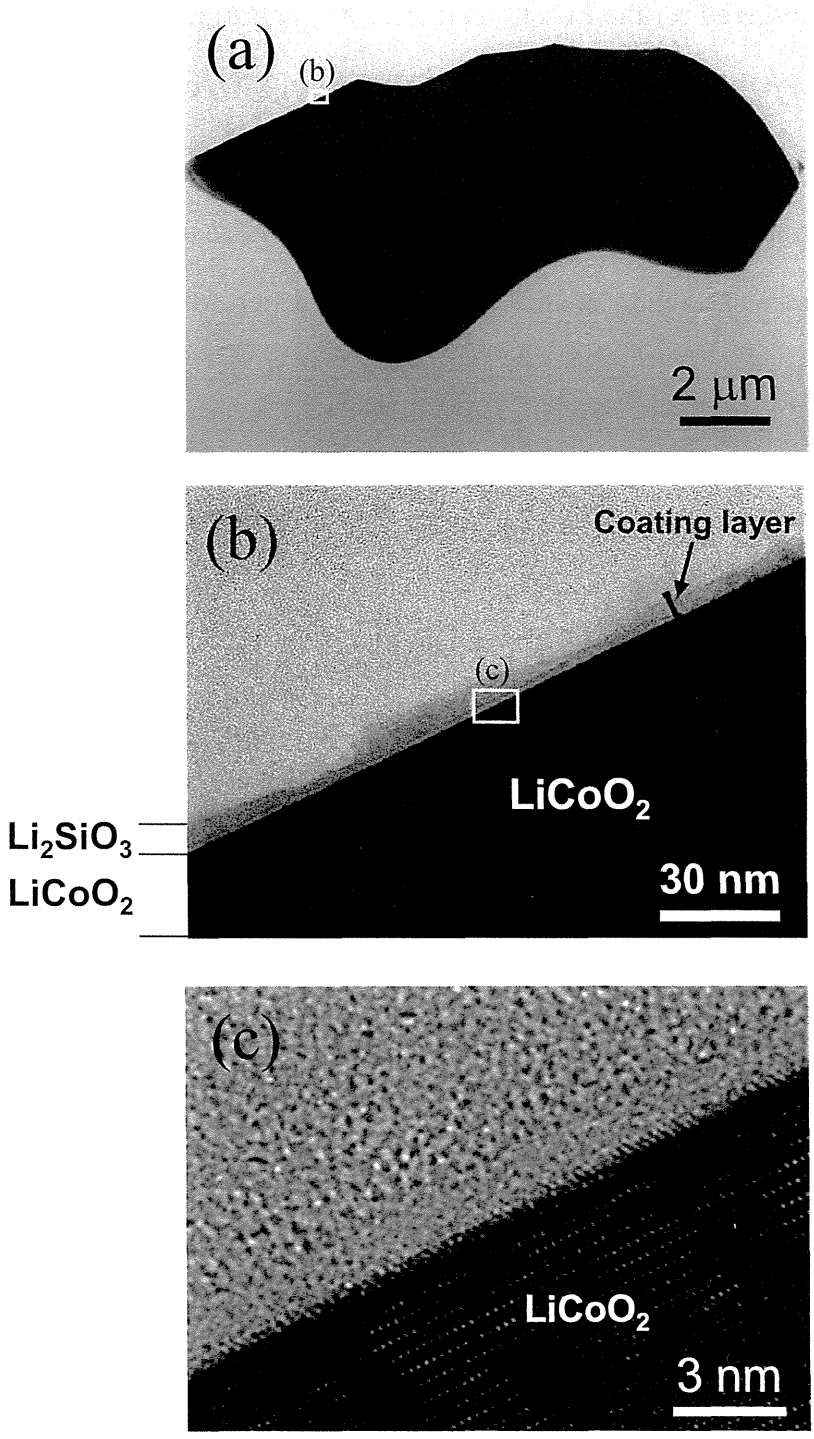

Figure 2-9 TEM images of Li_2SiO_3-coated $LiCoO_2$ particle.

The crystalline lattice is observed for the $LiCoO_2$ particle. In contrast, the crystalline lattice is not observed for the Li_2SiO_3 coating layer, indicating that the Li_2SiO_3 coating is amorphous. The presence of Si and O atoms in the coating layer was supported by EDX point analysis of the coating layer as shown in Fig. 2-10. In the EDX profiles, the existence of Co element of $LiCoO_2$ is not observed, indicating that cobalt diffusion from $LiCoO_2$ to Li_2SiO_3 during heat treatment is negligible.

(ii) Electrochemical performance

Figure 2-11 presents impedance profiles of the as-prepared all-solid-state cells with uncoated, 0.06 wt % SiO_2-coated, and 0.6 wt % SiO_2-coated $LiCoO_2$. Similar profiles to SS/80Li_2S·20P_2S_5/SS cells, as presented in Fig. 2-3 (b), were obtained in each cell; no remarkable difference is observed between uncoated and coated $LiCoO_2$. Figure 2-12 shows the impedance profiles of cells after charging to 3.6 V vs Li–In at a current density of 0.13 mA cm^{-2}. The total resistances of the cells using uncoated, 0.06 wt % SiO_2-coated, and 0.6 wt % SiO_2-coated $LiCoO_2$ are about 500, 440, and 630 Ω, respectively. In fact, R_{SE} at >100 kHz and R_{NE} at 1 Hz show almost the same values in the three cells. R_{PE} at 500 Hz of uncoated, 0.06 wt % SiO_2-coated, and 0.6 wt % SiO_2-coated $LiCoO_2$ are 270, 220, and 450 Ω, respectively. Although the SiO_2 coating contains no lithium ions, 0.06 wt % of SiO_2 coating reduces R_{PE}, where the coating layer is expected to be sufficiently thin. The coating layer is expected to play a role in a buffer layer to prevent direct contact between $LiCoO_2$ and sulfide solid electrolyte. Consequently, the formation of a high-resistance layer, which would form between bare $LiCoO_2$ and sulfide solid electrolyte, is suppressed. R_{PE} of 0.6 wt % of the SiO_2 coating is larger than that of no coating, because the SiO_2 coating itself acts as a highly resistive layer for a case in which the coating layer is thick. Figure 2-13 shows impedance profiles of all-solid-state cells with uncoated, 0.06 wt % Li_2SiO_3-coated, and 0.6 wt %

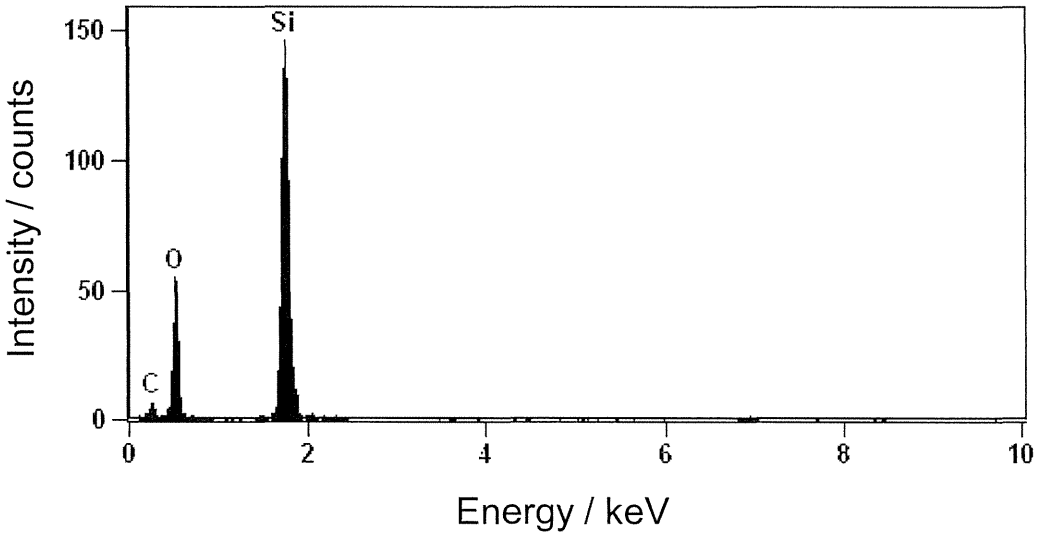

Figure 2-10 EDX spectrum of Li_2SiO_3-coating layer on $LiCoO_2$ particles.

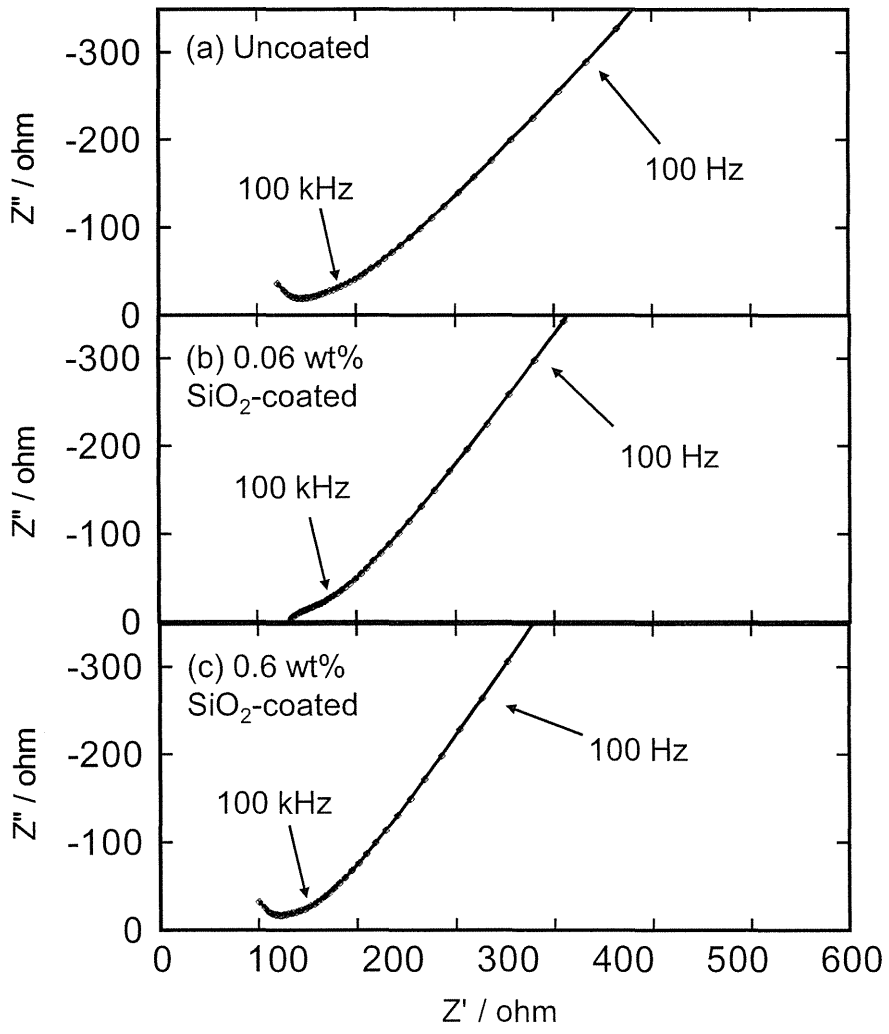

Figure 2-11 Impedance profiles of as-prepared all-solid-state cells In/80Li_2S·20P_2S_5 glass-ceramic/$LiCoO_2$ with (a) uncoated, (b) 0.06 wt % SiO_2-coated, and (c) 0.6 wt % SiO_2-coated $LiCoO_2$.

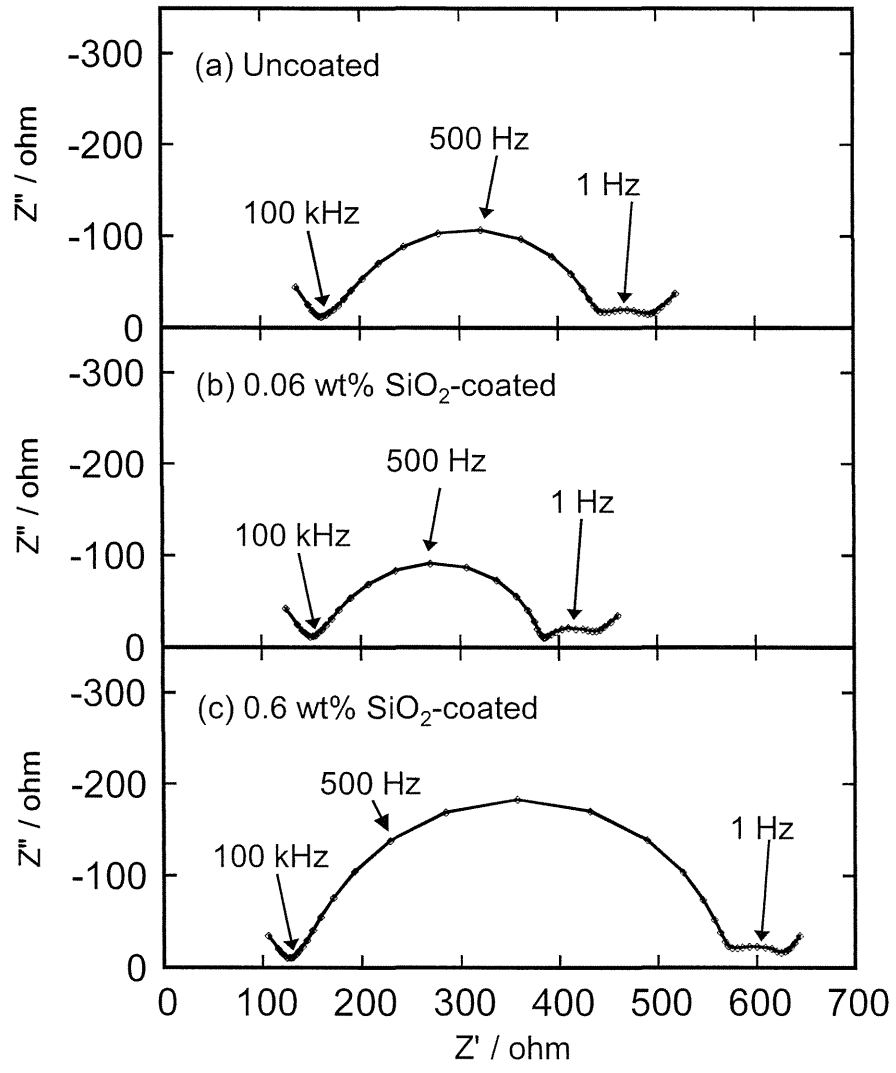

Figure 2-12 Impedance profiles of In/80Li_2S·20P_2S_5 glass-ceramic/$LiCoO_2$ cells with (a) uncoated, (b) 0.06 wt % SiO_2-coated, and (c) 0.6 wt % SiO_2-coated $LiCoO_2$. The measurements were conducted after charging to 3.6 V vs. Li-In at a current density of 0.13 mA cm^{-2}.

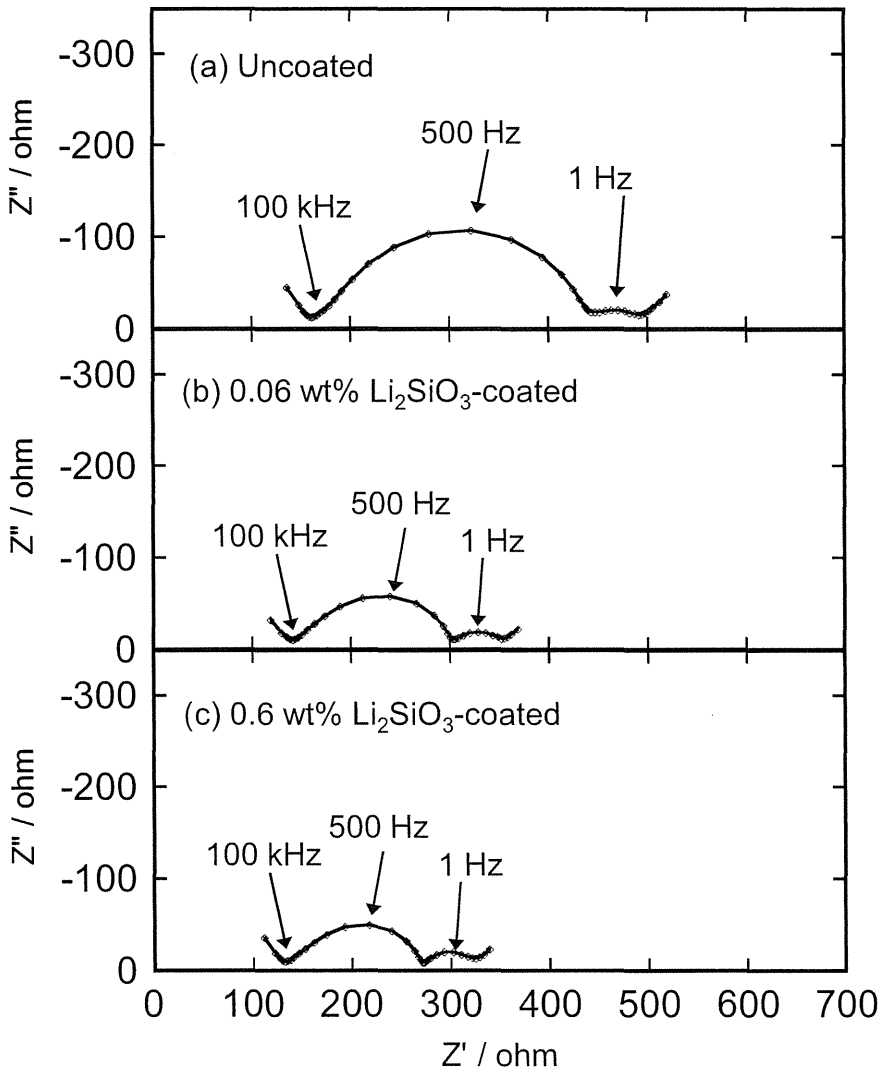

Figure 2-13 Impedance profiles of In/80Li_2S·20P_2S_5 glass-ceramic/$LiCoO_2$ cells with (a) uncoated, (b) 0.06 wt % Li_2SiO_3-coated, and (c) 0.6 wt % Li_2SiO_3-coated $LiCoO_2$. The measurements were conducted after charging to 3.6 V vs. Li-In at a current density of 0.13 mA cm^{-2}.

Li_2SiO_3-coated $LiCoO_2$. R_{PE} at 500 Hz of the cell with 0.06 wt % Li_2SiO_3 coating is 160 Ω. Unlike the SiO_2 coating, 0.6 wt % Li_2SiO_3 coating further reduces R_{PE} to 130 Ω. The Li_2SiO_3 coatings, which contain lithium ions, are more effective in reduction of R_{PE} than the SiO_2 coatings, indicating that lithium-ion conductivity of the coating layer is important to form a better interface between $LiCoO_2$ and Li_2S–P_2S_5 solid electrolytes. Temperature dependence of these resistances was investigated to elucidate in greater detail the coating effects on the R_{SE} and R_{PE} resistance.

Figure 2-14 shows the temperature dependence of (a) R_{SE} and (b) R_{PE} of uncoated and coated $LiCoO_2$. Reciprocal resistance ($1/R_{SE}$, $1/R_{PE}$) obeys the Arrhenius equation, expressed as

$$1/R_{(SE,PE)} = A \exp(-E_a/RT)$$

where *Ea* is the activation energy, *A* is the pre-exponential factor, and *R* is the gas constant. Figure 2-14 (a) indicates that almost identical profiles are observed in all the cells. Their activation energies were calculated from the slope of the plots to be 36 kJ mol^{-1} in each cell, which is similar to the activation energy of the $80Li_2S \cdot 20P_2S_5$ glass-ceramic solid electrolyte (about 30 kJ mol^{-1}) [31]. These results support that the value of R_{SE} is attributable to the resistance of the solid electrolyte layer. Figure 2-14 (b) indicates that almost equal activation energies are obtained in all the cells. The activation energies of lithium-ion conduction at the interface between the $LiCoO_2$ and solid electrolyte of the cells with uncoated, SiO_2-coated, and Li_2SiO_3-coated $LiCoO_2$ were calculated as 61, 62, and 61 kJ mol^{-1}, respectively. These results indicate that the decrease of R_{PE} was not caused by a decrease of activation energy but rather by an increase of pre-exponential factor for conduction in the Arrhenius equation. The activation energy of about 61 kJ mol^{-1} resembles that in the 1 mol dm^{-3} $LiClO_4$–propylene carbonate/$LiCoO_2$ system (61 kJ mol^{-1}) [32] and the LiPON/$LiCoO_2$

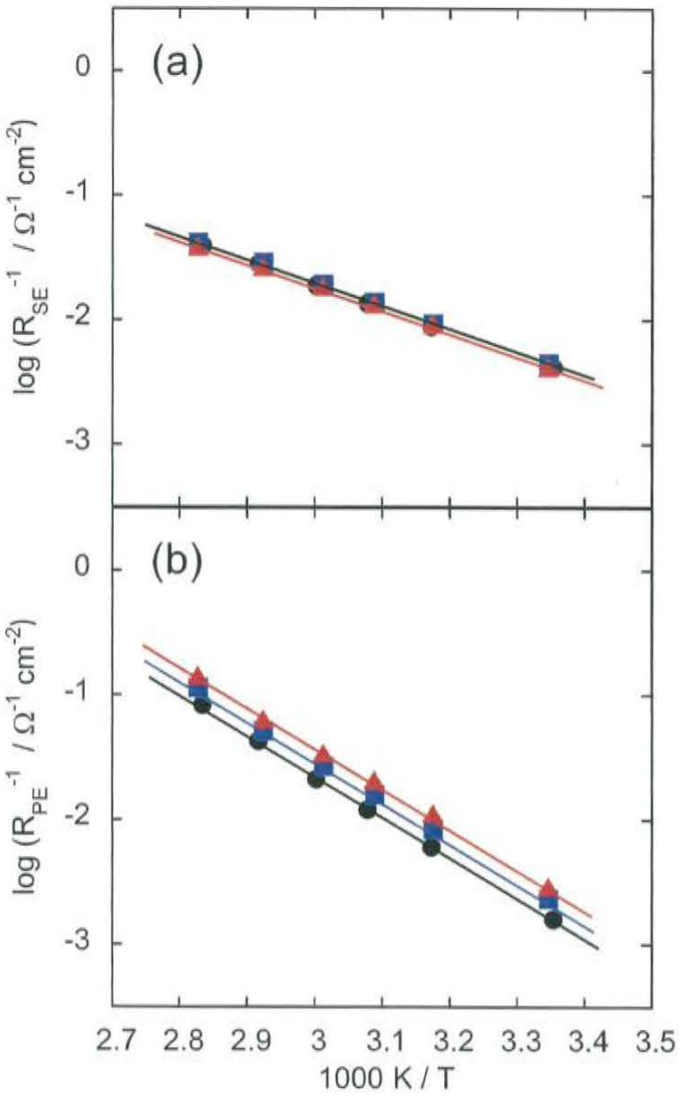

Figure 2-14 Temperature dependence of (a) $1/R_{SE}$ and (b) $1/R_{PE}$ for cells using uncoated (circles), 0.06 wt % SiO_2-coated (squares), and 0.06 wt % Li_2SiO_3-coated (triangles) $LiCoO_2$.

system (57 kJ mol^{-1}) [33]. Iriyama *et al.* reported that the decrease of interfacial resistance and the increase of pre-exponential factor by a thermal treatment of LiPON/$LiCoO_2$ interface are brought about by an increase in the electrochemically active area at the interface between LiPON and $LiCoO_2$ [33]. In the present study, one possible explanation for the increase in pre-exponential factor is that the oxide coating increases the electrochemically active area. The pre-exponential factor would also be affected by the lithium-ion concentration at the interface. The Li_2SiO_3 coating is more effective in increasing the pre-exponential factor than the SiO_2 coating, suggesting that the high lithium-ion concentration at the interface increases the pre-exponential factor. In ion conductors, ion conductivity is usually related directly to the mobile ion concentration, which is mainly included in the pre-exponential factor in the Arrhenius equation; the ion concentration does not exponentially depend on temperature [34]. The pre-exponential factor of the cell with uncoated $LiCoO_2$ is the smallest in each cell. Uchimoto and Wakihara reported from X-ray absorption spectroscopy that a compound whose electronic state resembles that of CoS formed at the interface between $LiCoO_2$ and sulfide electrolyte during charge–discharge cycling [35]. The compound at the interface would have poor lithium-ion concentration. Consequently, the pre-exponential factor for the uncoated $LiCoO_2$ is the smallest. The coatings of SiO_2 and Li_2SiO_3 suppress the reaction between $LiCoO_2$ and sulfide electrolyte by preventing their direct contact; the coatings also increase lithium-ion concentration at the $LiCoO_2$-sulfide electrolyte interface. These results support the findings in the Li–In/thio-LISICON/$LiCoO_2$ system reported by Ohta *et al.* [4, 5]. They described that the high interfacial resistance between $LiCoO_2$ and thio-LISICON was originated from the formation of a lithium-deficient layer at the interface; the lithium-ion conducting oxides prevented the formation of the lithium-deficient layer. Therefore, it was inferred in this study that the highly resistive layer was attributable to poor lithium-ion conductivity at the interface between the $LiCoO_2$ and sulfide electrode.

After charging the cells to 3.6 V vs. Li–In at the current density of 0.13 mA cm^{-2}, discharge measurements were carried out at the various current densities of 0.13–6.4 mA cm^{-2}. Figure 2-15 shows discharge curves of the cell $In/80Li_2S{\cdot}20P_2S_5/LiCoO_2$. In a high-rate discharge at current densities more than 1.3 mA cm^{-2}, the cutoff voltage is 1 V vs Li–In electrode, which corresponds to 1.6 V vs. Li. At a low-rate discharge (0.13 mA cm^{-2}), the discharge capacities of the uncoated, SiO_2-coated, and Li_2SiO_3-coated $LiCoO_2$ are 63, 70, and 95 mAh g^{-1}, respectively. The discharge capacities depend on the charge capacities, which are increased by somewhat lowering the charging plateau in the case using coated $LiCoO_2$. The difference of discharge-voltage plateaus between the cells with uncoated and coated $LiCoO_2$ is more remarkable in discharge at higher current densities. The average discharge voltages of uncoated, SiO_2-coated, and Li_2SiO_3-coated $LiCoO_2$ at 1.3 mA cm^{-2} are 2.5, 2.75, and 2.9 V vs. Li–In, respectively. The cells can be discharged at a high current density of 6.4 mA cm^{-2}. At the current density, the capacity of the cell with the Li_2SiO_3-coated $LiCoO_2$ is 30 mAh g^{-1}, whereas that of the uncoated $LiCoO_2$ is less than 10 mAh g^{-1}. The rate capability of the all-solid-state lithium secondary batteries is strongly related to the R_{PE}. The decrease of the R_{PE} by oxide coating would lead to a high voltage plateau and large discharge capacity. Rate capability of the cell with lithium-ion-conductive Li_2SiO_3-coated $LiCoO_2$ is much better than that of the cell with insulative SiO_2-coated $LiCoO_2$, suggesting that the lithium-ion conductivity of coating materials affects the electrochemical performance of all-solid-state cells at higher current densities.

Figure 2-16 shows the discharge curves of the cell using 0.06 and 0.6 wt % of SiO_2-coated and Li_2SiO_3-coated $LiCoO_2$ at a current density of 1.3 mA cm^{-2}. The discharge voltage and capacity of the cell using 0.6 wt % Li_2SiO_3-coated $LiCoO_2$ are somewhat higher than those using 0.06 wt % Li_2SiO_3-coated $LiCoO_2$. However, the discharge voltage and capacity of the cell using 0.6 wt % SiO_2-coated $LiCoO_2$ are lower than those using 0.06 wt %

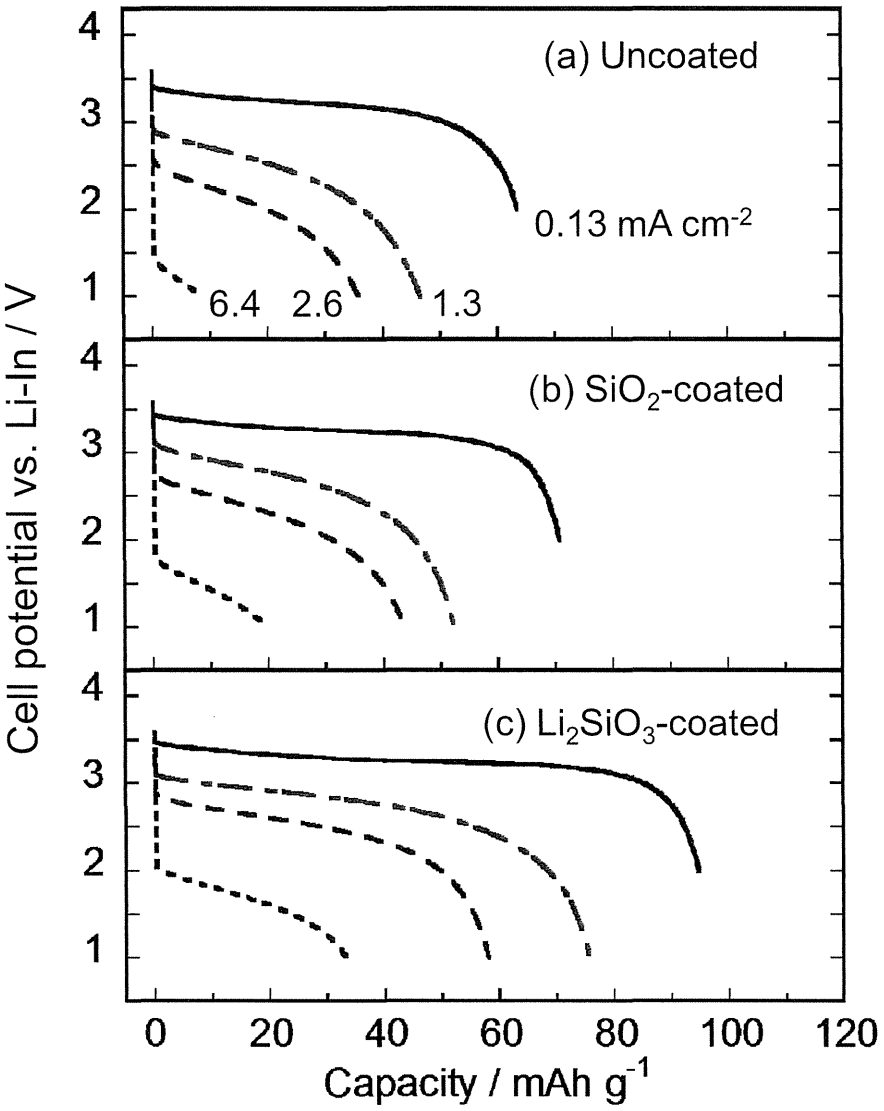

Figure 2-15 Discharge curves of In/80Li_2S·20P_2S_5 glass-ceramic/coated $LiCoO_2$ cells. The $LiCoO_2$ particles with (a) no coating, (b) SiO_2 coating, and (c) Li_2SiO_3 coating were used. The charging current density and cutoff voltage were 0.13 mA cm^{-2} and 3.6 V vs. Li–In, respectively.

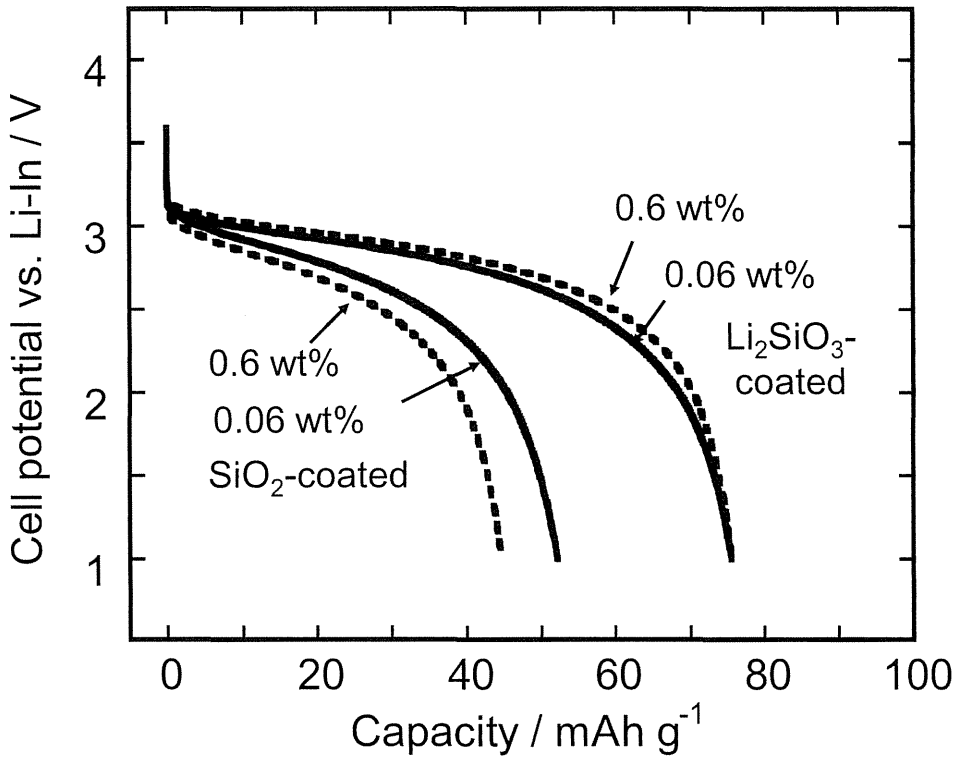

Figure 2-16 Discharge curves for In/$80Li_2S \cdot 20P_2S_5$ glass-ceramic/$LiCoO_2$ cells using 0.06 wt % SiO_2-coated, 0.6 wt % SiO_2-coated, 0.06 wt % Li_2SiO_3-coated, and 0.6 wt % Li_2SiO_3-coated $LiCoO_2$ at a current density of 1.3 mA cm^{-2}.

SiO_2-coated $LiCoO_2$. These results correspond to the cell resistance, as shown in Fig. 2-12 and 2-13. The interfacial modification using Li_2O–SiO_2 glass coating is an effective technique to improve the rate capability of the all-solid-state batteries.

The charge-discharge performance at a high cutoff voltage was investigated for all-solid-state In/$LiCoO_2$ cells. Figure 2-17 (a) shows the charge-discharge curves of the all-solid-state cells with uncoated, 0.06 wt% SiO_2-coated, and 0.06 wt% Li_2SiO_3-coated $LiCoO_2$. The cutoff voltage is 2.0-4.0 V vs. Li–In, which is equivalent to 2.6-4.6 V vs. Li. The cutoff voltage of 4.0 V vs. Li–In was selected as a standard of high voltage in order to evaluate coating effects at high voltage cutoff. The current density used was 0.13 mA cm^{-2}. The initial charge capacities of the cells using uncoated, SiO_2-coated, and Li_2SiO_3-coated $LiCoO_2$ are respectively 120, 160, and 190 mAh g^{-1}. The initial discharge capacities of the cells are respectively 90, 120, and 130 mAh g^{-1}. The average discharge voltages of those are 3.7, 3.9, and 4.0 V, respectively. For comparison, the charge-discharge curves of the all-solid-state cells with uncoated, SiO_2-coated, and Li_2SiO_3-coated $LiCoO_2$ using the cutoff voltage of 2.0-3.6 V vs. Li–In are shown in Fig 2-17(b); the initial discharge capacities of the cells using uncoated, SiO_2-coated, and Li_2SiO_3-coated $LiCoO_2$ with 3.6 V charging cutoff were respectively 63, 70, and 95 mAh g^{-1}. The discharge capacities were increased by increasing cutoff voltage from 3.6 V to 4.0 V vs. Li–In. Larger reversible capacities and higher discharge voltages are obtained in the cells with Li_2SiO_3-coated and SiO_2-coated $LiCoO_2$ than in the cell with uncoated $LiCoO_2$. The cell with Li_2SiO_3-coated $LiCoO_2$ showed superior charge-discharge capacity to the cell with SiO_2-coated $LiCoO_2$. In order to investigate the coating effect in the high cutoff voltage of 4.0 V vs. Li–In, the electrochemical impedance spectroscopy measurements of the all-solid-state cells were carried out.

Figure 2-18 shows the impedance profiles of the all-solid-state cells after the 1st charge process to 4.0 V vs. Li–In at a current density of 0.13 mA cm^{-2}. The resistance of the solid

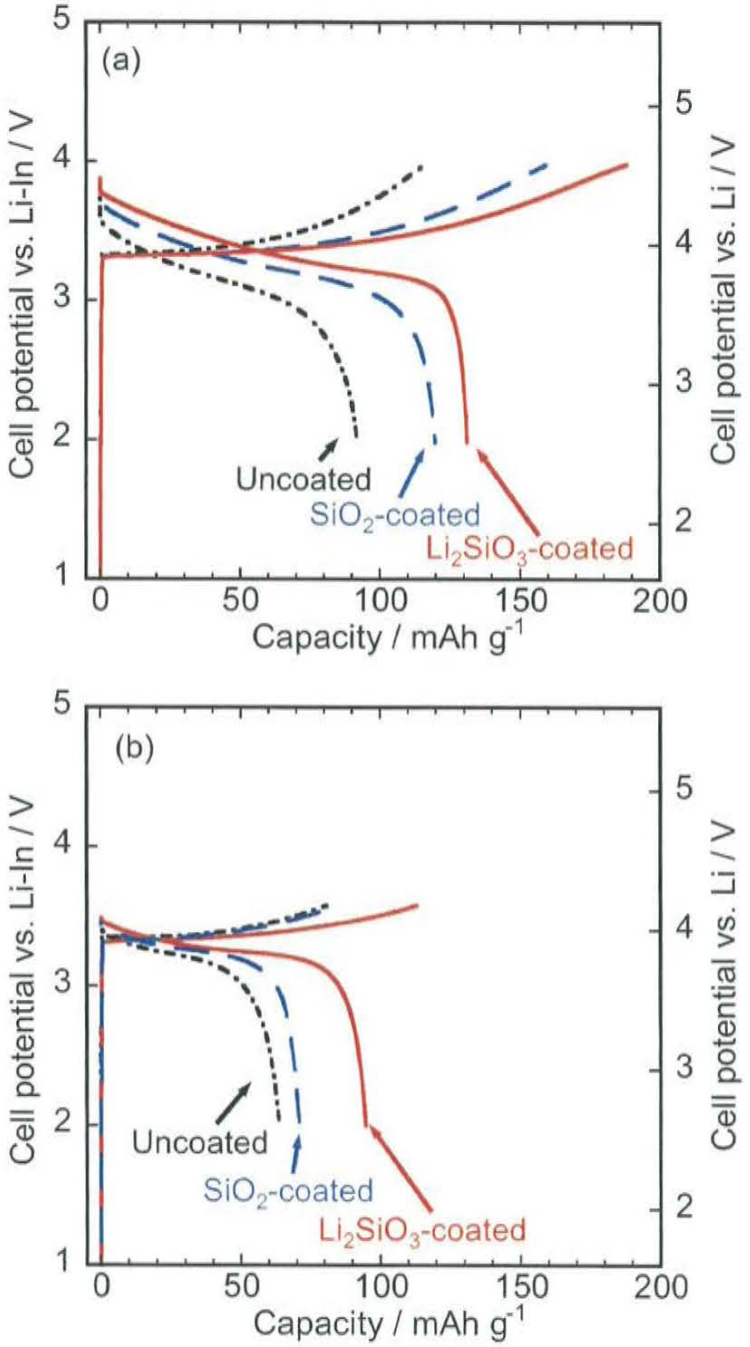

Figure 2-17 Charge–discharge curves of the all-solid-state cells In/80Li_2S·20P_2S_5 glass-ceramic/$LiCoO_2$ with uncoated, SiO_2-coated, and Li_2SiO_3-coated $LiCoO_2$ with the cutoff voltages of (a) 3.6 V and (b) 4.0 V vs. Li-In, respectively. The current densities for charging and discharging were 0.13 mA cm^{-2}.

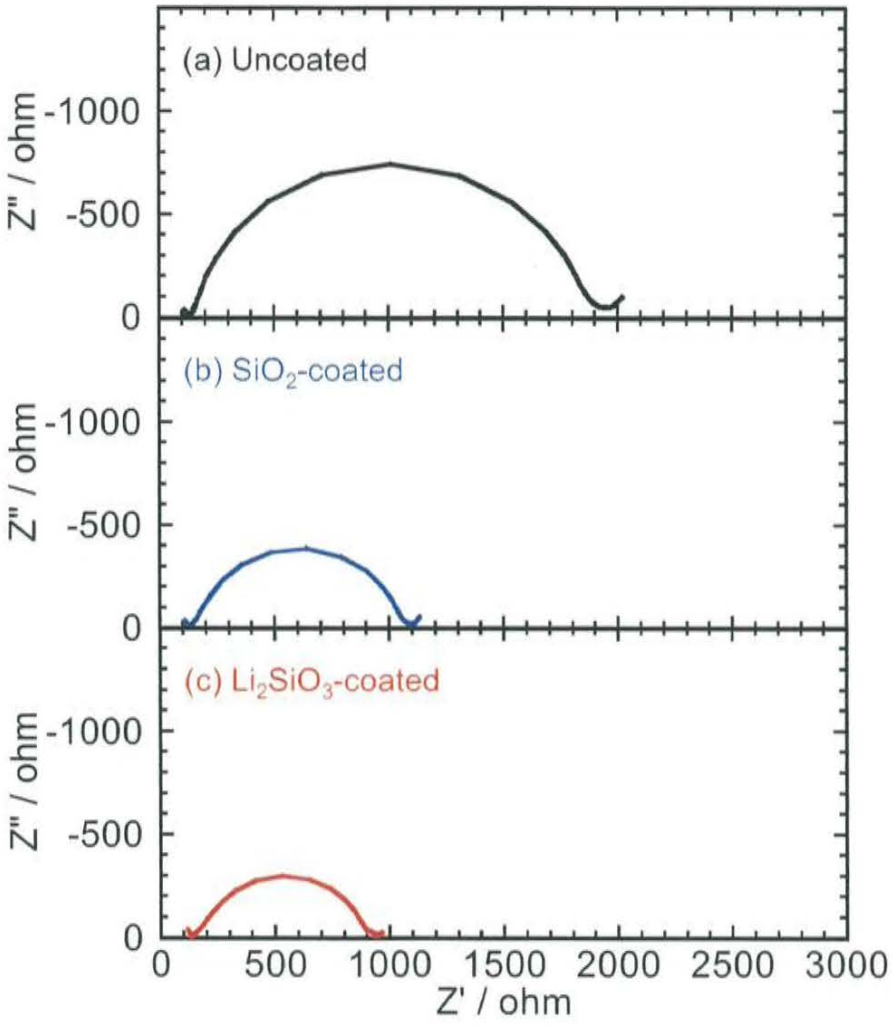

Figure 2-18 Impedance profiles of the all-solid-state cells with (a) uncoated, (b) SiO_2-coated, and (c) Li_2SiO_3-coated $LiCoO_2$ after the first charge process to 4.0 V vs. Li-In.

electrolyte layer (R_{SE}) shows almost no difference between the cells with coated $LiCoO_2$ and the cell with uncoated $LiCoO_2$; the resistance does not increase during a charge process. The interfacial resistances (R_{PE}) of uncoated, SiO_2-coated, and Li_2SiO_3-coated $LiCoO_2$ are respectively 1700, 900, and 750 Ω. The R_{PE} after charging to 4.6 V vs. Li is larger than those after charging to 3.6 V vs. Li–In shown in Figs. 2-12 and 2-13. The charge transfer resistance of the cell using $LiCoO_2$ is reported to increase at a high potential above 3.6 V vs. Li–In [15, 36, 37]. Similar behavior is observed in the all-solid-state cells with Li_2S–P_2S_5 solid electrolytes.

Figure 2-19 shows the potential dependence of (a) R_{SE} and (b) R_{PE} in the all-solid-state cells using uncoated and Li_2SiO_3-coated $LiCoO_2$. The R_{SE} shows almost constant values of about 200 Ω, while the R_{PE} changed with the cell potentials. The small resistance of *ca.* 100 Ω is observed below 3.6 V in each cells. The resistance increases with increasing the potential over 3.6 V vs. Li–In; the R_{PE} of all-solid-state cells using uncoated and Li_2SiO_3-coated $LiCoO_2$ after charging to 4.0 V vs. Li–In are 1730 and 950 Ω, respectively. The R_{PE} of the cells with Li_2SiO_3-coated and SiO_2-coated $LiCoO_2$ is smaller than that with uncoated $LiCoO_2$, indicating that the coatings are effective in suppressing an increase of the R_{PE} at a high potential.

Figure 2-20 shows the cycle performance of In/$80Li_2S \cdot 20P_2S_5$ glass-ceramic/$LiCoO_2$ cells at the current density of 0.13 mA cm^{-2} in the potential range of 2.0-4.0 V vs. Li–In. The reversible capacities of the cells with uncoated, SiO_2-coated, and Li_2SiO_3-coated $LiCoO_2$ at the 50th discharge process are respectively 60, 80, and 110 mAh g^{-1}. All the cells retain charge-discharge efficiency of almost 100% except for initial a few cycles. All the cells show relatively good capacity retention at a cutoff voltage of 4.0 V vs. Li–In. The cells with coated $LiCoO_2$ have better capacity retention than the cell with uncoated $LiCoO_2$. In the case of using liquid and polymer electrolytes, it is reported that the capacity of the cells with

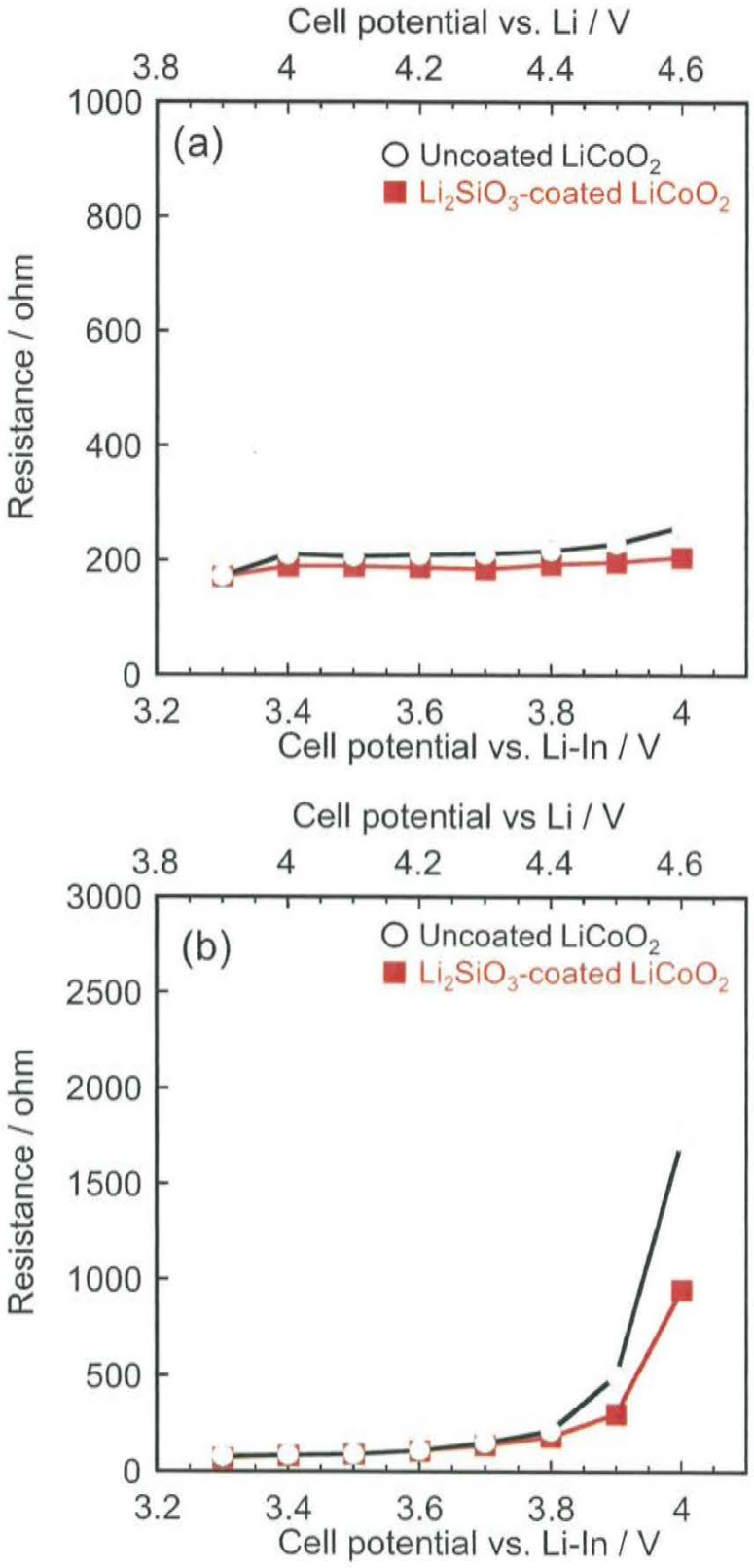

Figure 2-19 Potential dependence of (a) resistance of solid electrolyte layer (R_{SE}) and (b) interfacial resistance between $LiCoO_2$ and Li_2S–P_2S_5 solid electrolyte (R_{PE}) in all-solid-state cells using uncoated and Li_2SiO_3-coated $LiCoO_2$.

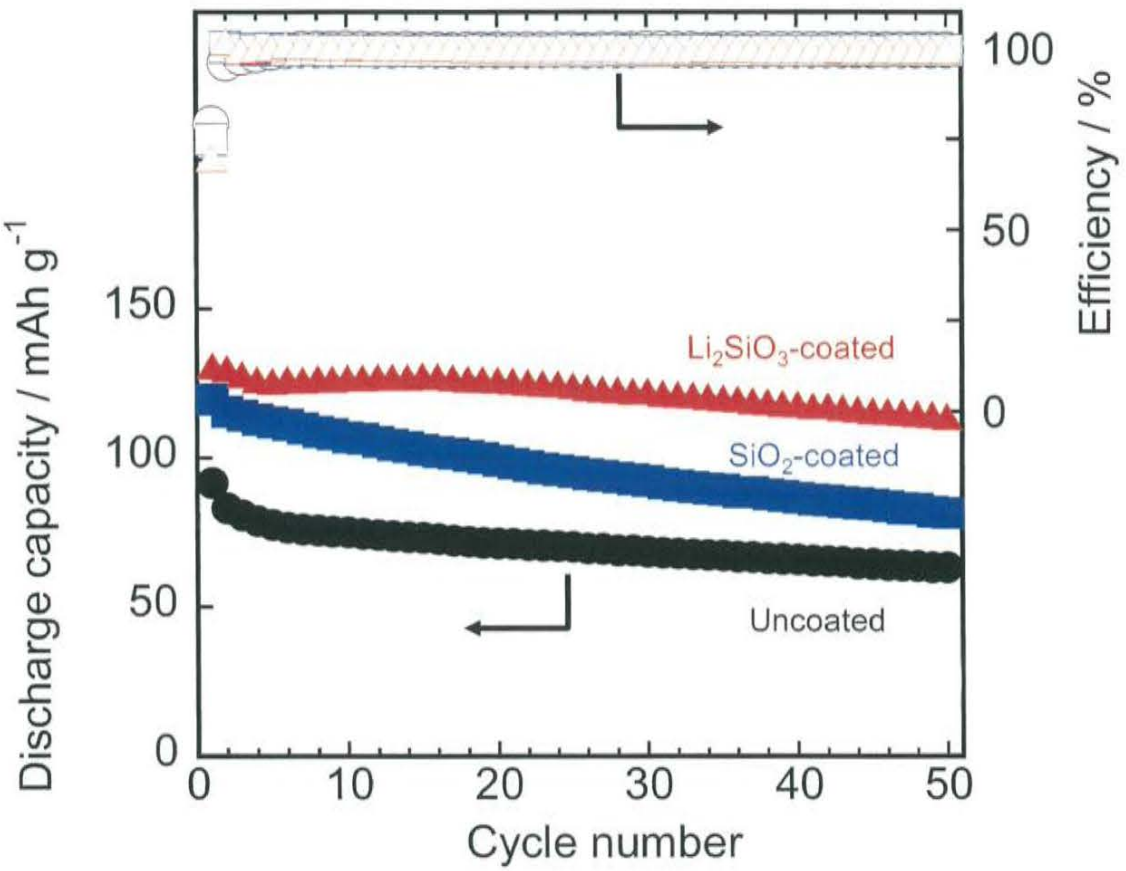

Figure 2-20 Cycle performance for discharge capacity and columbic efficiency of the all-solid-state cells In/$80Li_2S{\cdot}20P_2S_5$ glass-ceramic/$LiCoO_2$. The current density and cutoff voltage were 0.13 mA cm^{-2} and 4.0V vs. Li-In, respectively.

uncoated $LiCoO_2$ decreased drastically during charge-discharge cycling at 0.1-1 C under the cutoff voltage above 4.6 V vs. Li [10, 14, 15, 19, 21]. The all-solid-state cells operate stably even in the case using uncoated $LiCoO_2$ at 0.13 mA cm^{-2} (0.1 C) under the high cutoff voltage of 4.0 V vs. Li–In (4.6 V vs. Li). This result indicates that the Li_2S–P_2S_5 solid electrolyte is more stable than the other electrolytes at the high potential. In the cells with liquid and polymer electrolytes, the degradation of the cells at high potential is explained as follows: (i) cobalt dissolution from $LiCoO_2$ to liquid electrolyte, (ii) structural change due to phase transition of $LiCoO_2$ between a hexagonal phase and a monoclinic phase, and (iii) impedance growth with cycling [9, 15, 16, 21, 37, 38]. In the all-solid-state system, the Co dissolution would be suppressed at the interface between $LiCoO_2$ and the solid electrolyte, and thus the degradation of $LiCoO_2$ is restrained even in the case using uncoated $LiCoO_2$. However, the Co diffusion from $LiCoO_2$ to solid electrolyte could be strongly related to impedance growth. The capacity after 50th cycle of the all-solid-state cells using oxide-coated $LiCoO_2$ is larger than that using uncoated $LiCoO_2$. Chen and Dahn have reported that oxide coatings suppress side reactions between electrode and electrolyte [14, 15]. In this study, it is also assumed that oxide coatings act as a buffer layer and suppress the reaction which forms highly resistive layer at the interface between $LiCoO_2$ and Li_2S–P_2S_5 solid electrolyte, which will be discussed in Chapter 3 using TEM observations. The electrochemical performances of the cell with Li_2SiO_3-coated $LiCoO_2$ at the high cutoff voltage are superior to those with SiO_2-coated $LiCoO_2$

Figure 2-21 (a) shows the charge-discharge curves of the all-solid-state cells using uncoated and 0.6 wt% Li_2SiO_3-coated $LiCoO_2$ at a relatively high current density of 1.3 mA cm^{-2}. The cutoff voltage is 2.0-4.0 V vs. Li–In, which is equivalent to 2.6-4.6 V vs. Li. Average voltage for discharging of the cell using Li_2SiO_3-coated $LiCoO_2$ is higher than that of the cell using uncoated $LiCoO_2$. The reversible capacities of the cells with uncoated and

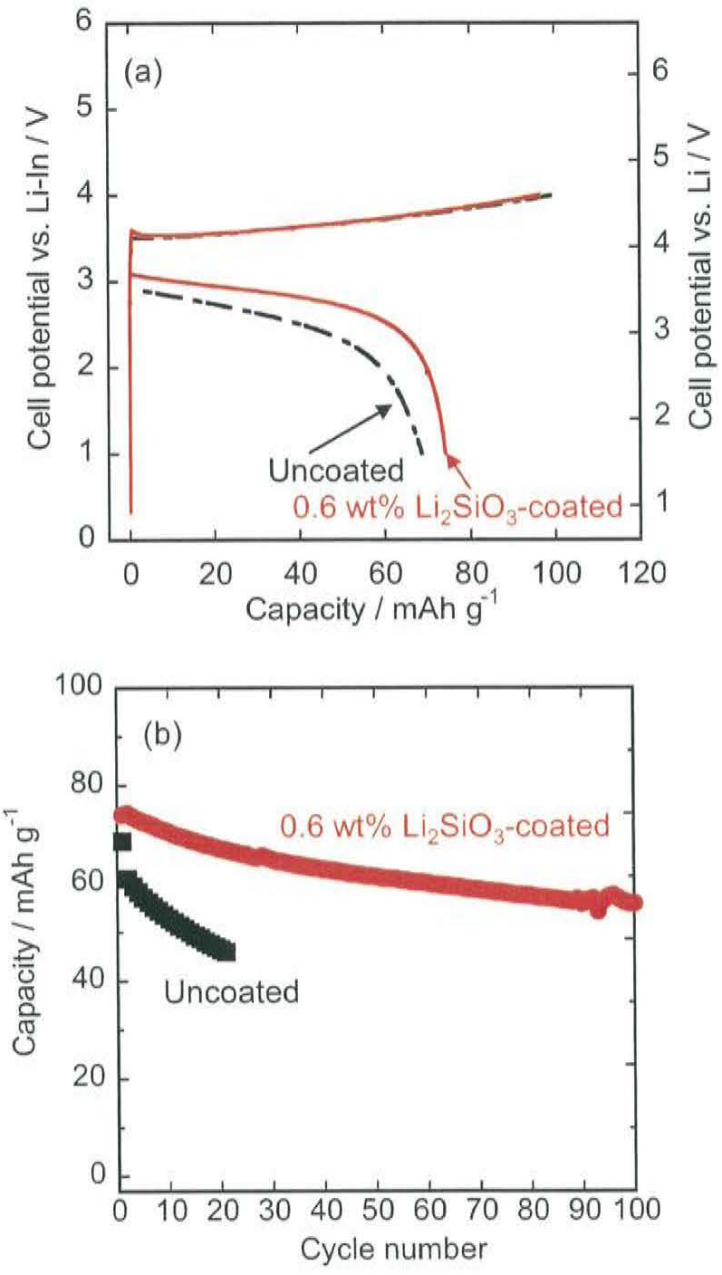

Figure 2-21 Charge-discharge curves (a) and cycle performance (b) of the all-solid-state cells using uncoated and 0.6 wt% Li_2SiO_3-coated $LiCoO_2$ at a relatively high current density of 1.3 mA cm^{-2}. The cutoff voltage used was 1.0-4.0 V vs. Li-In.

Li_2SiO_3-coated $LiCoO_2$ are respectively 69 and 74 mAh g^{-1} for the 1st cycle. Figure 2-21 (b) shows the cycle performance of the all-solid-state cells. The capacity of the cell using uncoated $LiCoO_2$ decreases to 47 mAh g^{-1} after 20 cycles. In contrast, the capacity of the cell using Li_2SiO_3-coated $LiCoO_2$ after 100 cycles is 56 mAh g^{-1}. The Li_2SiO_3 coating significantly suppresses capacity fading. The cyclability of the all-solid-state cells at high current density can be improved by interfacial modification using Li_2SiO_3 coating.

All-solid-state batteries using Li_2SiO_3-coated $LiCoO_2$ particles show good electrochemical performance at room temperature as shown above. Herein, electrochemical performance of the all-solid-state batteries using $LiCoO_2$ electrode and Li_2S–P_2S_5 solid electrolytes at extremely low and high temperatures will be shown.

Figure 2-22 shows impedance profiles of the all-solid-state cells using uncoated and Li_2SiO_3-coated $LiCoO_2$ at -30°C after charging to 3.6 V vs. Li–In. The internal resistance of the cells at the low temperature of -30°C is much larger than that at room temperature, as presented in Fig. 2-13. The resistances attributed to a solid electrolyte layer (R_{SE}) are *ca.* 3000 Ω in each cell. This resistance corresponds to that calculated from the conductivity and activation energy as descried in Fig. 2-14 (a). The interfacial resistances between $LiCoO_2$ and solid electrolytes (R_{PE}) are, respectively, 1.6×10^5 Ω (a) and 6.0×10^4 Ω (b). The R_{PE} of the cell using Li_2SiO_3-coated $LiCoO_2$ is about one-third of that of a cell using uncoated $LiCoO_2$. Figure 2-23 presents discharge curves of the all-solid-state cells under the current density of 0.064 mA cm^{-2} at -30°C. The all-solid-state cells are discharged even at the low temperature of -30°C. The discharge capacity of the cell using the Li_2SiO_3-coated $LiCoO_2$ is 60 mAh g^{-1}, although that of the non-coated $LiCoO_2$ is less than 40 mAh g^{-1}. The decrease of the R_{PE} by oxide coating contributes to a high voltage plateau and large discharge capacity.

The all-solid-state batteries are expected to operate even under high temperatures at which the operation of conventional batteries is difficult. Figure 2-24 presents the 10th

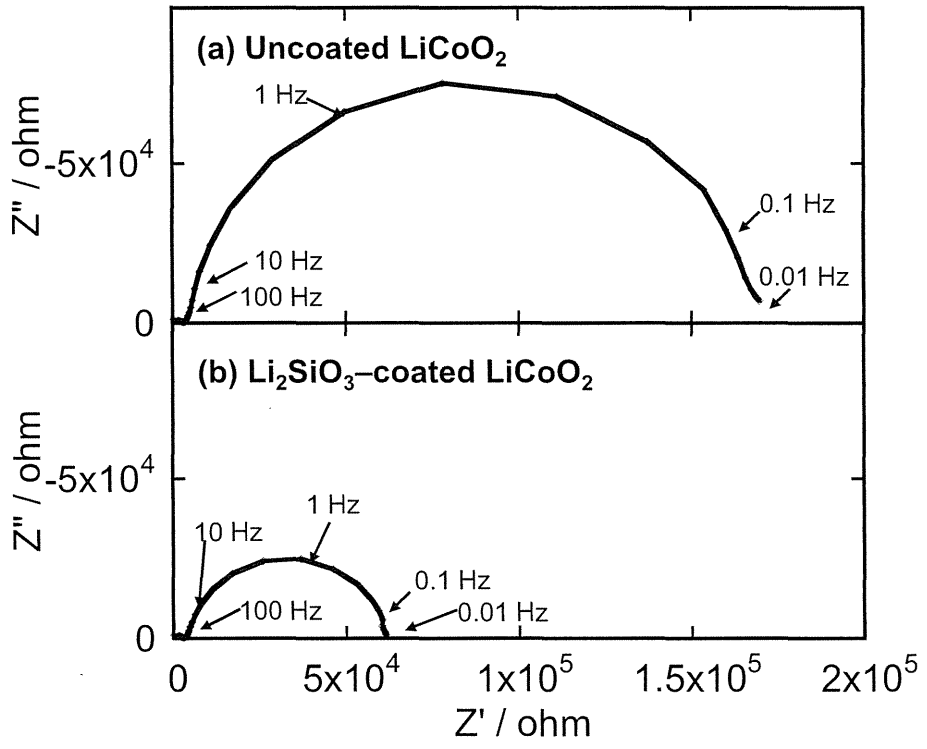

Figure 2-22 Impedance profiles of the all-solid-state cells In / Li_2S–P_2S_5 solid electrolyte / uncoated (a) and Li_2SiO_3-coated (b) $LiCoO_2$ at -30°C after charging to 3.6 V vs. Li–In.

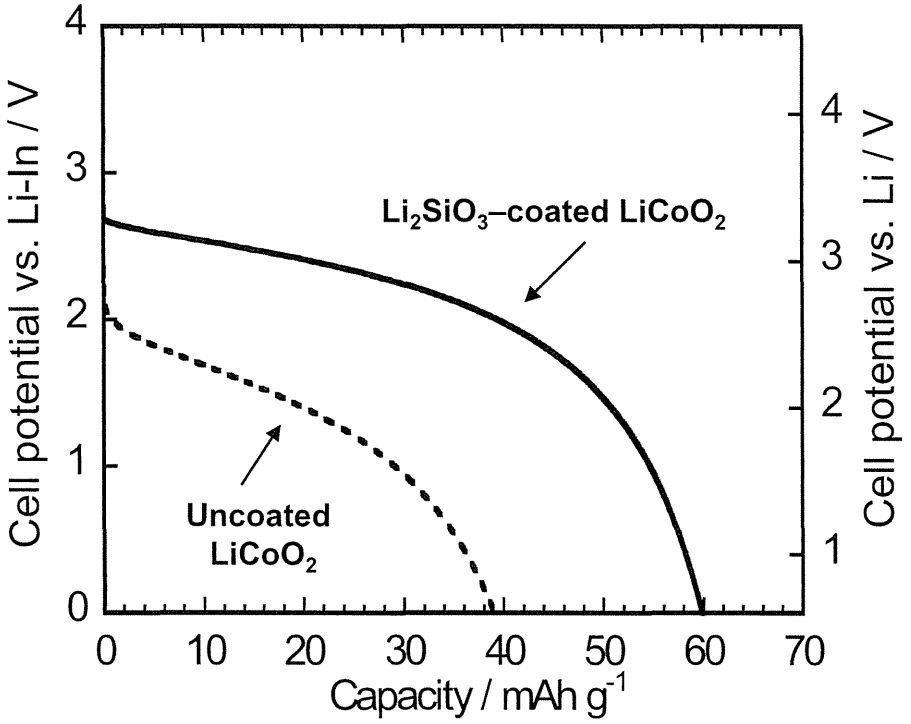

Figure 2-23 Discharge curves of the all-solid-state cells under the current density of 0.064 mA cm^{-2} at -30°C.

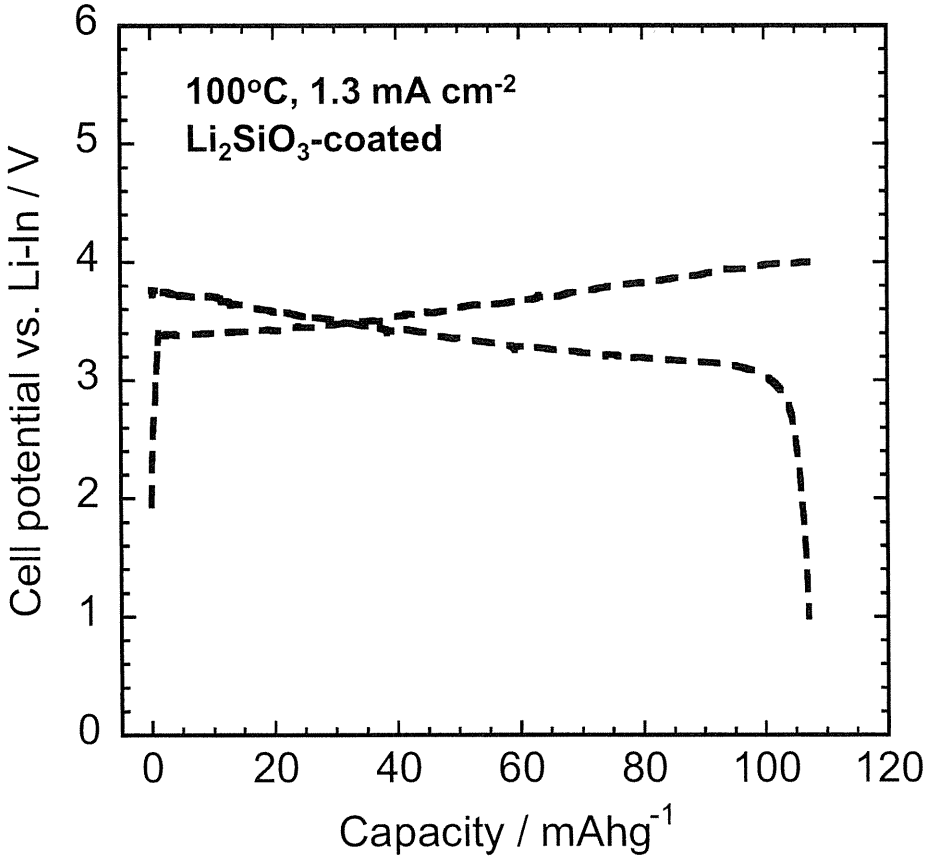

Figure 2-24 Charge-Discharge curves of 10th cycle of the all-solid-state cell In / Li_2S–P_2S_5 solid electrolyte / Li_2SiO_3-coated $LiCoO_2$ under the current density of 1.3 mA cm^{-2} at 100°C.

charge–discharge curves of the all-solid-state cells using $LiCoO_2$ coated with 0.06 wt% Li_2SiO_3 at 100°C under the current density of 1.3 mA cm^{-2}. All-solid-state cells operate even under the high temperature of 100°C. The charge-discharge curves show almost no IR drop because of a low internal resistance at a high temperature 100°C. Figure 2-25 shows the charge–discharge curves of the all-solid-state cells using $LiCoO_2$ coated with 0.06 wt% Li_2SiO_3 at 100°C under the current density of 40 mA cm^{-2}. The all-solid-state cell using Li_2SiO_3-coated $LiCoO_2$ works at an extremely high current density of 40 mA cm^{-2}, which corresponds to 40 C; the charge–discharge capacity is more than 100 mAh g^{-1}.

(II) Li_2O–TiO_2 system

The results of the study for the Li_2O–SiO_2 coatings on $LiCoO_2$ particles indicated that the lithium-ion conductivity of coating materials is important for good electrochemical performance. The electrochemical performance of the batteries is affected by lithium-ion and electron conductivities of coating materials. The influence of metal-ions in metal oxide coatings is worth investigating. Here, amorphous Li_2O–TiO_2 films were used as coating materials by changing metal oxide from silicate to titanate which is a common transition metal oxide. This substitution was performed in order to examine what kinds of materials are suitable in all-solid-state batteries using Li_2S–P_2S_5 glass-ceramic solid electrolytes. The Li_2O–TiO_2 films at two different compositions of 33 mol% Li_2O ($Li_2Ti_2O_5$) and 0 mol% Li_2O (TiO_2) were used as coating materials in order to study the influence of lithium-ion conductivity in the coating films. Moreover, the electrochemical performances such as rate capability and cyclability of the all-solid-state cells using Li_2S–P_2S_5 solid electrolytes and $LiCoO_2$ coated with titanate films were compared with those of the cells using $LiCoO_2$ coated with silicate films.

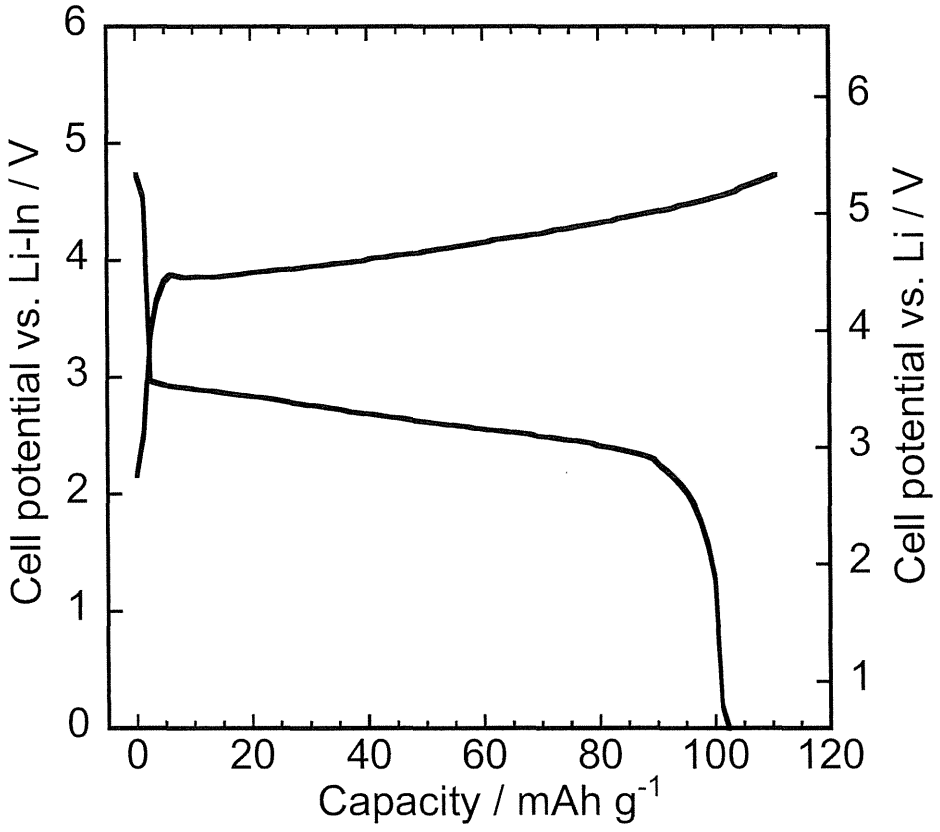

Figure 2-25 Charge–discharge curves of the all-solid-state cell In / Li_2S–P_2S_5 solid electrolyte / Li_2SiO_3-coated $LiCoO_2$ at 100°C under the current density of 40 mA cm^{-2}.

(i) Morphology of coated $LiCoO_2$

The surface morphology of the coated $LiCoO_2$ particles was investigated using FE-SEM observation. Figure 2-26 shows FE-SEM images of the surface of the $LiCoO_2$ particles coated with 0.1 wt% of TiO_2 and $Li_2Ti_2O_5$. The surface of uncoated $LiCoO_2$ is also shown for comparison. The surface of the $LiCoO_2$ particles with or without oxide coatings is relatively smooth. Average thickness of coating materials estimated from the weight of coating materials and BET surface area of $LiCoO_2$ was *ca.* 2 nm. Since the coating thickness is very small, the coating layer would not be confirmed in FE-SEM observation.

(ii) Electrochemical performance of all-solid-state cells using coated $LiCoO_2$.

The all-solid-state cells In/$80Li_2S \cdot 20P_2S_5$ glass-ceramic /$LiCoO_2$ were constructed and their electrochemical performance was investigated. Figure 2-27 shows the impedance profiles of the all-solid-state cells with uncoated, TiO_2-coated, and $Li_2Ti_2O_5$-coated $LiCoO_2$ after charging to 3.6 V vs. Li–In, which corresponds to 4.2 V vs. Li, at the current density of 0.13 mA cm^{-2}. Two semicircles are observed and their peak top frequencies are about 1 kHz and 1 Hz in each impedance profile. As shown in Fig. 2-5, the resistance observed at the high-frequency region (>100 kHz) corresponds to the resistance of the solid electrolyte layer (R_{SE}); the semicircles observed in the medium-frequency (about 1 kHz) and the low frequency region (about 1 Hz) are due to the interfacial resistance between $LiCoO_2$ and solid electrolyte (R_{PE}) and negative electrode layer (R_{NE}), respectively. R_{SE} and R_{NE} of the three cells are about 150 and 50 Ω, respectively. Similar values of the resistances are observed in the three cells. R_{PE} of the cells with uncoated, TiO_2-coated, and $Li_2Ti_2O_5$-coated $LiCoO_2$ are 270, 200, and 140 Ω, respectively. The R_{PE} are decreased by the oxide coatings. The R_{PE} of the cell with $Li_2Ti_2O_5$-coated $LiCoO_2$ is lower than that with TiO_2-coated $LiCoO_2$. The lithium containing oxide is more effective in decreasing the R_{PE}. This result corresponds to the

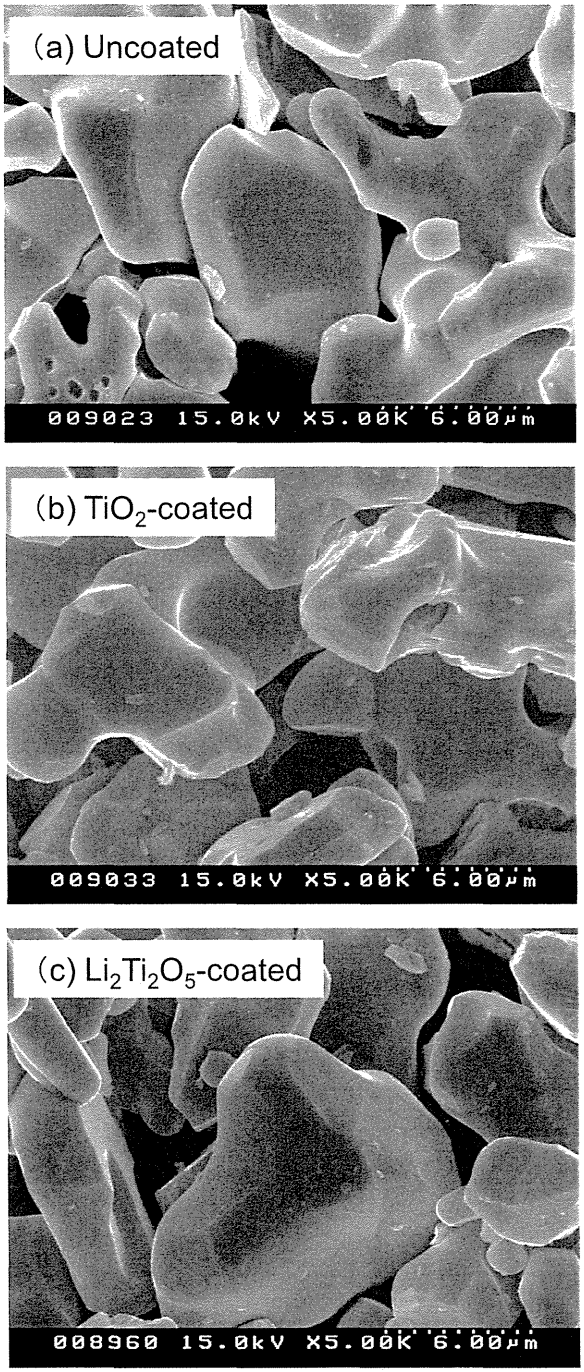

Figure 2-26 FE-SEM images of (a) uncoated, (b) TiO_2-coated, and (c) $Li_2Ti_2O_5$-coated $LiCoO_2$ particles.

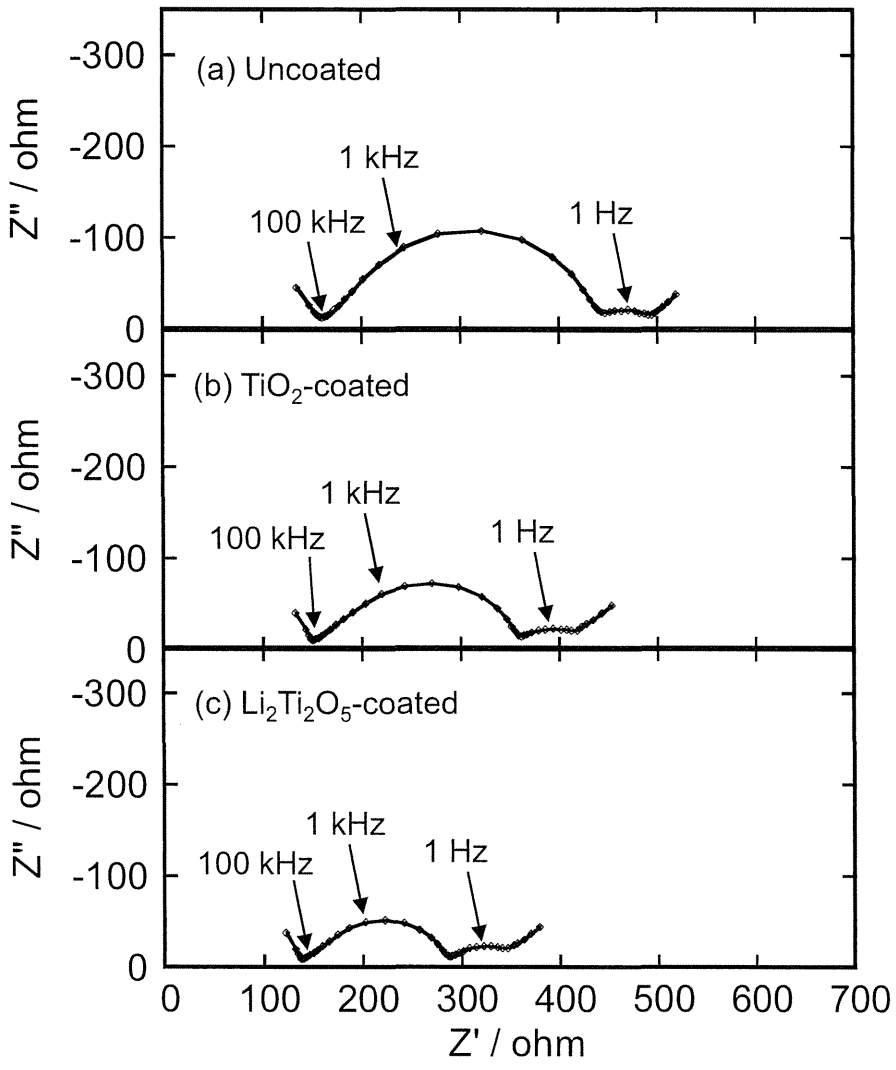

Figure 2-27 Impedance profiles of the cells In/80Li_2S·20P_2S_5 glass-ceramic/(a) uncoated, (b) TiO_2-coated, and (c) $Li_2Ti_2O_5$-coated $LiCoO_2$.

results using the cells with the $LiCoO_2$ coated with Li_2O–SiO_2 glassy films shown in Figs. 2-12 and 2-13. The R_{PE} of the cell with TiO_2-coated $LiCoO_2$ and $Li_2Ti_2O_5$-coated $LiCoO_2$ are respectively as small as those with SiO_2-coated $LiCoO_2$ and Li_2SiO_3-coated $LiCoO_2$, indicating that the presence of transition metal oxide in coating materials is not so important to decrease the R_{PE}. The R_{PE} would be caused by the formation of high-resistance interface between $LiCoO_2$ and sulfide electrolyte. The oxide coatings would act as a buffer layer to prevent direct contact between $LiCoO_2$ and the sulfide solid electrolyte, resulting in the suppression of the formation of the highly resistive layer. Ohta and Takada *et al.* reported that the coatings of oxide films on $LiCoO_2$ brought about a significant decrease of the interfacial resistance [4-6]. They used $Li_4Ti_5O_{12}$, $LiNbO_3$, and $LiTaO_3$ as coating materials in the all-solid-state cells Li–In /$Li_{3.25}Ge_{0.25}P_{0.75}S_4$ (thio-LISICON)/$LiCoO_2$. The coating layers suppressed the formation of a highly resistive layer between the $LiCoO_2$ and solid electrolyte. They suggested that $LiNbO_3$ and $LiTaO_3$ were more effective in improving the battery performance than $Li_4Ti_5O_{12}$ because $LiNbO_3$ and $LiTaO_3$ show higher lithium-ion conductivities. The results in this thesis are consistent with the conclusion by Ohta and Takada [6].

Figure 2-28 shows discharge curves of the all-solid-state cells In/$LiCoO_2$ with uncoated and $Li_2Ti_2O_5$-coated $LiCoO_2$ at a relatively high current density of 1.3 mA cm^{-2} after charging to 3.6 V vs. Li–In at the current density of 0.13 mA cm^{-2}. The average discharge voltages of the cells with uncoated and $Li_2Ti_2O_5$-coated $LiCoO_2$ are 2.5 and 2.8 V vs. Li–In, respectively. The discharge capacities of those cells are 47 and 72 mAh g^{-1}, respectively. The discharge performance of the cell with $Li_2Ti_2O_5$-coated $LiCoO_2$ is better than that with uncoated $LiCoO_2$ in a high current density operation. This improvement is attributable to the decrease of the R_{PE} by $Li_2Ti_2O_5$ coating.

The charge-discharge measurements of the all-solid-state cells were carried out at

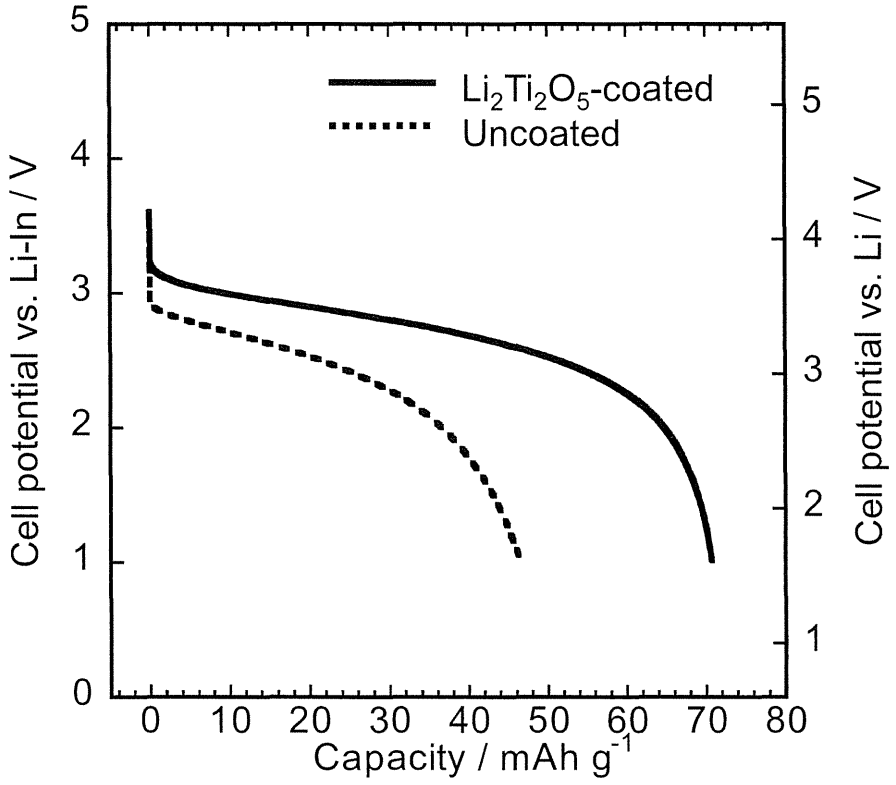

Figure 2-28 Discharge curves of the cells In/80Li_2S·20P_2S_5 glass-ceramic/uncoated and $Li_2Ti_2O_5$-coated $LiCoO_2$ at the current density of 1.3mA cm^{-2}.

different cutoff voltages to investigate coating effects on the cell performance in different cutoff voltage operations. Cycle performances of the all-solid-state cells with uncoated, TiO_2-coated, and $Li_2Ti_2O_5$-coated $LiCoO_2$ are shown in Fig. 2-29. The current density was 0.13 mA cm^{-2}. The cutoff voltages were 2.0-3.6 V (until the 15th cycle) and 2.0-4.0 V (after the 16th cycle) vs. Li–In, respectively. The measurements were carried out after pre-cycles under high current densities over 1 mA cm^{-2}. The three cells are charged and discharged with the capacity of *ca.* 80 mAh g^{-1} at a charging cutoff voltage of 3.6 V vs. Li–In. In this cutoff voltage, the three cells do not show fading capacity. The capacities of the cells increase by increasing cutoff voltage from 3.6 to 4.0 V vs. Li–In. The 16th discharge capacities of the cells using uncoated, TiO_2-coated, and $Li_2Ti_2O_5$-coated $LiCoO_2$ are respectively 113, 121 and 129 mAh g^{-1}. At the high cutoff voltage, the decreases of the capacity are confirmed. The 50th discharge capacities of the cells using uncoated, TiO_2-coated, and $Li_2Ti_2O_5$-coated $LiCoO_2$ are respectively 73, 79 and 103 mAh g^{-1}. The cells with coated $LiCoO_2$ have better capacity retention than the cell with uncoated $LiCoO_2$; the cell with $Li_2Ti_2O_5$-coated $LiCoO_2$ exhibits better cycle performance than that with TiO_2-coated $LiCoO_2$. The 16th and 50th charge-discharge curves of the all-solid-state cells with uncoated and $Li_2Ti_2O_5$-coated $LiCoO_2$ are shown in Fig. 2-30. The charge-discharge capacities decrease during charge-discharge cycles in the cells with both uncoated and $Li_2Ti_2O_5$-coated $LiCoO_2$. The charging plateau voltages of the both cells increase during charge-discharge cycles. The discharging plateau voltage of the cell with uncoated $LiCoO_2$ slightly decreases with charge-discharge cycles at a high charging cutoff voltage of 4.0 V vs. Li–In, whereas the cell with $Li_2Ti_2O_5$-coated $LiCoO_2$ keeps almost the same discharging plateau voltage even after the 50th charge-discharge cycles. One of the causes of the fading capacity is the resistance increase, resulting in the decrease of the discharging plateau voltage. The discharging plateau voltage of the cell with uncoated $LiCoO_2$ decreases, indicating that

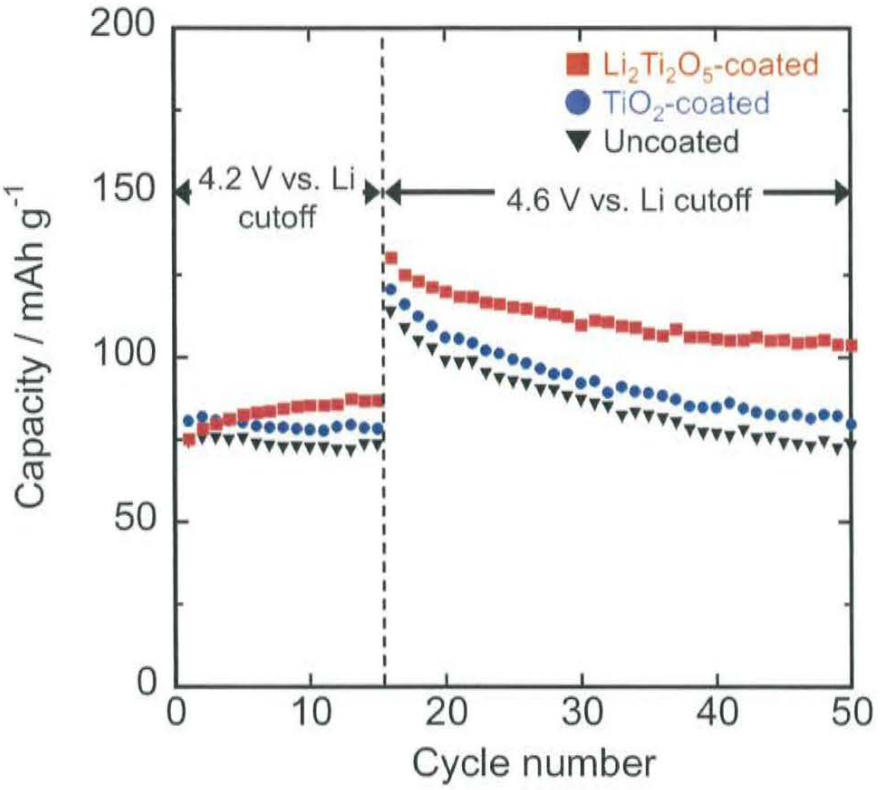

Figure 2-29 Cycle performances of the cells In/$80Li_2S{\cdot}20P_2S_5$ glass-ceramic/uncoated, TiO_2-coated, and $Li_2Ti_2O_5$-coated $LiCoO_2$ at the current density of 0.13 mA cm^{-2}. The cutoff voltages were 2.0–3.6 V (until 15th cycles) and 2.0–4.0 V (after 16th cycles) vs. Li–In, respectively.

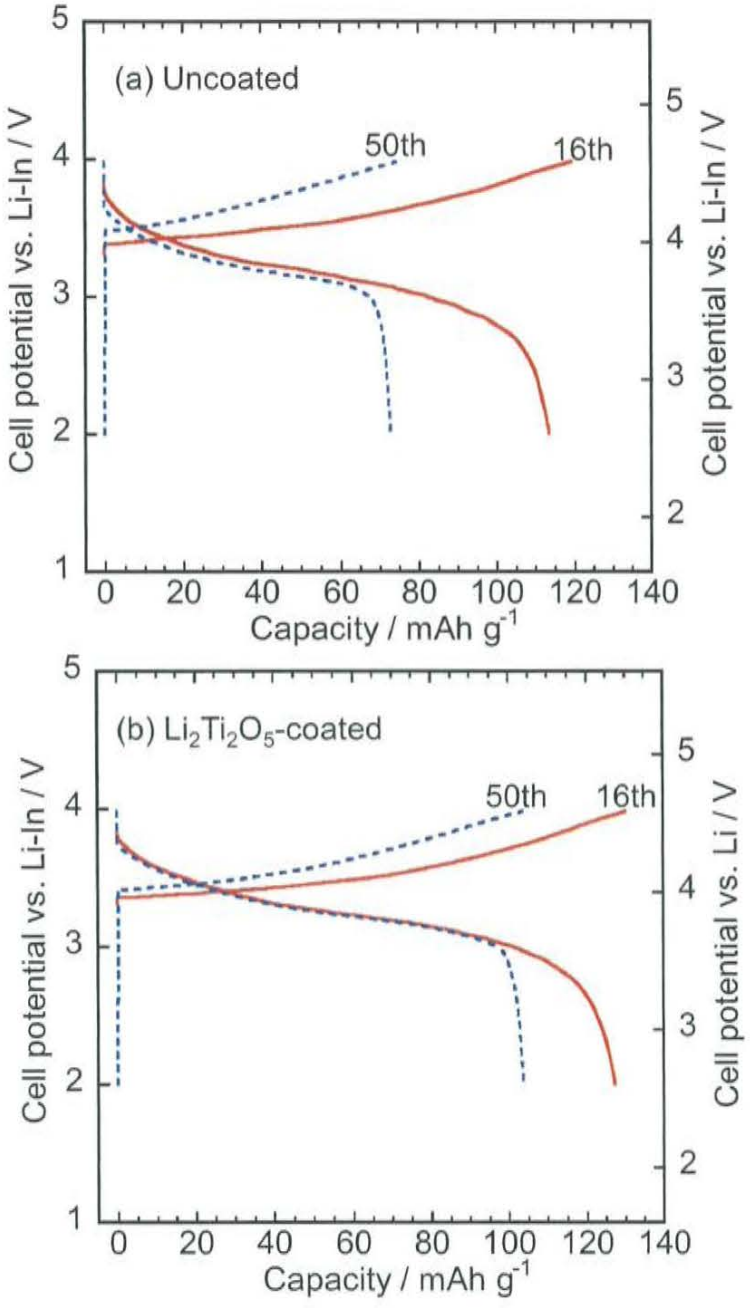

Figure 2-30 The 16th and 50th charge–discharge curves of the cells In/80Li_2S·20P_2S_5 glass-ceramic/uncoated (a) and (b) $Li_2Ti_2O_5$-coated $LiCoO_2$. The current density and cutoff voltage were 0.13 mA cm^{-2} and 4.0 V vs. Li-In, respectively.

the resistance of the cell increases. This resistance increase would be caused by the formation of highly resistive interfacial layer between $LiCoO_2$ and sulfide electrolyte by charging to a high potential. The discharging plateau voltage of the cell with $Li_2Ti_2O_5$-coated $LiCoO_2$ hardly decreases, indicating that the resistance of the cell using $Li_2Ti_2O_5$-coated $LiCoO_2$ would not increase significantly. The $Li_2Ti_2O_5$ coating is effective in suppressing the resistance increase.

The coatings of Li_2O–SiO_2 film on $LiCoO_2$ improved cyclability of the all-solid-state cells at the high cutoff voltage of 4.6 V vs. Li as shown in Fig. 2-20; coatings of lithium-ion conducting Li_2SiO_3 were more effective in improving cycle performance than those of an insulative SiO_2. The Li_2O–TiO_2 films with transition metal coated on $LiCoO_2$ by a sol-gel technique are also effective in improving cyclability of the all-solid-state cells at the high cutoff voltage as the Li_2O–SiO_2 coating films without transition metal. In addition, the $Li_2Ti_2O_5$ coating is more effective in improving cyclability than the TiO_2 coating. The existence of lithium in coating materials on the $LiCoO_2$ particles was more important than the kinds of coating oxide (SiO_2 or TiO_2) for electrochemical performance of all-solid-state lithium secondary batteries using Li_2S–P_2S_5 solid electrolytes.

2.3.3.2. Oxide-coated $LiCoO_2$ prepared by pulsed laser deposition technique

In Section 2.3.3.1, it has been indicated that oxide coatings on $LiCoO_2$ are effective in decreasing the interfacial resistance (R_{PE}) and the lithium-ion conductivity of the coating materials is important in further decrease of the resistance. The amorphous thin films which have high lithium-ion concentration show high lithium-ion conductivity. Such materials are expected to be more effective in decreasing R_{PE}. In oxide-based solid electrolyte, the glasses in the systems with two lithium ortho-oxosalts such as Li_3BO_3–Li_4GeO_4 and Li_4SiO_4–Li_3BO_3, have been prepared by rapid quenching of melts with a twin-roller quenching apparatus.

However, they are difficult to be prepared by a sol-gel technique. Amorphous thin films in the system Li_4SiO_4–Li_3PO_4 were prepared by vapor-phase process (rf-sputtering) [39]. In this study, a pulsed laser deposition (PLD) technique was used to prepare the lithium ortho-oxosalts film because PLD can prepare thin films with high quality. The characteristics in PLD are the ability to transfer almost stoichiometrically a bulk target to the deposited films by controlling many parameters such as ambient gas pressure and laser fluence. Using PLD technique, lithium ortho-oxosalt films such as Li_3PO_4 [40, 41] and LiPON [42] have been prepared. The preparation of Li_4SiO_4–Li_3PO_4 thin films by PLD has not been reported so far.

In this section, amorphous lithium ortho-oxosalt films such as Li_4SiO_4–Li_3PO_4 were prepared by PLD as coating materials on $LiCoO_2$ particles. To obtain good quality films, laser fluence and Ar gas pressure of PLD were varied. The lithium-ion conductivities of the prepared films were evaluated. The amorphous lithium ortho-oxosalt films were coated on $LiCoO_2$ particles to obtain oxide-coated $LiCoO_2$. The lithium-ortho-oxosalt-coated $LiCoO_2$ particles were applied to bulk type all-solid-state cells using Li_2S–P_2S_5 solid electrolytes to improve the electrochemical performance of the cells.

(i) Preparation of lithium ortho-oxosalts

The X-ray diffraction pattern of the prepared target was shown in Fig. 2-31 (a). The diffraction pattern is almost consistent with that of the $50Li_4SiO_4 \cdot 50Li_3PO_4$ solid solution reported so far [43]. A typical amorphous pattern is observed in the $50Li_4SiO_4 \cdot 50Li_3PO_4$ thin film prepared under the laser fluence of 6 J cm^{-2} and Ar gas pressure of 10^{-2} Pa on a quartz substrate, as shown in Fig. 2-31 (b). All the other films prepared showed no X-ray diffraction peaks, suggesting that these thin films were amorphous.

The morphology of the thin film depends on the deposition condition for each target

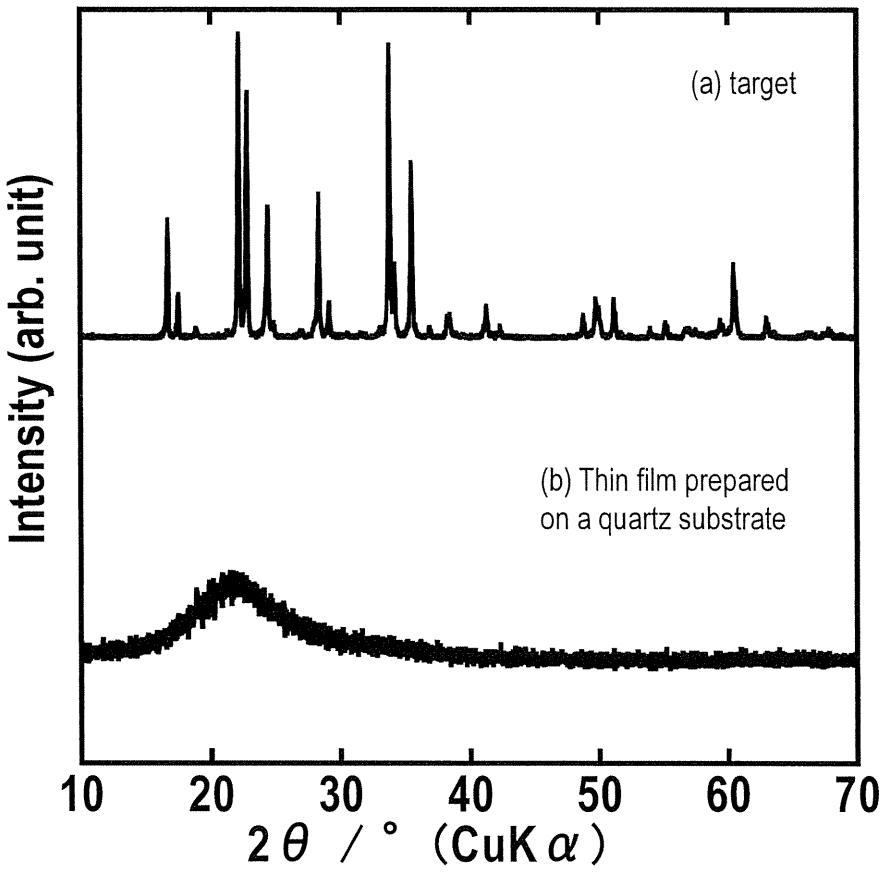

Figure 2-31 X-ray diffraction patterns of (a) $50Li_4SiO_4 \cdot 50Li_3PO_4$ target and (b) $50Li_4SiO_4 \cdot 50Li_3PO_4$ thin film on a quartz substrate prepared under laser fluence of 6 J cm^{-2}.

material. The parameters such as laser fluence and ambient gas pressure influenced the morphology of thin film. Figure 2-32 shows the cross sectional FE-SEM image of the $50Li_4SiO_4 \cdot 50Li_3PO_4$ thin film deposited under the laser fluence of 6 J cm^{-2} and the Ar gas pressure of 10^{-2} Pa on a silicon substrate. The thin film is dense and its surface is flat, suggesting that good contact with $LiCoO_2$ particle will be obtained. By the deposition for 60 min, the film with the thickness of 1.2 μm was obtained; the deposition rate was 20 nm min^{-1}.

Conductivities of the films of $50Li_4SiO_4 \cdot 50Li_3PO_4$, Li_4SiO_4 and Li_3PO_4 parallel to the film surface were measured. Figure 2-33 shows the complex impedance plots at 346 K of the $50Li_4SiO_4 \cdot 50Li_3PO_4$ thin film prepared under the laser fluence of 6 J cm^{-2} and Ar gas pressure of 10^{-2} Pa. A large semicircle and a subsequent straight line are observed by using Au electrodes as ion-blocking ones, indicating that the thin film is an ion conductor. The peak top frequency of the semicircle is 60 kHz; the estimated capacitance is 4×10^{-12} F, which suggests that the resistance of the semicircle is attributable to the bulk resistance of the film because the capacitance of typical oxide bulk materials (grain interior) is known to be 10^{-11}-10^{-12} F [44]. The ionic conductivity of the $50Li_4SiO_4 \cdot 50Li_3PO_4$ thin film at room temperature was 1.6×10^{-6} S cm^{-1} which was calculated with the film thickness, area of the comb-like electrode, the interelectrode distance and the film resistance. The impedance of the film vertical to the film surface was also measured. The ionic conductivity was in good agreement with that parallel to the film surface. The temperature dependence of ionic conductivity of the $50Li_4SiO_4 \cdot 50Li_3PO_4$, Li_4SiO_4 and Li_3PO_4 thin films is shown in Fig. 2-34. Ionic conductivities were calculated with the impedances at each temperature measured using comb-like Au electrode. Conductivities of the films follow the Arrhenius equation; the activation energy for ionic conduction was calculated from the slope of the plots. Table 2-2 summarizes the ionic conductivities at room temperature and activation energies for ionic conduction. The ionic conductivity of Li_3PO_4 thin film was 5.1×10^{-7} S cm^{-1} at room

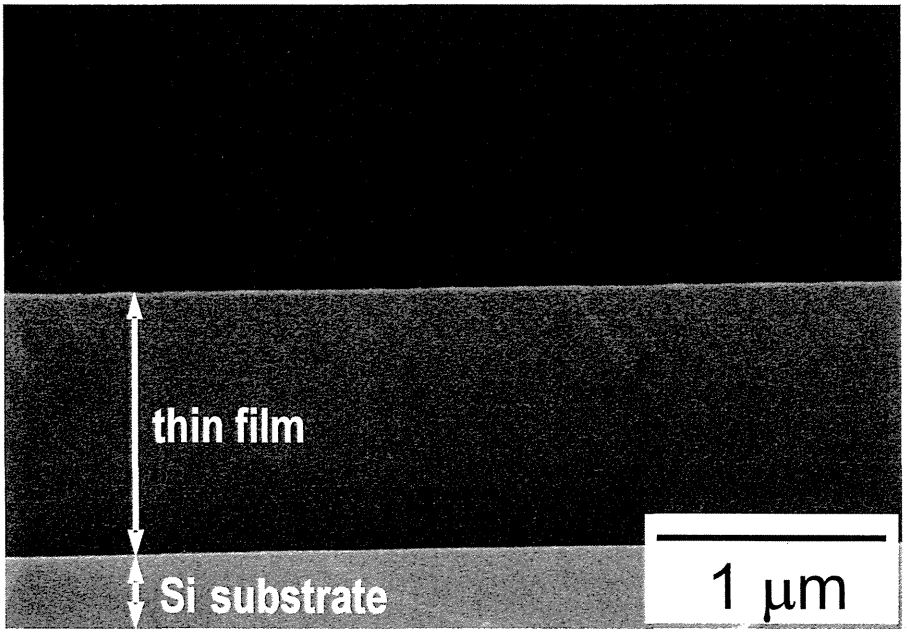

Figure 2-32 Cross sectional FE-SEM image of the $50Li_4SiO_4 \cdot 50Li_3PO_4$ thin film prepared under laser fluence of 6 J cm^{-2} on silicon substrate.

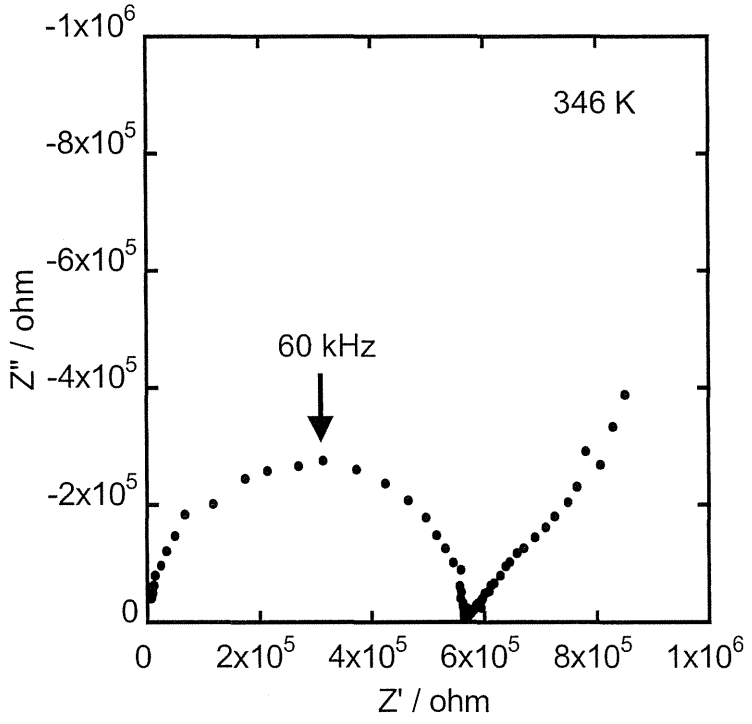

Figure 2-33 Complex impedance plots of the $50Li_4SiO_4 \cdot 50Li_3PO_4$ thin film at 346 K.

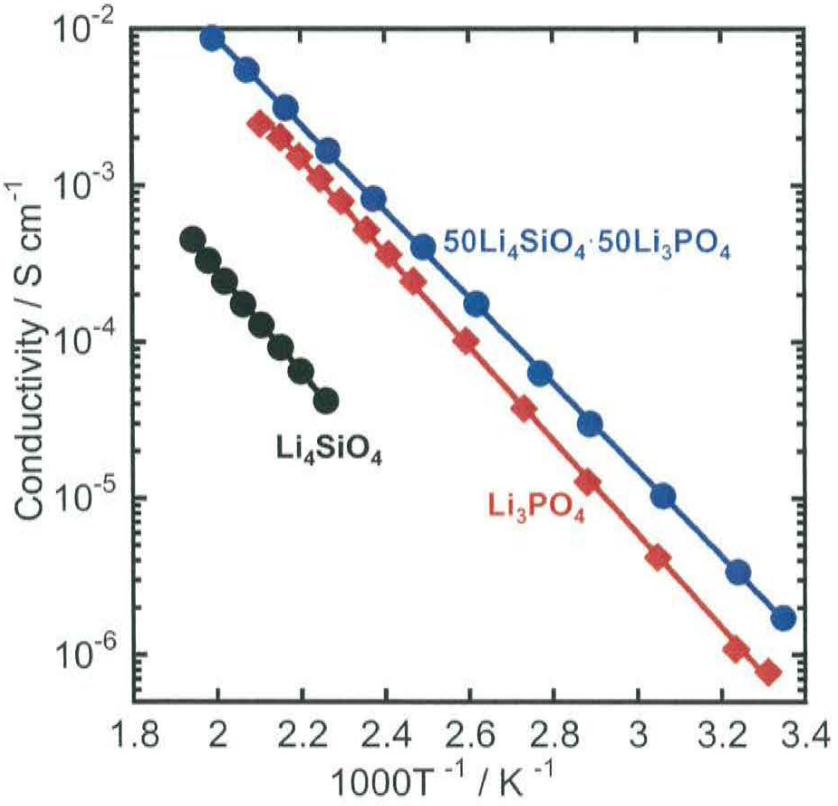

Figure 2-34 Temperature dependence of electrical conductivity of the $50Li_4SiO_4 \cdot 50Li_3PO_4$, Li_4SiO_4 and Li_3PO_4 thin films.

Table 2-2 Lithium ion conductivities at room temperature (σ_{298K}) and the activation energies for conduction (Ea) of thin films.

Thin film	$\sigma_{298\,K}$ (S cm^{-1})	Ea (kJ mol^{-1})
$50Li_4SiO_4 \cdot 50Li_3PO_4$	1.6×10^{-6}	52
Li_3PO_4	5.1×10^{-7}	57
Li_4SiO_4	1.2×10^{-8}	62

temperature and the activation energy was 57 kJ mol^{-1}. Kuwata *et al* reported that the Li_3PO_4 thin film prepared by PLD (ArF excimer laser) showed the ionic conductivity of 4.6×10^{-7} S cm^{-1} and the activation energy of 56 kJ mol^{-1} for ionic conduction [40, 41]. The ionic conductivity and the activation energy of Li_3PO_4 thin film in this study well agree with the reported ones. The ionic conductivity of Li_4SiO_4 thin film at room temperature determined by the extrapolation of the Arrhenius equation was 1.2×10^{-8} S cm^{-1}. On the other hand, the ionic conductivity of the $50Li_4SiO_4\cdot50Li_3PO_4$ thin film was 1.6×10^{-6} S cm^{-1} at room temperature, which was higher than that of the Li_4SiO_4 and Li_3PO_4 thin films. The activation energy of the $50Li_4SiO_4\cdot50Li_3PO_4$ thin film was the lowest among them. This result indicates that the lithium-ion conductivity becomes higher by the coexistence of SiO_4^{4-} and PO_4^{3-}, which can be called as the mixed anion effect [45].

The thin films were applied as the coatings on $LiCoO_2$ particles. The surface morphology of the coated $LiCoO_2$ particles was investigated using FE-SEM and EDX observation. Figure 2-35 shows the FE-SEM images of uncoated and $50Li_4SiO_4\cdot50Li_3PO_4$-coated $LiCoO_2$ particles. The surface of uncoated $LiCoO_2$ particles is relatively smooth. On the other hand, for the $50Li_4SiO_4\cdot50Li_3PO_4$-coated $LiCoO_2$ particles, a rough surface caused by coating materials is observed. Both Si and P atoms of the $50Li_4SiO_4\cdot50Li_3PO_4$ and Co atoms of the $LiCoO_2$ were detected at the same area in EDX mappings, which indicates that the $LiCoO_2$ particles were covered with the $50Li_4SiO_4\cdot50Li_3PO_4$ electrolyte.

(ii) Electrochemical performance of all-solid-state cells using coated $LiCoO_2$.

The all-solid-state cells In / $80Li_2S\cdot20P_2S_5$ glass-ceramic electrolyte / $LiCoO_2$ were constructed using uncoated and $50Li_4SiO_4\cdot50Li_3PO_4$-coated $LiCoO_2$ particles. The electrochemical properties of the cells were investigated with electrochemical impedance

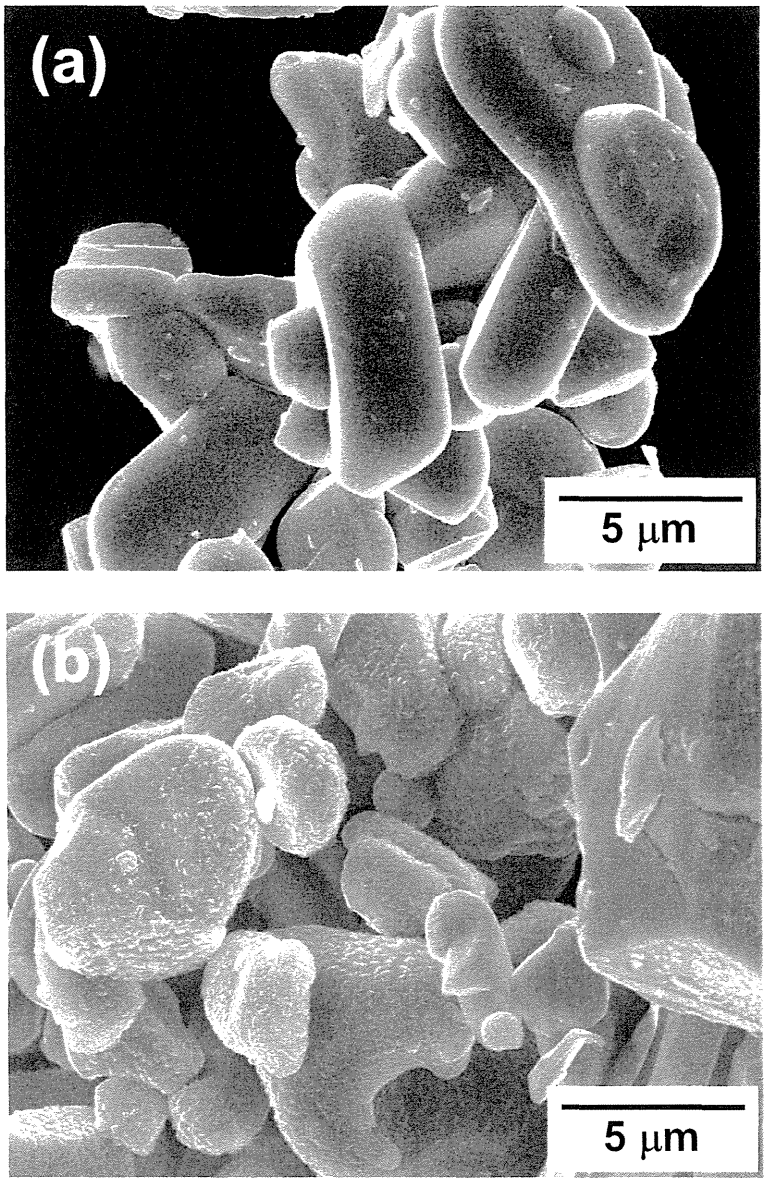

Figure 2-35 FE-SEM images of (a) Uncoated and (b) $50Li_4SiO_4 \cdot 50Li_3PO_4$-coated $LiCoO_2$ particles.

spectroscopy (EIS) and charge-discharge measurements. Figure 2-36 shows impedance profiles of the all-solid-state cells with uncoated and $50Li_4SiO_4 \cdot 50Li_3PO_4$-coated $LiCoO_2$ after the first charge process. The cells were charged at 0.13 mA cm^{-2} and the cut-off voltage was 3.6 V vs. Li–In. The resistances of solid electrolyte (R_{SE}) and negative electrode (R_{NE}) are almost the same in the two cells. On the other hand, The interfacial resistance between $LiCoO_2$ and Li_2S–P_2S_5 solid electrolyte (R_{PE}) of uncoated and $50Li_4SiO_4 \cdot 50Li_3PO_4$-coated $LiCoO_2$ are 190 and 48 Ω, respectively. In other words, R_{PE} was decreased considerably by the coating of $50Li_4SiO_4 \cdot 50Li_3PO_4$ on $LiCoO_2$ electrode. The R_{PE} of the cell using $50Li_4SiO_4 \cdot 50Li_3PO_4$-coated $LiCoO_2$ particles was significantly small compared with that of the cell using Li_2SiO_3-coated $LiCoO_2$ particles which was prepared by the sol-gel method; the R_{PE} of the cell was 160 Ω as shown in Fig. 2-13. The conductivity at room temperature of the Li_2SiO_3 thin film prepared by the sol-gel method was 1.0×10^{-9} S cm^{-1}, which is three orders of magnitude lower than that of the $50Li_4SiO_4 \cdot 50Li_3PO_4$ thin film prepared by PLD. The high lithium ion conductivity of the $50Li_4SiO_4 \cdot 50Li_3PO_4$ thin film is probably responsible for the significant decrease in the R_{PE} of all-solid-state cells.

The cells were discharged at the high current density of 6.4 mA cm^{-2} after charging the cells to 3.6 V vs. Li–In at the current density of 0.13 mA cm^{-2}. Figure 2-37 shows the discharge curves at 6.4 mA cm^{-2}. The discharge potential of the cell with $50Li_4SiO_4 \cdot 50Li_3PO_4$-coated $LiCoO_2$ is higher than that of the cell with uncoated $LiCoO_2$. The discharge capacity of the cell with uncoated $LiCoO_2$ is 33 mAh g^{-1}, while that of $50Li_4SiO_4 \cdot 50Li_3PO_4$-coated $LiCoO_2$ is 46 mAh g^{-1}. The decrease of the R_{PE} by oxide coatings with high lithium ion conductivity prevents IR drop and brings about a high voltage plateau, which lead to a large capacity at the discharge process.

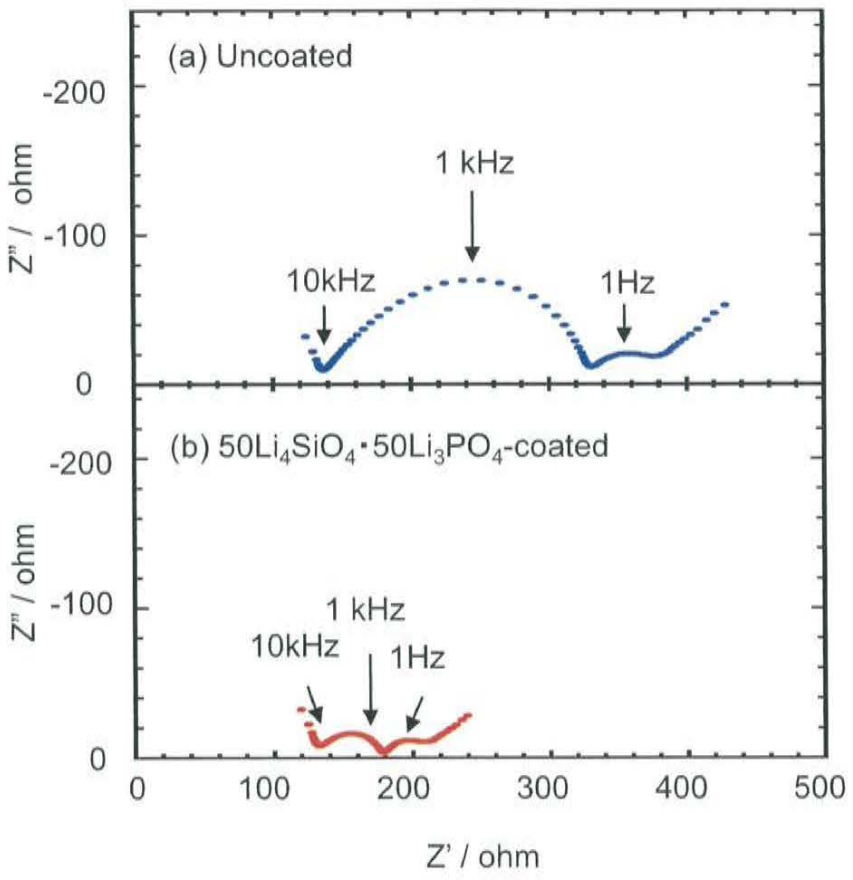

Figure 2-36 Impedance profiles of the all-solid-state cells with (a) uncoated and (b) $50Li_4SiO_4 \cdot 50Li_3PO_4$-coated $LiCoO_2$ after the first charge process. The cells were charged at 0.13 mA cm^{-2} and the cut-off voltage was 3.6 V vs. Li-In.

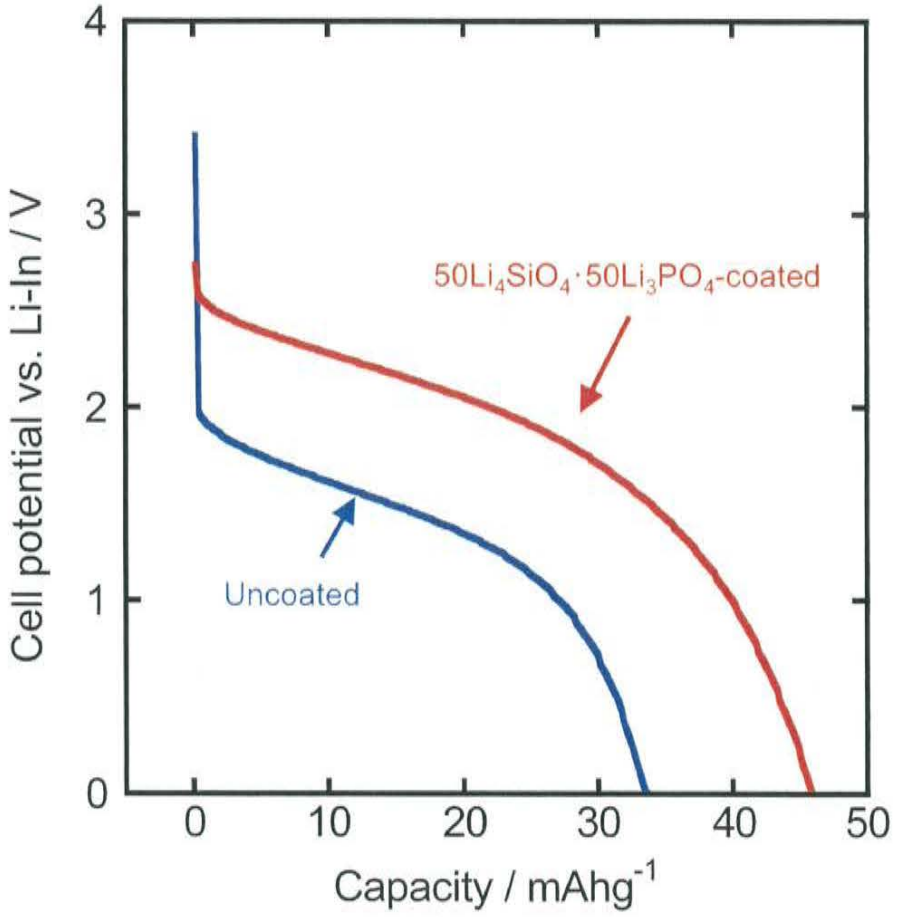

Figure 2-37 Discharge curves of all-solid-state cells with uncoated and $50Li_4SiO_4 \cdot 50Li_3PO_4$-coated $LiCoO_2$. The cells were discharged at 6.4 mA cm^{-2}.

2.3.3.3. Sulfide-coated $LiCoO_2$ prepared by thermal decomposition technique

(i) Preparation of cobalt sulfide and nickel sulfide by thermal decomposition technique

The thermal decomposition behavior of the dithiocarbamato complexes was characterized with DTA-TG measurements. Figure 2-38 shows DTA-TG curves of (a) $Co[S_2CN(C_2H_5)_2]_2$ and (b) $Ni[S_2CN(C_2H_5)_2]_2$ with a heating rate of 10 K min^{-1}. In the DTA-TG curves of $Co[S_2CN(C_2H_5)_2]_2$, two endothermic peaks with weight loss from 250 to 350°C are observed. The sharp endothermic peak observed at 270°C is due to melting of the Co complex. The broad endothermic peak near 310°C accompanied with weight loss is attributable to the decomposition of the Co complex. The weight change before and after the decomposition is 72 %, which closely corresponds to the theoretical weight change from $Co[S_2CN(C_2H_5)_2]_2$ to CoS (71%). Similar to Co complex, the DTA-TG curves of $Ni[S_2CN(C_2H_5)_2]_2$ give two endothermic peaks with weight loss from 320 to 370°C. The weight change before and after the decomposition is 74 % which also corresponds to the theoretical weight change from $Ni[S_2CN(C_2H_5)_2]_2$ to NiS (74%).

The XRD measurements were conducted to identify CoS and NiS prepared by thermal decomposition of $Co[S_2CN(C_2H_5)_2]_2$ and $Ni[S_2CN(C_2H_5)_2]_2$, respectively. Figure 2-39 shows XRD patterns of Co and Ni complexes before and after heat treatment at 400°C under N_2 atmosphere. The XRD patterns show that CoS and NiS are prepared after the heat treatment of $Co[S_2CN(C_2H_5)_2]_2$ and $Ni[S_2CN(C_2H_5)_2]_2$, respectively.

(ii) Morphology of sulfide-coated $LiCoO_2$

The $Co[S_2CN(C_2H_5)_2]_2$ and $Ni[S_2CN(C_2H_5)_2]_2$ were coated on $LiCoO_2$ particles (Honjo chemical) and heated at 400°C under N_2 atmosphere to coat CoS and NiS on $LiCoO_2$ particles. The XRD measurements were conducted on the CoS-coated and NiS-coated $LiCoO_2$ particles. Only XRD patterns of $LiCoO_2$ were observed in all the coated $LiCoO_2$ particles; the patterns

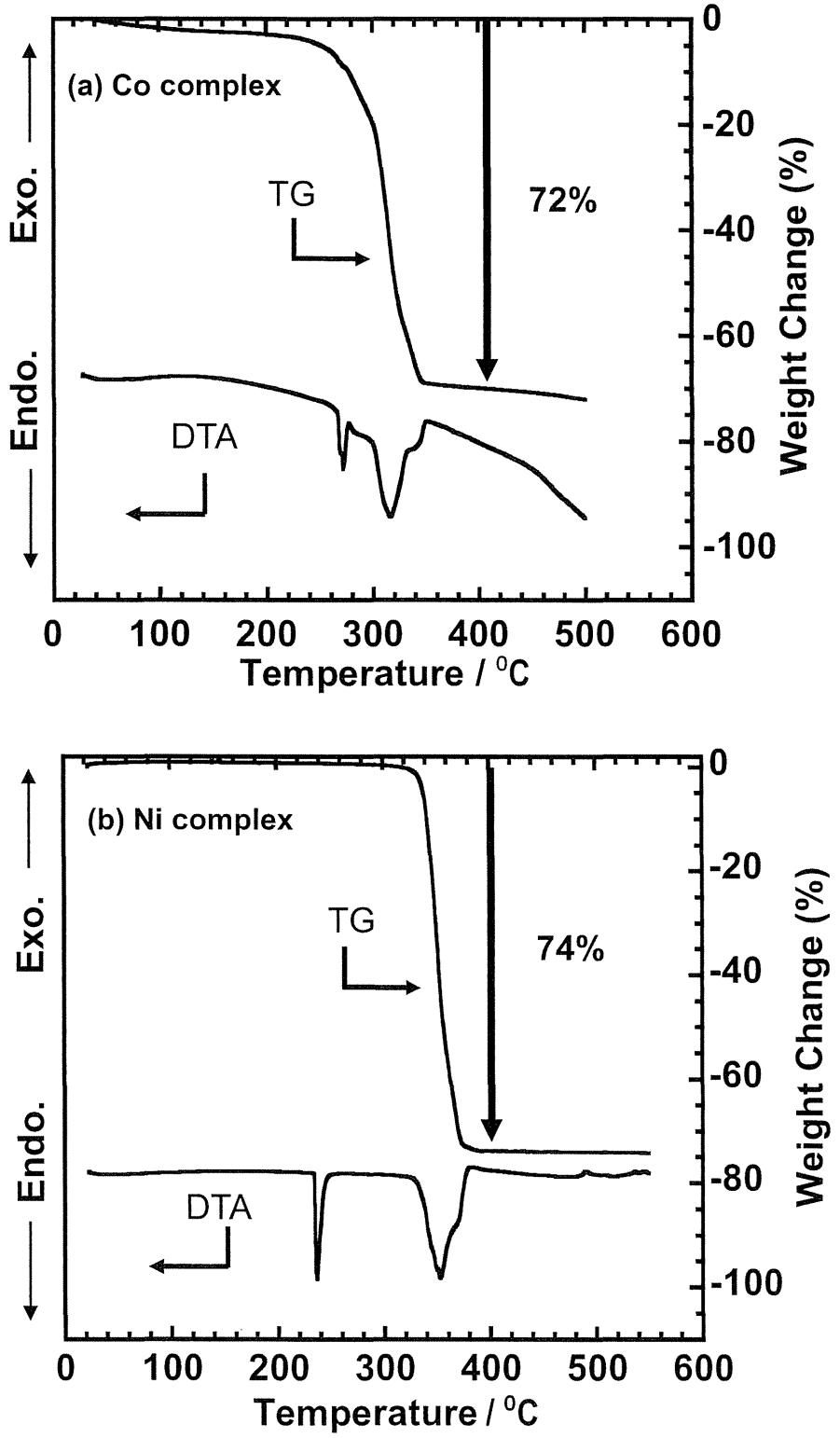

Figure 2-38 DTA-TG curves of (a) Co complex and (b) Ni complex.

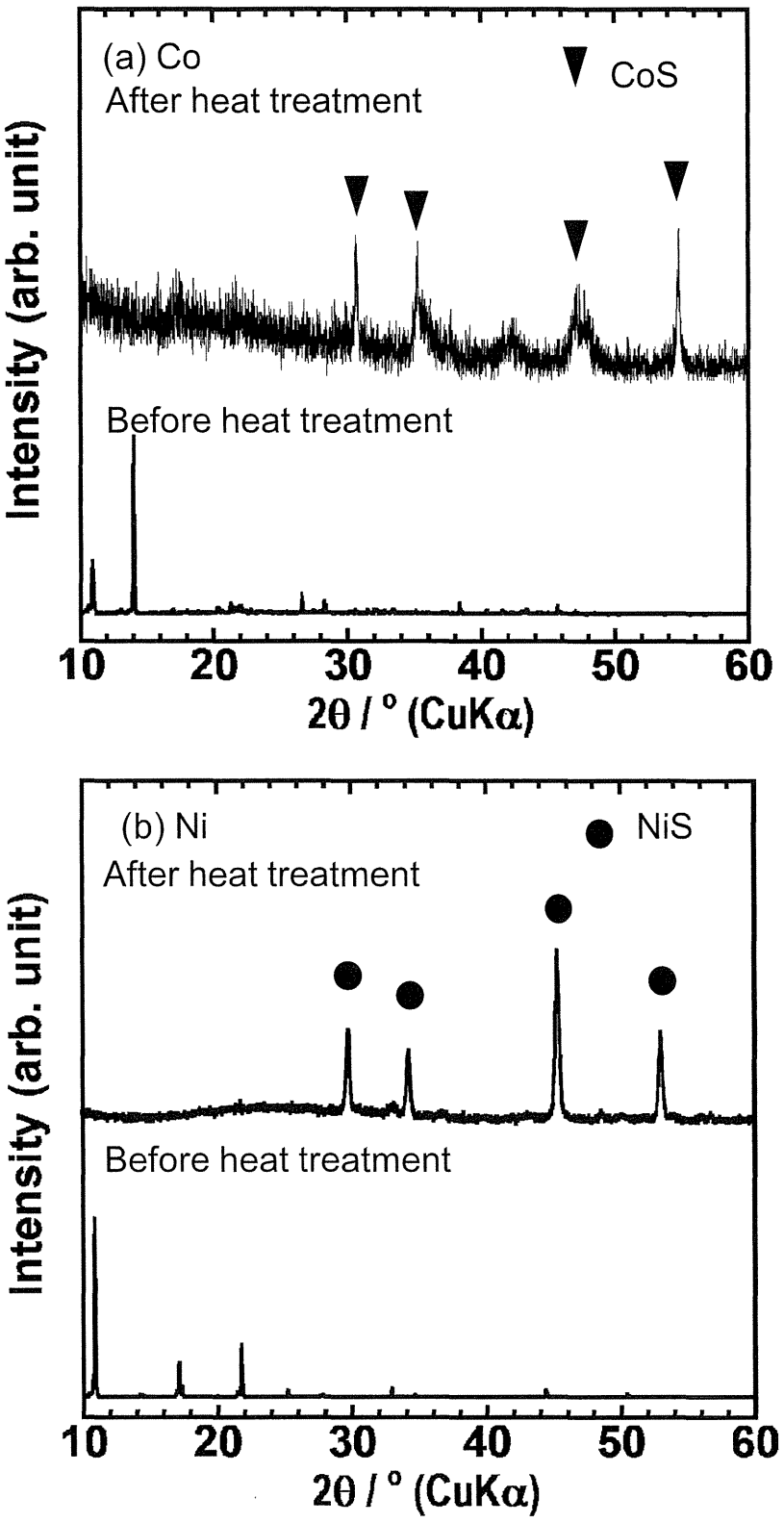

Figure 2-39 XRD patterns of (a) Co and (b) Ni complexes before and after heat treatment at 400°C.

of CoS and NiS were not observed because the coating amounts were very small. The surface morphology of the coated $LiCoO_2$ particles was investigated using FE-SEM observation. Figure 2-40 shows FE-SEM images of the surfaces of the $LiCoO_2$ particles coated with CoS and NiS. The surface of uncoated $LiCoO_2$ is also shown for comparison. The surface of the uncoated $LiCoO_2$ particles is relatively smooth. In contrast, rough surface due to coating materials is observed for 1 wt% CoS-coated and 1wt% NiS-coated $LiCoO_2$ particles. The $LiCoO_2$ particles are almost covered with the sulfide coatings. The surface of NiS-coated $LiCoO_2$ was also characterized using TEM observation. Figure 2-41 (a-c) shows TEM images of the surface of 0.1 wt% NiS-coated $LiCoO_2$ particle. The coating layer with 1-10 nm thick is observed on each coated $LiCoO_2$ particle.

(iii) Electrochemical performance of all-solid-state cells using sulfide-coated $LiCoO_2$ particles

All-solid-state cells were constructed using composite electrode of the mixture of $LiCoO_2$, $80Li_2S{\cdot}20P_2S_5$ solid electrolyte, and VGCF with weight ratios of 40 : 60 : 4.

Figure 2-42 shows impedance profiles of the all-solid-state cells using uncoated, 0.01 wt% CoS-coated, 0.1 wt% CoS-coated, and 1 wt% CoS-coated $LiCoO_2$. The measurements were conducted after charging to 110 mAh g^{-1}, which is the capacity corresponding to $Li_{0.6}CoO_2$. The resistance of the solid electrolyte layer (R_{SE}) was 120-130 Ω in all the four cells. The semicircles are attributable to the interfacial resistance between $LiCoO_2$ and Li_2S–P_2S_5 solid electrolyte (R_{PE}). The R_{PE} of the cells using uncoated, 0.01wt% CoS-coated, 0.1wt% CoS-coated, and 1wt% CoS-coated $LiCoO_2$ are 800, 230, 130, and 230 Ω, respectively. The R_{PE} was decreased by the CoS coatings. The favorable coating amount was near 0.1 wt% in this case. Figure 2-43 shows the charge-discharge curves of all-solid-state cells using uncoated and 0.1 wt% CoS-coated $LiCoO_2$. The cells were

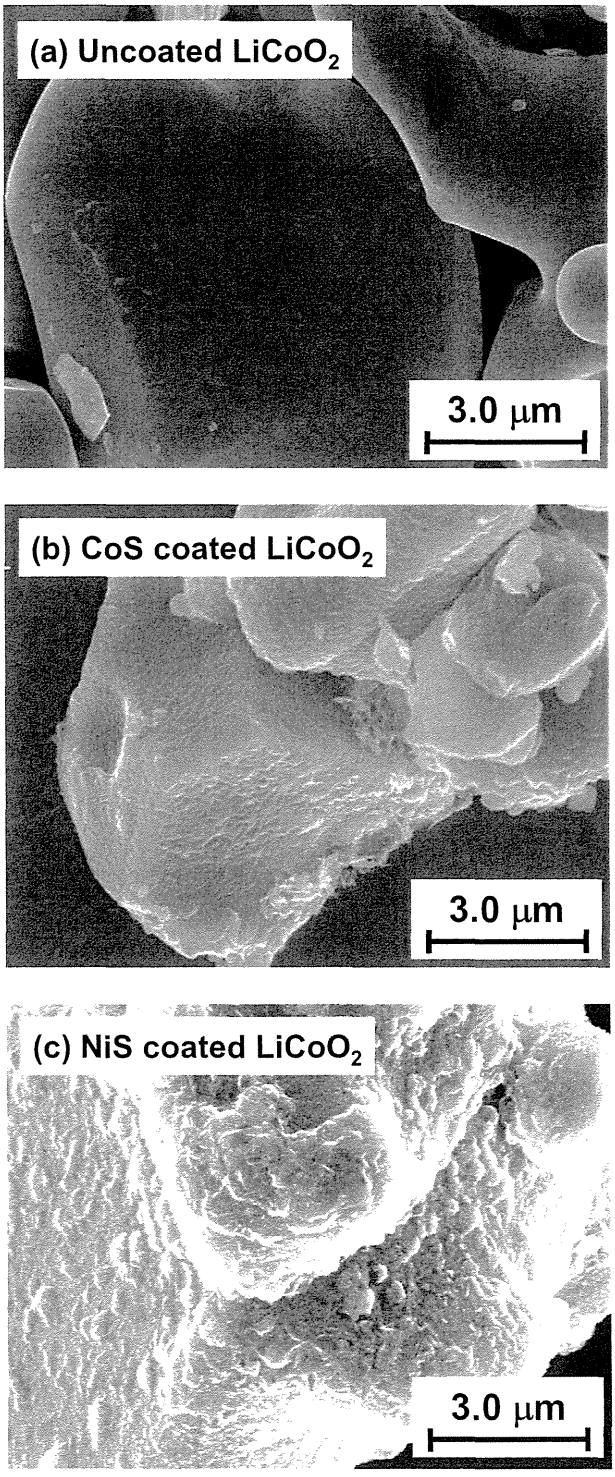

Figure 2-40 FE-SEM images of (a) uncoated, (b) 1.0 wt% CoS-coated, and (c) 1.0 wt% NiS-coated $LiCoO_2$ particles.

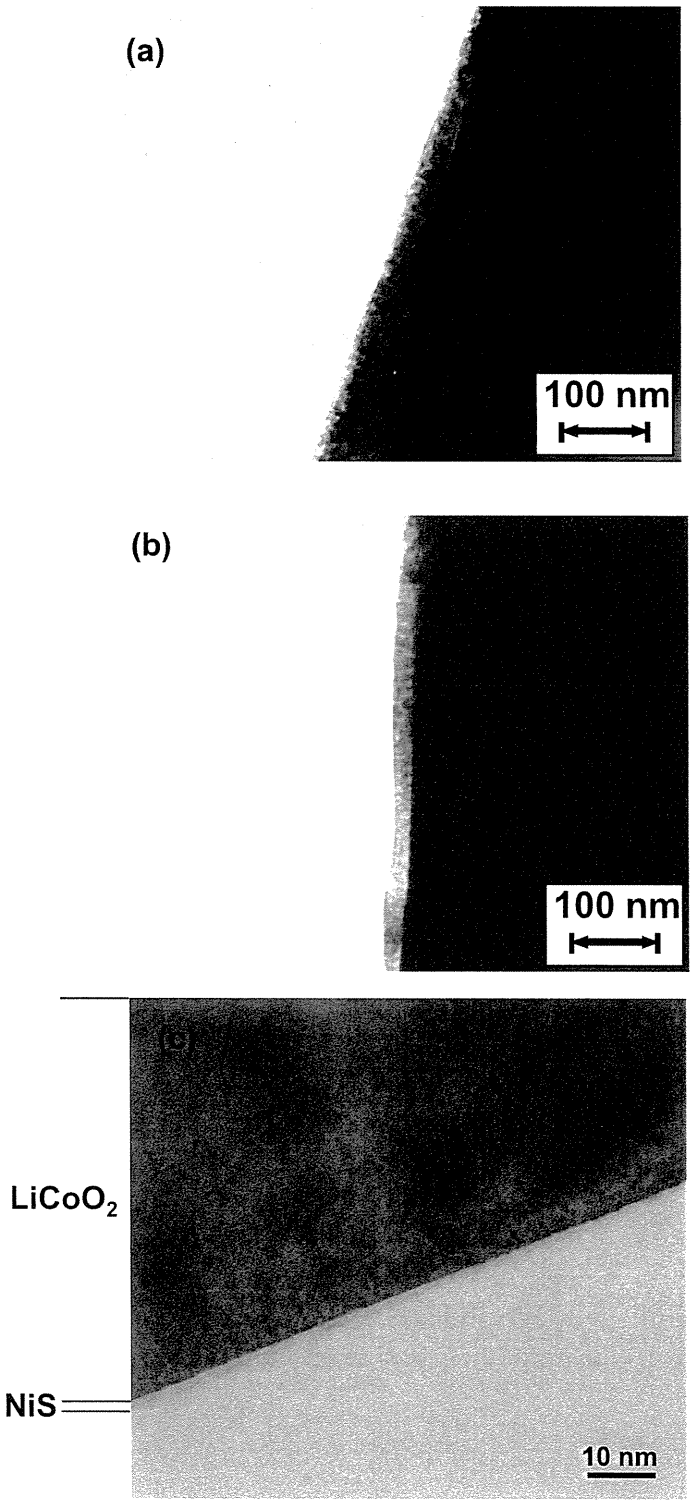

Figure 2-41 TEM images of 0.1 wt% NiS-coated $LiCoO_2$ particles.

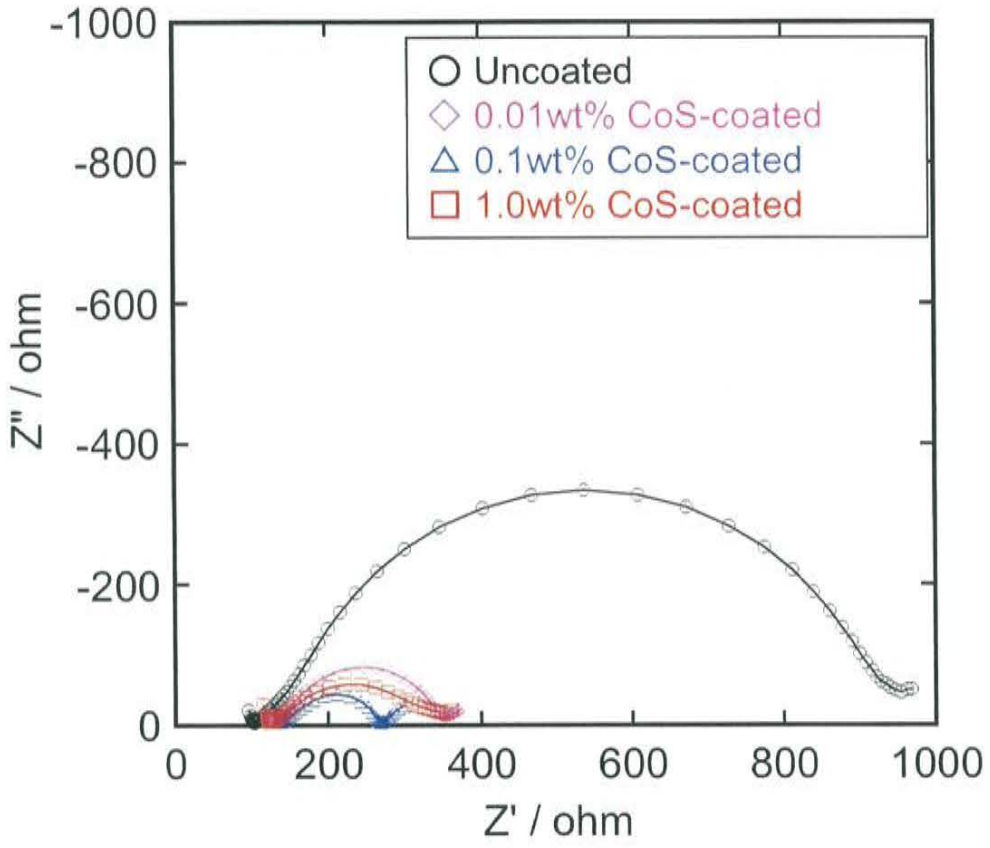

Figure 2-42 Impedance profiles of all-solid-state cells using uncoated and CoS-coated $Li_{1-x}CoO_2$ after charging to 109 mAh g^{-1} (x = 0.4) at the current density of 1.3 mA.

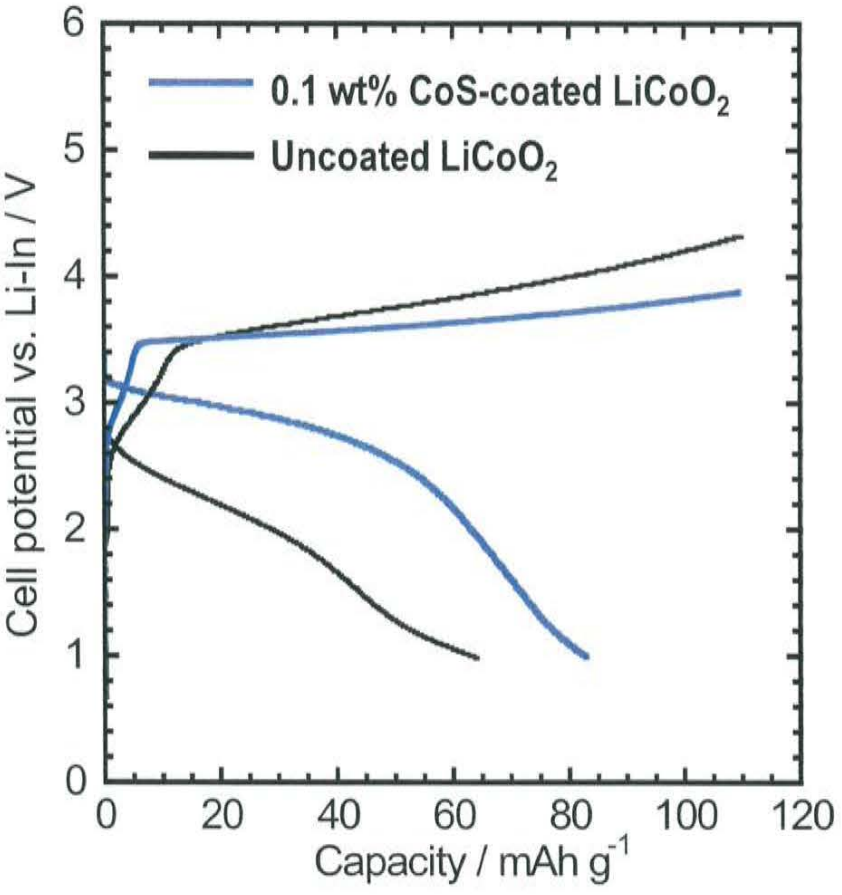

Figure 2-43 Charge-discharge curves of all-solid-state cell In / $80Li_2S{\cdot}20P_2S_5$ glass-ceramics / $LiCoO_2$ with uncoated and 0.1 wt% CoS-coated $LiCoO_2$. The current density used was 1.3 mA cm^{-2}.

charged up to 110 mAh g^{-1} and discharged to 1.0 V vs. Li–In and the current density was 1.3 mA cm^{-2}. The discharge capacities of the cells using uncoated and CoS coated $LiCoO_2$ are respectively 64 and 83 mAh g^{-1}. The average charge voltages of those are 3.8 and 3.6 V, respectively. The average voltages for discharge plateau are 1.9 and 2.6 V, respectively. The IR drop was decreased by the CoS coating, which results from the lower R_{PE} shown in Fig. 2-42. Figure 2-44 shows the charge-discharge curves of all-solid-state cells using 0.1 wt% CoS-coated $LiCoO_2$ at various current densities of 1.3, 3.8, and 13 mA cm^{-2}. The charging voltage increases with increasing the current density. The all-solid-state cell can be charged and discharged at a high current density of 13 mA cm^{-2} with a reversible capacity of 53 mAh g^{-1}.

Figure 2-45 shows impedance profiles of the all-solid-state cells using uncoated, and 0.1 wt% NiS-coated $LiCoO_2$. The measurements were conducted after charging to 110 mAh g^{-1}. The R_{SE} was 120-130 Ω in each cell. The R_{PE} of the cells using uncoated and 0.1wt% NiS-coated are 800 and 60 Ω, respectively. The interfacial modification using NiS brings about the significant decrease of the R_{PE}. Figure 2-46 (a) shows initial charge-discharge curves of all-solid-state cell In / $80Li_2S{\cdot}20P_2S_5$ glass-ceramics / $LiCoO_2$ with uncoated and 0.1 wt% NiS-coated $LiCoO_2$ at the current density of 1.3 mA cm^{-2}. The charge-discharge curves of all-solid-state cell using 0.1 wt% NiS coated $LiCoO_2$ for 10 cycles are shown in (b). The discharge capacities of the cells using uncoated and NiS coated $LiCoO_2$ are respectively 61 and 83 mAh g^{-1}. The average charging voltages of those are 3.9 and 3.5 V, respectively. The average voltages for discharge plateau are 2.0 and 3.1 V, respectively. The all-solid-state cell was charged up to the capacity of 110 mAh g^{-1} and discharged to 2.0 V until the 3rd cycle, and then charge-discharge cycles were repeated between 4.0 V and 2.0 V after the 4th cycle. At the 2nd and 3rd discharging processes, a high capacity more than 100 mAh g^{-1} is obtained at the current density of 1.3 mA cm^{-2}. The capacity of the 10th

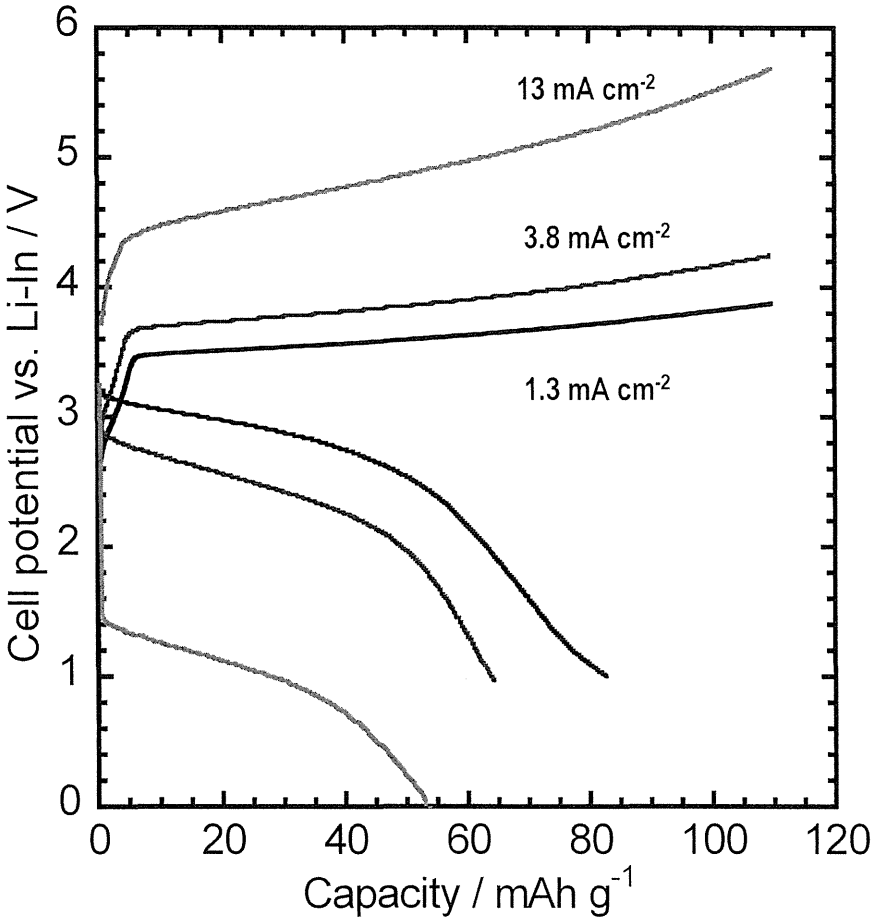

Figure 2-44 Initial charge discharge curves of all-solid-state cells In / $80Li_2S{\cdot}20P_2S_5$ glass-ceramic / 0.1 wt% CoS-coated $LiCoO_2$ at various current densities of 1.3, 3.8, and 13 mA cm^{-2}.

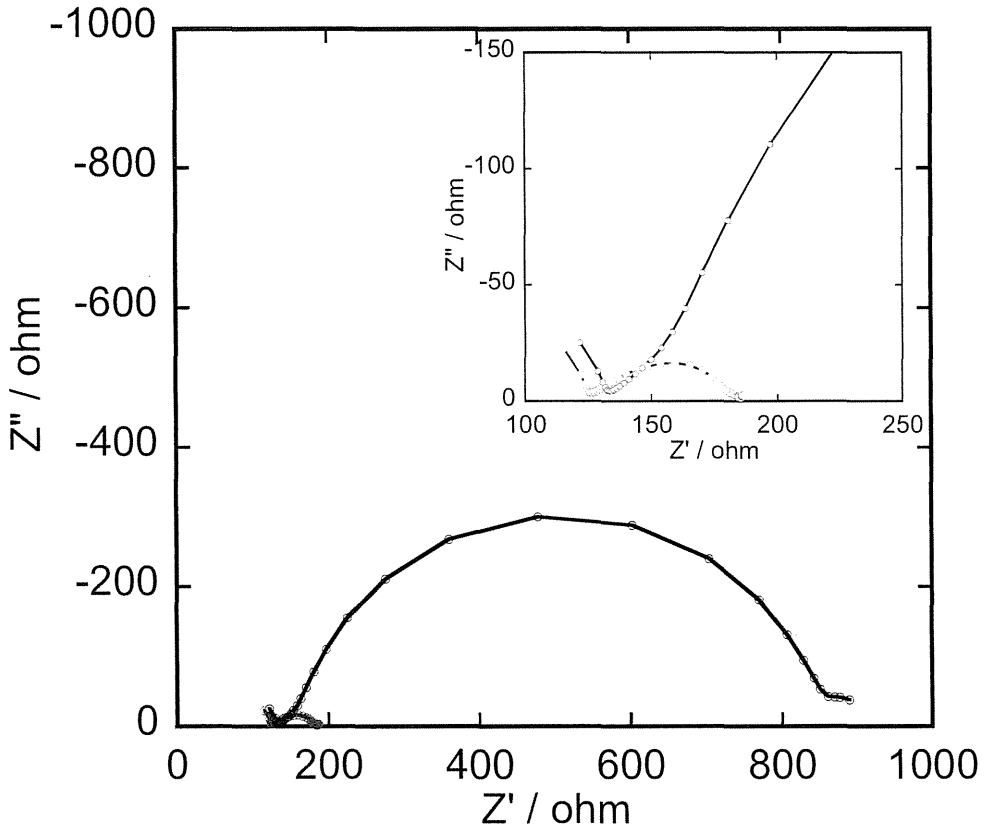

Figure 2-45 Impedance profiles of all-solid-state cells using uncoated and 0.1 wt% NiS-coated $Li_{1-x}CoO_2$ after charging to 109 mAh g^{-1} (x = 0.4) at the current density of 1.3 mA.

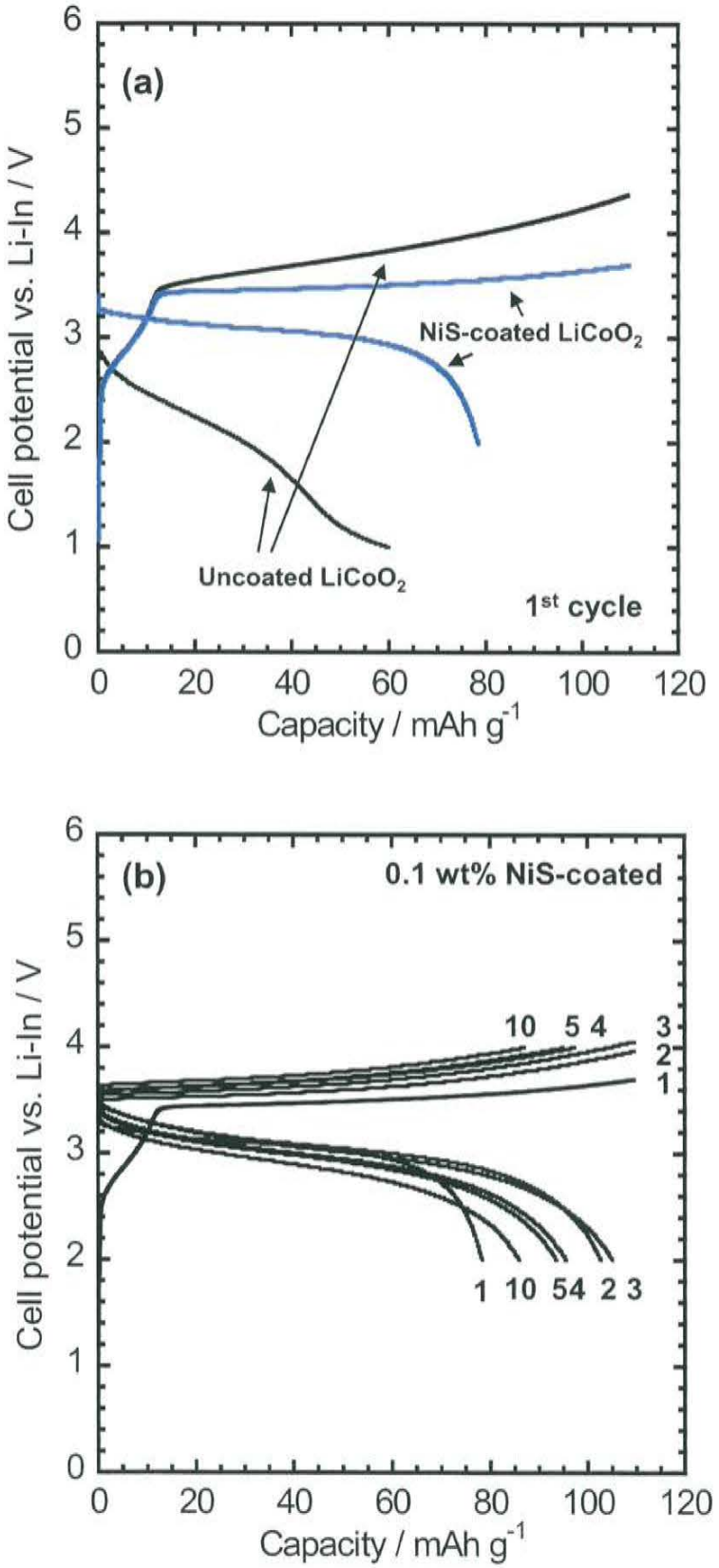

Figure 2-46 (a) Initial charge-discharge curves of all-solid-state cells In / $80Li_2S{\cdot}20P_2S_5$ glass-ceramics / $LiCoO_2$ with uncoated and 0.1 wt% NiS-coated $LiCoO_2$ at the current density of 1.3 mA cm^{-2}. The charge-discharge curves of all-solid-state cell using 0.1 wt% NiS coated $LiCoO_2$ for 10 cycles are shown in (b).

discharging is 87 mAh g^{-1}. The cycle performance of the all-solid-state cell using NiS-coated $LiCoO_2$ shown in Fig. 2-46 (b) is better than that using uncoated $LiCoO_2$ reported in Ref. 37. Figure 2-47 shows the charge discharge curves of all-solid-state cells using 0.1 wt% Ni-coated $LiCoO_2$ at current densities of 1.3 and 13 mA cm^{-2}. The all-solid-state cell can be charged and discharged at a high current density of 13 mA cm^{-2} with a reversible capacity of 72 mAh g^{-1}. The capacity of the cell using 0.1 wt% NiS-coated $LiCoO_2$ is larger than that using 0.1 wt% CoS-coated $LiCoO_2$ shown in Fig. 2-44. The discharge voltage of the cell using NiS-coated $LiCoO_2$ is also higher than that using CoS-coated $LiCoO_2$ at the current density of 13 mA cm^{-2}. Results show that NiS coating is more effective in improving battery performance of the all-solid-state batteries when coating amount is 0.1 wt%.

Figure 2-48 shows the charge-discharge curves of the all-solid-state cells using uncoated and NiS-coated $LiCoO_2$ with the charging cutoff voltage of 4.0 V vs. Li–In at the current density of 0.13 mA cm^{-2}. By using the relatively low current density and high cutoff voltage, high charging capacities of more than 150 mAh g^{-1} are obtained in each cell. The discharge capacities of the cell using uncoated and NiS-coated $LiCoO_2$ are 75 and 148 mAh g^{-1}, respectively. The all-solid-state cell using NiS-coated $LiCoO_2$ showed much better performance. After charging to 4.0 V at a low current density, the all-solid-state cells showed large charging capacity, indicating that the cells underwent the high potential. At the high potential region, the R_{PE} increased as shown in Fig 2-19 (b). This is the cause of the large IR drop observed at the discharging process of the cell using uncoated $LiCoO_2$. In the cell using NiS-coated $LiCoO_2$, the increase of the R_{PE} was suppressed; the cell using NiS-coated $LiCoO_2$ showed a higher voltage discharging.

As shown above, the interfacial modification using CoS and NiS was effective in improving the electrochemical performance of the all-solid-state batteries. The CoS analog compounds produced at the interface between $LiCoO_2$ and sulfide electrolyte [35], indicating

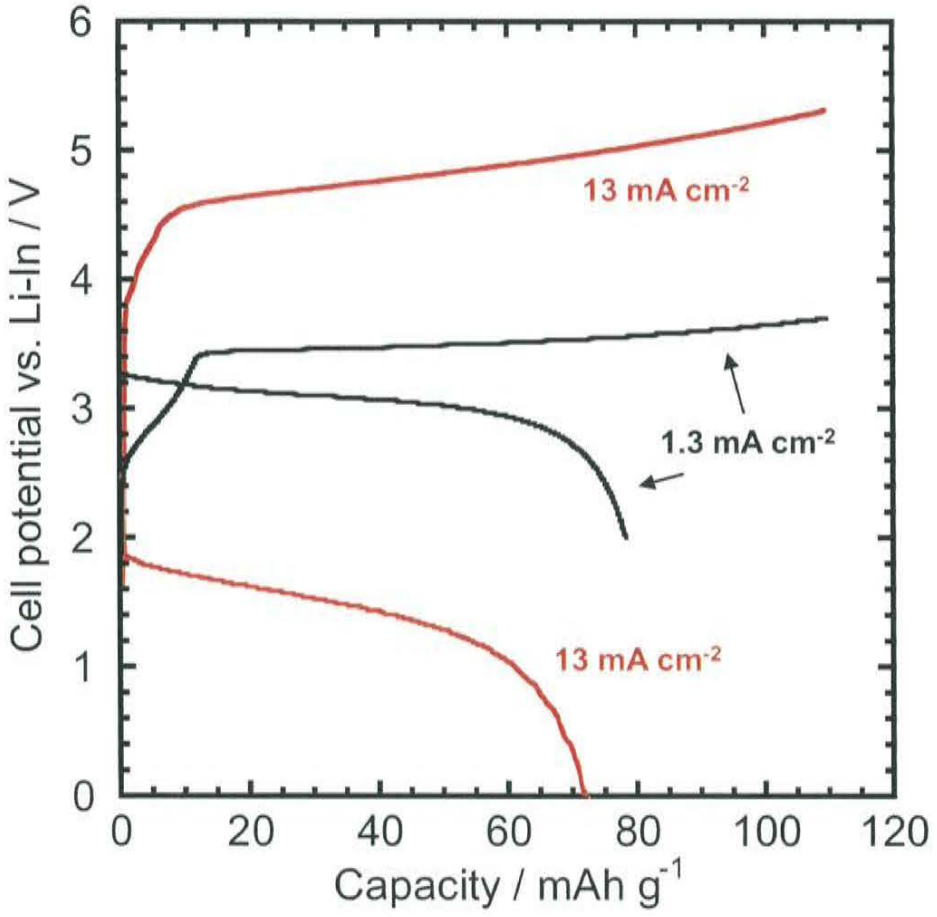

Figure 2-47 Initial charge discharge curves of all-solid-state cells In / $80Li_2S \cdot 20P_2S_5$ glass-ceramic / 0.1 wt% CoS-coated $LiCoO_2$ at current densities of 1.3 and 13 mA cm^{-2}.

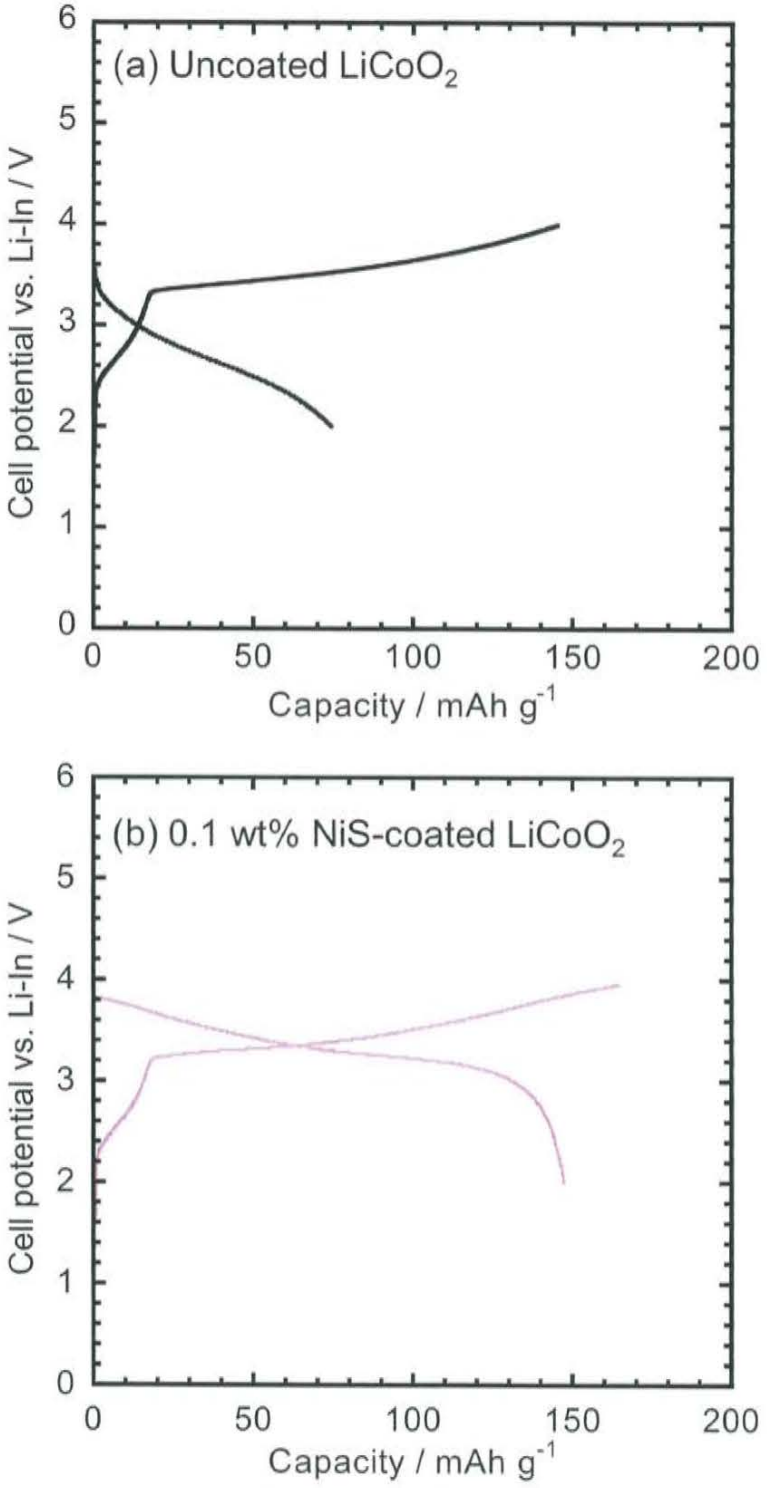

Figure 2-48 Initial charge–discharge curves of the all-solid-state cells In/$80Li_2S{\cdot}20P_2S_5$ glass-ceramic/$LiCoO_2$ with (a) uncoated and (b) 0.1 wt% NiS-coated $LiCoO_2$ with the cutoff potentials of 4.0 V vs. Li-In. The current densities for charging and discharging were 0.13 mA cm^{-2}.

that the reaction between $LiCoO_2$ and the sulfide electrolyte. The reaction causes the decomposition of the particle surface of the sulfide electrolyte and $LiCoO_2$ particle surface. The interfacial reaction is discussed in details using the result obtained by TEM observation in Chapter 3 in this thesis. The CoS coating preformed on $LiCoO_2$ suppresses the interfacial decomposition reactions and decreases the R_{PE}. It is considered that the cause of the large R_{PE} is not the existence CoS-analog layer itself but decomposition of the solid electrolyte and/or $LiCoO_2$ electrode surface. Thin CoS and NiS coatings rather acts as a buffer layer to suppress the decomposition at the highly reactive interface between charged $LiCoO_2$ and Li_2S–P_2S_5 solid electrolyte, although thick coatings should be act as a high resistive layer.

2.4. Summary

This chapter described the identification of the resistance components of all-solid-state cells and the improvement of electrochemical performance of all-solid-state cells by interfacial modification between $LiCoO_2$ electrode and Li_2S–P_2S_5 solid electrolyte.

Electrochemical impedance spectroscopy measurements revealed that the cells after the initial charge process have a large resistance component at the interface between $LiCoO_2$ and Li_2S–P_2S_5 solid electrolyte. The large resistance is the main cause of the low rate performance of all-solid-state cells using $LiCoO_2$ and Li_2S–P_2S_5 solid electrolytes.

An interfacial modification between layered metal oxide electrodes of $LiCoO_2$ and Li_2S–P_2S_5 solid electrolytes was carried out to study the effects of the modification on the electrochemical performance of all-solid-state cells. Oxide films such as Li_2O–SiO_2, Li_2O–TiO_2, and Li_4SiO_4–Li_3PO_4 were coated on the electrode particles by sol-gel and PLD techniques to modify the interface between electrode and solid electrolyte.

The interfacial resistance between $LiCoO_2$ and Li_2S–P_2S_5 solid electrolyte was decreased with the coatings. It has been clarified that the lithium-ion conductivity of coating

materials on the $LiCoO_2$ particles is important for high rate performance of the all-solid-state lithium secondary batteries; coating materials with higher lithium-ion conductivity are more effective in decreasing the interfacial resistance. The all-solid-state cells using $LiCoO_2$ particles coated with $50Li_4SiO_4 \cdot 50Li_3PO_4$ solid electrolyte coating showed the lowest interfacial resistance of 48 Ω and the highest rate performance among the oxide solid electrolyte coatings studied in this thesis. Nevertheless, insulative SiO_2 and TiO_2 coatings were also effective in decreasing the interfacial resistance when coating amounts were small. The interfacial resistance increased with increasing the charging voltage of the cells. When the all-solid-state cells were charged to 3.6 V vs. Li–In, the activation energies of lithium-ion conduction at $LiCoO_2$ / solid electrolyte interface were approximately 60 kJ mol^{-1}; they were almost the same in the cells using coated $LiCoO_2$. The interfacial resistance decreased by an increase of the pre-exponential factor in the Arrhenius equation. The charge-discharge performance of the all-solid-state cells is improved by the interfacial modifications. The decrease of the interfacial resistance led to a high voltage plateau and large discharge capacity. The average discharge voltages at high current densities increased because of the resistance decreased by the coatings; the all-solid-state cells using coated $LiCoO_2$ was discharged even at extremely high current densities more than 5 mA cm^{-2} at room temperature. The all-solid-state cells using coated $LiCoO_2$ showed larger capacity and better cycle performance. The oxide coatings suppress the increase in resistance during charge-discharge cycles.

The interfacial modification using CoS and NiS was also effective in improving the electrochemical performance of the all-solid-state batteries. Thin CoS and NiS coatings act as a buffer layer to suppress the decomposition at the interface between charged $LiCoO_2$ and Li_2S–P_2S_5 solid electrolyte.

The use of coated $LiCoO_2$ showed many advantages as (i) suppression of the increase in interfacial resistance, (ii) large capacity, (iii) high voltage discharging, and (iv) long cycle life.

The interfacial modification between positive electrode and Li_2S–P_2S_5 solid electrolyte is essential to develop all-solid-state batteries with high performance.

2.5. References

[1] T. Minami, A. Hayashi, and M. Tatsumisago, *Solid State Ionics*, **177** (2006) 2715.

[2] F. Mizuno, A. Hayashi, K. Tadanaga, and M. Tatsumisago, *J. Electrochem. Soc.*, **152** (2005) 1499.

[3] F. Mizuno, A. Hayashi, K. Tadanaga, and M. Tatsumisago, *J. Power Sources*, **146** (2005) 711.

[4] N. Ohta, K. Takada, L. Zhang, R. Ma, M. Osada, and T. Sasaki, *Adv. Mater.*, **18** (2006) 2226.

[5] N. Ohta, K. Takada, I. Sakaguchi, L. Zhang, R. Ma, K. Fukuda, M. Osada, and T. Sasaki, *Electrochem. Commun.*, **9** (2007) 1486.

[6] K. Takada, N. Ohta, L. Zhang, K. Fukuda, I. Sakaguchi, R. Ma, M. Osada, and T. Sasaki, *Solid State Ionics*, **179** (2008) 1333.

[7] J. Cho, C.-S. Kim, and S. Yoo, *Electrochem. Solid-State Lett.*, **3** (2000) 362.

[8] J. Cho, Y.J. Kim, and B. Park, *Chem. Mater.*, **12** (2000) 3788.

[9] J. Cho, Y.J. Kim, J.T. Kim, and B. Park, *Angew. Chem. Int. Ed.*, **40** (2001) 3367.

[10] J. Cho, B. Kim, J.-G. Lee, Y.-W. Kim, and B. Park, *J. Electrochem. Soc.*, **152** (2005) A32.

[11] M. Mladenov, R. Stoyanova, E. Zhecheva, and S. Vassilev, *Electrochem. Commun.*, **3** (2001) 410.

[12] Z. Wang, C. Wu, L. Liu, F. Wu, L. Chen, and X. Huang, *J. Electrochem. Soc.*, **149** (2002) A466.

[13] Z.X. Wang, X.J. Huang, and L.Q. Chen, *J. Electrochem. Soc.*, **150** (2003) A199.

[14] Z. Chen and J.R. Dahn, *Electrochem. Solid-State Lett.*, **6** (2003) A221.

[15] Z. Chen and J.R. Dahn, *Electrochim. Acta*, **49** (2004) 1079.

[16] Y.-K. Sun, S.-W. Cho, S.-T. Myung, and K. Amine, J. Prakash, *Electrochim. Acta*, **53** (2007) 1013.

[17] Y.-K. Sun, C.-S. Yoon, S.-Y. Myung, I. Belharouak, and K. Amine, *J. Electrochem. Soc.*, **156** (2009) A1005.

[18] J. Zhang, Y.-J. Xiang, Y. Yu, S. Xie, G.-S. Jiang, and C.-H. Chen, *J. Power Sources*, **132** (2004) 187.

[19] S. Seki, Y. Kobayashi, H. Miyashiro, Y. Mita, and T. Iwahori, *Chem. Mater.*, **17** (2005) 2041.

[20] Y. Kobayashi, S. Seki, M. Tabuchi, H. Miyashiro, Y. Mita, and T. Iwahori, *J. Electrochem. Soc.*, **152** (2005) A1985.

[21] S. Seki, Y. Kobayashi, H. Miyashiro, Y. Ohno, A. Usami, Y. Mita, M. Watanabe, and N. Terada, *Chem. Commun.* (2006) 544.

[22] H. Okamoto, S. Hikazudani, C. Inazumi, T. Takeuchi, M. Tabuchi, and K. Tatsumi, *Elrctrochem. Solid-State Lett.*, **11** (2008) A97.

[23] R. Nomura, K. Kanaya, and H. Matsuda, *Bull. Chem. Soc. Jpn.*, **62** (1989) 939.

[24] R. Nomura, K. Kanaya, and H. Matsuda, *Ind. Eng. Chem. Res.*, **28** (1989) 877.

[25] R.D. Pike, H. Cui, R. Kershaw, K. Dwight, A. Wold, T.N. Blanton, A.A. Wernbergand, and H.J. Gysling, *Thin Solid Films*, **224** (1993) 221.

[26] T. Iwami, K. Tadanaga, M. Tatsumisago, and T. Minami, *J. Am. Ceram. Soc.*, **78** (1995) 1668.

[27] A. Hayashi, S. Hama, T. Minami, and M. Tatsumisago, *Electrochem. Commun.*, **5** (2003) 111.

[28] S. Zhao, Z. Fu, and Q. Qin, *Thin Solid Films*, **415** (2002) 108.

[29] T. Minami, *J. Non-Cryst. Solids*, **73** (1985) 273.

[30] C. J. Brinker and G. W. Scherer, *Sol-Gel Science: The Physics and Chemistry of Sol-Gel Processing*, Academic Press, Boston, MA (1990) p. 105.

[31] F. Mizuno, A. Hayashi, K. Tadanaga, and M. Tatsumisago, *Solid State Ionics*, **177**, (2006)

2721.

[32] Y. Iriyama, H. Kuriya, I. Yamada, T. Abe, and Z. Ogumi, *J. Power Sources*, **137** (2004) 111.

[33] Y. Iriyama, T. Kako, C. Yada, T. Abe, and Z. Ogumi, *Solid State Ionics*, **176** (2005) 2371.

[34] J.B. Goodenough, in *Solid State Electrochemistry*, P.G. Bruce, Editor, Cambridge University Press, Cambridge, U.K. (1995) p. 53.

[35] Y. Uchimoto and M. Wakihara, in *Solid State Ionics for Batteries*, T. Minami, Editor, Springer-Verlag, Tokyo (2005) p.126.

[36] K. Takada, N. Aotani, K. Iwamoto and S. Kondo, *Solid State Ionics*, **79** (1995) 284.

[37] S. Seki, Y. Kobayashi, H. Miyashiro, A. Yamanaka, Y. Mita, and T. Iwahori, *J. Power Sources*, **146** (2005) 741.

[38] G.G. Amatucci, J.M. Tarascon, and L.C. Klein, *Solid State Ionics*, **83** (1996) 167.

[39] K. Kanehori, K. Matsumoto, K. Miyauchi, and T. Kudo, *Solid State Ionics*, **9** (1983) 1445.

[40] N. Kuwata, N. Iwagami, and J. Kawamura, *Solid State Ionics*, **180** (2009) 644.

[41] N. Kuwata, N. Iwagami, Y. Matsuda, Y. Tanji, and J. Kawamura, *ECS Trans.*, **16** (2009) 53.

[42] S. Zhao, Z. Fu, and Q. Qin, *Thin Solid Films*, **415** (2002) 108.

[43] J.F Whitacre, W.C. West, *Solid State Ionics*, **175** (2004) 251.

[44] E. Barsoukov and J.R.Macdonald ed., "Impedance spectroscopy", 2nd ed., John Wily & Sons, New Jersey (2005) p.241.

[45] M. Tatsumisago, N. Machida, and T. Minami, *J. Ceram. Soc. Jpn.*, **95** (1985) 197.

3. Interfacial Observation between $LiCoO_2$ Electrode and Li_2S–P_2S_5 Solid Electrolytes Using Transmission Electron Microscopy

3.1. Introduction

Commercially produced lithium-ion secondary batteries consist mainly of $LiCoO_2$ as a positive electrode, carbon as a negative electrode, and an organic liquid electrolyte. As an effective approach to improve the electrochemical performance of batteries, interfacial modifications between the positive electrode and electrolyte by coatings such as Al_2O_3, ZrO_2, SiO_2, $AlPO_4$, and AlF_3 on the $LiCoO_2$ positive electrode have been studied [1-6]. That modification efficiently improves the cycle performance, rate capability, and thermal stability of batteries. The effects of the modification are (i) suppression of structural change caused by phase transition of $LiCoO_2$, (ii) decrease of cobalt dissolution from $LiCoO_2$ to liquid electrolyte, and (iii) suppression of side reactions between the electrode and electrolyte.

The interface between the electrode and electrolyte in all-solid-state batteries differs from that in conventional batteries using liquid electrolytes. Both electrode and electrolyte materials in all-solid-state batteries are solid; electrochemical reactions occur through the solid-solid interface between the electrode and solid electrolyte materials. Therefore, formation of an effective electrode-electrolyte interface is important for all-solid-state batteries to achieve high performance [7]. Many studies have been conducted to form an effective electrode-electrolyte interface in all-solid-state batteries [8-12 and Chapter 2 in this thesis]. Among them, interfacial modification between electrode and solid electrolyte is an effective technique to improve electrochemical performance of batteries using liquid electrolytes. All-solid-state batteries using $LiCoO_2$ positive electrodes and sulfide solid electrolytes showed a large interfacial resistance between $LiCoO_2$ and solid electrolytes. The interfacial resistances were decreased greatly through the use of coatings using $LiNbO_3$,

$Li_4Ti_5O_{12}$, $LiTaO_3$, Li_2O–SiO_2, Li_2O–TiO_2, $50Li_4SiO_4 \cdot 50Li_3PO_4$, CoS, and NiS on $LiCoO_2$ [10-12 and Chapter 2 in this thesis]. The reason for decreasing an interfacial resistance remains unclear.

Observation and structural analysis of the interface between $LiCoO_2$ and sulfide solid electrolyte is beneficial to reveal the reasons for the large interfacial resistance of the all-solid-state batteries and for the decrease of the interfacial resistance by the coatings. Electrochemical impedance measurements have so far been used mainly to analyze the electrode-electrolyte interface of the all-solid-state batteries using sulfide-based solid electrolytes. On the other hand, transmission electron microscopy (TEM) is a powerful tool to analyze structure and morphology of the electrode-electrolyte interface. Brazier *et al.* reported TEM observation of the electrode-electrolyte interface on the thin film batteries using oxide-based solid electrolyte (amorphous Li_2O–V_2O_5–SiO_2). Their TEM observations suggested that the deterioration of the interface upon cycling was caused by the migration of the chemical elements between stacked layers [13]. The morphology, structure, and elemental distribution at the interfacial region directly affect the electrochemical performance of the all-solid-state batteries; their investigation enables us to obtain guidelines for an ideal electrode-electrolyte interface in all-solid-state batteries with high performance. As described above, it is readily apparent that the interfacial observation between positive electrode and sulfide solid electrolyte is important. Therefore, we have conducted TEM observations of the interface between $LiCoO_2$ and sulfide solid electrolyte.

In the present chapter, the interface between the $LiCoO_2$ electrode and $80Li_2S \cdot 20P_2S_5$ glass-ceramic solid electrolyte of all-solid-state cells was studied using TEM and scanning TEM (STEM) with energy dispersive X-ray spectroscopy (EDX). Samples for TEM observation were prepared using a focused ion beam (FIB). The electrode-electrolyte interface of the cell using Li_2SiO_3-coated $LiCoO_2$ was compared with that using uncoated

$LiCoO_2$ to clarify the coating effect from the viewpoint of structural changes.

3.2. Experimental

3.2.1. Cross-sectional observation of electrode-electrolyte interface

After charge-discharge measurements, the layered pellets of In/$80Li_2S \cdot 20P_2S_5$/ $LiCoO_2$ were obtained by removing of stainless steel current collector from the all-solid-state cells. Samples of the $LiCoO_2$/solid electrolyte cross section for TEM observations were obtained using focused ion beam (FIB) milling of the positive electrode layer. The electrode-electrolyte interface was analyzed using TEM (JEM2100F; JEOL). An elemental mapping analysis for the cross-section of the positive electrode layer was conducted using STEM equipped with EDX (JED-2300T; JEOL). The samples were transferred in Ar atmosphere from a glove box to the equipments for FIB and TEM.

3.3. Results and discussion

3.3.1. Interfacial observation between $LiCoO_2$ electrode and Li_2S–P_2S_5 solid electrolyte

To analyze the interface between $LiCoO_2$ electrode and Li_2S–P_2S_5 solid electrolyte, we conducted TEM observations of the positive electrode layer of the all-solid-state cells. The all-solid-state cell using uncoated $LiCoO_2$ after charging to 3.6 V vs. Li–In at the current density of 0.13 mA cm^{-2} was used for observations.

Figure 3-1 (a) shows cross-sectional high-angle annular dark field (HAADF) TEM images near the interface between uncoated $LiCoO_2$ and Li_2S–P_2S_5 solid electrolyte. The measurements were conducted after 1st charging to 3.6 V vs. Li–In at the current density of 0.13 mA cm^{-2}. Figure 3-1 (b) shows a magnified image of $LiCoO_2$/Li_2S–P_2S_5 interface presented as a square in Figure 3-1 (a). The TEM images show that $LiCoO_2$ electrode and Li_2S–P_2S_5 solid electrolyte retains a smooth contact after charging. An interfacial layer is

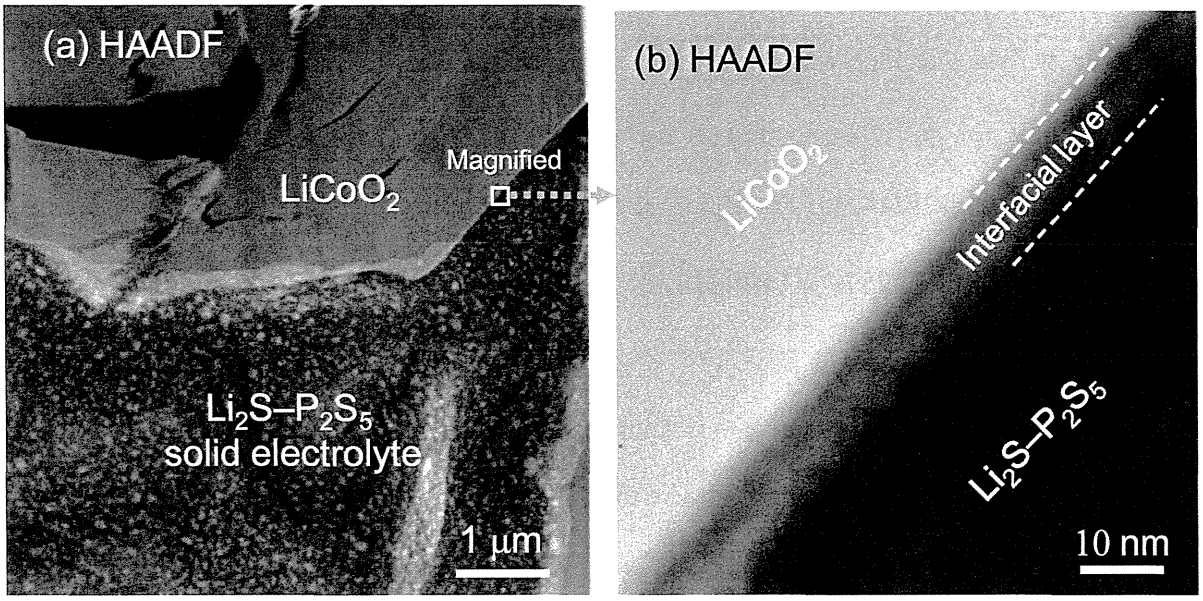

Figure 3-1 (a) Cross-sectional high-angle annular dark field (HAADF) TEM images of the interface between the $LiCoO_2$ electrode and the Li_2S–P_2S_5 solid electrolyte. (b) Magnified image of the area described by the square in Fig. 3-1a. Observations were conducted after initial charging to 3.6 V vs Li–In.

visible at the interface between $LiCoO_2$ electrode and Li_2S–P_2S_5 solid electrolyte in Figure 3-1(b). The layer thickness is ca. 10 nm.

Figure 3-2 shows a HAADF-STEM image and EDX mapping for the Co element near the $LiCoO_2$ electrode/Li_2S–P_2S_5 solid electrolyte interface. Existence of a Co element of $LiCoO_2$ electrode is observed in Li_2S–P_2S_5 solid electrolyte, indicating that Co diffusion from $LiCoO_2$ to Li_2S–P_2S_5 occurs. More details are available from EDX line profiles at the region near the $LiCoO_2$ electrode/Li_2S–P_2S_5 solid electrolyte interface.

Figure 3-3 (a) shows the HAADF-STEM image of the $LiCoO_2$/Li_2S–P_2S_5 interface. Figure 3-3 (b) presents the EDX line profiles of the existence ratio for Co, S, and P elements at the position indicated by the arrow in Fig. 3-3 (a). The coexistence of Co, S, and P elements is observed at the interfacial layer, indicating that the elements of $LiCoO_2$ and Li_2S–P_2S_5 solid electrolyte mutually diffuse. In particular, the Co diffusion from $LiCoO_2$ to Li_2S–P_2S_5 is outstanding; the Co element is observed even at a distance of 50 nm from the interface. Moreover, the EDX line profile shows small S diffusion into $LiCoO_2$. The mutual diffusion of Co, S, and P is related to the formation of the interfacial layer.

The nanostructure at the interfacial region was analyzed using nanoarea electron diffraction (n-ED). Figure 3-4 presents a cross-sectional HAADF-STEM image and the n-ED pattern at several points of the Li_2S–P_2S_5 solid electrolyte, interfacial layer, and $LiCoO_2$ electrode. The n-ED pattern of the solid electrolyte (position 1) shows that the solid electrolyte is amorphous. The n-ED patterns of $LiCoO_2$ electrode show the same diffraction patterns from inside to the surface (position 4 and 5), indicating that the $LiCoO_2$ is a single crystal and that large degradation does not occur. On the other hand, the n-ED patterns of the interface layer (position 2 and 3) show patterns suggesting the presence of a nanosize polycrystal. The EDX analysis shows that the interfacial layer mainly comprises Co and S. Uchimoto *et al.* reported from X-ray absorption spectroscopy that a compound whose

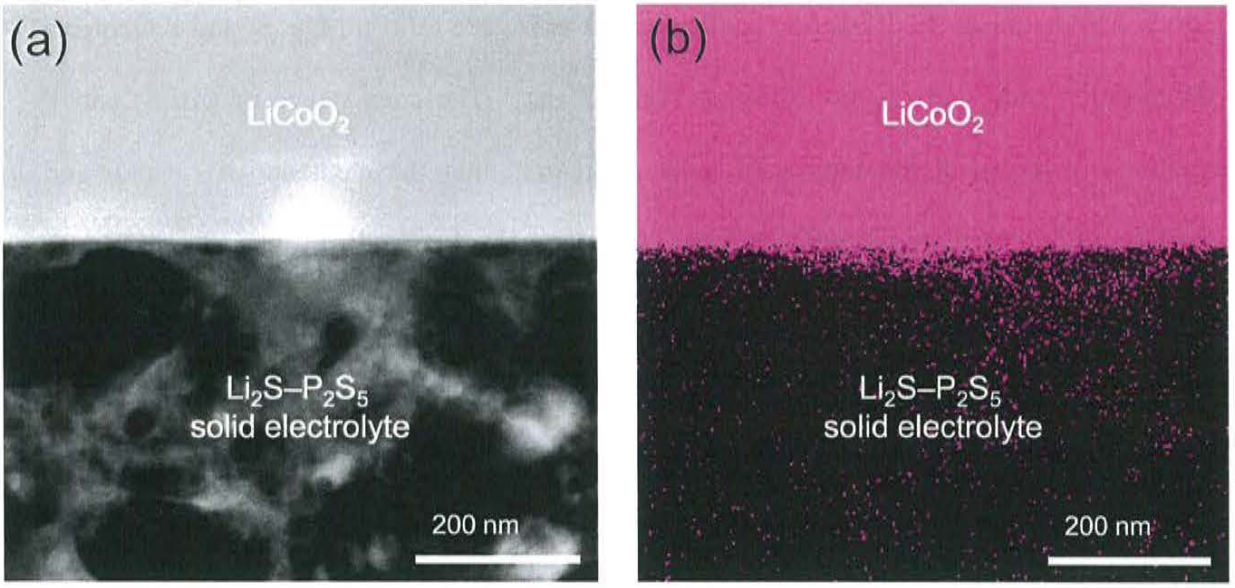

Figure 3-2 (a) Cross-sectional HAADF–STEM image and (b) the corresponding EDX mapping for the Co element near the $LiCoO_2$ electrode/Li_2S–P_2S_5 solid electrolyte interface after initial charging.

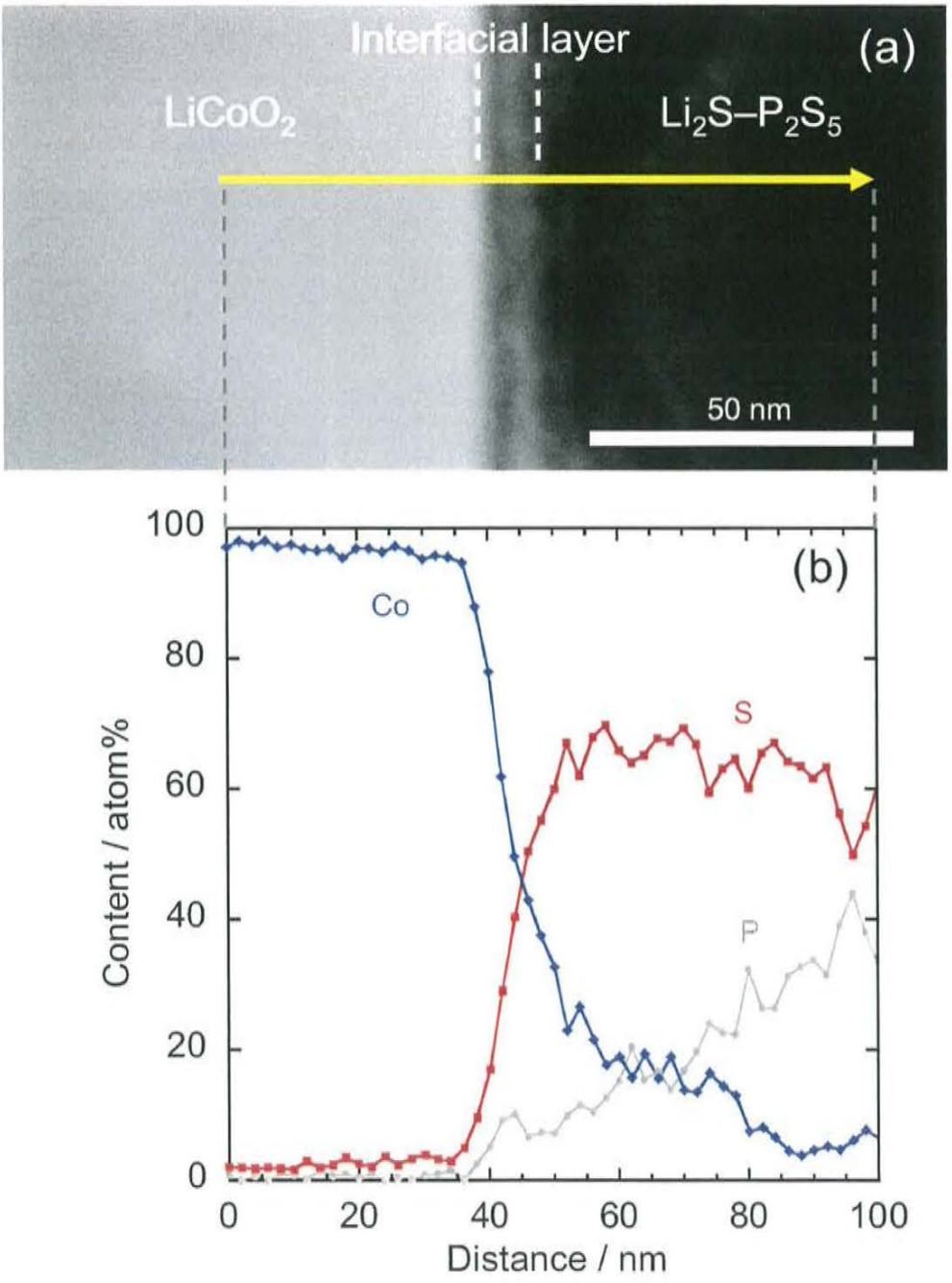

Figure 3-3 (a) Cross-sectional HAADF–STEM image of $LiCoO_2$ electrode / Li_2S–P_2S_5 solid electrolyte interface after initial charging and (b) cross-sectional EDX line profiles for Co, P, and S elements. The arrow in Fig. 3-3(a) presents the positions at which EDX measurements were taken.

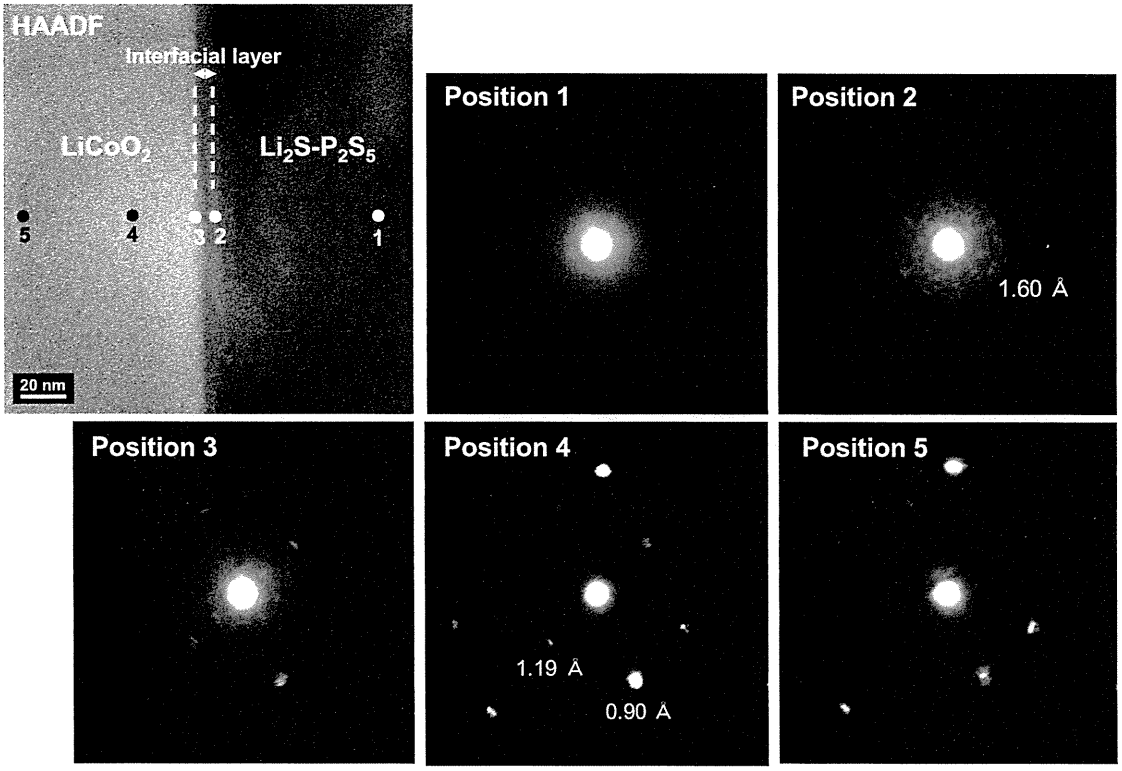

Figure 3-4 Cross-sectional HAADF–STEM image and the n–ED patterns of the Li_2S–P_2S_5 solid electrolyte, the interfacial layer, and the $LiCoO_2$ electrode after initial charging. The numbered points in the HAADF–STEM image correspond to the positions of n–ED measurements.

electronic state resembles that of CoS is produced at the interface between $LiCoO_2$ and a sulfide electrolyte during charge-discharge cycling [14]. Consequently, it is assumed that polycrystalline cobalt sulfides with nanosize exist at the interfacial layer. However, identification of the polycrystals is difficult because there are no remarkable spots in the n-ED pattern.

The interfacial TEM observation revealed that the interfacial layer was formed at the interface between $LiCoO_2$ and Li_2S–P_2S_5 solid electrolyte. Moreover, mutual diffusion of Co, P, and S was observed at the interface. The formation of the interfacial layer and the mutual diffusion indicates the degradation of the $LiCoO_2$ electrode and Li_2S–P_2S_5 solid electrolyte near the interface. Degradation of the interface is inferred as one cause of the large interfacial resistance of the electrode-electrolyte interface of the all-solid-state batteries using $LiCoO_2$ electrode and Li_2S–P_2S_5 solid electrolytes. Suppression of both the formation of the interfacial layer and the diffusion is expected to be effective in decreasing the interfacial resistance and bringing about improvement of the electrochemical performance of all-solid-state cells.

3.3.2. Interfacial observation between Li_2SiO_3-coated $LiCoO_2$ electrode and Li_2S–P_2S_5 solid electrolyte

In Section 3.3.1, it has been revealed that the interfacial layer was formed and that the elements of Co, P, and S mutually diffused at the interface between $LiCoO_2$ and the Li_2S–P_2S_5 solid electrolyte. These results suggest that the interfacial structural changes cause the high interfacial resistance for lithium-ion conduction between $LiCoO_2$ and solid electrolyte. Oxide coatings have been reported as an effective means to decrease the interfacial resistance of the all-solid-state cells using sulfide solid electrolyte, as presented in Chapter 2. In this section, the electrode-solid electrolyte interface of the cell using

Li_2SiO_3-coated $LiCoO_2$ particles as a positive electrode material was investigated. The Li_2SiO_3 coating is effective in decreasing the interfacial resistance and improving the high rate performance of the all-solid-state cells using $LiCoO_2$ electrode and Li_2S–P_2S_5 solid electrolyte. The $LiCoO_2$ / Li_2S–P_2S_5 interface of the cell using Li_2SiO_3-coated $LiCoO_2$ after charging to 3.6 V vs. Li–In. was specifically examined.

Figure 3-5 (a, b) shows the HAADF–STEM image and (c) the EDX mapping for Co element near the Li_2SiO_3-coated $LiCoO_2$ electrode / Li_2S–P_2S_5 solid electrolyte interface. The $LiCoO_2$ and Li_2S–P_2S_5 solid electrolyte retain their smooth contact (Fig. 3-5 (a)). The EDX mapping shows that the Co diffusion from $LiCoO_2$ to Li_2S–P_2S_5 is suppressed by Li_2SiO_3 coatings. Figure 3-6 (a) shows the HAADF–STEM image and Fig. 3-6 (b) shows EDX line profiles of the existence ratio for Co, P, S, and Si elements at the position indicated by the arrow in Fig. 3-6 (a). In the STEM image, the interfacial layer is visible. The EDX line profile shows that the Si element of the Li_2SiO_3 coating is visible at the interface. The EDX line profile also shows coexistence of Co, P, and S elements at the interfacial region. Figure 3-7 presents the cross-sectional HAADF–STEM image and the n–ED patterns of the interface between Li_2SiO_3-coated $LiCoO_2$ electrode and Li_2S–P_2S_5 solid electrolyte. The n–ED pattern of Li_2S–P_2S_5 solid electrolyte (position 5) shows that the solid electrolyte is amorphous. The n–ED pattern of the interfacial layer (position 4) shows that the interfacial layer is amorphous. The n–ED patterns of $LiCoO_2$ (positions 1–3) show the same patterns, indicating that the $LiCoO_2$ particle is single-crystal and that large degradation does not occur. The Co and S elements were observed at the interfacial layer, where the Li_2SiO_3 thin films were present; cobalt sulfides would form partially at the interfacial layer. However, the Co diffusion at the interface in the presence of the Li_2SiO_3 thin film decreases compared to that at the interface without Li_2SiO_3 thin film (Figs. 3-2 and 3-3). The Co diffusion is thus suppressed by the Li_2SiO_3 coating layer. The Li_2SiO_3 acts as a buffer layer preventing the

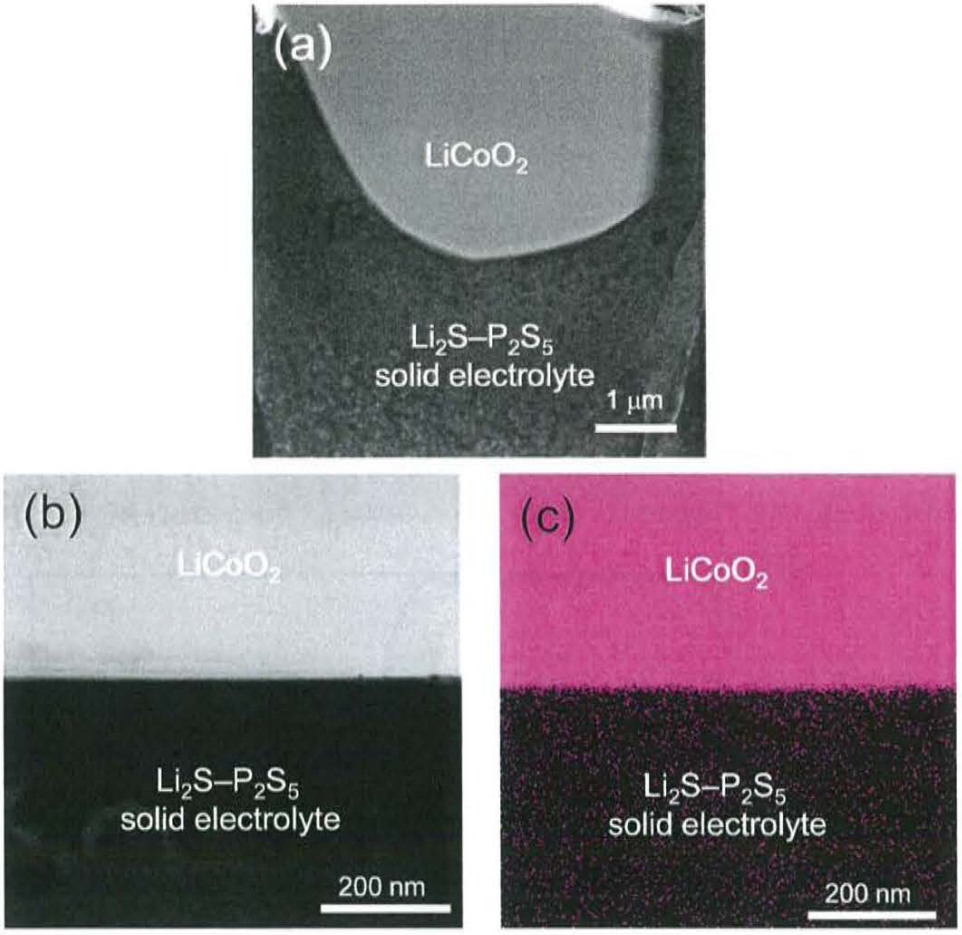

Figure 3-5 (a) Cross-sectional HAADF–STEM image near the Li_2SiO_3-coated $LiCoO_2$ electrode/Li_2S–P_2S_5 solid electrolyte interface after initial charging. (b) Magnified image of cross-sectional HAADF–STEM image. (c) EDX mapping for the Co element in the area corresponding to (b).

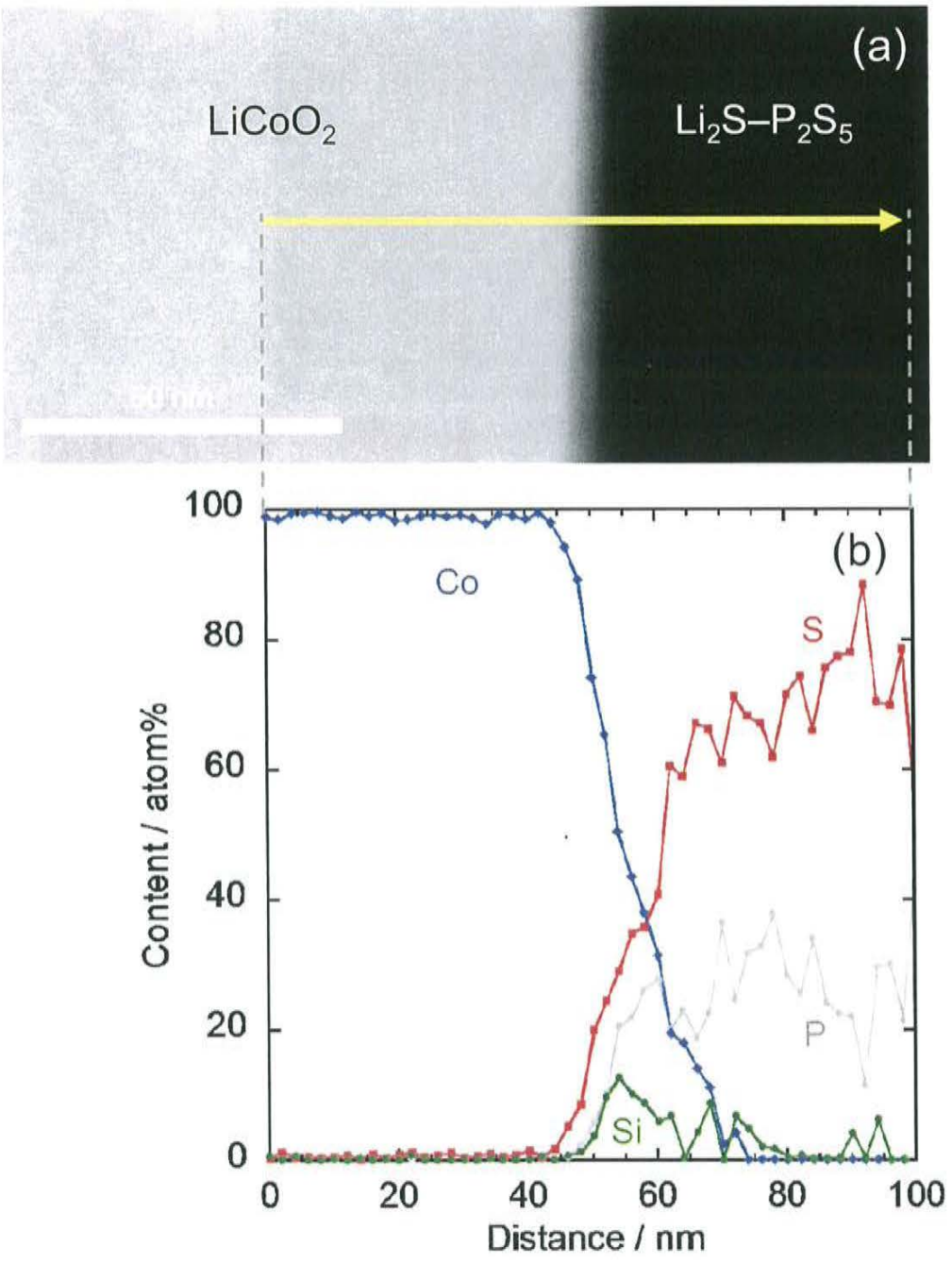

Figure 3-6 (a) Cross-sectional HAADF–STEM image of the Li_2SiO_3-coated $LiCoO_2/Li_2S–P_2S_5$ interface after initial charging and (b) cross-sectional EDX line profiles for Co, P, S, and Si elements. The arrow in (a) indicates the positions of the EDX measurements.

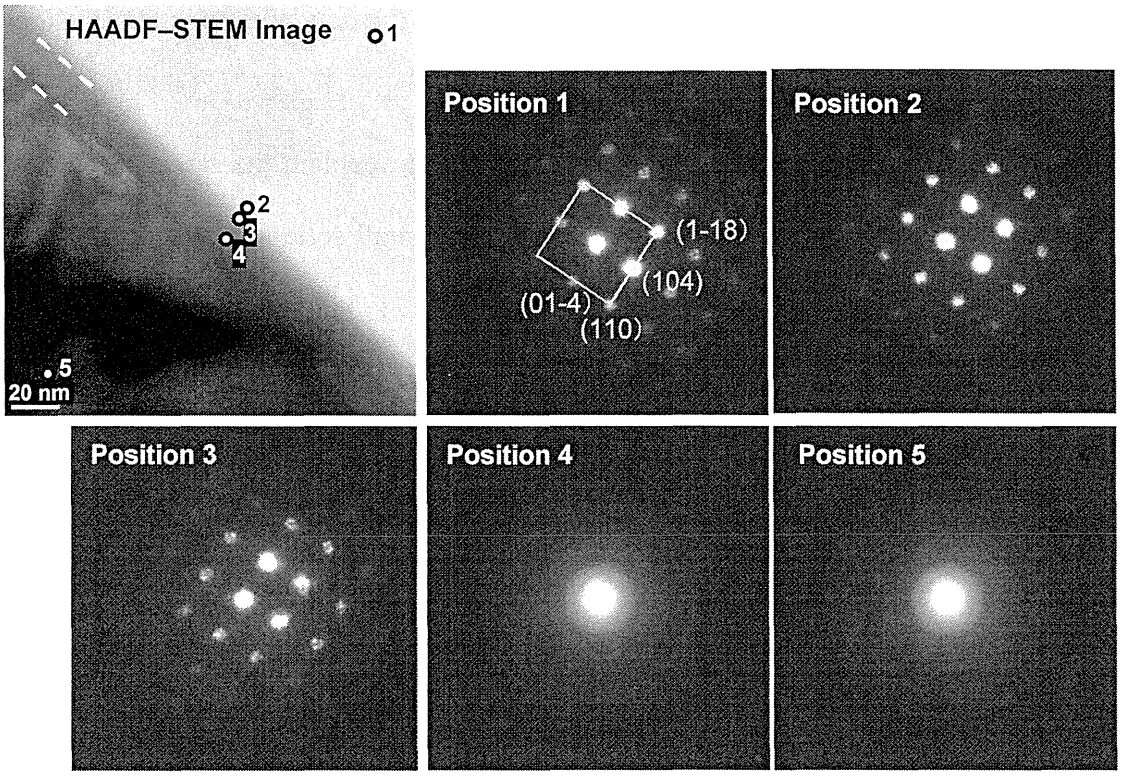

Figure 3-7 Cross-sectional HAADF–STEM image and the n–ED patterns of the interface between Li_2SiO_3-coated $LiCoO_2$ electrode and Li_2S–P_2S_5 solid electrolyte after initial charging. The numbered points in the HAADF–STEM image correspond to the positions of n–ED measurements.

elemental diffusion from the $LiCoO_2$ electrode to Li_2S–P_2S_5 solid electrolyte. Nanocrystalline materials are not observed in the n–ED patterns when using Li_2SiO_3-coated $LiCoO_2$. The interfacial layer in this case is considered as an amorphous Li_2SiO_3 coating layer. The Li_2SiO_3 coatings suppress formation of the polycrystalline interfacial products. The Li_2SiO_3 coating layer is effective in preventing the direct contact between $LiCoO_2$ and Li_2S–P_2S_5 and suppressing degradation of the interface such as the mutual elemental diffusion and the formation of interfacial products.

Ohta *et al.* proposed a "space–charge layer model" to explain the large interfacial resistance between $LiCoO_2$ and the sulfide solid electrolytes in all-solid-state batteries using $Li_{3.25}Ge_{0.25}P_{0.75}S_4$ (thio–LISICON) as a solid electrolyte [10-12]. In the model, the reason for the large interfacial resistance is considered to be formation of a lithium-deficient layer (space-charge layer) at the interface. The space-charge layer results from lithium-ion transfer from the sulfide electrolyte to $LiCoO_2$ because of the large difference of electrochemical potentials in these materials. The coatings of $Li_4Ti_5O_{12}$, $LiNbO_3$, and $LiTaO_3$ on the $LiCoO_2$ electrode yielded a low interfacial resistance in the all-solid-state batteries, and Ohta *et al.* suggested that the oxide coatings act as a buffer layer to suppress the formation of the space-charge layer [10-12]. Structural changes caused by the diffusion of Co, P, and S elements and the formation of new interfacial layers mainly composed of Co and S at the $LiCoO_2$ / Li_2S–P_2S_5 interface were identified. These phenomena are one reason for the large interfacial resistance of the all-solid-state batteries. The coatings of Li_2SiO_3 on $LiCoO_2$ were effective in suppressing the interfacial layers. The suppression of the interfacial layers would be the main reason for the reduction of interfacial resistance between $LiCoO_2$ electrode and Li_2S–P_2S_5 solid electrolyte.

So far, observations of the electrode-electrolyte interface of all-solid-state cells after 1st charging to 3.6 V vs. Li–In at the current density of 0.13 mA cm^{-2} were discussed. The

interface of the all-solid-state cell after charge-discharge process for 100 cycles at the current density of 1.3 mA cm^{-2} has been analyzed. The cycle performance of the cell was shown in Fig. 2-21.

Figure 3-8 presents the cross-sectional HAADF–STEM images and the n–ED patterns of the interface between Li_2SiO_3-coated $LiCoO_2$ electrode and Li_2S–P_2S_5 solid electrolyte after the charge-discharge processes at 1.3 mA cm^{-2}. The HAADF–STEM images show that the contact between the Li_2S–P_2S_5 solid electrolyte and the $LiCoO_2$ electrode is maintained after charge-discharge measurements. The n–ED patterns shows that the crystal structure of the $LiCoO_2$ particle near the interface shown as positions 3 and 4 is similar to that of the inside shown as positions 1 and 2. Nevertheless, lattice parameter of *c* axis at the interface is smaller than that at the particle inside. The relationship between the lattice parameter and electrochemical performance is not clear at the present stage and further studies are needed to explain this result. Figure 3-9 shows cross-sectional HAADF–STEM image and EDX mappings for O, Si, P, S, and Co elements at the Li_2SiO_3-coated $LiCoO_2$ electrode/Li_2S–P_2S_5 solid electrolyte interface after charge-discharge cycles for 100 times at the current density of 1.3 mA cm^{-2}. At the interface between $LiCoO_2$ particles and Li_2S–P_2S_5 solid electrolyte, Si element of the Li_2SiO_3 coating is observed. The Co diffusion from $LiCoO_2$ to Li_2S–P_2S_5 is not visible. Figure 3-10 (a) shows the HAADF–STEM image and Fig. 3-10 (b) shows EDX line profiles of the existence ratio for P, S, Co, Si and O elements at the position indicated by the arrow in Fig. 3-10 (a). The Si element of the Li_2SiO_3 coating is visible at the interface. The EDX line profile shows coexistence of Co, P, and S elements at the interfacial region. A large Co diffusion is not observed; the diffusion is suppressed by the Li_2SiO_3 coating, although the existence of about 1 atom% Co is observed at a distance of 50 nm from the interface. After 100th charge-discharge measurement at the current density of 1.3 mA cm^{-2}, the formation of the high resistive interfacial layer between $LiCoO_2$ and Li_2S–P_2S_5 would be

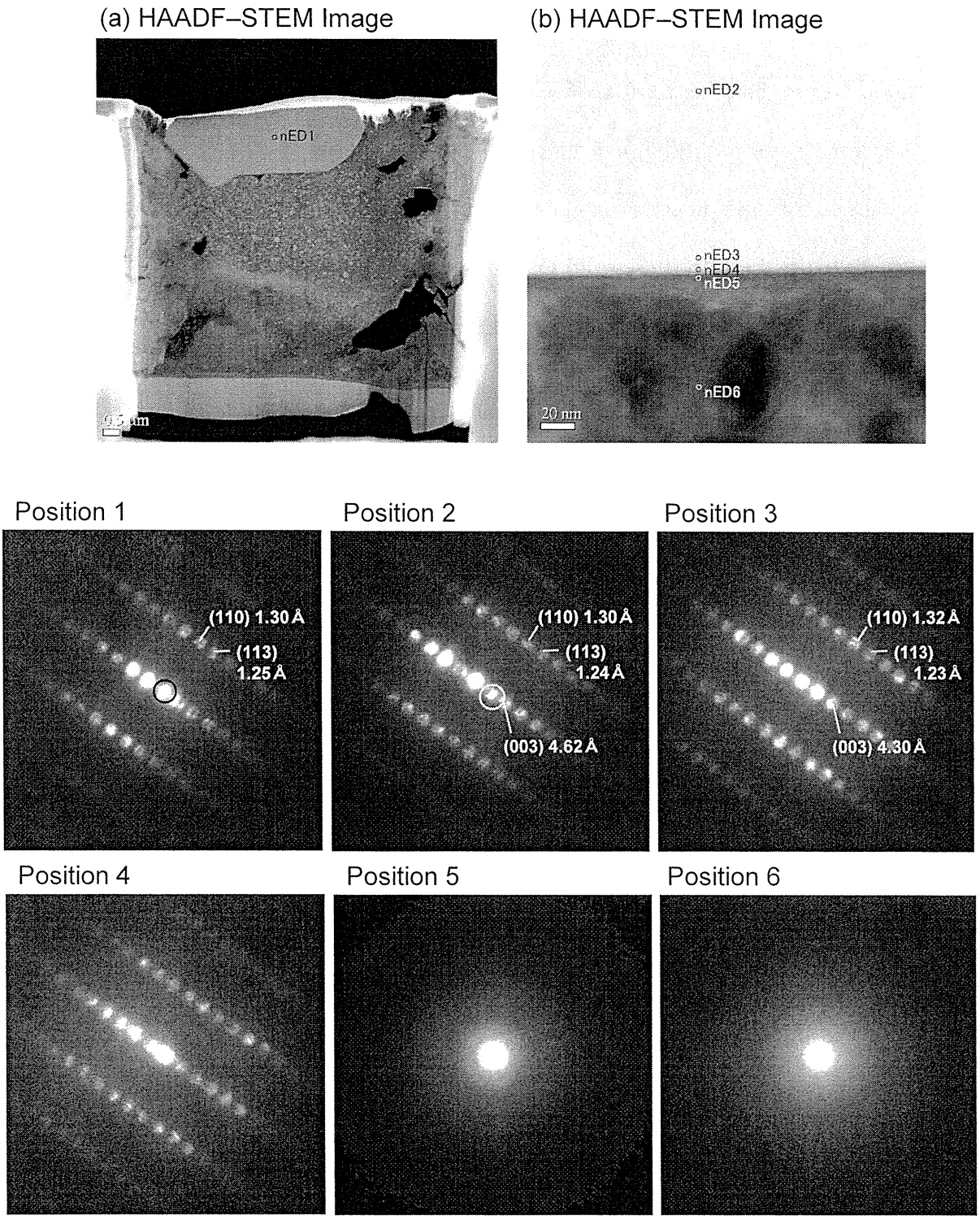

Figure 3-8 Cross-sectional HAADF–STEM image and the n–ED patterns of the interface between Li_2SiO_3-coated $LiCoO_2$ electrode and Li_2S–P_2S_5 solid electrolyte after 100 the charge-discharge process at the current density of 1.3 mA cm^{-2}. The numbered points in the HAADF–STEM image correspond to the positions of n–ED measurements.

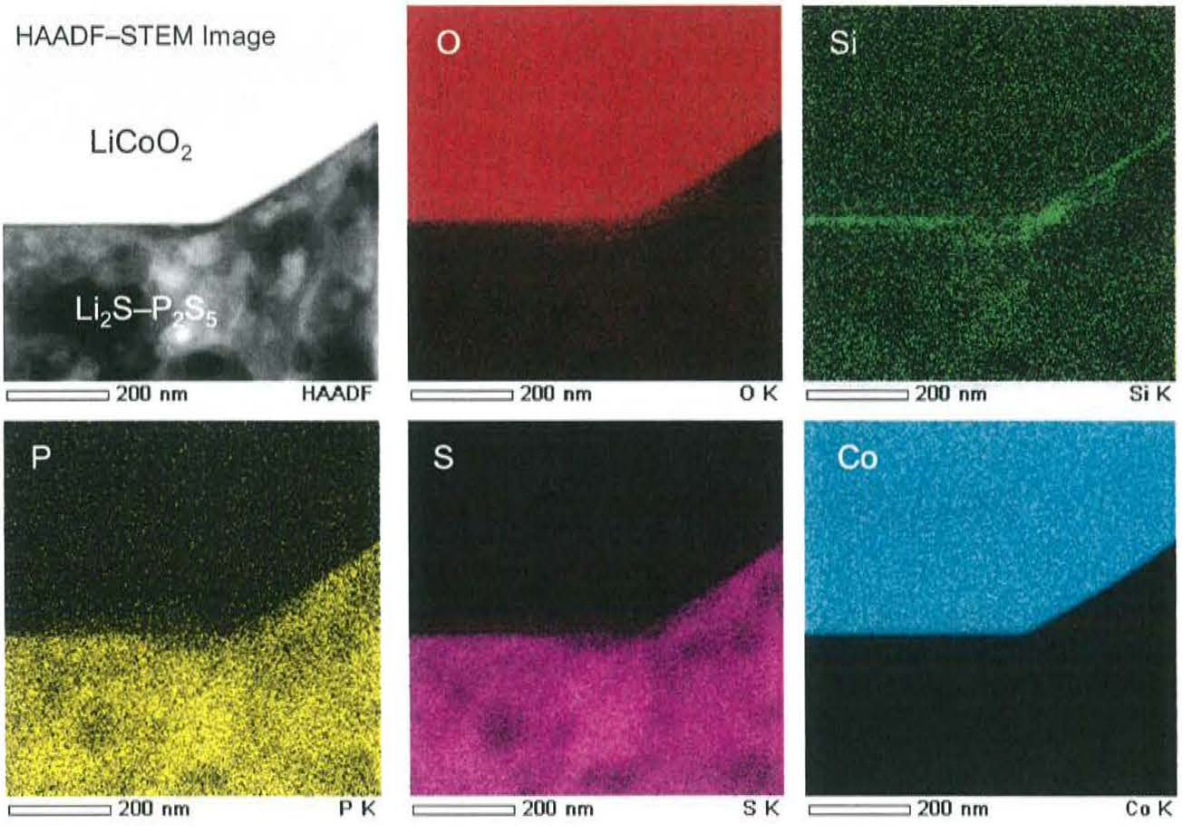

Figure 3-9 Cross-sectional HAADF–STEM image and EDX mappings for O, Si, P, S, and Co elements near the Li_2SiO_3-coated $LiCoO_2$ electrode/Li_2S–P_2S_5 solid electrolyte interface after 100 cycles at the current density of 1.3 mA cm^{-2}.

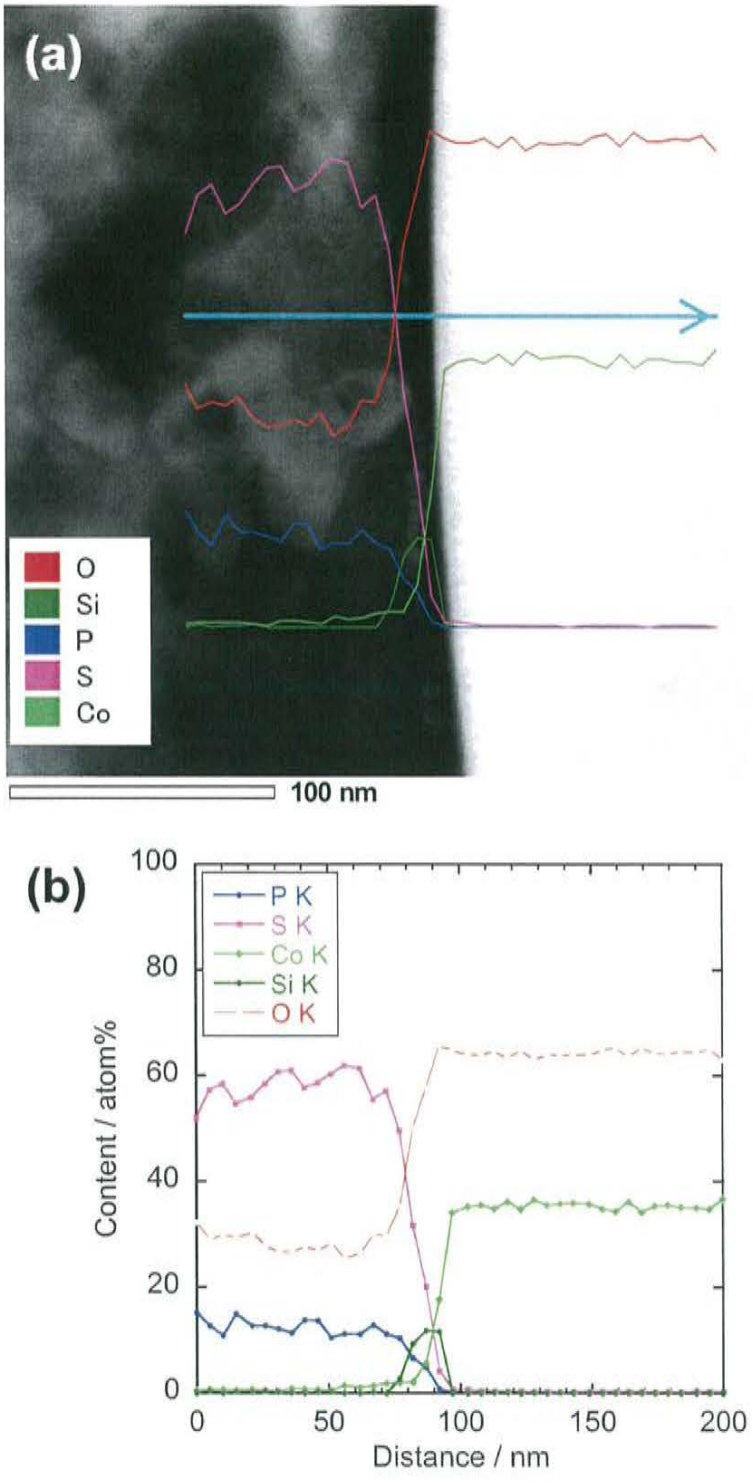

Figure 3-10 (a) Cross-sectional HAADF–STEM image of the Li_2SiO_3-coated $LiCoO_2/Li_2S–P_2S_5$ interface after 100th discharging and (b) cross-sectional EDX line profiles for P, S, Co, Si and O elements. The arrow in (a) indicates the positions of the EDX measurements.

suppressed by the Li_2SiO_3 coating. These results support the good cycle performance of the all-solid-state cell using Li_2SiO_3-coated $LiCoO_2$ shown in Fig. 2-21. The cycle performance the all-solid-state cells operated at a high current density is improved by oxide coatings because of the suppression of the interfacial reaction between $LiCoO_2$ and Li_2S–P_2S_5 solid electrolytes during charge-discharge process. The effects of the oxide coatings are significant in the interface with a high reactivity such as that of the all-solid-state cells charged to a high potential. The interfacial resistances of the cells using uncoated and Li_2SiO_3-coated $LiCoO_2$ after charging to 4.0 V vs. Li–In were respectively 1700 and 750 Ω as shown in Fig. 2-18. The increase in impedance was effectively suppressed by the Li_2SiO_3 coating. Results showed that suppression of the formation of the high resistive interfacial layer was effective in improving the electrochemical performance of the all-solid-state batteries.

3.4. Summary

In this chapter, the interface between the $LiCoO_2$ electrode and the $80Li_2S{\cdot}20P_2S_5$ glass-ceramic solid electrolyte of all-solid-state cells was studied using TEM. In addition, the electrode-electrolyte interface of the cell using the coated $LiCoO_2$ was compared with that using uncoated $LiCoO_2$ to clarify the coating effects from the perspective of structural changes.

The interfacial TEM observation revealed that the interfacial layer formed after charging the all-solid-state cells was observed between the electrode and the solid electrolytes. Moreover, Co, P, and S elements mutually diffused between $LiCoO_2$ and the Li_2S–P_2S_5 solid electrolyte. These results reflect that side reactions occurred at the electrode-electrolyte interface, which indicates the degradation of the $LiCoO_2$ electrode and Li_2S–P_2S_5 solid electrolyte near the interface. Degradation of the interface is inferred as one cause of the

large interfacial resistance of the electrode-electrolyte interface of the all-solid-state batteries. Those phenomena at the interface were suppressed using Li_2SiO_3 coatings. The Li_2SiO_3 coatings act as a buffer layer to suppress the side reaction at the interface such as the mutual diffusion of Co, P, and S. The suppression of the interfacial layers is the main reason for the reduction of interfacial resistance between $LiCoO_2$ electrode and Li_2S–P_2S_5 solid electrolyte.

3.5. References

[1] J. Cho, Y.-J. Kim, B. Park, *Chem. Mater.,* **12** (2000) 3788.

[2] J. Cho, Y.-J. Kim, J.-T. Kim, B. Park, *Angew. Chem. Int. Ed.,* **40** (2001) 3367.

[3] J. Cho, B. Kim, J-G. Lee, Y.-W. Kim, B. Park, *J. Electrochem. Soc.* **152** (2005) A32.

[4] Z. Chen, J.R. Dahn, *Electrochem. Solid-State Lett.,* **6** (2003) A221.

[5] Z. Chen, J.R. Dahn, *Electrochim. Acta* **49** (2004) 1079.

[6] Y.-K. Sun, S.-W. Cho, S.-T. Myung, K. Amine, J. Prakash, *Electrochim. Acta* **53** (2007) 1013.

[7] T. Minami, *Solid State Ionics for Batteries*; Springer–Verlag, Tokyo, 2005.

[8] F. Mizuno, A. Hayashi, K. Tadanaga, M. Tatsumisago, *J. Electrochem. Soc.* **152** (2005) A1499.

[9] A. Hayashi, Y. Nishio, H. Kitaura, M. Tatsumisago, *Electrochem. Commun.* **10** (2008) 1860.

[10] N. Ohta, K. Takada, L. Zhang, R. Ma, M. Osada, T. Sasaki, *Adv. Mater.* **18** (2006) 2226.

[11] N. Ohta, K. Takada, I. Sakaguchi, L. Zhang, R. Ma, K. Fukuda, M. Osada, T. Sasaki, *Electrochem. Commun.* **9** (2007) 1486.

[12] K. Takada, N. Ohta, L. Zhang, K. Fukuda, I. Sakaguchi, R. Ma, M. Osada, T. Sasaki, *Solid State Ionics* **179** (2008) 1333.

[13] A. Brazier, L. Dupont, L. Dantras–Laffont, N. Kuwata, J. Kawamura, J.-M. Tarascon, *Chem. Mater.,* **20** (2008) 2352.

[14] Y. Uchimoto, M. Wakihara, in *Solid State Ionics for Batteries*, Minami, T. Editor, *Solid State Ionics for Batteries*; p. 126, Springer–Verlag, Tokyo, 2005.

4. Enhancement of Performance of All-Solid-State Cells Using Highly Conducting Solid Electrolyte Films

4.1. Introduction

All-solid-state lithium secondary batteries with nonflammable solid electrolytes have attracted attention because of their excellent potential for improving the safety of lithium-ion secondary batteries. One disadvantage of all-solid-state batteries is the difficulty of formation of an effective electrode-electrolyte interface. Designing a favorable composite electrode is important for the development of all-solid-state batteries. In all-solid-state battery systems using sulfide-based solid electrolytes, a high interfacial resistance between positive electrode and solid electrolyte was observed after the initial charging process when $LiCoO_2$ was used as the electrode active material [1-3 and Chapter 2]. As described in Chapter 3, the high resistance was caused by degradation of the interface between $LiCoO_2$ and Li_2S–P_2S_5 solid electrolytes. Forming a favorable electrode/electrolyte interface by interfacial modification effectively decreased the interfacial resistance. Coatings of oxides such as $Li_4Ti_5O_{12}$, $LiNbO_3$, $LiTaO_3$, Li_2O–SiO_2, Li_2O–TiO_2, and Li_4SiO_4-Li_3PO_4 on $LiCoO_2$ particles have been reported as an effective modification technique [1-3 and Chapter 2].

The formation of effective electron and lithium-ion conducting paths to the electrode active materials in composite electrode is also important in addition to the electrode/electrolyte interfacial modification. In this chapter, new all-solid-state batteries using highly conducting solid electrolyte films as shown in Fig. 1-2 in Chapter 1 have been prepared. In typical all-solid-state cells (Fig. 1-2 (a)), a composite electrode composed of $LiCoO_2$ electrode particles and Li_2S–P_2S_5 solid electrolyte particles is used as a working electrode to provide a lithium-ion conducting path to the $LiCoO_2$. The amount of solid electrolyte particles needed in the composite electrode is currently approximately 20-30 wt%

[4]. A decrease in solid electrolyte content can effectively increase the energy density of a composite electrode. In the all-solid-state cells using Solid-Electrolyte (SE)-coated $LiCoO_2$ shown in Fig. 1-2 (b), a favorable contact between $LiCoO_2$ electrode and Li_2S–P_2S_5 solid electrolytes can be formed. In addition, the contents of solid electrolyte in the working electrode would be reduced effectively. This will lead to a dramatic improvement of energy density of all-solid-state batteries. In the all-solid-state cell based on thin solid electrolyte layer shown in Fig. 1-2 (c), the positive composite electrode and the negative electrode are separated using thin solid electrolyte layer. High energy density and high rate capability are expected by using solid electrolyte thin film because of decreasing thickness and resistance of solid electrolyte.

The solid electrolyte thin films for SE-coated $LiCoO_2$ particles require high lithium-ion conductivity to form lithium-ion conducting paths in the composite electrode. The highly conducting thin films are also preferred to be used for the thin solid electrolyte layer for the improvement of rate performance. Sulfide-based solid electrolytes, especially Li_2S–P_2S_5 systems, exhibit high ionic conductivity of more than 10^{-3} S cm^{-1} at 25°C and high electrochemical stability [5-9].

Pulsed laser deposition (PLD) is a useful tool to prepare thin films with good quality. It has been used for preparation of thin films designed for use in lithium secondary batteries [10-14]. Only a couple of articles have described sulfide-base solid electrolyte thin films prepared using PLD: amorphous $Li_{3.25}Ge_{0.25}P_{0.75}S_4$ (thio-LISICON) [15] and Li_2S–P_2S_5 [16] thin films. Sulfide thin films prepared using PLD exhibited high lithium-ion conductivity of more than 10^{-4} S cm^{-1}. Although it is important to clarify the effects of preparation conditions on the structure, composition, and ionic conductivity of the sulfide films, such effects have not been reported in detail.

In this chapter, the preparation of highly conducting sulfide-based solid electrolyte

films and their application to new bulk-type all-solid-state batteries are described.

Firstly, the Li_2S–P_2S_5 glassy solid electrolyte thin films were prepared by PLD. Thin films with composition of $xLi_2S \cdot (100\text{-}x)P_2S_5$ (mol%; x = 50-80) were investigated. The chemical composition, local structure, and ionic conductivity of the films prepared under various ambient gas pressures were studied to clarify the effect of ambient gas pressure on sulfide film properties.

Secondly, Solid-Electrolyte (SE)-coated $LiCoO_2$ particles were prepared by coating Li_2S–P_2S_5 solid electrolyte films onto $LiCoO_2$ particles using PLD; the battery performance of all-solid-state cells using the SE-coated $LiCoO_2$ particles were evaluated. Cross-sections of the composite electrodes in the all-solid-state cells were observed using a transmission electron microscope (TEM) to investigate the packing morphology of the SE-coated $LiCoO_2$ particles and the elemental distribution at the interfaces between the particles.

Finally, the sulfide-based solid electrolyte thin films were applied to the electrolyte layer which separates the positive composite electrode and the negative electrode.

The possibility of those new types of all-solid-state batteries will be discussed.

4.2. Experimental

4.2.1. Preparation of sulfide based solid electrolyte thin films

Thin films of the solid electrolyte were fabricated using PLD with a KrF excimer laser (λ = 248 nm, LPXPro, Lambda Physik). The deposition condition was summarized in Table 4-1. The pulse energy was 200 mJ/pulse and the repeating frequency was 10 Hz. The energy density of the focused laser beam was estimated as about 2 J/cm^2 at the target. Argon gas (99.99%) was used as an ambient gas; various pressures of the ambient argon gas (10^{-2} – 10 Pa) were used. The distance from the target to the substrate was 7 cm. The pelletized mixture of Li_2S (99.9%) and P_2S_5 (99%) crystalline powder was used as a target

Table 4-1 Deposition condition

Laser	KrF eximer laser (248 nm)
Frequency	10 Hz
Laser fluence	2 J cm^{-2}
Target	$Li_2S : P_2S_5$ = 80 : 20 (molar ratio)
	= 75 : 25
	= 70 : 30
	= 50 : 50
Substrate temperature	Room temperature
Target-substrate distance	7 cm
Ambient gas	Ar gas
Gas pressure	10^{-2} – 10 Pa
Substrate	Si, SiO_2 glass

without sintering for the preparation of Li_2S–P_2S_5 films. Similarly, the pelletized mixture of (99.9%) and GeS_2 (99%) crystalline powder was used as a target without sintering for the preparation of Li_2S–GeS_2 films. Solid electrolyte thin films were deposited on a silicon substrate and a quartz glass substrate with comb-like gold electrodes. The deposition was conducted at room temperature. To avoid air exposure of the deposited thin films, an Ar-filled glove box was connected to a vacuum chamber.

The thin film morphology was observed using a scanning electron microscope (SEM, VE-8800; Keyence Co., or Tiny SEM Mighty-8; Technex Lab. Co.). The film thickness was measured using SEM and a thin film measurement system (F20; Filmetrics Inc.). X-ray diffraction (XRD) measurements (CuKα) were performed using a diffractometer (M18XHF^{22}-SRA; Mac Science Ltd.). Local structures of the samples were analyzed using Raman spectroscopy with a spectrometer (RMP-210; Jasco Inc.) equipped with a green laser (532 nm). Lithium-ion conductivities were measured for the thin films deposited on a quartz glass substrate with comb-like gold electrodes. Electrochemical impedance spectroscopy measurements of the thin films were performed using an impedance analyzer combined with a dielectric interface (SI 1260 and SI 1296; Solartron Analytical). Measurements were conducted under an Ar atmosphere. The chemical composition of the thin films and targets were determined as an elemental analysis of Li and P using inductively coupled plasma atomic emission spectroscopy (ICP–AES, SPS7800; Seiko Instruments Inc.).

4.2.2. Preparation of Li_2S–P_2S_5 solid electrolyte-coated electrode particles

The Li_2S–P_2S_5 solid electrolyte was coated on $LiCoO_2$ particles (D10; Toda Kogyo Co.) using a PLD technique. The solid electrolyte thin films of the $80Li_2S{\cdot}20P_2S_5$ (mol%) solid electrolyte were fabricated using PLD with a KrF excimer laser as shown above. The $LiCoO_2$ particles used in this study were coated with $LiNbO_3$ film in advance because

$LiNbO_3$-coated $LiCoO_2$ shows a good rate performance in the all-solid-state batteries using sulfide-based solid electrolyte [2]. In the PLD vacuum chamber used in this study, target holders were attached at the upper side and a sample holder with a vibrator was equipped at the bottom side. This PLD system allows us to form the solid electrolyte films on electrode particles. During deposition of the solid electrolyte, $LiCoO_2$ particles were fluidized by a vibration system (VIB–FB, Nara Machinery Co.) in order to form the solid electrolyte layer uniformly on $LiCoO_2$ particles (Fig. 4-1). The frequency of square pulse for fluidizing the particles was 50 Hz. Deposition time was varied from 0 min to 240 min to obtain the Li_2S–P_2S_5 coatings with different thickness. Heat treatment of SE-coated $LiCoO_2$ was carried out in the Ar atmosphere. Morphology of $LiCoO_2$ particles was observed using a SEM equipped with an energy dispersive X-ray spectroscopy (EDX) system.

4.2.3. Preparation of all-solid-state cells

All-solid-state cells (In / $80Li_2S{\cdot}20P_2S_5$ glass-ceramic solid electrolyte / $LiCoO_2$) were constructed to investigate electrochemical performance of $LiCoO_2$ coated with $80Li_2S{\cdot}20P_2S_5$ solid electrolyte. Indium foil (99.999%; Furuuchi Chemical Corp.) was used as a counter electrode. The Li_2S–P_2S_5 solid electrolyte particles were usually added to the working electrode layer in previous reports; the working electrode consisting of 70 wt% $LiCoO_2$ particles and 30 wt% Li_2S–P_2S_5 glass-ceramic solid electrolyte particles. In contrast, the solid electrolyte particles were not added to the working electrode layer in this study to investigate the effect of the solid electrolyte coating on $LiCoO_2$ particles; the working electrode consisting of only SE-coated $LiCoO_2$ particles. In addition, the working electrode consisting of 90 wt% SE-coated $LiCoO_2$ particles and 10 wt% Li_2S–P_2S_5 solid electrolyte particles was also prepared, where the contents of solid electrolyte particles were reduced. A bilayer pellet consisting of the working electrode (10 mg) and glass-ceramic solid electrolytes

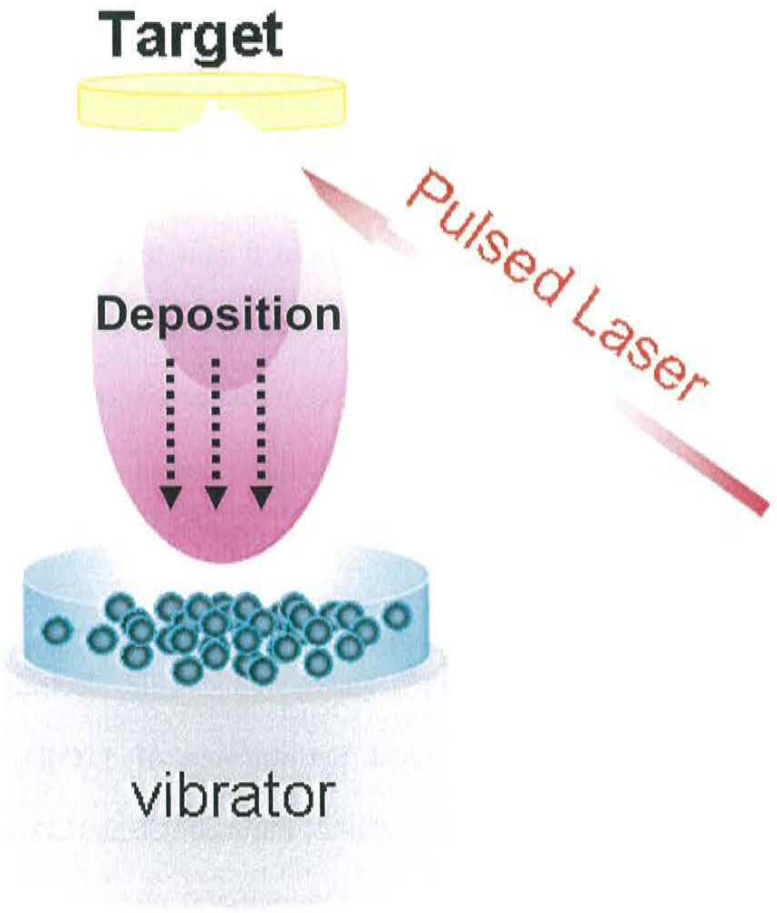

Figure 4-1 Schematic diagram of a coating apparatus in a vacuum chamber.

(80 mg) was obtained by pressing under 360 MPa (ϕ = 10 mm); then indium foil was attached to the bilayer pellet by pressing under 240 MPa. The pellet was pressed using two stainless steel rods; the stainless steel rods were used as current collectors for both working and counter electrodes.

The all-solid-state cells were charged and discharged using a charge–discharge measuring device (BTS–2004; Nagano Co., Ltd.) at room temperature. Electrochemical impedance spectroscopy measurements of the all-solid-state cells were performed using an impedance analyzer (SI 1260; Solartron) after charging them to 3.6 V vs. Li–In under 0.13 mA cm^{-2} at room temperature. The applied voltage was 50 mV and the frequency range was from 1 Hz to 1 MHz. The interface among $LiCoO_2$ particles coated with the $80Li_2S{\cdot}20P_2S_5$ film in the working electrode was observed using TEM (JEM2100F; JEOL) to investigate how the coated Li_2S–P_2S_5 solid electrolyte films exist among $LiCoO_2$ particles. Samples for TEM observations were obtained using FIB milling. The samples were transferred in Ar atmosphere from the glove box to the equipments for FIB and TEM.

4.3. Results and discussion

4.3.1. Preparation of sulfide solid electrolyte films by pulsed laser deposition

4.3.1.1. Li_2S–P_2S_5 solid electrolyte films

To determine preparation conditions of sulfide thin films, the composition of $80Li_2S{\cdot}20P_2S_5$ (mol%) was firstly selected because the composition has the highest lithium-ion conductivity in the Li_2S–P_2S_5 glass system [9]. The XRD pattern of the $80Li_2S{\cdot}20P_2S_5$ thin film prepared under 10^{-2} Pa is presented in Fig. 4-2. The $80Li_2S{\cdot}20P_2S_5$ thin film as-deposited shows no peaks in the XRD pattern, suggesting that the thin film prepared at room temperature is amorphous. Figure 4-3 shows an SEM image of cross-section of the $80Li_2S{\cdot}20P_2S_5$ thin film deposited under 10^{-2} Pa on a Si substrate. The

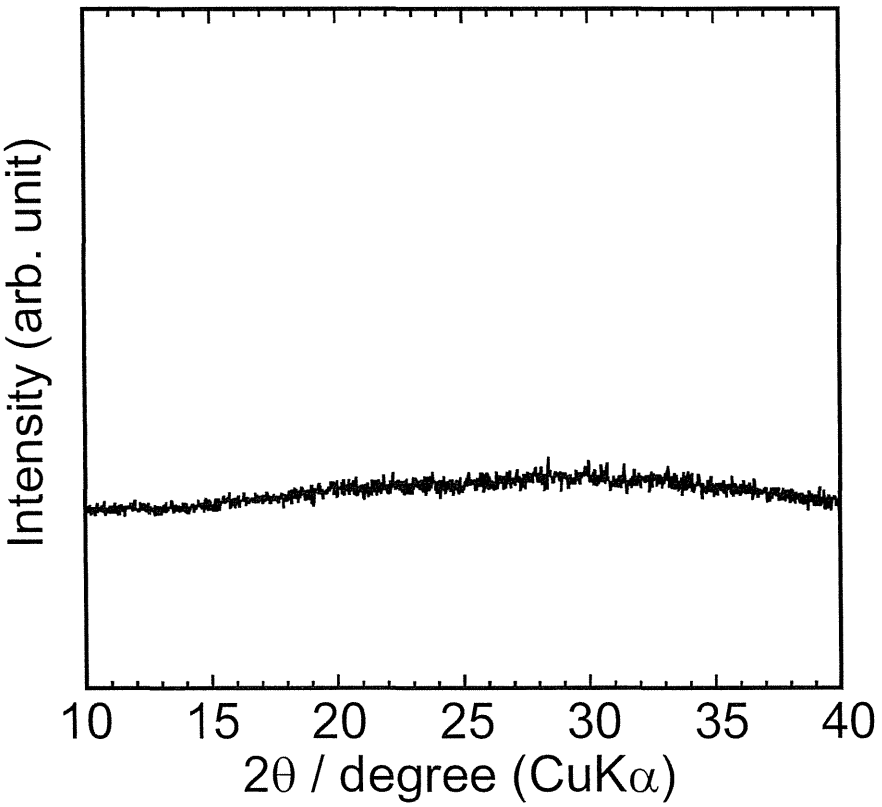

Figure 4-2 XRD pattern of the $80Li_2S \cdot 20P_2S_5$ thin film prepared under ambient Ar gas pressure of 10^{-2} Pa.

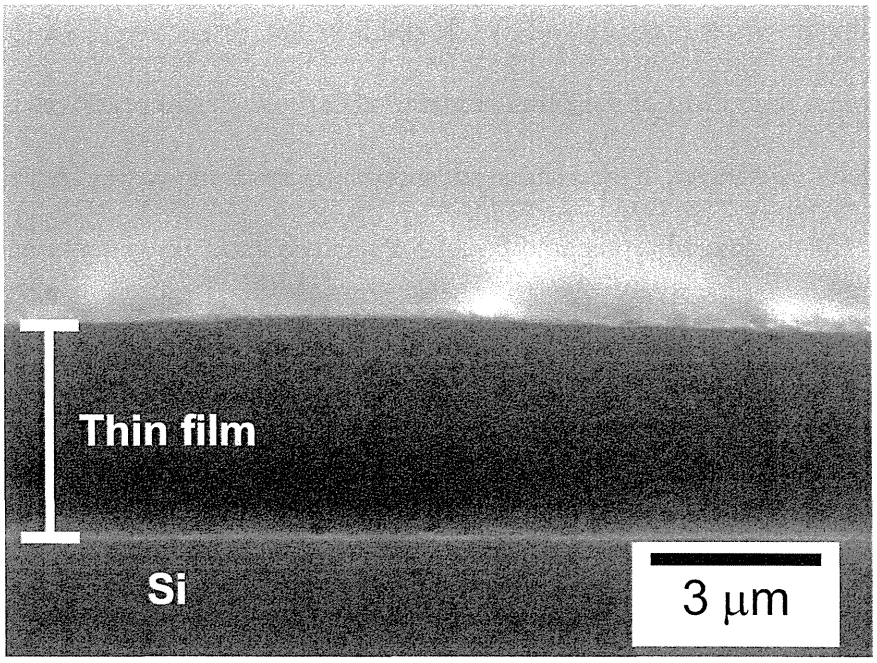

Figure 4-3 SEM image of the cross section of the $80Li_2S{\cdot}20P_2S_5$ thin film prepared under ambient Ar gas pressure of 10^{-2} Pa.

prepared thin film is dense and has a generally smooth surface without large droplets. The film thickness is ca. 3 μm; the thicknesses of all thin films prepared in this study were several micrometers.

The atomic ratios of Li and P in the targets and the prepared thin films were determined by ICP–AES. Table 4-2 presents chemical compositions of the $80Li_2S{\cdot}20P_2S_5$ (mol%) target and the thin film prepared under various Ar gas pressures. The atomic ratio of Li:P of the target determined by ICP is 80:20, which corresponds to the nominal composition. The films prepared under Ar gas pressures of 10^{-2}, 1, and 5 Pa are, respectively, 85:15, 82:18, and 80:20. The atomic ratio of Li of the films prepared under low Ar gas pressures is larger than that of the target. Moreover, it decreases concomitantly with increasing Ar gas pressure. The atomic ratio of the thin film prepared under 5 Pa shows good agreement with that of the target. Figure 4-4 shows the Raman spectra of the $80Li_2S{\cdot}20P_2S_5$ thin films prepared by PLD under various Ar gas pressures (10^{-2}-10 Pa). Peaks at around 385, 420, and 475 cm^{-1} are observed for the films obtained. Tachez *et al.* [17] have reported that the Raman peaks at 382 and 418 cm^{-1} were, respectively, attributed to $P_2S_6^{4-}$ ions in the $Li_4P_2S_6$ crystal and PS_4^{3-} ions in the Li_3PS_4 crystal. The Raman peak at around 475 cm^{-1} is attributable to S–S bonds in elemental sulfur and/or lithium polysulfides: Li_2S_x. [18] The films obtained comprise $P_2S_6^{4-}$, PS_4^{3-}, and S–S bonds. The relative intensities of Raman peaks at 385 and 475 cm^{-1} against that at 420 cm^{-1} decrease with increased Ar gas pressure during deposition; the thin films deposited under 5 and 10 Pa are composed mainly of PS_4^{3-} ions. Lithium polysulfides Li_2S_x, which give the peak at 475 cm^{-1}, would be present in the thin films prepared under high vacuum because the lithium content of the films determined by ICP analysis (Table 4-2) was relatively higher than the targeted composition. Figure 4-5 shows Raman spectra of (a) the $80Li_2S{\cdot}20P_2S_5$ target, which is the pelletized mixture of Li_2S and P_2S_5 crystal powders, (b) the $80Li_2S{\cdot}20P_2S_5$ glass powder prepared using a mechanical milling technique, which exhibits

Table 4-2 Chemical compositions of the target and the thin film prepared by PLD under the Ar gas pressure of 10^{-2}, 1, and 5 Pa determined by ICP–AES

	Ar gas pressure / Pa	Li : P (Atomic ratio)
$80Li_2S \cdot 20P_2S_5$ target	—	80 : 20
Thin film	10^{-2}	85 : 15
	1	82 : 18
	5	80 : 20

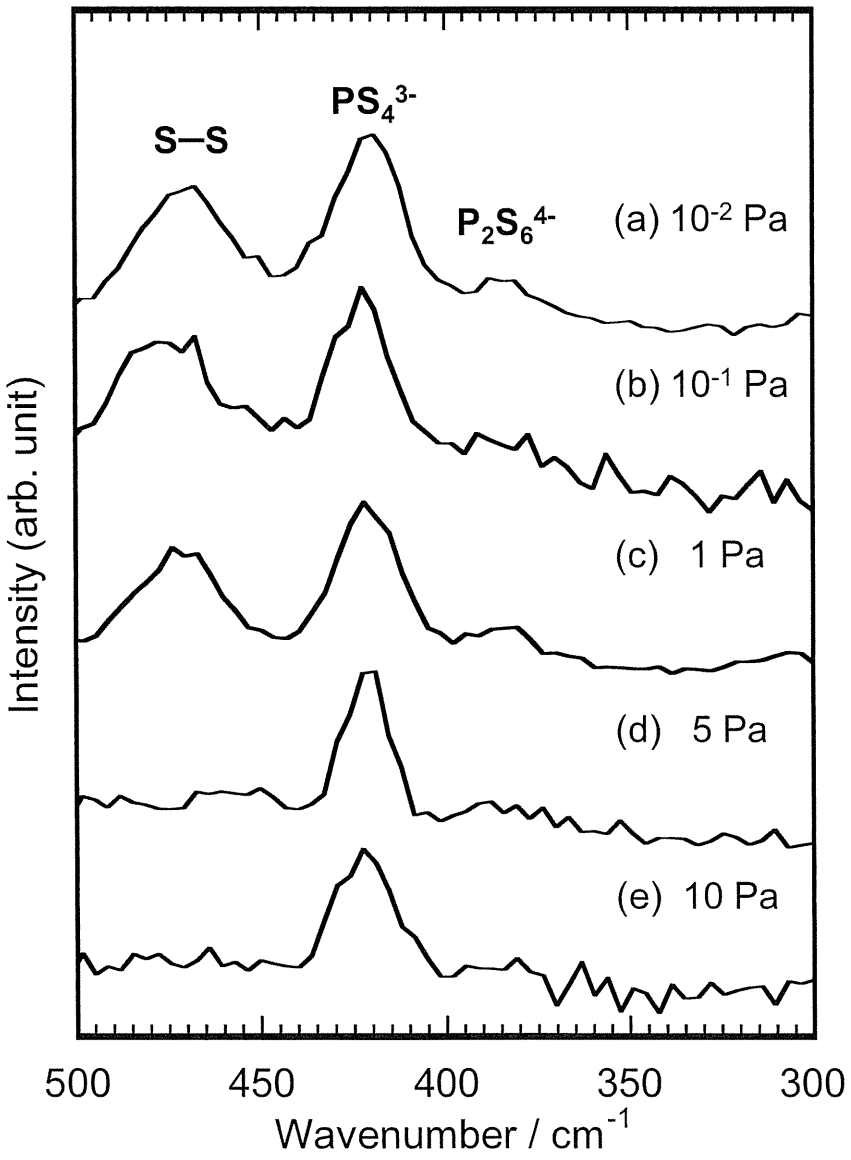

Figure 4-4 Raman spectra of the $80Li_2S{\cdot}20P_2S_5$ thin films prepared under Ar gas pressure of (a) 10^{-2} Pa, (b) 10^{-1} Pa, (c) 1 Pa, (d) 5 Pa, and (e) 10 Pa.

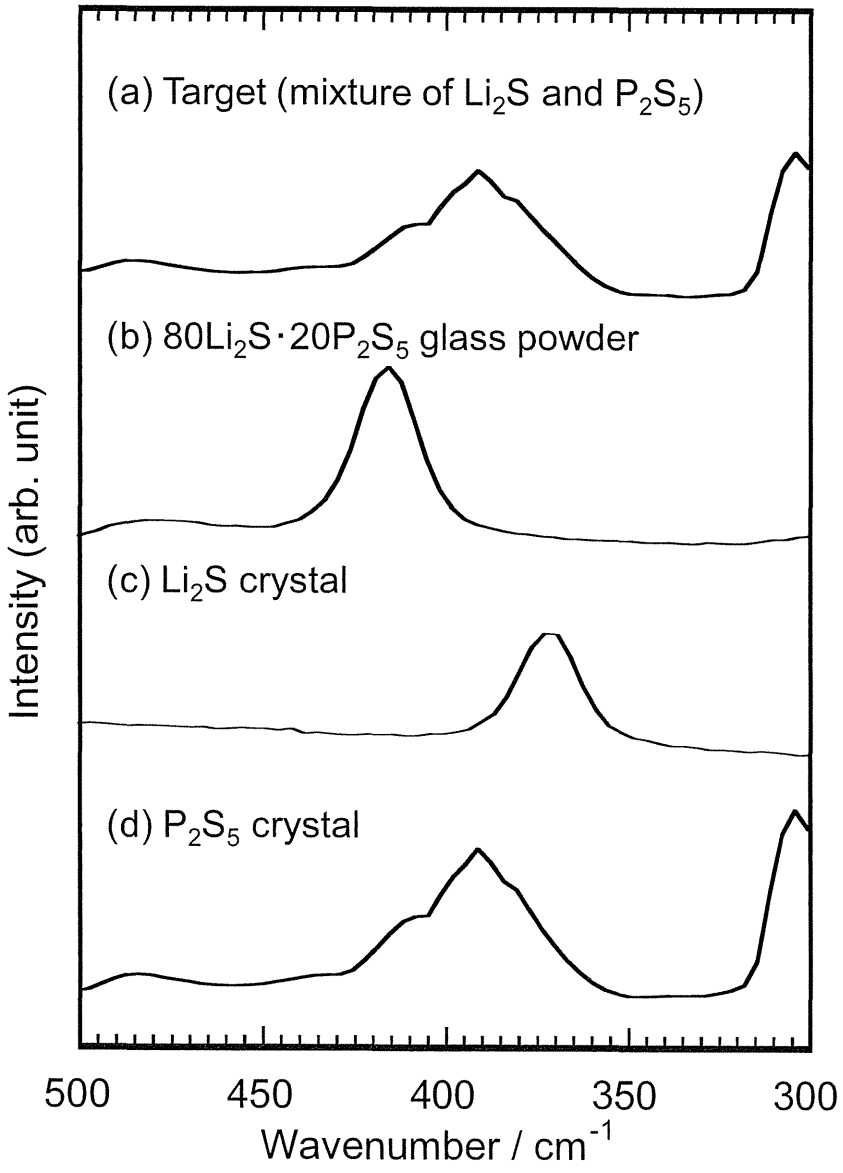

Figure 4-5 Raman spectra of (a) the $80Li_2S \cdot 20P_2S_5$ target (mixture of Li_2S and P_2S_5 crystals), (b) the $80Li_2S \cdot 20P_2S_5$ glass powder prepared using a mechanical milling technique, (c) Li_2S crystal powder, and (d) P_2S_5 crystal powder.

high lithium-ion conductivity, (c) Li_2S crystal powder, and (d) P_2S_5 crystal powder. The peaks observed in the target comprise peaks of Li_2S and P_2S_5. The Raman spectrum of the $80Li_2S{\cdot}20P_2S_5$ glass powder prepared by milling shows a peak at 420 cm^{-1}, which corresponds to the peak of the PS_4^{3-} ions. Results show that the local structures of the $80Li_2S{\cdot}20P_2S_5$ thin films prepared at 5 and 10 Pa resemble those of the glass powder. In general, it is necessary to use the sintered compound as a target for the preparation of oxide thin films by PLD. It is noteworthy that amorphous thin films with a similar local structure to the corresponding glass were obtained even in the case using the mixture of starting materials as a target. Although fundamental processes occurring during laser ablation and deposition remain unclear, ambient Ar gas pressure is an important factor for the preparation of sulfide-based solid electrolyte thin films by PLD.

Lithium-ion conductivities of the $80Li_2S{\cdot}20P_2S_5$ films were measured using comb-like gold electrodes. Figure 4-6 shows an impedance plot of the $80Li_2S{\cdot}20P_2S_5$ thin film prepared under 10^{-2} Pa at 25°C. A large semicircle and a subsequent straight line are observed in the plot, which indicates that the thin film is an ion conductor. The peak top frequency of the semicircle is 10 kHz; the estimated capacitance is 2.8×10^{-11} F, indicating that the resistance of the semicircle is attributable to the bulk resistance of the film because the bulk capacitance is known to be 10^{-11}-10^{-12} F. Figure 4-7 shows the temperature dependence of ionic conductivities of the as-deposited and the heat-treated $80Li_2S{\cdot}20P_2S_5$ thin films prepared under the Ar gas pressure of 5 Pa. Heat treatment was conducted at 200°C for 1 h. Conductivities of the films follow the Arrhenius equation; the activation energy for ionic conduction was calculated from the slope of the plots. Table 4-3 presents the ionic conductivities and activation energies for ionic conduction of the $80Li_2S{\cdot}20P_2S_5$ thin films prepared under 10^{-2}, 1, and 5 Pa. The respective ionic conductivities at 25°C of the as-prepared films deposited under 10^{-2}, 1, and 5 Pa are 7.2×10^{-5}, 6.2×10^{-5}, and 7.9×10^{-5} S cm^{-1}.

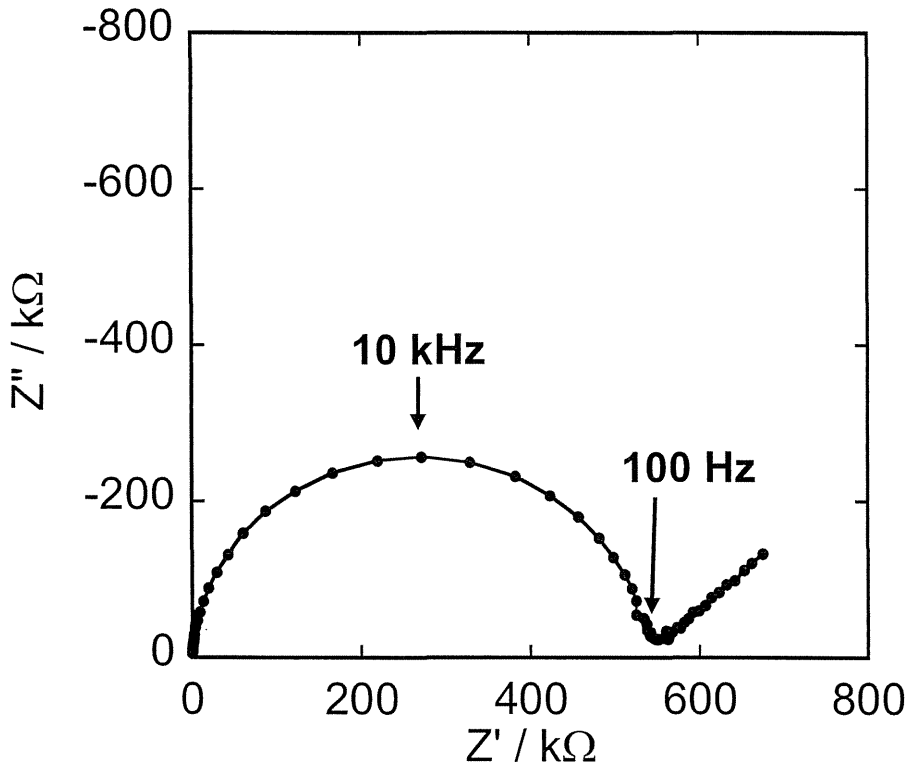

Figure 4-6 Impedance plot of the $80Li_2S{\cdot}20P_2S_5$ thin film prepared at 10^{-2} Pa. Measurements were performed using comb-like gold electrode.

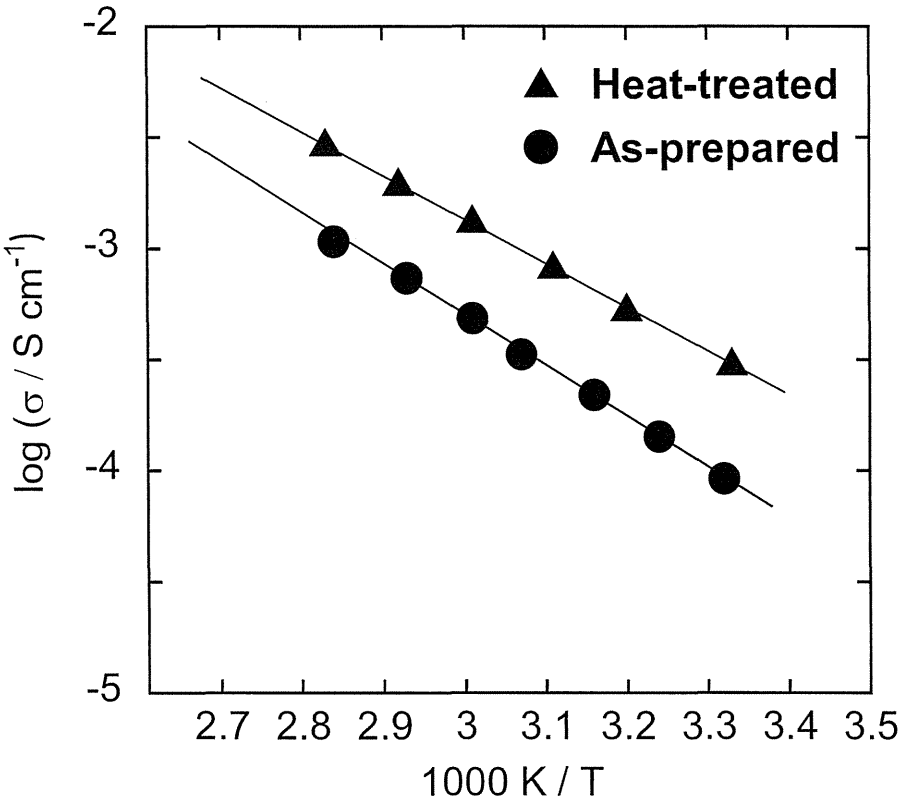

Figure 4-7 Temperature dependence of ionic conductivities of the as-deposited and heat-treated $80Li_2S{\cdot}20P_2S_5$ thin films prepared at 5Pa. Heat treatment was conducted at 200°C for 1 h.

Table 4-3 Ionic conductivities at 25°C (σ_{25}) and activation energies (*Ea*) for conduction of the as-deposited and heat-treated $80Li_2S \cdot 20P_2S_5$ thin films prepared under 10^{-2}, 1, and 5 Pa

Pressure / Pa	Heat treatment / °C	σ_{25} / S cm^{-1}	*Ea* / kJ mol^{-1}
10^{-2}	—	7.2×10^{-5}	40
1	—	6.2×10^{-5}	42
5	—	7.9×10^{-5}	43
5	200	2.8×10^{-4}	38

The activation energies of the thin films are 40-43 kJ mol^{-1}. All as-prepared films show similar ionic conductivity and activation energy. Although structural units of S–S and $P_2S_6^{4-}$, which decrease the ionic conductivity of glass [18], exist in the thin films deposited under 10^{-2} and 1 Pa, the conductivities of all the thin films are similar. The lithium-ion conductivities of the glasses in the system Li_2S–P_2S_5 are known to increase with increased Li_2S contents and to attain a maximum at the composition of around 80 mol% Li_2S [19]. A possible reason for the similar ionic conductivity of the films is the fact that the higher lithium-ion content of the films deposited under 10^{-2} and 1 Pa compensates for the decrease of the lithium-ion conductivity because of the existence of the low-conductivity structures such as S–S and $P_2S_6^{4-}$. The lithium-ion conductivities of the as-deposited and heat-treated films prepared under the Ar gas pressure of 5 Pa are 7.9×10^{-5} and 2.8×10^{-4} S cm^{-1} at 25°C; their activation energies for ionic conduction are, respectively, 43 and 38 kJ mol^{-1}. The heat-treated film exhibits higher conductivity and lower activation energy than the as-deposited film. The $80Li_2S\cdot20P_2S_5$ glass prepared by ball milling exhibited a crystallization peak at 210°C and the highly lithium-ion conducting thio-LISICON analog crystal was precipitated over the temperature. As a result, the conductivity of the glass was increased by crystallization [9, 20]. However, clear crystalline XRD peaks were not observed for the film with heat treatment at 200°C. This is probably because the crystallite size is too small to be detected by XRD. Taking into consideration the fact that the crystalline phase was formed from the ball-milled glass powder, a highly conducting phase would be formed in the $80Li_2S\cdot20P_2S_5$ films. Therefore, the conductivity of the films was increased by the heat treatment. The Raman spectra of the heat-treated films were almost the same as those of the as-deposited films, indicating that the main component ions of Li^+ and PS_4^{3-} were not changed by the heat treatment.

The Li_2S–P_2S_5 thin films using the targets composed of other compositions were

prepared. The films showed similar behavior with table 4-2 and Fig. 4-4. Figure 4-8 shows the Raman spectra of the $70Li_2S{\cdot}30P_2S_5$ thin films prepared under Ar gas pressures of (a) 10^{-2} and (b) 5 Pa. The Raman spectrum of $70Li_2S{\cdot}30P_2S_5$ glass powder prepared by mechanical milling is shown in Fig. 4-8 (c) for comparison. The Raman spectrum of $70Li_2S{\cdot}30P_2S_5$ film prepared under 10^{-2} Pa is similar to that of $80Li_2S{\cdot}20P_2S_5$ film prepared under 10^{-2} Pa which is shown in Fig. 4-4; the film comprises $P_2S_6^{4-}$, PS_4^{3-}, and S-S bonds. A peak at around 410 cm^{-1} is observed for the film prepared under 5 Pa and the $70Li_2S{\cdot}30P_2S_5$ glass powder. Tachez *et al.* [17] have reported that the Raman peaks at 406 cm^{-1} was attributed to $P_2S_7^{4-}$ ions in the $Li_4P_2S_7$ glass. The film prepared under 5 Pa and the $70Li_2S{\cdot}30P_2S_5$ glass powder comprise of PS_4^{3-} and $P_2S_7^{4-}$. Figure 4-9 shows the Raman spectra of (a) $50Li_2S{\cdot}50P_2S_5$, (b) $70Li_2S{\cdot}30P_2S_5$, (c) $75Li_2S{\cdot}25P_2S_5$, and (d) $80Li_2S{\cdot}20P_2S_5$ thin films prepared under an Ar gas pressure of 5 Pa. The local structures of all the Li_2S–P_2S_5 thin films prepared at 5 Pa resemble those of the glass powder of the each composition.

Table 4-4 summarized the lithium-ion conductivities of the Li_2S–P_2S_5 films prepared at 5 Pa. The films with high lithium-ion contents show high lithium-ion conductivities of more than 5×10^{-5} S cm^{-1} at 25°C. In addition, the conductivities of the films increase with the heat treatment. The conductivities are more than 10^{-4} S cm^{-1}. The Li_2S–P_2S_5 thin films exhibit much higher ionic conductivities than oxide solid electrolyte thin films such as LiPON (2×10^{-6} S cm^{-1}) [21]. Therefore, the $80Li_2S{\cdot}20P_2S_5$ thin films are more suitable for application not only to all-solid-state thin-film batteries but also to bulk-type all-solid-state batteries. The thin films are effective in the formation of an ideal interface between solid electrode and solid electrolyte, which is necessary to investigate electrochemical properties at the electrode/electrolyte interface of the all-solid-state batteries. Moreover, the formation of an ideal interface by coating sulfide thin films on electrode particles is expected to improve

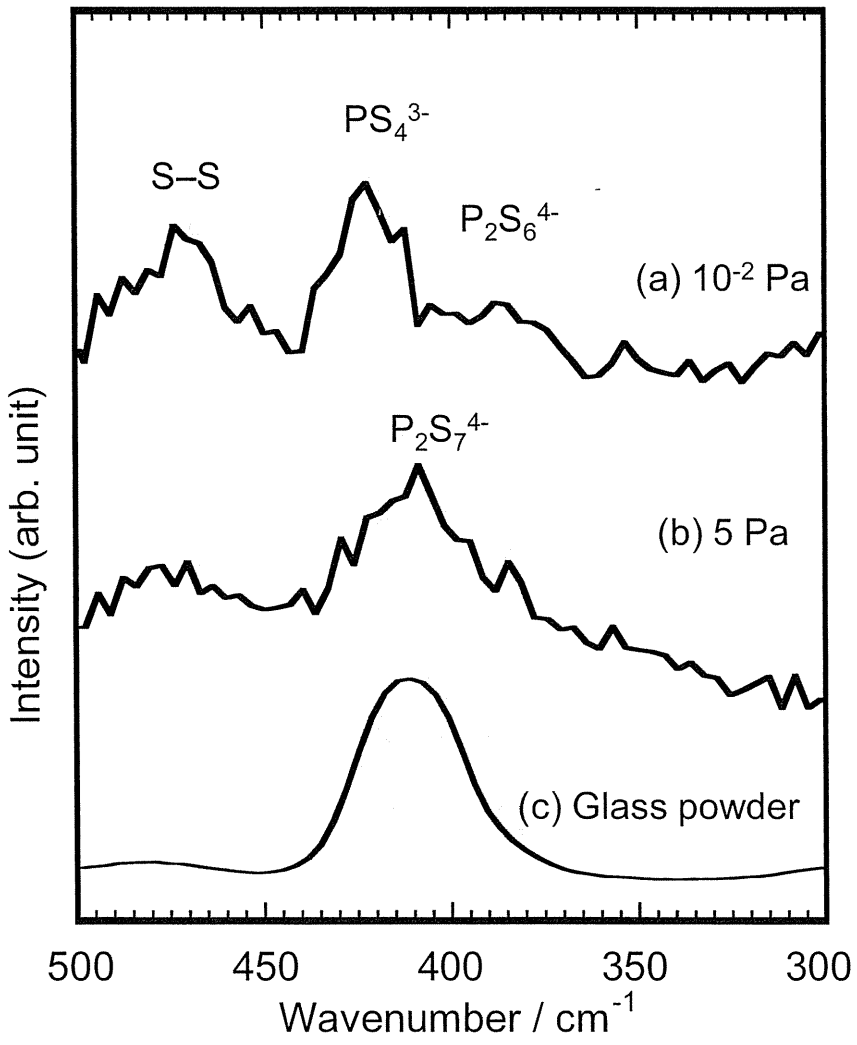

Figure 4-8 Raman spectra of $70Li_2S{\cdot}30P_2S_5$ thin films prepared under Ar gas pressures of (a) 10^{-2} and (b) 5 Pa and (c) $70Li_2S{\cdot}30P_2S_5$ glass powder prepared using a mechanical milling technique.

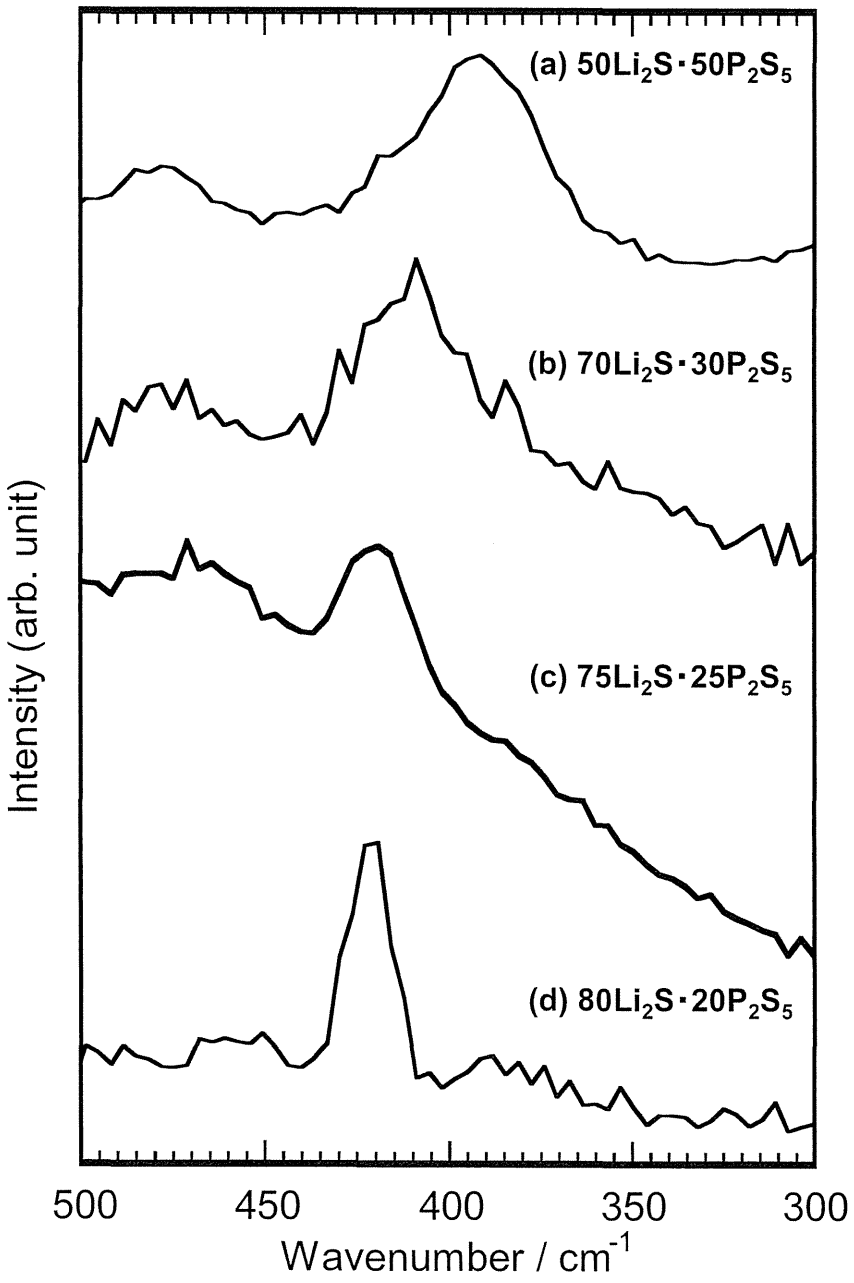

Figure 4-9 Raman spectra of (a) $50Li_2S{\cdot}50P_2S_5$, (b) $70Li_2S{\cdot}30P_2S_5$, (c) $75Li_2S{\cdot}25P_2S_5$, and (d) $80Li_2S{\cdot}20P_2S_5$ thin films prepared under an Ar gas pressure of 5 Pa

Table 4-4 The lithium ion conductivities of Li_2S–P_2S_5 thin films prepared under 5 Pa.

Composition	Heat treatment temperature (°C)	Conductivity at 25°C (S cm^{-1})
$80Li_2S \cdot 20P_2S_5$	—	7.9×10^{-5}
$80Li_2S \cdot 20P_2S_5$	200°C	3.1×10^{-4}
$75Li_2S \cdot 25P_2S_5$	—	8.7×10^{-5}
$70Li_2S \cdot 30P_2S_5$	—	4.2×10^{-5}
$70Li_2S \cdot 30P_2S_5$	280°C	3.4×10^{-4}
$50Li_2S \cdot 50P_2S_5$	—	1.0×10^{-6}

the rate capability of the bulk-type batteries.

4.3.1.2. Li_2S–GeS_2 solid electrolyte films

Table 4-5 presents chemical compositions of the Li_2S–GeS_2 thin films prepared under an Ar gas pressure of 5 Pa. The atomic ratio of Li:Ge of the films prepared using $67Li_2S{\cdot}33GeS_2$ and $75Li_2S{\cdot}25GeS_2$ targets are, respectively, 63:37 and 67:33. The films with the Li:Ge ratio of 77:23 and 80:20 in the table corresponds to the compositions $63Li_2S{\cdot}37GeS_2$ and $67Li_2S{\cdot}33GeS_2$ (mol%), respectively. Although the atomic ratios of Li of the films are lower than that of the targets, the films with high lithium contents were prepared. Figure 4-10 (a) shows the Raman spectra of the films prepared by PLD using $67Li_2S{\cdot}33GeS_2$ and $75Li_2S{\cdot}25GeS_2$ (mol%) targets prepared under an Ar gas pressure of 5 Pa. A broad peak around 370 cm^{-1} is observed in each film. Figure 4-10 (b) shows the Raman spectra of $67Li_2S{\cdot}33GeS_2$ powder prepared by mechanical milling (MM) for comparison. The Raman spectra of obtained two films prepared using both $67Li_2S{\cdot}33GeS_2$ and $75Li_2S{\cdot}25GeS_2$ targets reassemble that of $67Li_2S{\cdot}33GeS_2$ prepared by MM. The thin films with a similar local structure to glass powder with high lithium contents were obtained by the deposition using an ambient Ar gas pressure of 5 Pa.

Figure 4-11 (a) shows impedance plot of the $75Li_2S{\cdot}25GeS_2$ thin film. A large semicircle and a subsequent straight line are observed in the plot, which indicates that the thin film is an ion conductor. Figure 4-11 (b) shows the temperature dependence of ionic conductivities of $67Li_2S{\cdot}33GeS_2$ and $75Li_2S{\cdot}25GeS_2$ thin films prepared under the Ar gas pressure of 5 Pa. Conductivities of the films follow the Arrhenius equation; the activation energy for ionic conduction was calculated from the slope of the plots. Table 4-6 presents the ionic conductivities and activation energies for ionic conduction of the Li_2S–GeS_2 thin films prepared by PLD, the Li_2S–GeS_2 glassy flakes prepared by rapid quench with

Table 4-5 Chemical compositions of Li_2S–GeS_2 thin films determined by ICP–AES. The ambient Ar gas pressure was 5 Pa.

Target	Li /Ge	Li : Ge
$66Li_2S \cdot 33GeS_2$	3.3	77 : 23
$75Li_2S \cdot 25GeS_2$	4.0	80 : 20

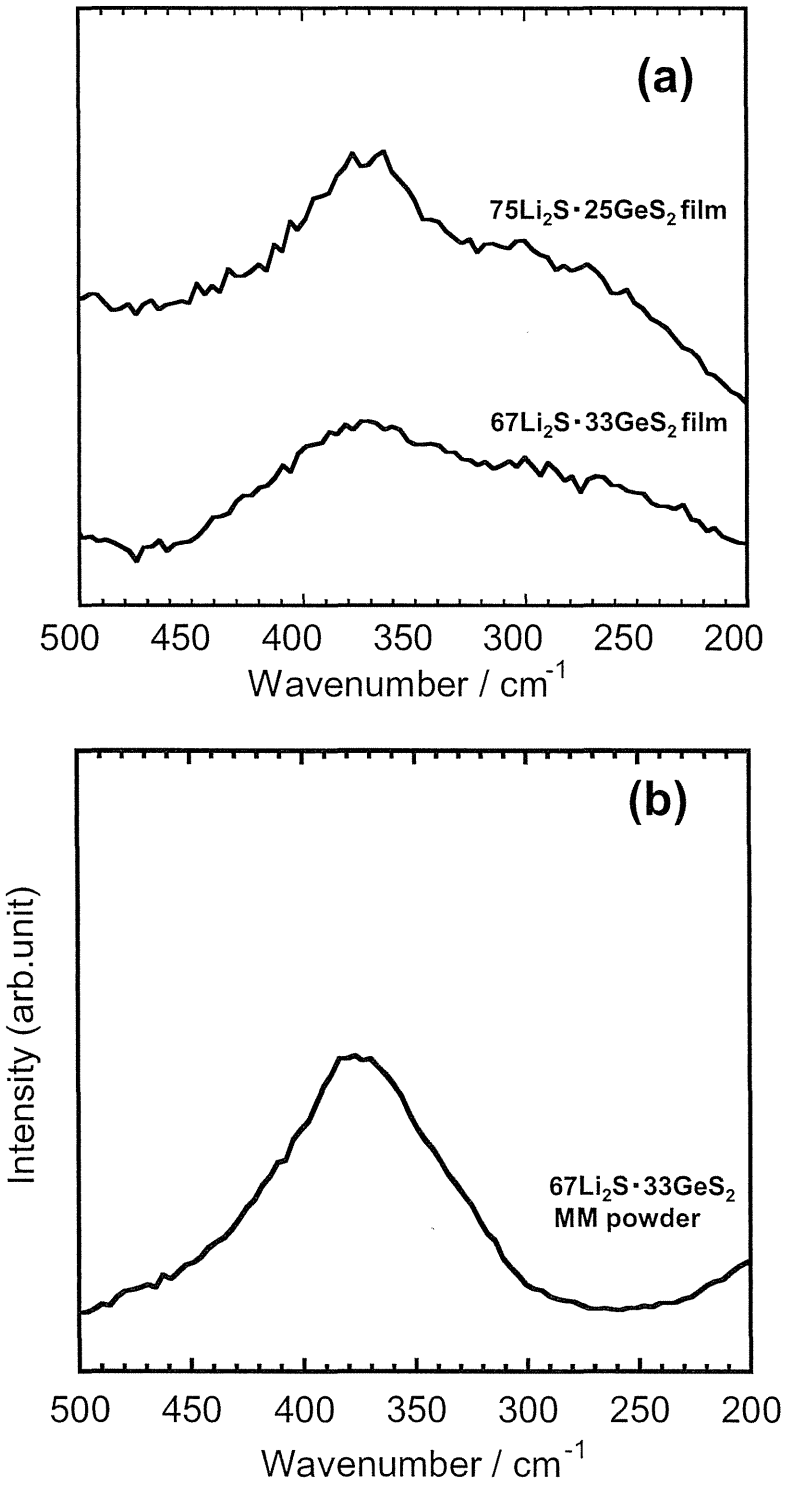

Figure 4-10 Raman spectra of (a) the films prepared by PLD using $67Li_2S{\cdot}33GeS_2$ and $75Li_2S{\cdot}25GeS_2$ targets prepared under an Ar gas pressure of 5 Pa and (b) $67Li_2S{\cdot}33GeS_2$ glassy powder prepared by mechanical milling (MM).

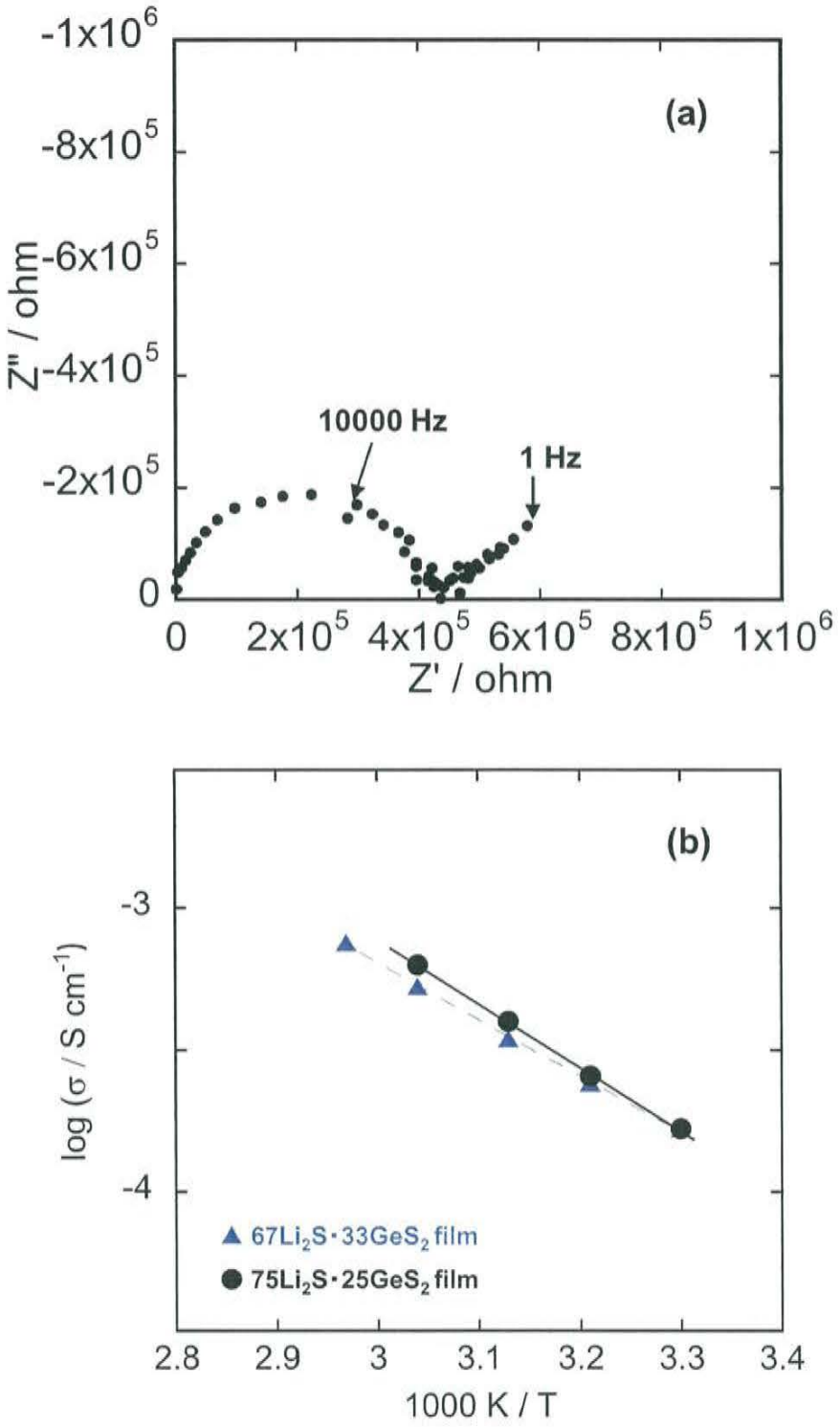

Figure 4-11 (a) impedance plot of the $75Li_2S{\cdot}25GeS_2$ thin film at 30 °C and (b) temperature dependence of ionic conductivities of $67Li_2S{\cdot}33GeS_2$ and $75Li_2S{\cdot}25GeS_2$ thin films.

Table 4-6 The ionic conductivities and activation energy for conduction of Li_2S–GeS_2 thin films prepared under 5 Pa. Those of the Li_2S–GeS_2 glasses prepared by rapid quench with twin-roller (TR), and $67Li_2S{\cdot}33GeS_2$ glassy powder prepared by mechanical milling (MM) were shown for comparison.

Composition (Experiment) (mol%)	Type (method)	Conductivity at 25°C (S cm^{-1})	Activation energy (kJ mol^{-1})	Ref.
$67Li_2S{\cdot}33GeS_2$ ($63Li_2S{\cdot}33GeS_2$)	Film (PLD)	1.2×10^{-4}	39	This study
$75Li_2S{\cdot}25GeS_2$ ($67Li_2S{\cdot}33GeS_2$)	Film (PLD)	1.2×10^{-4}	44	This study
$63Li_2S{\cdot}37GeS_2$	Flake (TR)	1.5×10^{-4}	31	[23]
$67Li_2S{\cdot}33GeS_2$	Flake (TR)	1.0×10^{-4}	36	[23]
$70Li_2S{\cdot}30GeS_2$	Flake (TR)	1.2×10^{-4}	33	[23]
$67Li_2S{\cdot}33GeS_2$	Powder (MM)	2.5×10^{-5}	38	This study

twin-roller [22], and $67Li_2S{\cdot}33GeS_2$ glassy powder prepared by MM. The ionic conductivities at 25°C of $67Li_2S{\cdot}33GeS_2$ and $75Li_2S{\cdot}25GeS_2$ thin films are 1.2×10^{-4} S cm^{-1} for each film. The activation energies of the thin films are 39 and 44 kJ mol^{-1}. The conductivity of $xLi_2S{\cdot}(100\text{-}x)GeS_2$ glassy flakes (x = 63, 67, and 70) are 1.0×10^{-4} to 1.5×10^{-4} S cm^{-1}; that of the $67Li_2S{\cdot}33GeS_2$ glassy powder prepared by MM is 2.5×10^{-5} S cm^{-1}. The Li_2S–GeS_2 films prepared by PLD show similar ionic conductivities to the Li_2S–GeS_2 glassy flakes prepared by twin-roller rapid quench. The conductivities of the Li_2S–GeS_2 films prepared by PLD are similar to or higher than those of the Li_2S–P_2S_5 films shown in Table 4-4.

4.3.2. All-solid-state batteries using electrode particles coated with Li_2S–P_2S_5

4.3.2.1. Li_2S–P_2S_5 coated $LiCoO_2$

(i) Morphology of SE-coated $LiCoO_2$ particles

Figure 4-12 shows SEM images of $80Li_2S{\cdot}20P_2S_5$ SE coated $LiCoO_2$ (SE-coated $LiCoO_2$) with different coating times, ranging from 0 to 40 min. Figure 4-12 (a) shows an SEM image of $LiNbO_3$-coated $LiCoO_2$ without an Li_2S–P_2S_5 SE coating. The average particle diameter was ca. 10 μm, and the surface of the $LiNbO_3$-coated $LiCoO_2$ particles was relatively smooth. The particle size of the SE (10 min)-coated $LiCoO_2$, as shown in Fig. 4-12 (b), was similar to that without SE coating. Figures 4-12 (c) and (d) show SEM images of SE (20 min)-coated and SE (40 min)-coated $LiCoO_2$. The particle sizes of the 20-min and 40-min SE-coated $LiCoO_2$ were ca. 20 μm, which was larger than that without SE coating. Small aggregates were formed by depositing Li_2S–P_2S_5 SE on $LiCoO_2$ particles, and the size of the secondary particles increased with increasing deposition time. Figure 4-13 shows the SEM and EDX-mapping (Co, P, and S) images of the Li_2S–P_2S_5 solid-electrolyte-coated (SE-coated) $LiCoO_2$ (deposition time of 40 min). The SEM image shows that the particle

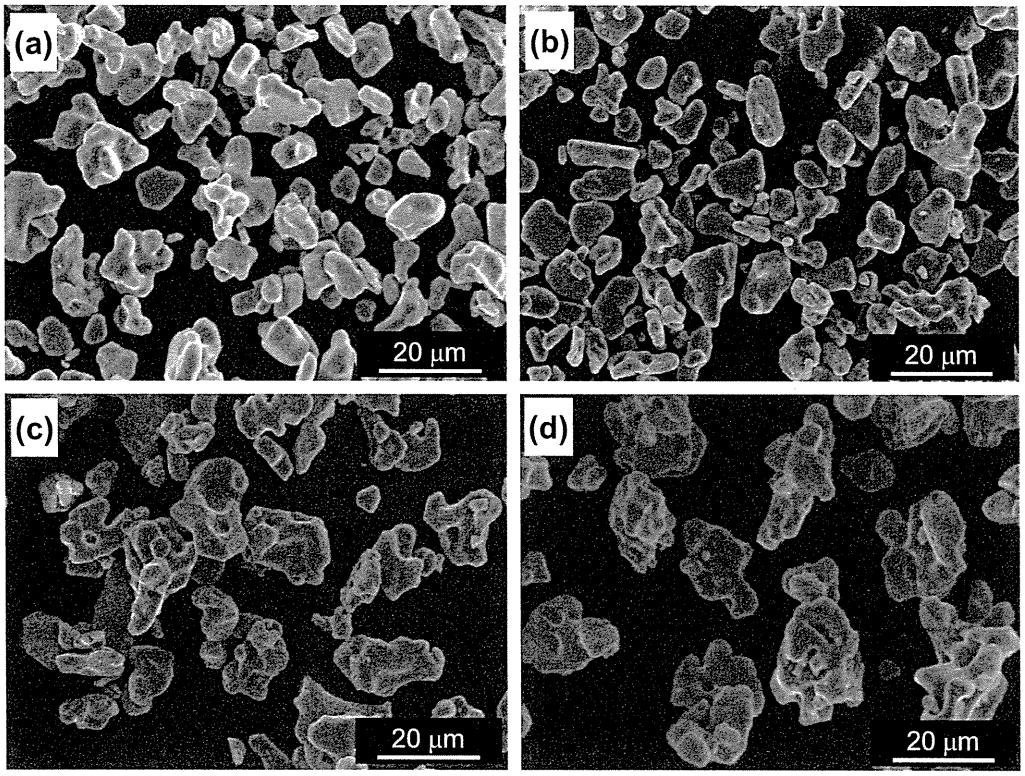

Figure 4-12 SEM images of Li_2S–P_2S_5 solid-electrolyte-coated $LiCoO_2$ particles with various coating times: (a) 0 min, (b) 10 min, (c) 20 min, and (d) 40min.

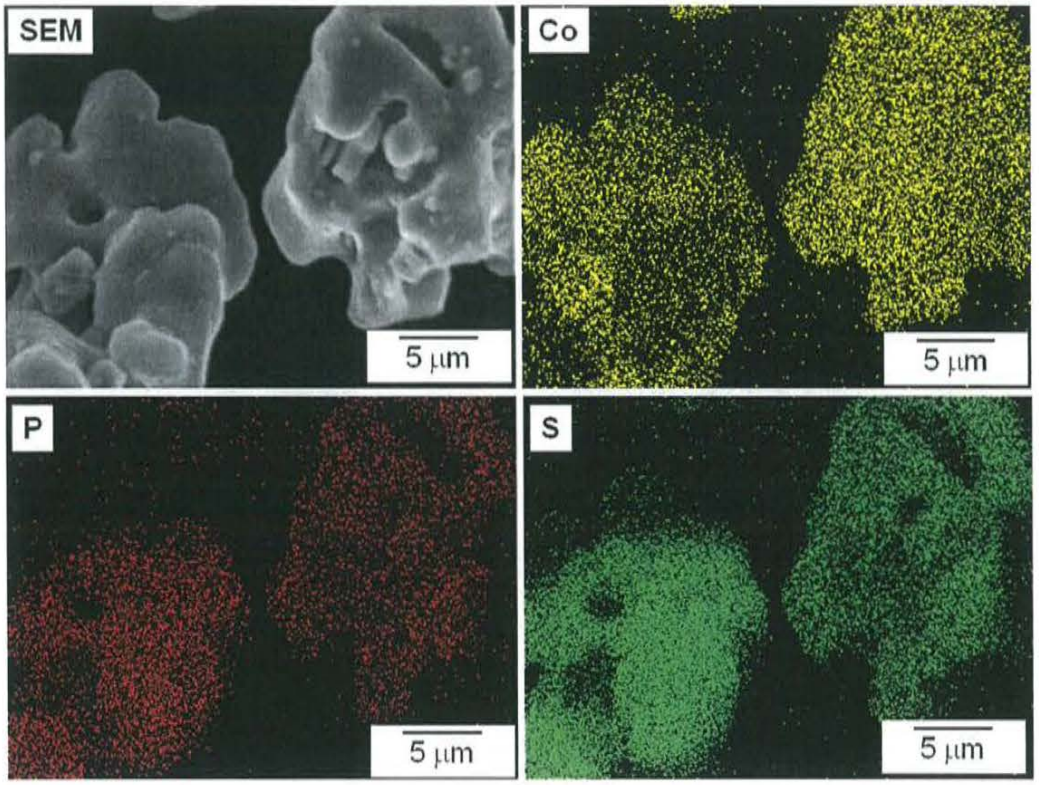

Figure 4-13 SEM image and EDX mapping images for Co element, P element, and S element of the Li_2S–P_2S_5 solid-electrolyte-coated $LiCoO_2$ particles.

size of the $LiCoO_2$ particles is about 20 μm; the coating materials are observed on the $LiCoO_2$ particles. Phosphorous and sulfur elements of Li_2S–P_2S_5 solid electrolyte film and cobalt element of $LiCoO_2$ particles are detected in the same area, indicating that the $LiCoO_2$ particles are covered with Li_2S–P_2S_5 solid electrolyte film. The chemical composition and the local structure of the Li_2S–P_2S_5 solid electrolyte film prepared on a Si substrate by PLD were almost the same as those of the Li_2S–P_2S_5 glass prepared by the mechanochemical method as shown in section 4.3.1.1 in this chapter. The Li_2S–P_2S_5 films prepared on $LiCoO_2$ would also have a similar chemical composition ($80Li_2S{\cdot}20P_2S_5$) and local structure to those of the film prepared on the Si substrate. Figure 4-14 shows a cross-sectional FE–TEM image of SE-coated $LiCoO_2$ particles. Coatings of $LiNbO_3$ with thickness of 7 nm were formed on $LiCoO_2$ particles in advance. A coating of Li_2S–P_2S_5 solid electrolyte was observed on the $LiNbO_3$-coated $LiCoO_2$ particles, with a film thickness of 50-70 nm. The calculated weight ratio of Li_2S–P_2S_5 coating to $LiCoO_2$ particles is *ca.* 1 : 100.

The interface of the SE-coated $LiCoO_2$ particles with no $LiNbO_3$ coating is observed for comparison. Figure 4-15 presents a cross-sectional HAADF–STEM image and the n–ED patterns for the SE-coated $LiCoO_2$ particles with no $LiNbO_3$ coating. An interfacial layer is visible at the interface between $LiCoO_2$ electrode and Li_2S–P_2S_5 solid electrolyte film. The layer thickness is ca. 5 nm. The n–ED pattern of the solid electrolyte (n–ED-7) shows that the solid electrolyte is amorphous. The n–ED patterns of $LiCoO_2$ electrode show the same diffraction patterns from inside to the surface (n–ED-1 and 2), indicating that the $LiCoO_2$ is a single crystal and that large degradation does not occur. On the other hand, the n–ED patterns of the interface layer (n–ED-3 to 5) show patterns suggesting the presence of a nanosized polycrystal. The EDX analysis showed that the interfacial layer mainly was composed of Co and S elements. Those results of formation of interfacial compound between $LiCoO_2$ and Li_2S–P_2S_5 are supported by the results discussed in Chapter 3. Those

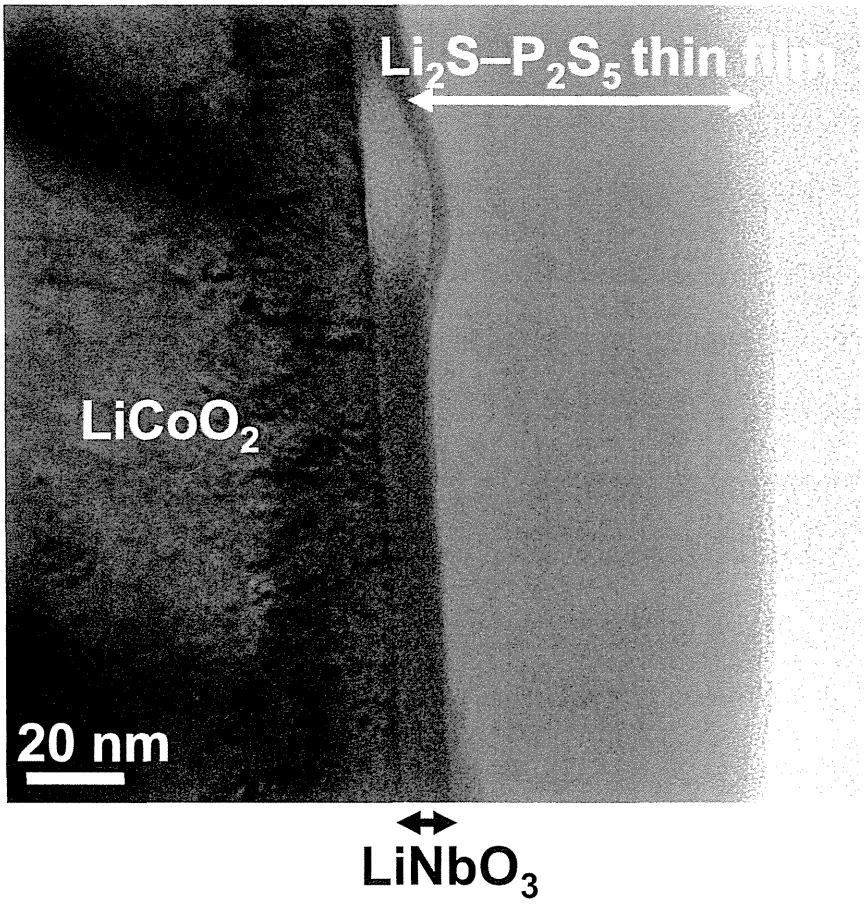

Figure 4-14 Cross-sectional TEM image of the Li_2S–P_2S_5 solid-electrolyte-coated $LiCoO_2$ particles.

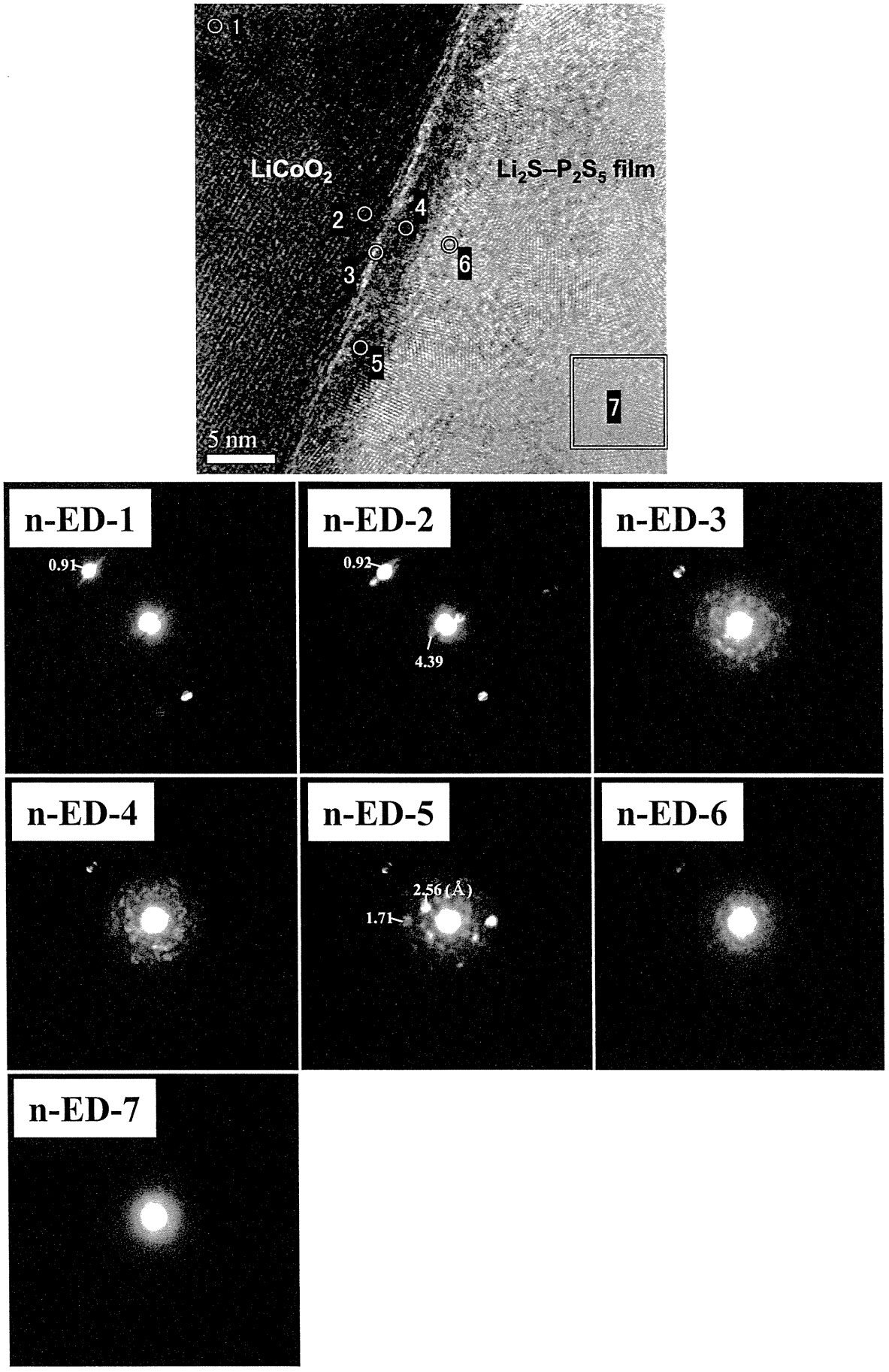

Figure 4-15 Cross-sectional TEM image and the n–ED patterns of SE-coated $LiCoO_2$ particles with no $LiNbO_3$ coating. The numbered points in the HAADF–STEM image correspond to the positions of n–ED measurements.

results suggest that the oxide coating such as $LiNbO_3$ should be formed on bare $LiCoO_2$ particles in advance in order to form an effective electrode-electrolyte interface in SE-coated $LiCoO_2$.

(ii) Cross-sectional TEM observation of all-solid-state lithium secondary cells using SE-coated $LiCoO_2$

All-solid-state cells were constructed using SE-coated $LiCoO_2$ particles with no SE particles mixed into the working electrode. Figure 4-16 shows the surface images of the positive electrode layer of the all-solid-state cells using (a) uncoated, (b) SE (40 min)-coated and (c) SE (240 min)-coated $LiCoO_2$ particles with no additional solid electrolyte particles. The observations were carried out after charge-discharge processes for 450 cycles for SE (40 min)-coated $LiCoO_2$ and after the 1st charging for SE (240 min)-coated $LiCoO_2$, respectively. Particles with a size distribution from 1 to 20 μm are observed in the SEM image of the surface of the cell using uncoated $LiCoO_2$ in Fig. 4-16 (a). In contrast, particles with the size smaller than 5 μm are hardly observed in the scanning ion microscope (SIM) images of the cells using SE (40 min)-coated and SE (240 min)-coated $LiCoO_2$ in Fig. 4-16 (b) and (c). This is due to the aggregates of the SE-coated $LiCoO_2$ particles during deposition as shown in Fig. 4-12. By the comparison of the surface of positive electrode using uncoated $LiCoO_2$ and that using SE-coated $LiCoO_2$, it is assumed that solid electrolyte films on $LiCoO_2$ particles connected the $LiCoO_2$ particles. Figure 4-17 shows the cross-sectional SIM images of positive electrode layer of the all-solid-state cells using (a) SE (40 min)-coated and (b) SE (240 min)-coated $LiCoO_2$ corresponding to the images shown in Fig. 4-16 (b) and (c). The SIM images show that the $LiCoO_2$ particles were closely packed in the composite electrode. Some voids are visible in the cross-sectional images of the positive electrode layer using SE (40 min)-coated $LiCoO_2$. The voids almost disappear in the positive electrode using SE (240

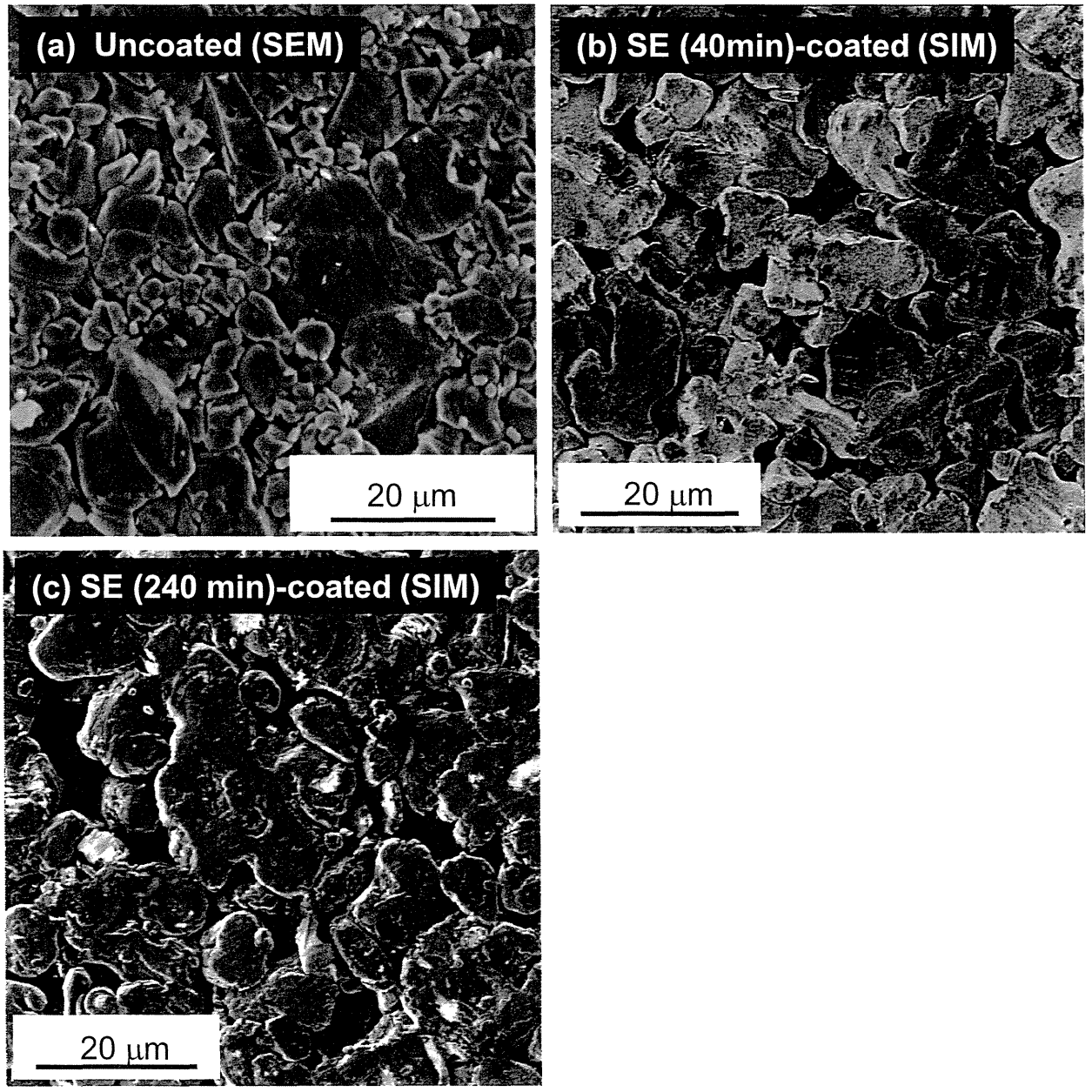

Figure 4-16 (a) SEM image and (b, c) scanning ion microscope (SIM) images of surface of positive electrode layer of all-solid-state cells using (a) uncoated, (b) SE (40 min)-coated $LiCoO_2$, and (c) SE (240 min)-coated $LiCoO_2$.

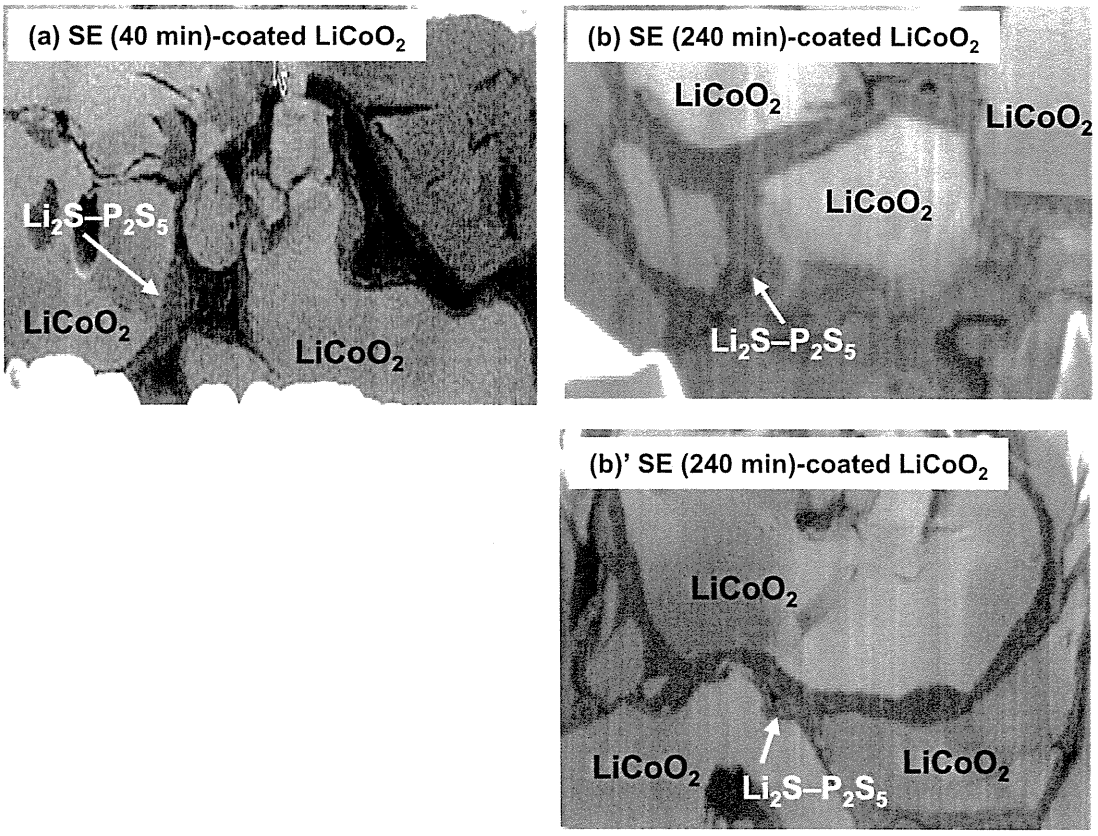

Figure 4-17 Cross-sectional SIM images of positive electrode layer of all-solid-state cells using (a) SE (40 min)-coated and (b and b') SE (240 min)-coated $LiCoO_2$.

min)-coated $LiCoO_2$. Thick solid electrolyte coating filled in the voids.

Figure 4-18 shows cross-sectional high-angle annular dark field (HAADF)–TEM images and EDX mappings of a working electrode from an all-solid-state cell based on SE (40 min)-coated $LiCoO_2$. The cross-sectional TEM image in Fig. 4-18 (a) shows that the $LiCoO_2$ particles are closely packed in the composite electrode. Figure 4-18 (b) shows a magnified image of the selected area in Fig. 4-18 (a) and EDX mappings for O, P, S, Co, and Nb at the interface between $LiCoO_2$ particles. Niobium (Nb) is observed on the $LiCoO_2$ particle surfaces, confirming that an $LiNbO_3$ coating forms on the $LiCoO_2$ particles. The observation of P and S at the interface between the $LiCoO_2$ particles indicates that an $80Li_2S{\cdot}20P_2S_5$ solid electrolyte layer is present. The all-solid-state cell was prepared by cold pressing. As a result of this pressing, the $LiCoO_2$ particles packed closely in the composite electrode layer and the solid electrolyte coating deposited on the $LiCoO_2$ particles was connected to form the all-solid-state cell. As a result, a favorable SE region was formed in the interfacial space between the $LiCoO_2$ particles. Furthermore, the contact between the solid electrolyte layer and the $LiCoO_2$ electrode is maintained after charge-discharge measurements. Retention of the electrode/electrolyte interface during charge-discharge cycling is important for capacity retention in all-solid-state batteries. Some voids at the interfaces between $LiCoO_2$ particles are observed, as shown in Fig. 4-18 (a). This is reduced by using $LiCoO_2$ with larger amounts of solid electrolyte coating as shown in Fig. 4-17.

Figure 4-19 shows cross-sectional HAADF–TEM images and EDX mappings of a working electrode from an all-solid-state cell based on SE (240 min)-coated $LiCoO_2$ with no additional solid electrolyte particles after the 1st charging. In an all-solid-state cell based on SE (240 min)-coated $LiCoO_2$ particles, the solid electrolyte is formed more effectively at the interface than that based on SE (40 min)-coated $LiCoO_2$, because the solid electrolyte coating thickness on the $LiCoO_2$ is about six times that of a composite electrode using SE (40

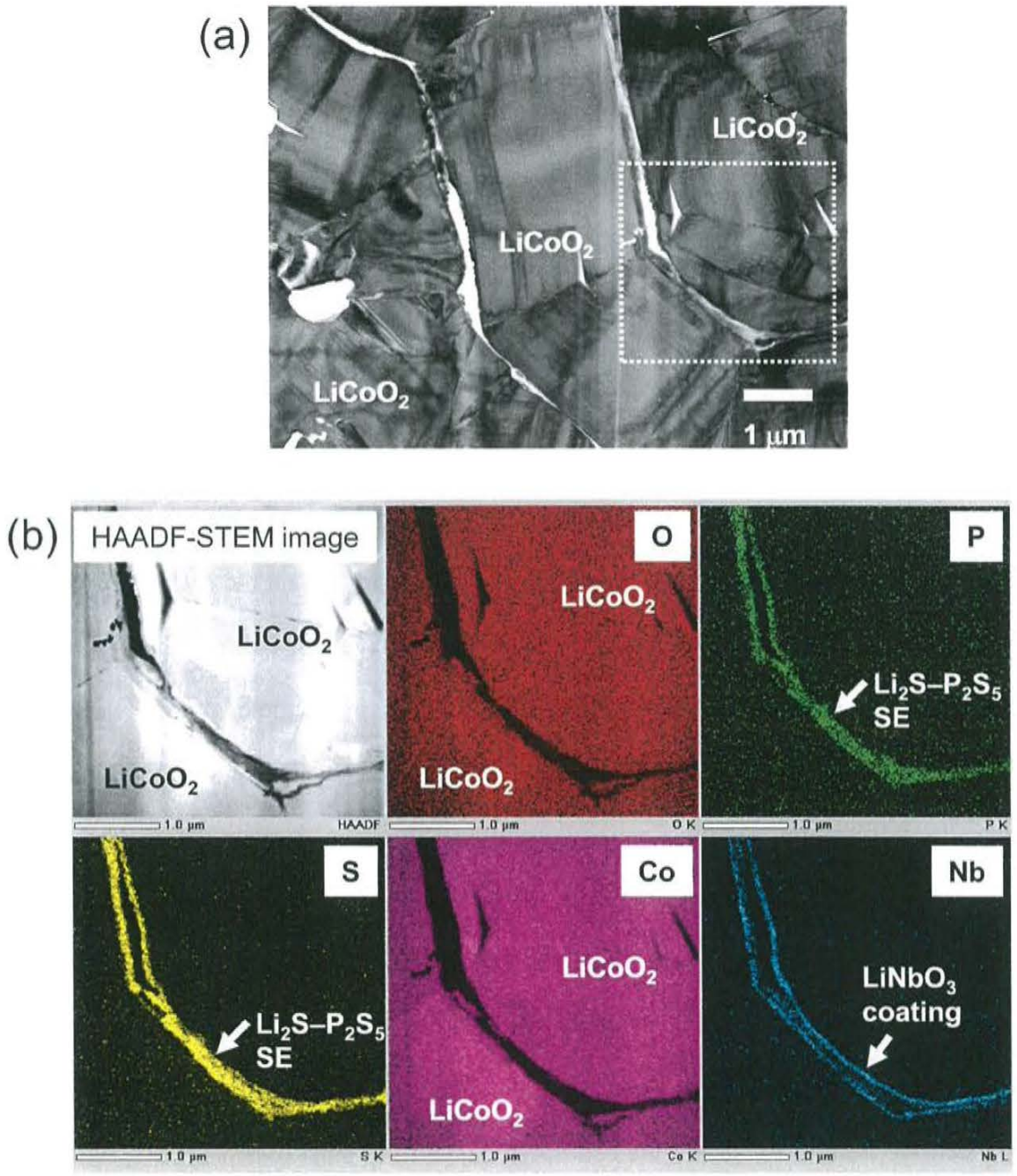

Figure 4-18 Cross-sectional high-angle annular dark field (HAADF) TEM images and EDX mappings of a composite electrode composed of SE (40 min)-coated $LiCoO_2$ in an all-solid-state cell after 450 cycles. The composite electrode was composed of solely SE-coated $LiCoO_2$, with no added solid electrolyte particles.

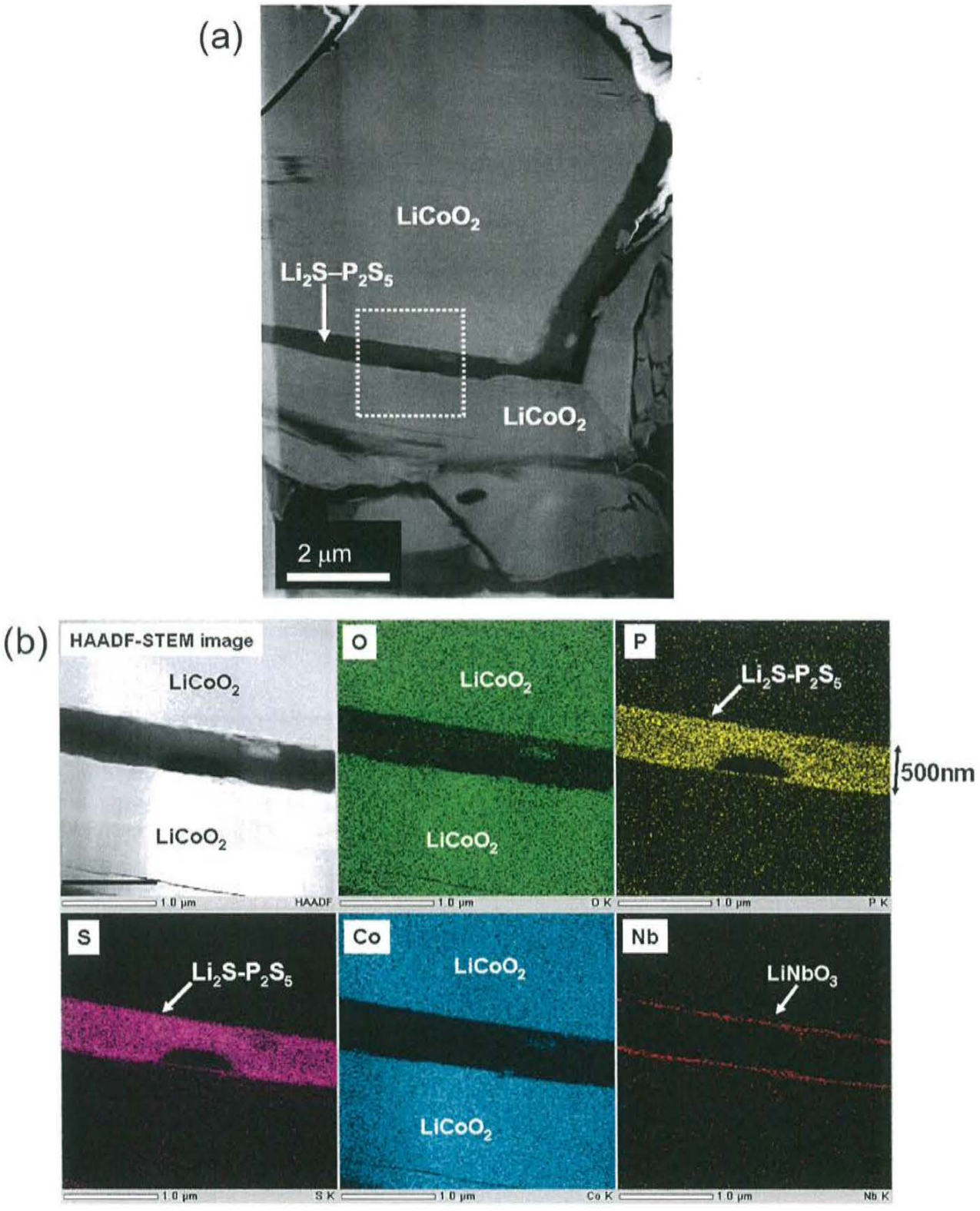

Figure 4-19 Cross-sectional high-angle annular dark field (HAADF) TEM images and EDX mappings of a composite electrode composed of SE (240 min)-coated $LiCoO_2$ in an all-solid-state cell after 1st charging. The composite electrode was composed of solely SE-coated $LiCoO_2$, with no added solid electrolyte particles.

min)-coated $LiCoO_2$. Actually, the thickness of solid electrolyte layer observed at the interface between $LiCoO_2$ particles increases with increasing the coating time from 40 min to 240 min.

Figure 4-20 shows the HAADF–STEM image of the interface between $LiCoO_2$ and Li_2S–P_2S_5 solid electrolyte of all-solid-state cell using SE (240 min)-coated $LiCoO_2$ after initial charging; figure 4-20 (b) shows EDX line profiles of the existence ratio for O, P, S, Co, and Nb elements at the position indicated by the points in Fig. 4-20 (a). In the STEM image, the interfacial layer is visible. The EDX line profile shows that the Nb element of the $LiNbO_3$ coating is visible at the interface. The EDX line profile also shows coexistence of Co, P, and S elements at the interfacial region. The Co diffusion is observed between about 10 nm. The $LiNbO_3$ coating on $LiCoO_2$ effectively suppresses the cobalt diffusion from $LiCoO_2$ to the Li_2S–P_2S_5 solid electrolyte layer.

(iii) Electrochemical performance of all-solid-state cells based on SE-coated $LiCoO_2$

All-solid-state cells using SE-coated $LiCoO_2$ particles with no SE particles mixed into the working electrode were charged and discharged. Figure 4-21 shows charge-discharge curves of all-solid-state cells using uncoated, $LiNbO_3$-coated, and SE (x min)-coated $LiCoO_2$ particles (x = 10, 40, 120, and 240 min) at the current density of 0.13 mA cm^{-2}. The measurements were carried out at 25°C. The cells were charged up to 3.6 V vs. Li–In and discharged to 2 V vs. Li–In. The solid electrolyte coatings were applied to $LiNbO_3$-coated $LiCoO_2$ particles. In the all-solid-state cells shown in Fig. 4-21, the solid electrolyte particles were not mixed into the composite electrode, and thus the working electrode was composed of only $LiCoO_2$ particles. The displayed capacity was normalized by the weight of the coated $LiCoO_2$. The all-solid-state cell based on uncoated $LiCoO_2$ could not be charged and discharged, which agrees with the results of our previous report [23]. The

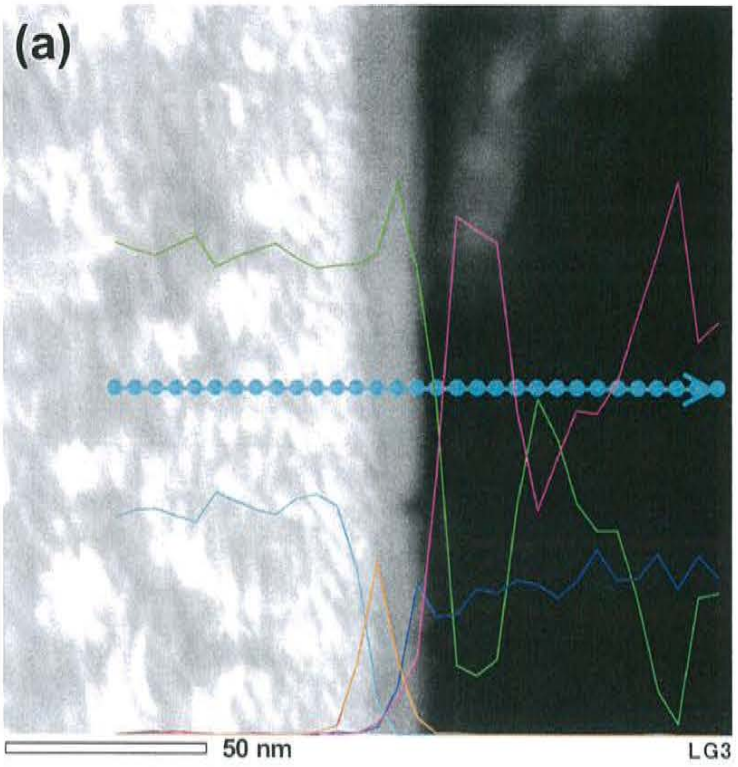

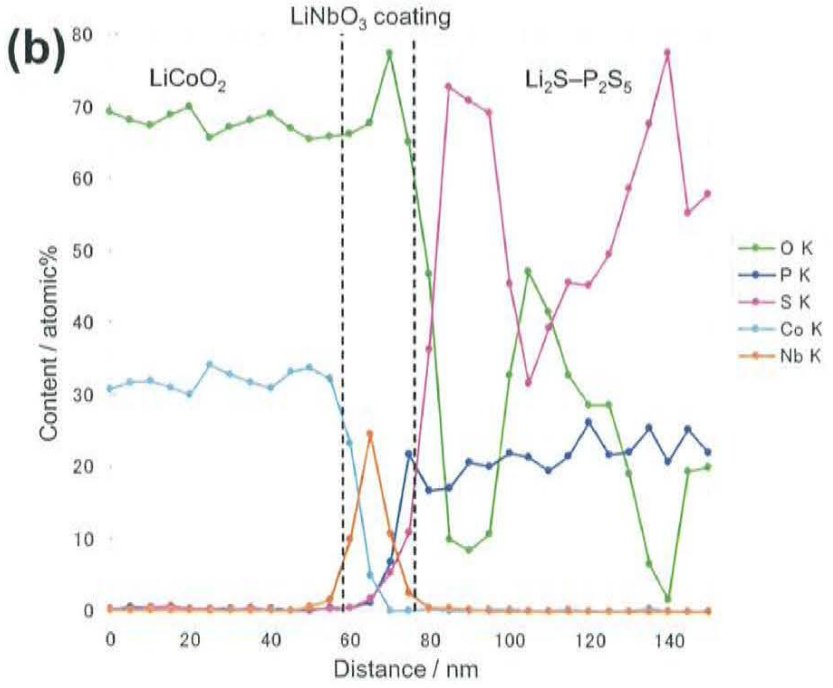

Figure 4-20 (a) Cross-sectional HAADF–STEM image of $LiCoO_2$ electrode/Li_2S–P_2S_5 solid electrolyte interface and (b) cross-sectional EDX line profiles for O, P, S, Co, and Nb elements of the cell using SE (240 min)-coated $LiCoO_2$ after initial charging. The points in (a) presents the positions at which EDX measurements were taken.

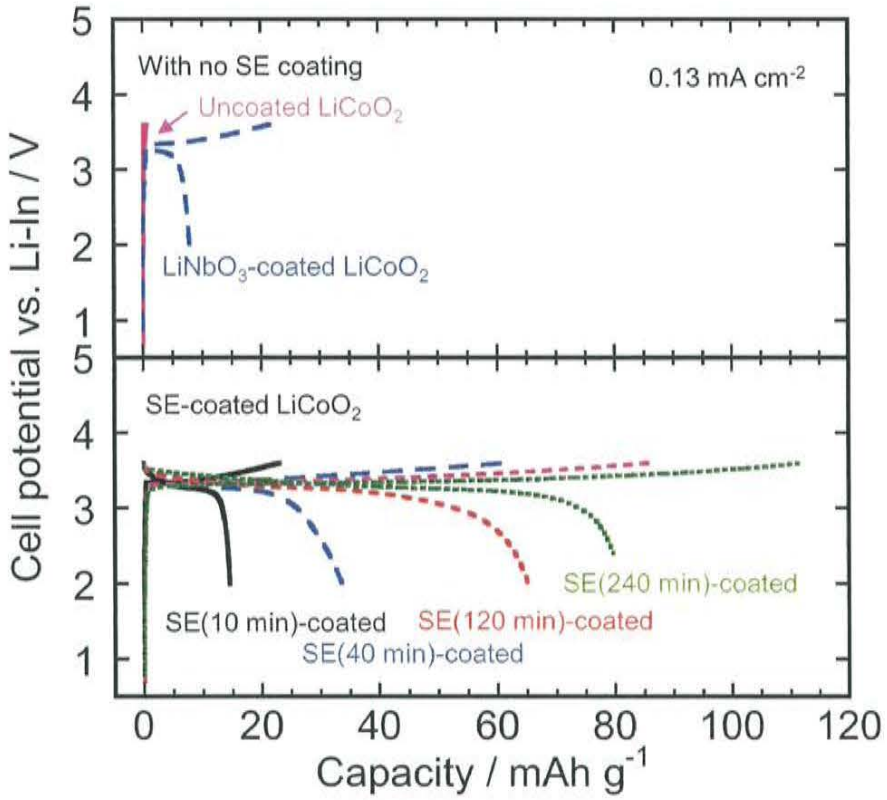

Figure 4-21 Initial charge-discharge curves of the all-solid-state cells using uncoated, $LiNbO_3$-coated, and SE (10, 40, 120, 240 min)-coated $LiCoO_2$.

all-solid-state cell using $LiNbO_3$-coated $LiCoO_2$ had a small reversible capacity of less than 10 mAh g^{-1}. All-solid-state cells using $LiCoO_2$ particles without Li_2S–P_2S_5 solid electrolyte coating were difficult to charge and discharge, because the lithium-ion conductivity in the composite electrode was insufficient. The all-solid-state cells using SE-coated $LiCoO_2$ particles could be charged and discharged with a higher capacity than $LiNbO_3$-coated $LiCoO_2$, and the all-solid-state cells using SE (10 min)-coated, SE (40 min)-coated, SE (120 min)-coated, and SE (240 min)-coated $LiCoO_2$ had reversible capacities of 15, 35, 65, and 80 mAh g^{-1}, respectively. The capacity increased with increasing coating time from 0 min to 240 min, which indicates that a solid electrolyte coating on $LiNbO_3$-coated $LiCoO_2$ enabled the formation of a lithium-ion conducting path to the $LiCoO_2$ particles.

Figure 4-22 shows the charge-discharge curves of all-solid-state cells based on SE (40 min)-coated and SE (120 min)-coated $LiCoO_2$. The cells demonstrated stable charge and discharge curves, without a significant fade in capacity, over 100 cycles in SE (40 min)-coated $LiCoO_2$. The all-solid-state cell based on SE (120 min)-coated $LiCoO_2$ was also charged and discharged for 10 cycles with no significant reduction in capacity.

Increasing the lithium-ion conductivity in composite electrodes seems to be important in achieving a high capacity. The conductivity of the $80Li_2S \cdot 20P_2S_5$ solid electrolyte film prepared using PLD was increased by heat treatment at 200°C as described in section 4-3-1-1. Therefore, the effect of heat treatment of SE-coated $LiCoO_2$ on cell performance was investigated. Figure 4-23 shows the charge-discharge curves of an all-solid-state cell based on SE (120 min)-coated $LiCoO_2$, after heat treatment at 200°C for 1 hour. The current density was 0.13 mA cm^{-2}. The charging and discharging capacities were 86 and 69 mAh g^{-1}, respectively. The charging capacities of cells based on SE (120 min)-coated $LiCoO_2$ with and without heat treatment were similar. The discharge capacity of the heat-treated SE (120 min)-coated $LiCoO_2$ cell was larger than the capacity without heat treatment. The discharge

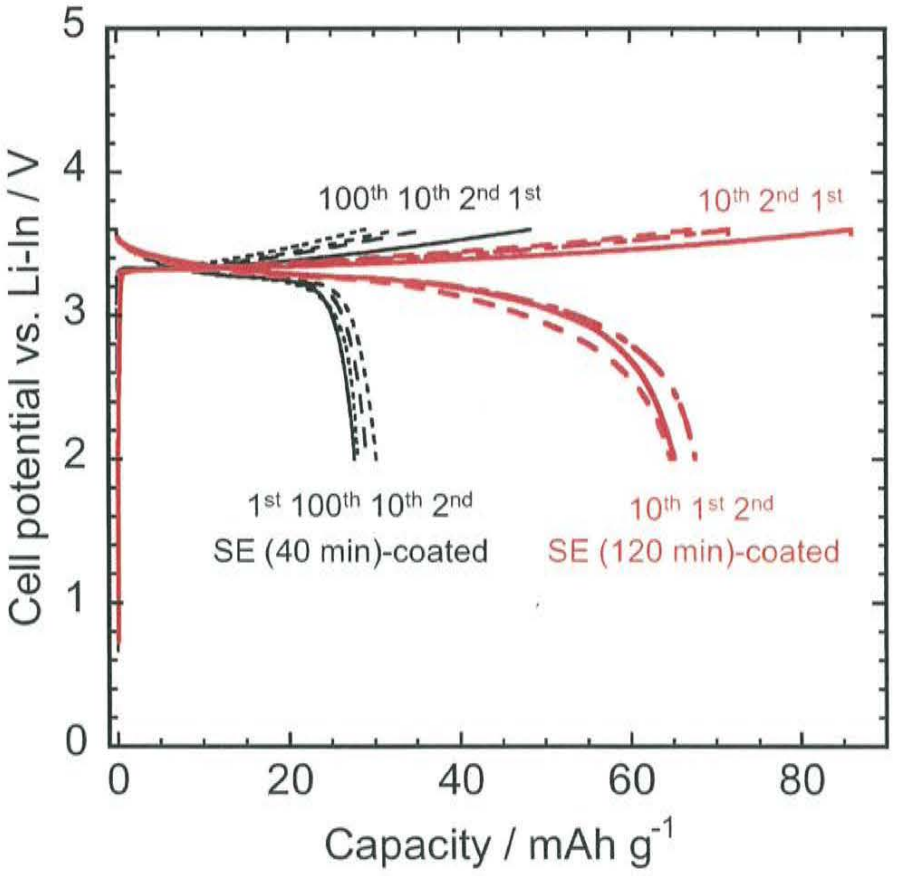

Figure 4-22 Charge-discharge curves of an all-solid-state cell based on SE (40 min)-coated and SE (120 min)-coated $LiCoO_2$.

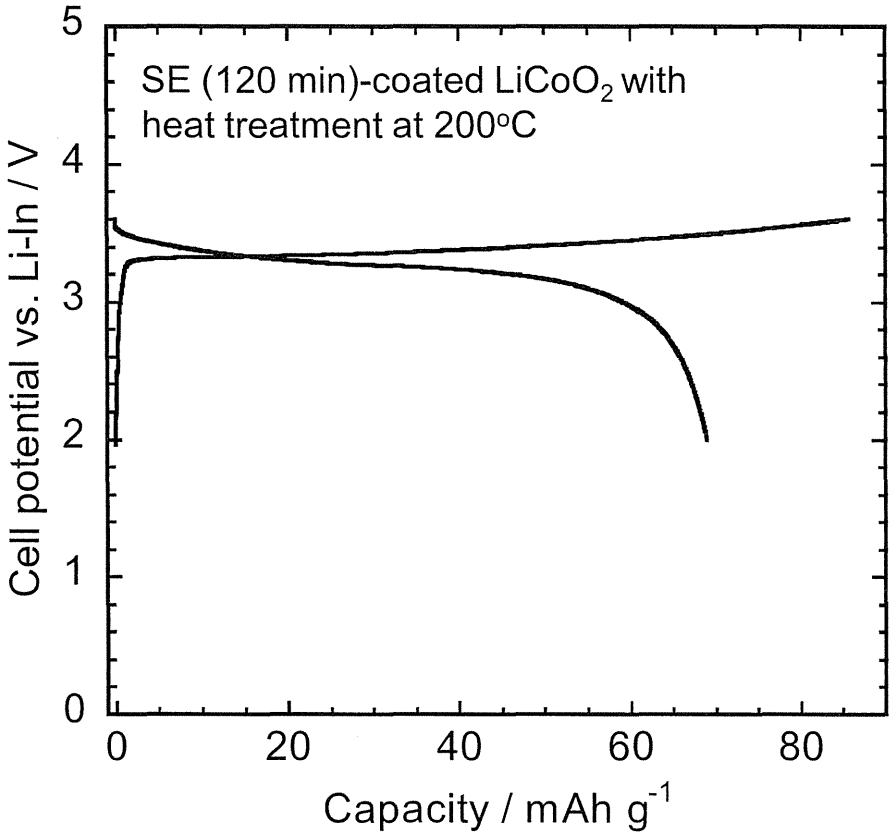

Figure 4-23 Charge-discharge curves of an all-solid-state cell based on SE (120 min)-coated $LiCoO_2$ with heat treatment at 200°C. The composite electrode was composed of SE-coated $LiCoO_2$, with no added SE particles.

capacity increased after heat treatment of the SE-coated $LiCoO_2$. The lithium-ion conductivity of the SE coated on the $LiNbO_3$-coated $LiCoO_2$ would likely be increased by heat treatment, as was observed in solid electrolyte films deposited on substrates, resulting in the observed increase in capacity.

Charge-discharge measurements were conducted at high temperature. Figure 4-24 shows the charge-discharge curves (a) and cycle performance (b) of the all-solid-state cell using SE (120 min)-coated $LiCoO_2$ without heat treatment at the current density of 0.26 mA cm^{-2} at 60°C. The measurement was conducted after charge-discharge measurement for 10 cycles at room temperature which is shown in Fig. 4-22. The cutoff voltage used was 3.8 V vs. Li–In. In this condition, charge-discharge cycles with a large capacity of 107 mAh g^{-1} can be achieved with no significant capacity fading.

As shown above, the solid electrolyte coating was effective in forming a lithium-ion conducting path to the $LiCoO_2$ particles in the electrode layer. However, the capacities of these all-solid-state cells remained smaller than the 95 mAh g^{-1} typical of all-solid-state cells containing composite electrodes composed of 70 wt% $LiNbO_3$-coated $LiCoO_2$ (with no solid electrolyte coating) and 30 wt% solid electrolyte particles mixing at a current density of 0.13 mA cm^{-2}.

To increase the lithium-ion conductivity in the composite electrodes, 10 wt% SE particles were added to the SE-coated $LiCoO_2$ particles. Figure 4-25 shows the impedance profiles of all-solid-state cells using composite electrodes consisting of uncoated, $LiNbO_3$-coated, or SE (20 min)-coated $LiCoO_2$ with 10 wt% solid electrolyte particles. The measurements were carried out after charging to 3.6 V vs. a Li–In electrode. The large semicircle observed in panel (a) of Fig. 4-25 is attributable to the interfacial resistance between $LiCoO_2$ and Li_2S–P_2S_5 solid electrolyte. The interfacial resistance of the all-solid-state cell based on uncoated $LiCoO_2$ in this study was ca. 850 Ω, which was higher

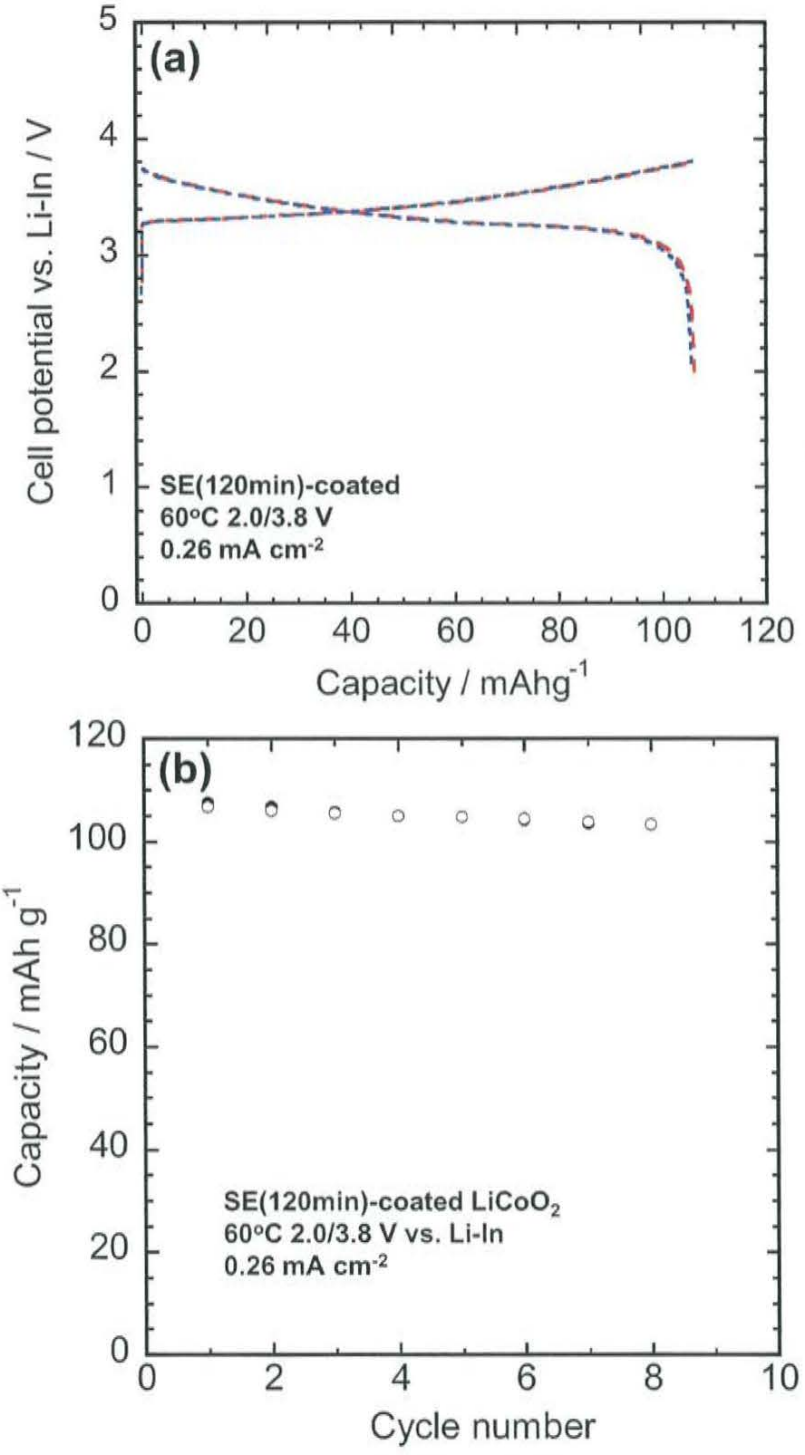

Figure 4-24 Charge-discharge curves (a) and cycle performance (b) of all-solid-state cell In/80Li_2S·20P_2S_5/SE(120min)-coated $LiCoO_2$ (without heat treatment) at the current density of 0.26 mA cm^{-2} at 60°C. The measurement was conducted after charge-discharge measurement for 10 cycles at room temperature which is shown in Figure 4-3-2-11.

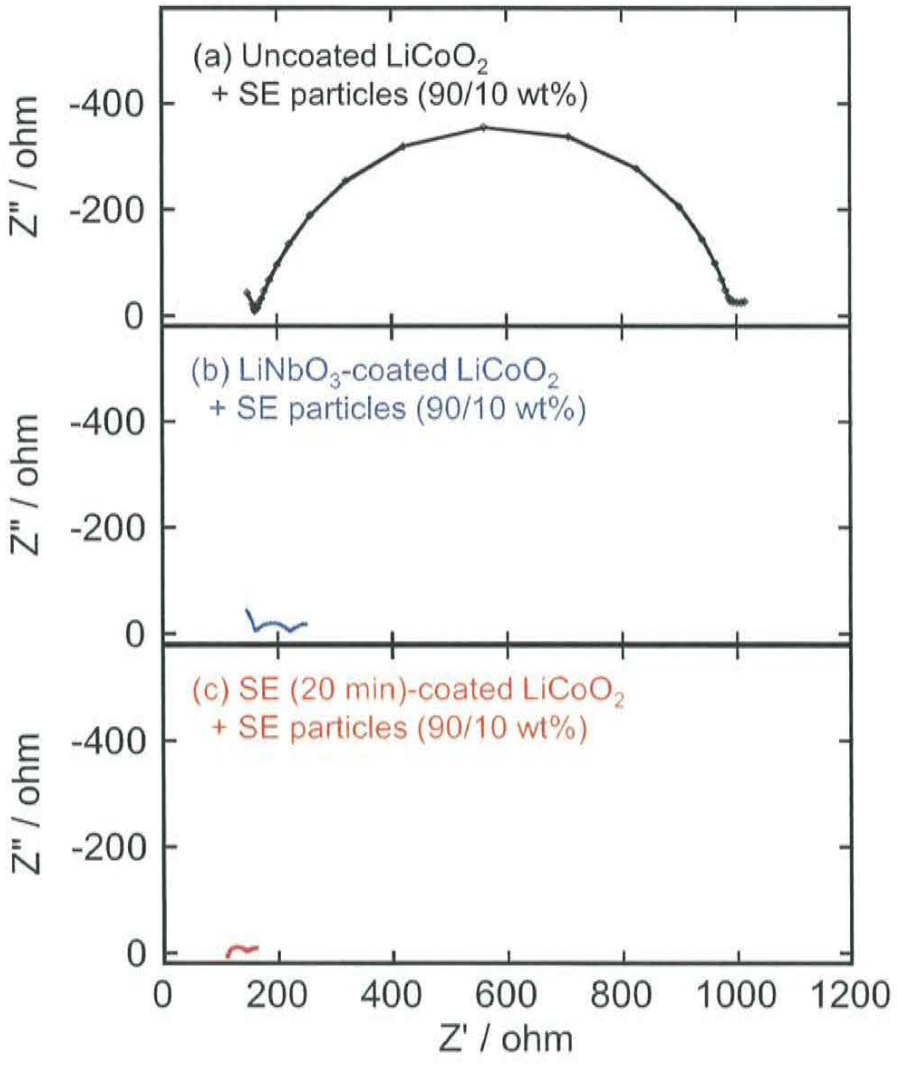

Figure 4-25 Impedance profiles of all-solid-state cells based on composite electrodes with 90 wt% $LiCoO_2$ and 10 wt% solid electrolyte particles after charging to 3.6 V vs. Li–In. The composite electrodes were prepared using (a) uncoated $LiCoO_2$, (b) $LiNbO_3$-coated $LiCoO_2$, and (c) SE (20 min)-coated $LiCoO_2$, which was coated with $LiNbO_3$ in advance.

than the results in Chapter 2 of ca. 300 Ω. This was because the contact area between the $LiCoO_2$ and the solid electrolyte particles in this section was smaller than that in Chapter 2; only 10 wt% solid electrolyte particles were added to the $LiCoO_2$ particles in this study, whereas 30 wt% SE particles were added in the previous studies. The all-solid-state cells based on $LiNbO_3$-coated and SE (20 min)-coated $LiCoO_2$ and shown in Figs. 4-25 (b) and (c) had a low interfacial resistance, although only 10 wt% SE particles were added to the $LiCoO_2$ particles. The $LiNbO_3$ coating on the $LiCoO_2$ decreased the interfacial resistance, and the additional SE (20 min) coating on the $LiCoO_2$ reduced the resistance further.

Figure 4-26 shows charge-discharge curves of all-solid-state cells based on composite electrodes composed of 90 wt% uncoated, $LiNbO_3$-coated, or SE (20 min)-coated $LiCoO_2$ and 10 wt% solid electrolyte particles, at a current density of 0.13 mA cm^{-2}. The capacities of the all-solid-state cells based on uncoated, $LiNbO_3$-coated, and SE (20 min)-coated $LiCoO_2$ particles were 20, 60, and 95 mAh g^{-1}, respectively. The capacities of the all-solid-state cells were increased by using cells combining 10 wt% solid electrolyte particles and a solid electrolyte coating, compared with the capacity of cells based on an solid electrolyte coating alone in the composite electrode, as shown in Fig. 4-21.

Figure 4-27 shows charge-discharge curves of all-solid-state cells based on (i) a conventional composite containing 70 wt% $LiNbO_3$-coated $LiCoO_2$ with no solid electrolyte coating and 30 wt% solid electrolyte particles, (ii) a composite containing 90 wt% SE (20 min)-coated $LiCoO_2$ and 10 wt% solid electrolyte particles, and (iii) a composite solely composed of $LiCoO_2$ with 240 min solid electrolyte coating. Each cell shows a similar capacity of about 80 to 92 mAh g^{-1}. The solid electrolyte coating was effective in decreasing the solid electrolyte ratio in the composite electrode, resulting in all-solid-state cells with an improved energy density. The energy density of the cells, normalized by the weight of the $LiCoO_2$ and Li_2S–P_2S_5 solid electrolyte composite electrode, was calculated. The

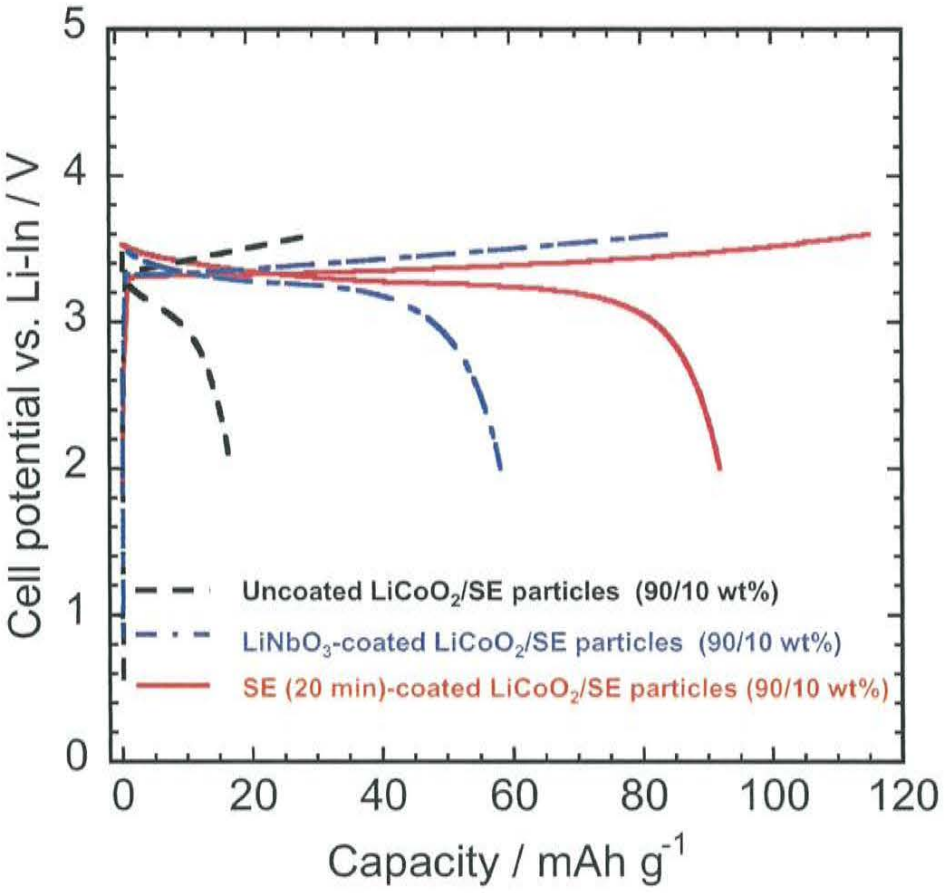

Figure 4-26 Initial charge-discharge cureves of all-solid-state cells based on composite electrodes consisting 90 wt% $LiCoO_2$ and 10 wt% solid electrolyte particles. The composite electrodes were prepared using (a) uncoated $LiCoO_2$, (b) $LiNbO_3$-coated $LiCoO_2$, and (c) SE (20 min)-coated $LiCoO_2$, which was coated with $LiNbO_3$ in advance.

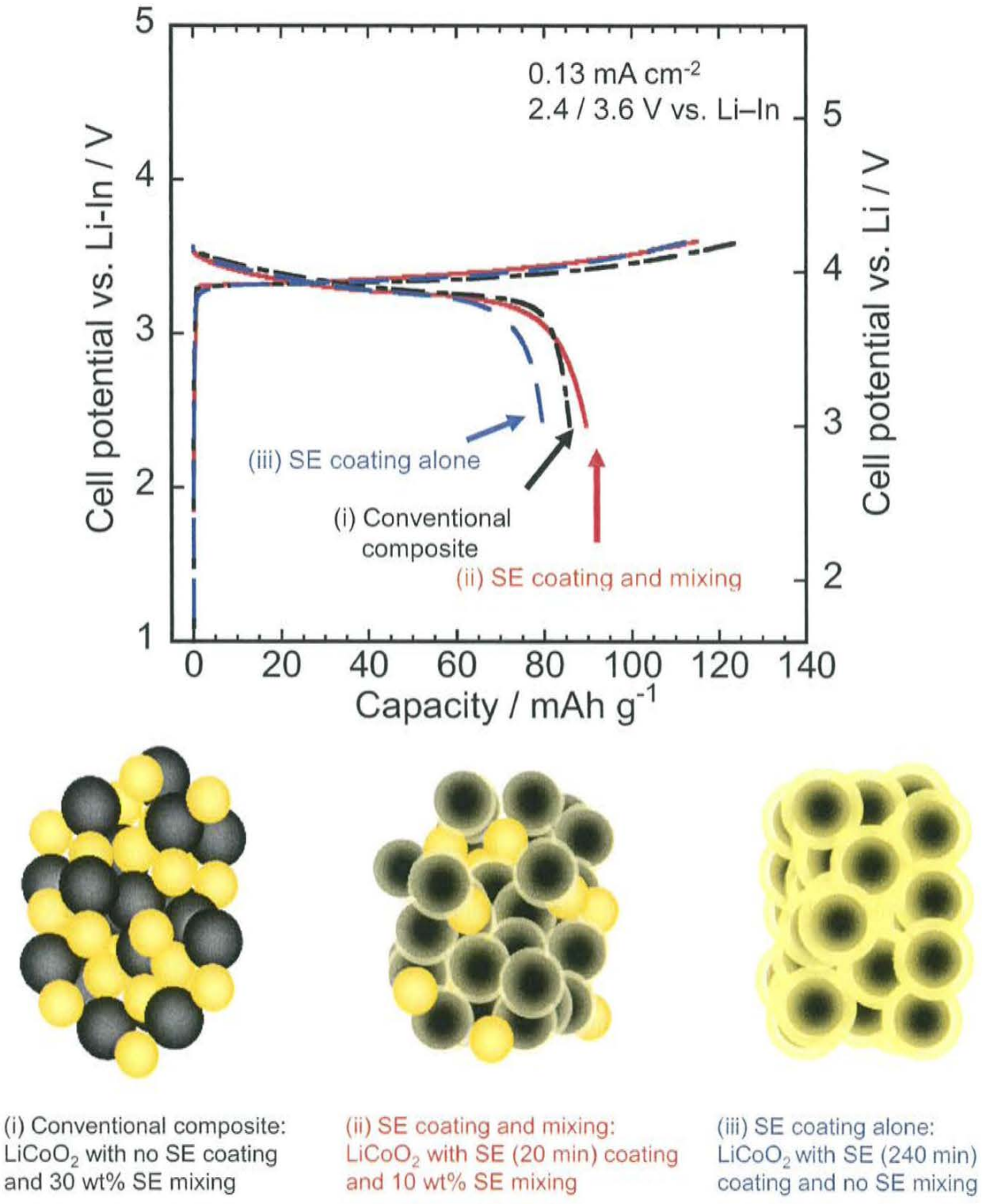

Figure 4-27 Charge-discharge curves of all-solid-state cells based on (i) a conventional composite containing 70 wt% $LiNbO_3$-coated $LiCoO_2$ with no solid electrolyte coating and 30 wt% solid electrolyte particles, (ii) a composite containing 90 wt% SE (20 min)-coated $LiCoO_2$ and 10 wt% solid electrolyte particles, and (iii) a composite solely composed of $LiCoO_2$ with 240 min solid electrolyte coating.

weight-normalized capacities of a composite containing 90 wt% SE (20 min)-coated $LiCoO_2$ and 10 wt% solid electrolyte particle and a composite solely composed of SE (240 min)-coated $LiCoO_2$ were 86 and 80 mAh g^{-1}, respectively. In contrast, that of a normal composite prepared using 70 wt% $LiNbO_3$-coated $LiCoO_2$ and 30 wt% solid electrolyte particles was 67 mAh g^{-1}. The capacity of the cells was thus increased by decreasing the amount of Li_2S–P_2S_5 solid electrolyte particles in the composite electrode.

4.3.2.2. Other electrodes

$LiCoO_2$ has been used in commercially available lithium-ion batteries. However, the cost of $LiCoO_2$ is very high; electrode active materials alternative to $LiCoO_2$ have been explored. The candidates are the layered $LiMO_2$ compounds, the spinels LiM_2O_4, the olivines $LiMPO_4$, and polyanions such as $Li_{3-x}V_2(PO_4)_3$ where M is a transition-metal atom. The layered lithium metal oxides such as $LiCoO_2$ [24-27], $LiNiO_2$ [27], $LiCo_{0.7}Ni_{0.3}O_2$ [28], $LiNi_{0.5}Mn_{0.5}O_2$ [29], $LiNi_{1/3}Co_{1/3}Mn_{1/3}O_2$ [30], the spinel $LiMn_2O_4$ [30, 31], and the olivine $LiCoPO_4$ [32] have been applied as positive active materials of all-solid-state lithium secondary batteries using sulfide-based solid electrolytes. Layered $LiNi_{1-x}Co_xO_2$ compounds are promising electrode materials. They form complete solid solutions for all the ranges of x. The introduction of increasing amounts of cobalt into the lattice of $LiNiO_2$ stabilizes the crystal lattice by suppressing "cation mixing", which is the tendency for Ni^{2+} to occupy the sites in the Li^+ layers [33]. Furthermore, volume change in the unite cell of $LiNi_{1-x}Co_xO_2$ (x = 0.2 - 0.4) during intercalation and de-intercalation is small. Aluminum substitution in $LiNiO_2$ also brings about advantages. It has been reported that a single hexagonal phase is preserved over the entire range of Li content in the $LiNi_{0.75}Al_{0.25}O_2$ [34, 35]. The $LiNi_{0.75}Al_{0.25}O_2$ is more stable compared to $LiNiO_2$ in the charged state. These features brought by cobalt and aluminum substitutions are beneficial in terms of long cycle life and

large capacity; the $LiNi_{1-x-y}Co_xAl_yO_2$ ($0.15 \leqq x \leqq 0.3$, $y \leqq 0.1$) has been reported as promising electrode materials [36, 37].

As the negative electrode materials graphite has been used in commercially available lithium-ion secondary batteries [38]. The theoretical capacity of graphite is about 370 mAh g^{-1}. $Li_4Ti_5O_{12}$ is known as "zero-stain material" during charging and discharging. The feature brings an excellent cycling ability. The all-solid-state cells using graphite and $Li_4Ti_5O_{12}$ have been reported to operate with good electrochemical performance [39, 40].

In this section, Li_2S–P_2S_5 solid electrolytes were coated on $Li_{1.05}Ni_{0.82}Co_{0.05}Al_{0.03}O_2$ (NCA), graphite, and $Li_4Ti_5O_{12}$ to confirm that the Li_2S–P_2S_5 coatings work as lithium-ion conducting path in the many electrodes.

Figure 4-28 shows the SEM and EDX-mapping (Ni, Co, A, P, and S) images of the SE-coated NCA which deposition time is 120 min. The SEM image shows that the particle size of the NCA particles is about 3 to 10 μm. The large change in morphology is not observed in the SEM image; the coating materials are not clearly visible on the NCA particles. Phosphorous and sulfur elements of Li_2S–P_2S_5 solid electrolyte film and nickel, cobalt, and aluminum elements of NCA particles are detected in the same area, indicating that the NCA particles are covered with Li_2S–P_2S_5 solid electrolyte film. The calculated weight ratio of Li_2S–P_2S_5 coating to $LiCoO_2$ particles is *ca.* 4 : 96. Figure 4-29 shows the charge-discharge curves of the all-solid-state cells using SE (120 min)-coated NCA. The composite electrode used was solely composed of the SE-coated NCA. The cell reversibly charged and discharged. The capacities for 1st charging and discharging are 115 and 62 mAh g^{-1}. The SE coating is effective in forming lithium-ion conducting path in NCA.

Figure 4-30 (a) shows the discharge-charge curves of the all-solid-state cell using SE (120 min)-coated graphite particles. Working electrode was solely composed of the SE (120 min)-coated graphite. As a counter electrode, Li–In was used in this case. The current

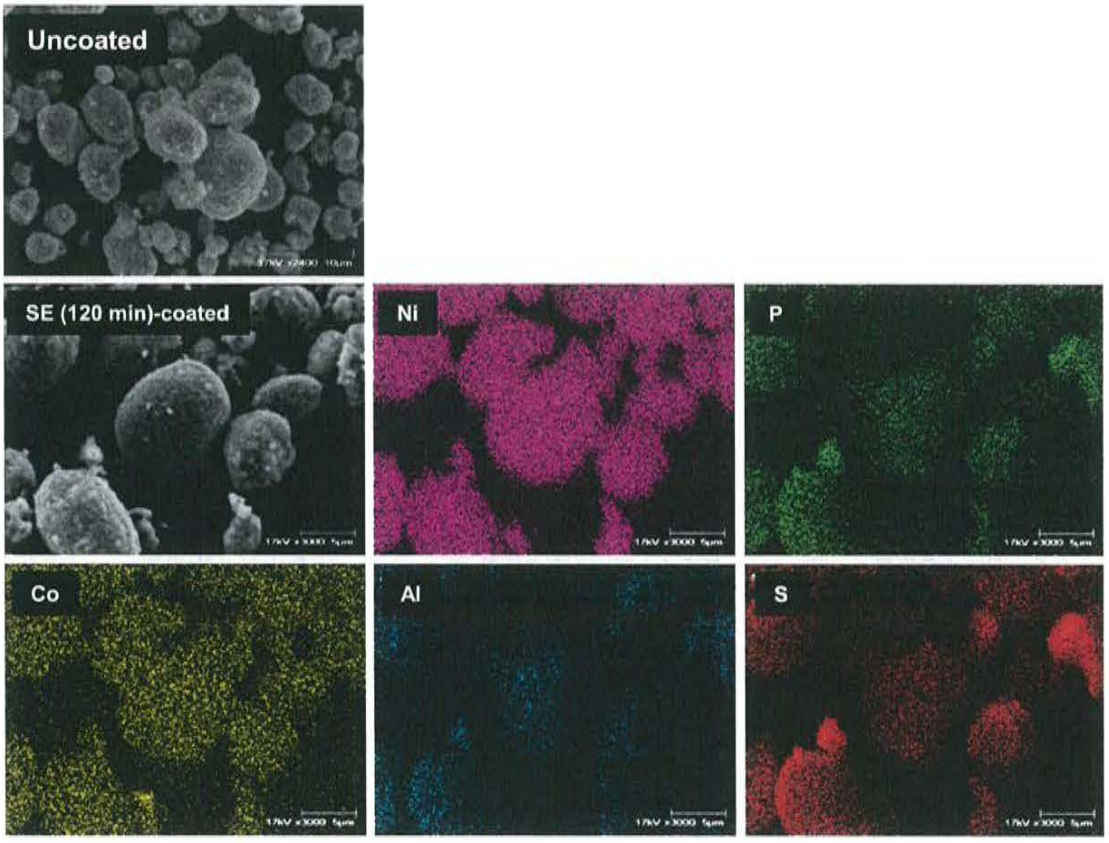

Figure 4-28 SEM image and EDX mapping images for Co element, P element, and S element of the Li_2S–P_2S_5 solid-electrolyte-coated $Li_{1.05}Ni_{0.82}Co_{0.15}Al_{0.03}O_2$ particles.

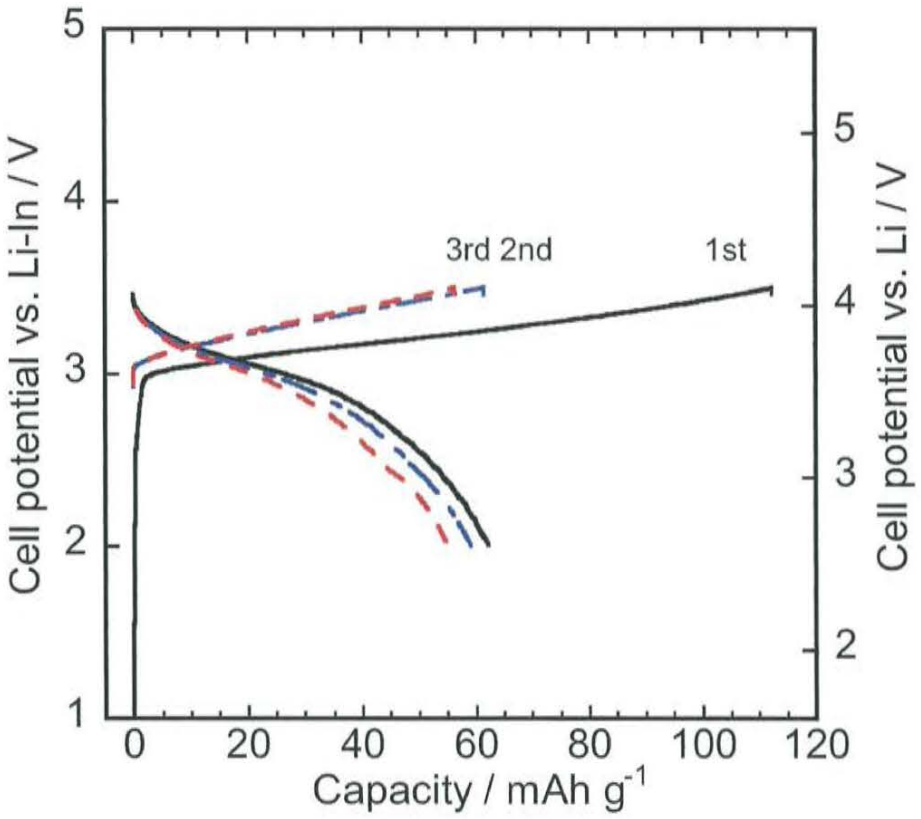

Figure 4-29 Charge-discharge curves (a) and cycle performance (b) of all-solid-state cell In/80Li_2S·20P_2S_5/SE(120min)-coated $Li_{1.05}Ni_{0.82}Co_{0.15}Al_{0.03}O_2$ at the current density of 0.13 mA cm^{-2} at 25°C.

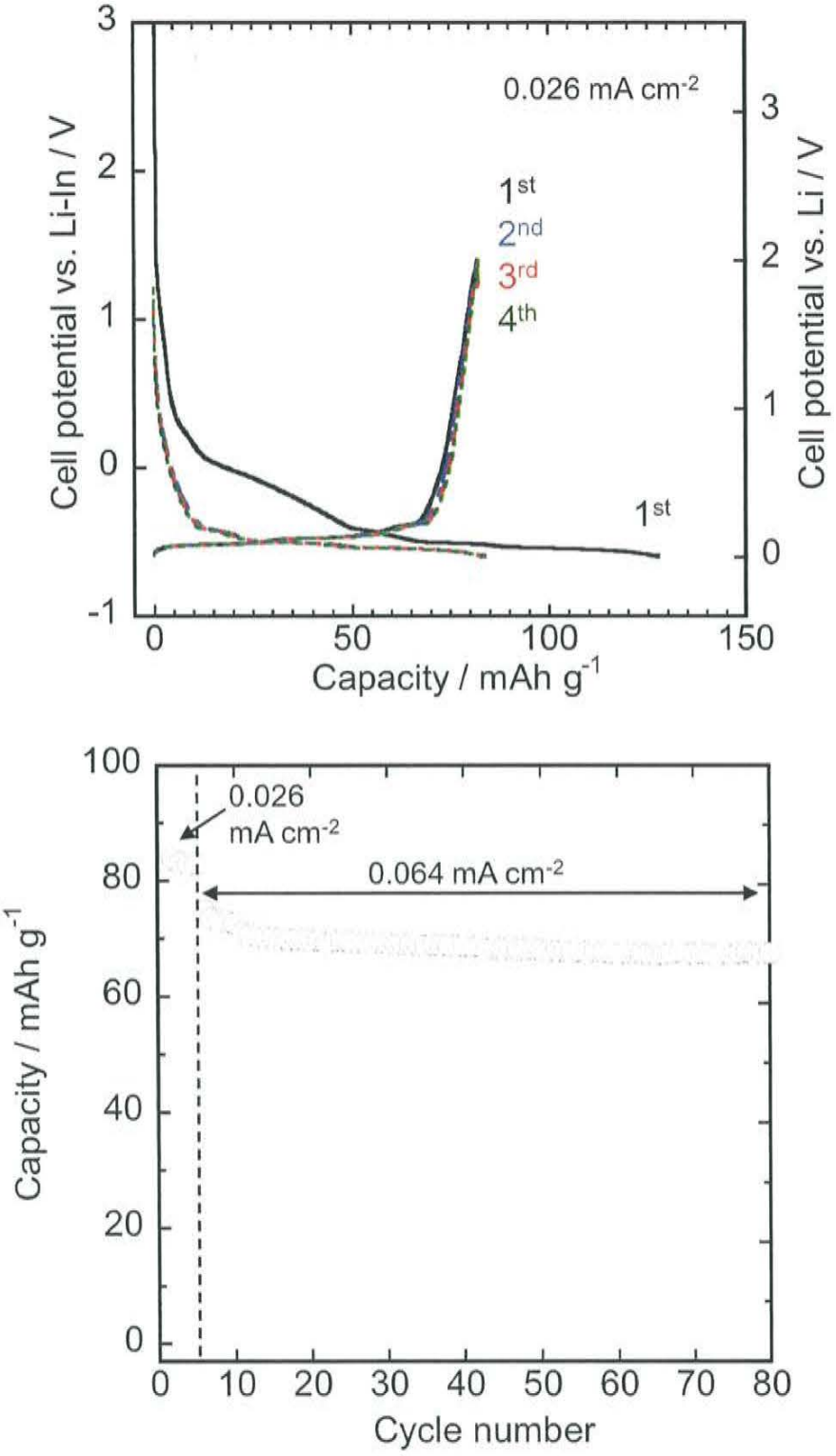

Figure 4-30 Discharge-charge curves (a) and cycle performance (b) of all-solid-state cell Li-In/ $80Li_2S{\cdot}20P_2S_5$/ SE (120 min)-coated graphite.

densities for initial 5 cycles and after 5th cycle are 0.026 and 0.064 mA cm^{-2}, respectively. The initial discharging capacity of all-solid-state cell is 128 mAh g^{-1} and the initial charging capacity is 82 mAh g^{-1}. The capacity is kept for 5 cycles. The discharge-charge capacities are slightly decreased from 82 to 73 mAh g^{-1} by increasing the current density to 0.064 mA cm^{-2}. The capacity of about 70 mAh g^{-1} is kept after 80 cycles as shown in Fig. 4-30 (b). The all-solid-state cell using SE (120 min)-coated graphite showed excellent cycle performance with the capacity of 70 mAh g^{-1}. The solid electrolyte coatings on graphite worked as a lithium-ion conducting path although the capacity was lower than the theoretical capacity of 370 mAh g^{-1}.

Figure 4-31 shows the discharge-charge curves of all-solid-state cells using the SE (120 min)-coated $Li_4Ti_5O_{12}$ at the current density of 0.013 mAh g^{-1} at 25°C. The reversible capacity is 49 mAh g^{-1}. The cell was difficult to operate under the current density of 0.064 mA cm^{-2} at room temperature. This would be due to the low electron conductivity of $Li_4Ti_5O_{12}$. It is considered that electrode materials with low electron conductivity are difficult to operate at the high current densities in the all-solid-state batteries using SE-coated electrode.

All-solid-state cells using SE-coated NCA, graphite, $Li_4Ti_5O_{12}$ particles operated in addition to that using $LiCoO_2$ particles.

4.3.3. Bulk type all-solid-state batteries based on thin solid electrolyte layer

In this section, bulk-type all-solid-state lithium secondary batteries based on thin solid electrolyte layer were fabricated; their morphology and electrochemical performance were investigated.

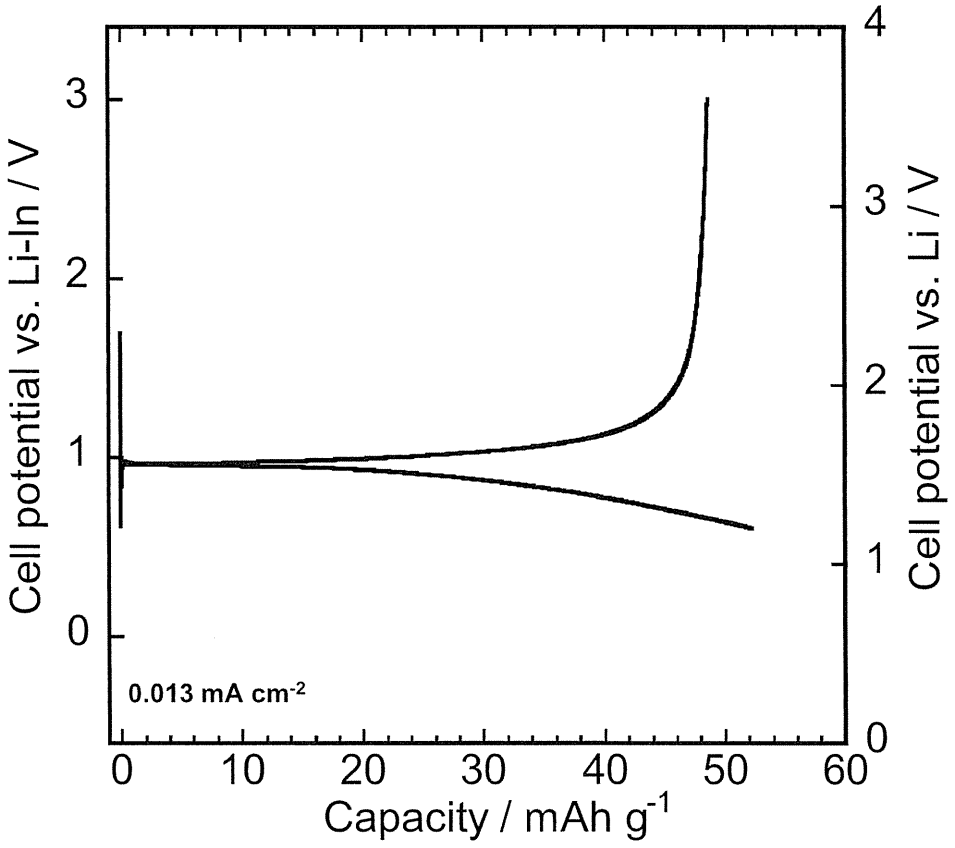

Figure 4-31 Discharge-charge curves of all-solid-state cell Li–In/ $80Li_2S{\cdot}20P_2S_5$/ SE (120 min)-coated $Li_4Ti_5O_{12}$ at the current density of 0.013 mA cm^{-2} at 25°C.

(i) Morphology of bulk type all-solid-state batteries based on thin solid electrolyte layer

The all-solid-state cells based on thin solid electrolyte layer were fabricated using $80Li_2S{\cdot}20P_2S_5$ solid electrolyte film prepared by PLD. Figure 4-32 shows SEM images and EDX elemental mappings of the surfaces of pelletized composite electrodes without and with $80Li_2S{\cdot}20P_2S_5$ solid electrolyte film on the composite electrodes. These composite electrode pellets contain 70 wt% $LiCoO_2$ and 30 wt% $80Li_2S{\cdot}20P_2S_5$ solid electrolyte particles. Those two pellets present basically plane surface, although a lot of voids are visible. At the surface of the pellet of the composite without the solid electrolyte coating shown in Fig. 4-32 (a), Co rich domain derived from $LiCoO_2$ particles and P and S rich domain derived from $80Li_2S{\cdot}20P_2S_5$ solid electrolyte particles are observed. In contrast, the Co rich domain is not observed at the surface of the pellet of the composite with solid electrolyte coating shown in Fig. 4-32 (b); the surface of the pellets is covered with the solid electrolyte film. In addition, the voids are dramatically reduced by solid electrolyte coating. Figure 4-33 shows the SEM images and EDX mappings for P, S, Co, and Fe of cross section of composite electrode pellet with the $80Li_2S{\cdot}20P_2S_5$ solid electrolyte PLD film. The composite electrode layer and Li_2S–P_2S_5 solid electrolyte film layer are observed on stainless steel current collector layer. The thickness of the composite electrode is approximately 50 μm; that of $80Li_2S{\cdot}20P_2S_5$ is 3 to 4 μm. The solid electrolyte film is uniformly formed on the composite electrode layer.

(ii) Charge-discharge measurements of bulk type all-solid-state batteries based on thin solid electrolyte layer

An all-solid-state cell was constructed by attaching an indium foil as a counter electrode on the bilayer pellet consisting of the electrode composite layer and the solid electrolyte film. The current collectors for both working and counter electrode were

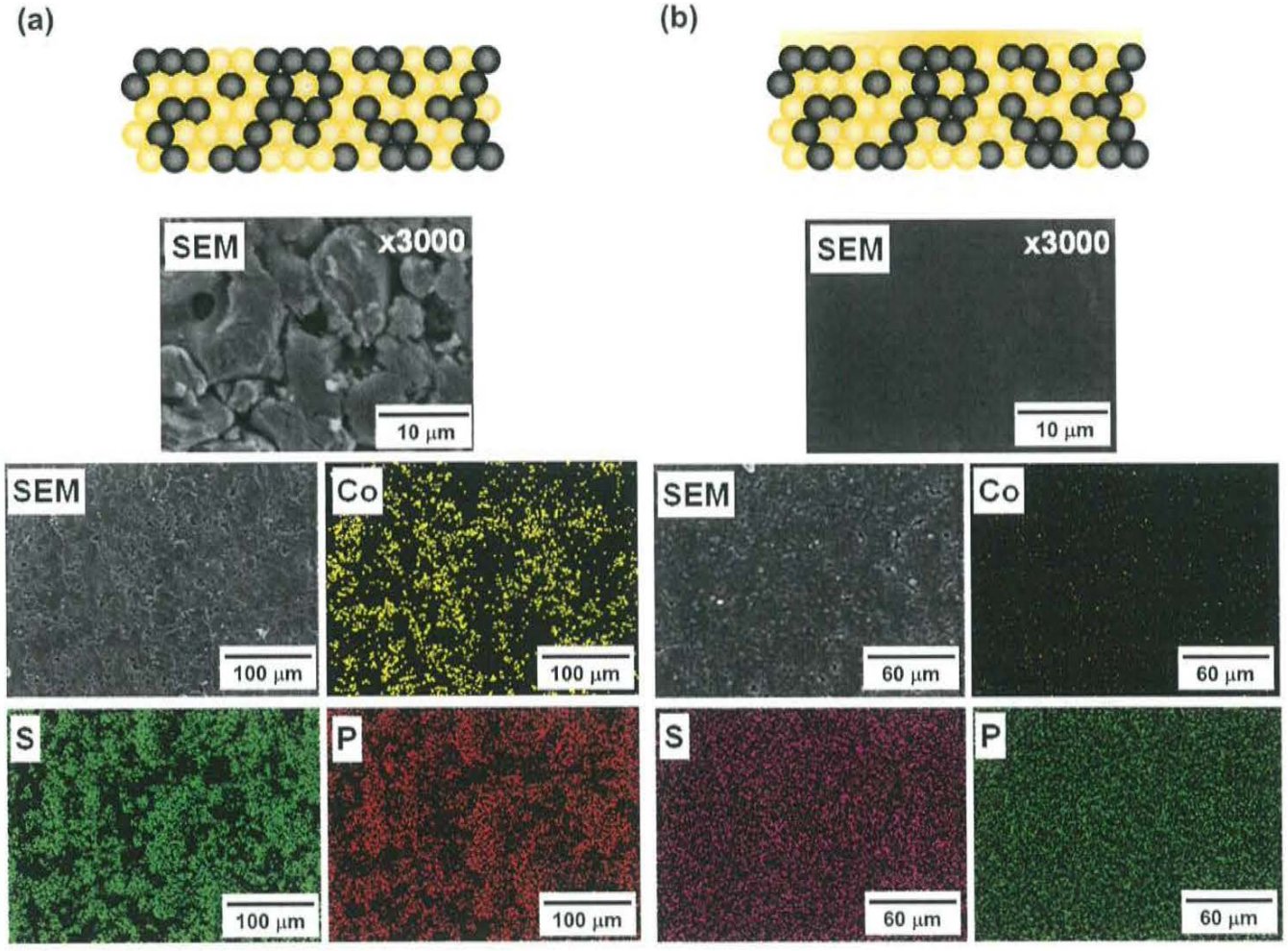

Figure 4-32 SEM images and EDX elemental mappings for Co, S, and P elements of the surface of pelletized composite electrodes without $80Li_2S{\cdot}20P_2S_5$ (mol%) solid electrolyte film (left) and with $80Li_2S{\cdot}20P_2S_5$ (mol%) solid electrolyte film on the composite electrodes (right).

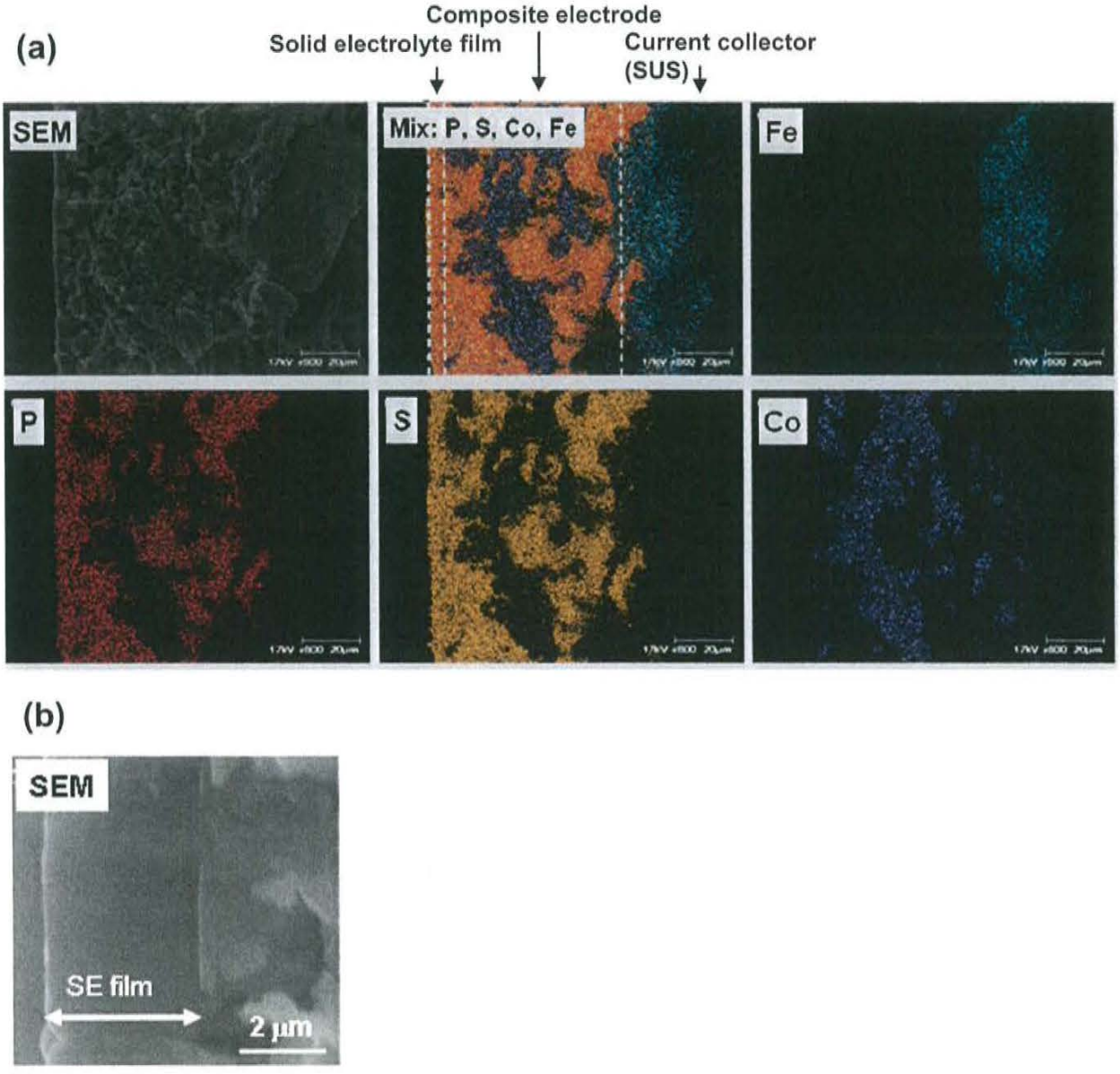

Figure 4-33 (a) SEM image and EDX mappings for P, S, Co, and Fe of cross section of composite electrode pellet with $80Li_2S{\cdot}20P_2S_5$ (mol%) solid electrolyte PLD film. Magnified SEM image of $80Li_2S{\cdot}20P_2S_5$ film observed near surface was shown in panel b.

stainless steel. Figure 4-34 shows the charge-discharge curves of a bulk-type all-solid-state cell using the solid electrolyte layer with micrometer thickness. The current densities for charging and discharging were 0.25 mA cm^{-2}. The all-solid-state cell was charged and discharged reversibly, and the reversible capacity is 93 mAh g^{-1}. The thickness of solid electrolyte layer of conventional all-solid-state cells is approximately 500 μm. The thickness was reduced less than 1 / 100 in the all-solid-state cell as shown here. This is the first report on the charge-discharge measurements for bulk type all-solid-state cells using a thin electrolyte layer with a few μm thickness.

The results obtained here are important in the development of all-solid-state batteries, although the details of the all-solid-state cells using a thin solid electrolyte layer were not cleared at the present stage. The reduced thickness brings about the low resistance of the solid electrolyte layer, which leads to the enhancement of rate capability and energy density of the cells.

4.4. Summary

This chapter reported preparation and application of highly conducting solid electrolyte thin films using pulsed laser deposition (PLD). As the solid electrolyte thin films, Li_2S–P_2S_5 and Li_2S–GeS_2 system were selected because these sulfide-based glass systems exhibited high conductivity of lithium ion. By using the prepared sulfide-based solid electrolyte thin films, two kinds of new all-solid-state batteries were constructed. One is the all-solid-state cells using solid-electrolyte (SE)-coated electrode particles shown in Fig. 1-2 (b) at Chapter 1 and the other is bulk-type all-solid-state cells with solid electrolyte thin layer also shown in Fig. 1-2 (c).

Amorphous Li_2S–P_2S_5 solid electrolyte thin films were prepared using PLD at room temperature. It was found that ambient Ar gas pressure during deposition influences the

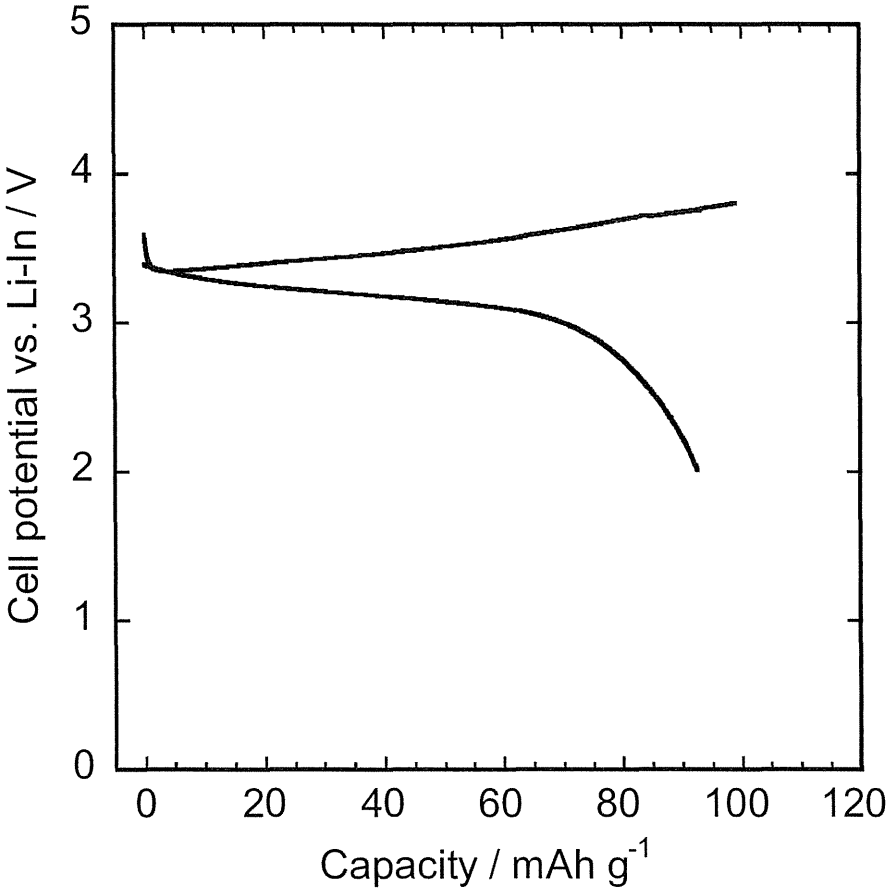

Figure 4-34 Charge-discharge curves of bulk-type all-solid-state cell with micrometer thick solid electrolyte layer. The current densities for charging and discharging were 0.25 mA cm^{-2}.

chemical composition and local structure of the films. The chemical composition and local structure of the $80Li_2S{\cdot}20P_2S_5$ thin film prepared under 5 Pa were almost identical to those of the $80Li_2S{\cdot}20P_2S_5$ glass prepared by mechanical milling. Ionic conductivities of as-deposited Li_2S–P_2S_5 solid electrolyte films with high lithium-ion contents were approximately 10^{-4} S cm^{-1}. The conductivities were increased by heat treatment.

New electrode-electrolyte composite materials named SE-coated $LiCoO_2$ were prepared by coating a highly conductive Li_2S–P_2S_5 solid electrolyte onto $LiCoO_2$ electrode particles using PLD. All-solid-state cells based on a composite electrode composed entirely of SE-coated $LiCoO_2$ were fabricated, and their performance was investigated. In all-solid-state cells based on SE-coated $LiCoO_2$ particles, the $LiCoO_2$ particles were closely packed in the composite electrode, and a Li_2S–P_2S_5 solid electrolyte coating occupied the interface between the $LiCoO_2$ particles.

All-solid-state cells containing SE-coated $LiCoO_2$ had a larger capacity than cells with no solid electrolyte coating, and the charge-discharge capacity increased with increasing coating time. All-solid-state cells using $LiCoO_2$ with thick solid electrolyte coatings, grown over 240 min, had a capacity of 80 mAh g^{-1}, without any addition of Li_2S–P_2S_5 solid electrolyte particles to the composite electrode. The capacity of the all-solid-state cell increased further after increasing the conductivity of the Li_2S–P_2S_5 solid electrolyte coating by heat treatment at 200°C. Furthermore, an all-solid-state cell based on a composite electrode using both a solid electrolyte coating and added solid electrolyte particles was fabricated, and the capacity of the resulting all-solid-state cell increased to 95 mAh g^{-1}. The Li_2S–P_2S_5 solid electrolyte on the $LiCoO_2$ particles formed a lithium-ion conducting path to the $LiCoO_2$ particles in the composite electrode. The solid electrolyte coating was also effective in other electrode particles such as $Li_{1.05}Ni_{0.82}Co_{0.15}Al_{0.03}O_2$, graphite, and $Li_4Ti_5O_{12}$. The coating of a highly conductive solid electrolyte on electrode particles is a promising

technique to form an effective electrode-electrolyte interface and a lithium-ion conducting path in the composite, which should both contribute to the development of advanced all-solid-state lithium secondary batteries.

Bulk-type all-solid-state lithium secondary batteries based on the solid electrolyte layer with micrometer thickness were successfully fabricated. The thickness of the electrode composite was approximately 50 μm; that of $80Li_2S \cdot 20P_2S_5$ layer was 3 μm. The all-solid-state cell was charged and discharged reversibly, and the reversible capacity was 93 mAh g^{-1}. The thickness of solid electrolyte layer of conventional all-solid-state cells is approximately 500 μm. The thickness was reduced less than 1 / 100 in the all-solid-state cell. The reduced thickness of the solid electrolyte layer brings about the low resistance of the solid electrolyte layer, which leads to the enhancement of rate capability and energy density of the cells. Although the details of the all-solid-state cells using a thin solid electrolyte layer were not clear at the present stage, bulk-type all-solid-state cells using a solid electrolyte layer with several μm thickness were charged and discharged, suggesting that all-solid-state batteries have a strong potential as an alternative to conventional batteries.

4.5. References

[1] N. Ohta, K. Takada, L. Zhang, R. Ma, M. Osada, and T. Sasaki, *Adv. Mater.*, **18** (2006) 2226.

[2] N. Ohta, K. Takada, I. Sakaguchi, L. Zhang, R. Ma, K. Fukuda, M. Osada, and T. Sasaki, *Electrochem. Commun.*, **9** (2007) 1486.

[3] K. Takada, N. Ohta, L. Zhang, K. Fukuda, I. Sakaguchi, R. Ma, M. Osada, and T. Sasaki, *Solid State Ionics*, **179** (2008) 1333.

[4] F. Mizuno, A. Hayashi, K. Tadanaga, and M. Tatsumisago, *J. Power Sources*, **146** (2005) 711.

[5] N. Aotani, K. Iwamoto, K. Takada, and S. Kondo, *Solid State Ionics*, **68** [1-2] (1994) 35.

[6] R. Kanno and M. Murayama, *J. Electrochem. Soc.*, **148** [7] (2001) A742.

[7] A. Hayashi, S. Hama, T. Minami, and M. Tatsumisago, *Electrochem. Commun.*, **5** [2] (2003) 111.

[8] F. Mizuno, A. Hayashi, K. Tadanaga, and M. Tatsumisago, *Adv. Mater.*, **17** [7] (2005) 918.

[9] A. Hayashi, S. Hama, F. Mizuno, K. Tadanaga, T. Minami and M. Tatsumisago, *Solid State Ionics*, **175** [1-4] (2004) 683.

[10] Y. Iriyama, M. Inaba, T. Abe, and Z. Ogumi, *J. Power Sources*, **94** [2] (2001) 175.

[11] P.J. Bouwman, B.A. Boukamp, H.J.M. Bouwmeester, and P.H.L. Notten, *J. Electrochem.Soc.*, **149** [6] (2002) A699.

[12] C. Julien, E.H. Poniatowski, M.A.C. Lopez, L.E. Alarcon, and J.J. Jarquin, *Mat. Sci. Eng. B*, **72** [1] (2000) 36.

[13] S. Zhao, Z. Fu, and Q. Qin, *Thin Solid Films,* **415** [1-2] (2002) 108.

[14] J. Kawamura, N. Kuwata, K. Toribami, N. Sata, O. Kamishima, and T. Hattori, *Solid State Ionic,* **175** [1-4] (2004) 273.

[15] N. Ohta, K. Takada, M. Osada, L. Zhang, T. Sasaki, and M. Watanabe, *J. Power Sources*,

146 [1-2] (2005) 707.

[16] N. Ota, N. Okuda, K. Emura, and A. Yamakawa, *SEI Technical Review*, **61** (2006) 41.

[17] M. Tachez, J.P. Malugani, R. Mercier, and G. Robert, *Solid State Ionics*, **14** [3] (1984) 181.

[18] T. Ohtomo, F. Mizuno, A. Hayashi, K. Tadanaga, and M. Tatsumisago, *Solid State Ionics,* **176** [31-34] (2005) 2349.

[19] F. Mizuno, A. Hayashi, K. Tadanaga, and M. Tatsumisago, *Solid State Ionics*, **177** [26-32] (2006) 2721.

[20] A. Hayashi, S. Hama, T. Minami, and M. Tatsumisago, *Electrochem. Commun.*, **5** [2] (2003) 111.

[21] X.-H. Yu, J.B. Bates, G.E. Jellison Jr., and F.X. Hart, *J. Elcectrochem. Soc.*, **144** [2] (1997) 524.

[22] F. Mizuno, A. Hayashi, K. Tadanaga, and M. Tatsumisago, *Solid State Ionics*, **177** (2006) 2731.

[23] A. Pradel, T. Pagnier, and M. Ribes, *Solid State Ionics*, **17** (1985) 147.

[24] K. Iwamoto, N. Aotani, K. Takada and S. Kondo, *Solid State Ionics*, **79** (1995) 288.

[25] K. Takada, N. Aotani, K. Iwamoto and S. Kondo, *Solid State Ionics*, **86-88** (1996) 877.

[26] K. Takada, T. Inada, A. Kajiyama, H. Sasaki, S. Kondo, M. Watanabe, M. Murayama and R. Kanno, *Solid State Ionics*, **158** (2003) 269.

[27] K. Takada, N. Aotani, K. Iwamoto and S. Kondo, *Solid State Ionics*, **79** (1995) 284.

[28] N. Machida, H. Maeda, H. Peng and T. Shigematsu, *J. Electrochem. Soc.*, **149** (2002) A688.

[29] F. Mizuno, A. Hayashi, K. Tadanaga, T. Minami and M. Tatsumisago, *J. Power Sources*, **124** (2003) 170.

[30] H. Kitaura, A. Hayashi, K. Tadanaga, and M. Tatsumisago, *Electrochim. Acta,* **55** (2010)

8821.

[31] H. Kitaura, A. Hayashi, K. Tadanaga, and M. Tatsumisago, *J. Electrochem. Soc.* **157** (2010) A407.

[32] K. Tadanaga, F. Mizuno, A. Hayashi, T. Minami and M. Tatsumisago, *Electrochemistry*, **71** (2003) 1192.

[33] C. Delmas, M. Menetrier, L. Croguennec, I. Saadoune, A. Rougier, C. Pouillerie, G. Prado, M. Grune, and L. Fournes, *Electrochim. Acta*, **45** (1999) 243.

[34] T. Ohzuku, A. Ueda, and M. Kouguchi, *J. Electrochem. Soc.* **142** (1995) 4033.

[35] T. Ohzuku, T. Yanagawa, M. Kouguchi, and A. Ueda, *J. Power Sources*, **68** (1997) 131.

[36] S. Madhavi, G.V. Subba Rao, B.V.R. Chowdari, and S.F.Y. Li, *J. Power Sources,* **93** (2001) 156.

[37] M. Broussely, Ph. Blanchard, Ph. Biensan, J.P. Planchat, K. Nechev, and R.J. Staniewicz, *J. Power Sources*, **119–121** (2003) 859.

[38] M. Endo, C. Kim, K. Nishimura, T. Fujino, and K. Miyashita, *Carbon*, **38** (2000) 183.

[39] Y. Seino, K. Takada, B.-C. Kim, L. Zhang, N. Ohta, H. Wada, M. Osada, and T. Sasaki, *Solid State Ionics*, **176** [31-34] (2005) 2389.

[40] H. Kitaura, A. Hayashi, K. Tadanaga, and M. Tatsumisago, *J. Mater. Res.* **25** [8] (2010) 1548.

5. General conclusions

In this thesis, oxide-based and sulfide-based solid electrolyte films were prepared using liquid-phase and vapor-phase processes; the prepared films are applied to the construction of electrode-electrolyte interface to improve electrochemical performance of all-solid-state lithium secondary batteries. The interfacial properties between electrode and solid electrolyte were investigated using electrochemical impedance measurements and TEM–EDX observations. The battery performance was improved by interfacial modification using oxide-based solid electrolyte film. Furthermore, two types of new all-solid-state batteries using highly conducting sulfide electrolyte films prepared using the vapor-phase process were developed.

The following results and considerations were obtained.

1. Electrochemical impedance spectroscopy measurements revealed that the cells after the initial charge process had a large resistance component at the interface between $LiCoO_2$ and Li_2S–P_2S_5 solid electrolyte. The large resistance was the main cause of the low rate performance of all-solid-state cells using $LiCoO_2$ and Li_2S–P_2S_5 solid electrolytes.

2. The interfacial resistance between $LiCoO_2$ and Li_2S–P_2S_5 solid electrolyte was decreased by interfacial modification. As a technique for the interfacial modification, the coatings of oxide-based solid electrolyte film on electrode particles by sol-gel and PLD techniques were effective. It has been clarified that the lithium-ion conductivity of coating materials on the $LiCoO_2$ particles is important for an interfacial resistance of the all-solid-state lithium secondary batteries. Coating materials with higher lithium-ion conductivity were more effective in decreasing the interfacial resistance. The

all-solid-state cells using $LiCoO_2$ particles with $50Li_4SiO_4 \cdot 50Li_3PO_4$ solid electrolyte coating showed the lowest interfacial resistance of 48 Ω and the highest rate performance among the oxide solid electrolyte coatings studied in this thesis. Nevertheless, insulative SiO_2 coatings were also effective in decreasing the interfacial resistance when coating amounts were small. The activation energies for lithium-ion conduction at $LiCoO_2$ / $80Li_2S \cdot 20P_2S_5$ solid electrolyte interface were unaffected by the coatings; they were about 60 kJ mol^{-1} with or without Li_2SiO_3 coatings. Therefore, an increase of the pre-exponential factor for ion conduction in the Arrhenius equation is main cause of the decreased interfacial resistance.

3. The charge-discharge performance of the all-solid-state cells with Li_2S–P_2S_5 solid electrolytes was improved by the interfacial modifications. The decrease of the interfacial resistance brought about a higher voltage plateau in the discharge process, larger discharge capacity, and longer cycle performance. In particular, improvement of rate capability due to decreasing the interfacial resistance was significant; the capacity of the cells using coated $LiCoO_2$ was larger than that of the cells using uncoated $LiCoO_2$ at the current densities from 0.064 to 6.4 mA cm^{-2}. The all-solid-state cell using Li_2SiO_3-coated $LiCoO_2$ operated under a high current density of 6.4 mA cm^{-2} with a capacity of 45 mAh g^{-1}. The capacity of the all-solid-state cells charging to a high cut off voltage of 4.0 V vs. Li–In, which corresponds to 4.6 V vs. Li, increased from 90 to 130 mAh g^{-1} by the interfacial modification. The all-solid-state cells functioned even at the low temperature of -30°C. Moreover, the all-solid-state cell using Li_2SiO_3-coated $LiCoO_2$ was charged and discharged under a significantly high current density of 40 mA cm^{-2} at 100°C. The interfacial modification using oxide-based solid electrolytes showed many advantages as (i) suppression of the increase in interfacial resistance, (ii) large capacity, (iii) high voltage

discharging, and (iv) long cycle life. It has been revealed that the formation of a favorable electrode-electrolyte interface with small resistance is important to obtain superior charge-discharge properties of the solid-state batteries; the interfacial modification using oxide-based solid electrolyte between positive electrode and Li_2S–P_2S_5 solid electrolyte is effective in developing all-solid-state batteries with high performance.

4. An interfacial layer was formed at the interface between $LiCoO_2$ electrode with no coatings and Li_2S–P_2S_5 solid electrolyte after the initial charge of battery. Furthermore, mutual diffusions of Co, P, and S at the interface between $LiCoO_2$ and Li_2S–P_2S_5 were observed. These results reflect that side reactions occurred at the electrode-electrolyte interface. The side reaction indicated the degradation of the $LiCoO_2$ electrode and Li_2S–P_2S_5 solid electrolyte near the interface. The large interfacial resistance observed at the interface between $LiCoO_2$ and Li_2S–P_2S_5 results from the formation of the high-resistance interface between $LiCoO_2$ and sulfide electrolyte. The mutual diffusion and the formation of the interfacial layer were suppressed using $LiCoO_2$ particles coated with Li_2SiO_3 thin film. The Li_2SiO_3 coatings acted as a buffer layer to suppress the side reaction at the interface. In conclusion, the suppression of the interfacial layers is the main reason for the reduction of interfacial resistance between $LiCoO_2$ electrode and Li_2S–P_2S_5 solid electrolyte.

5. Highly lithium-ion conductive Li_2S–P_2S_5 thin films were prepared using pulsed laser deposition at room temperature. The ambient Ar gas pressure during deposition strongly affected the chemical compositions and local structures of the films. The chemical composition and the local structure of the $80Li_2S{\cdot}20P_2S_5$ thin film prepared under 5 Pa were in good agreement with those of the highly lithium-ion conducting $80Li_2S{\cdot}20P_2S_5$

glass powder prepared by mechanical milling. The ionic conductivity at 25°C and the activation energy for conduction of the as-deposited $80Li_2S \cdot 20P_2S_5$ thin films were 7.9×10^{-5} S cm^{-1} and 43 kJ mol^{-1}, respectively. The ionic conductivity of the $80Li_2S \cdot 20P_2S_5$ thin film was increased up to 2.8×10^{-4} S cm^{-1} by a heat treatment at 200°C.

6. New electrode-electrolyte composite materials named "solid-electrolyte (SE)-coated electrode materials" were prepared by coating a highly conductive Li_2S–P_2S_5 solid electrolyte onto electrode particles using PLD. All-solid-state cells based on a composite electrode composed of only SE-coated $LiCoO_2$ were fabricated. In all-solid-state cells based on SE-coated $LiCoO_2$ particles, the $LiCoO_2$ particles were closely packed in the composite electrode, and a Li_2S–P_2S_5 solid electrolyte coating occupied voids between the $LiCoO_2$ particles. All-solid-state cells with SE-coated $LiCoO_2$ had a larger capacity than the cells with no solid electrolyte coatings, and the charge-discharge capacity increased with increasing coating time. All-solid-state cells using $LiCoO_2$ with thick solid electrolyte coatings, grown over 240 min PLD, had a capacity of 80 mAh g^{-1}, without any addition of Li_2S–P_2S_5 solid electrolyte particles to the composite electrode. The capacity of the all-solid-state cell increased further after increasing the conductivity of the Li_2S–P_2S_5 solid electrolyte coating by heat treatment at 200°C. Furthermore, an all-solid-state cell based on a composite electrode using both a solid electrolyte coating and added solid electrolyte particles was fabricated, and the capacity of the resulting all-solid-state cell increased up to 95 mAh g^{-1}. The Li_2S–P_2S_5 solid electrolyte on the $LiCoO_2$ particles formed lithium-ion conducting paths to the $LiCoO_2$ particles in the composite electrode. The coatings of a highly conductive solid electrolyte on electrode particles are a promising technique to form an effective electrode-electrolyte interface and lithium-ion conducting paths in the composite, which should both contribute to the development of advanced

all-solid-state lithium secondary batteries.

7. Bulk-type all-solid-state lithium secondary batteries based on the solid electrolyte layer with micrometer thickness were successfully fabricated. The thickness of the electrode composite was approximately 50 μm; that of solid electrolyte layer was 3 μm. The reduced thickness was less than 1 / 100 of that in the conventional all-solid-state cell. The all-solid-state cell using solid electrolyte layer with micrometer thickness was able to charge and discharge reversibly; the reversible capacity was 93 mAh g^{-1}. The reduced thickness of the solid electrolyte layer brings about the low resistance of the solid electrolyte layer, which leads to the enhancement of rate capability and energy density of the cells. Although the details have not been clear at the present stage, bulk-type all-solid-state cells using a solid electrolyte layer with a few μm thickness were charged and discharged, suggesting that all-solid-state batteries have a strong potential as an alternative to conventional batteries.

The solid electrolyte films are useful not only for the thin film batteries but also for bulk-type batteries; the performance of bulk-type all-solid-state batteries is improved by the application of solid electrolyte films. The construction of electrode-electrolyte interface is difficult in bulk-type all-solid-state batteries, but the favorable electrode-electrolyte interface using solid electrolyte film is constructed by coating solid electrolyte on electrode particles. A disadvantage of the difficulty of the control of electrode-electrolyte interface should be overcome using the solid electrolyte film. Furthermore, an advantage taken by "all-solid-state" should be used by the application of solid electrolyte films as the bulk-type all-solid-state batteries based on solid electrolyte layer with micrometer thickness.

Acknowledgements

First and foremost, I would like to express my deepest gratitude to Professor Masahiro Tatsumisago of Osaka Prefecture University for his fruitful guidance, suggestions and discussions as well as continuous encouragement during the course of this work. I would also like to express my sincere appreciation to Professor Hiroshi Inoue and Professor Masaya Matsuoka of Osaka Prefecture University for their valuable comments towards this thesis.

I am immensely grateful for valuable suggestions, discussions and assistance from Assistant Professor Akitoshi Hayashi of Osaka Prefecture University throughout the project. I would also like to extend my gratitude to Associate Professor Kiyoharu Tadanaga of Osaka Prefecture University for his fruitful suggestions and discussions.

Furthermore, I am fortunate to have had valuable advices towards this research from Professor Emeritus Tsutomu Minami of Osaka Prefecture University, Professor Shinya Machida of Konan University, Professor Atsunori Matsuda of Toyohashi University of Technology, Associate Professor Yoshiyuki Kowada of Hyogo University of Teacher Education, Professor Douglas R. MacFarlane of Monash University, Professor Maria Forsyth of Deakin University, and Dr. Adam S. Best of CSIRO Australia. Thank you.

I would like to thank all undergraduate and graduate students, researchers and alumni in the Laboratory of Inorganic Materials Science at Osaka Prefecture University, especially, Dr. Hirokazu Kitaura, Dr. Teruaki Tezuka, Dr. Keiichi Minami, Mr. Motohiro Nagao, Mr. Naoyuki Nakamoto, and Ms. Yuki Sakurai for their supports to this research and great discussions. Thank you also to Mr. Motoji Sekine of Monash University, Mr. Shigenori Hama, and Mr. Takamasa Ohtomo of Toyota Motor Corporation for their supports towards this thesis.

Finally, I would like to thank my parents and family for their immeasurable support and encouragement towards my studies over a long time.

List of publications

Original articles regarding this study are as follows:

1. "Improvement of High-Rate Performance of All-Solid-State Lithium Secondary Batteries Using $LiCoO_2$ Coated with Li_2O–SiO_2 Glasses"
   A. Sakuda, H. Kitaura, A. Hayashi, K. Tadanaga, and M. Tatsumisago,
   Electrochem. Solid-State Lett., **11** [1] (2008) A1-A3.
   (Chapter 2)

2. "Modification of Interface Between $LiCoO_2$ Electrode and Li_2S–P_2S_5 Solid Electrolyte Using Li_2O–SiO_2 Glassy Layers"
   A. Sakuda, H. Kitaura, A. Hayashi, K. Tadanaga, and M. Tatsumisago,
   J. Electrochem. Soc., **156** [1] (2009) A27-A32.
   (Chapter 2)

3. "All-Solid-State Lithium Secondary Batteries with Oxide-Coated $LiCoO_2$ Electrode and Li_2S–P_2S_5 Electrolyte"
   A. Sakuda, H. Kitaura, A. Hayashi, K. Tadanaga, and M. Tatsumisago,
   J. Power Sources, **189** (2009) 527-530.
   (Chapter 2)

4. "Electrochemical Performance of All-Solid-State Lithium Secondary Batteries Improved by the Coating of Li_2O–TiO_2 Films on $LiCoO_2$ Electrode"
   A. Sakuda, A. Hayashi, and M. Tatsumisago,
   J. Power Sources, **195** (2010) 599-603.
   (Chapter 2)

5. "Preparation of Amorphous Li_4SiO_4–Li_3PO_4 Thin Films by Pulsed Laser Deposition for All-Solid-State Lithium Secondary Batteries"
   Y. Sakurai, A. Sakuda, A. Hayashi, and M. Tatsumisago,
   Solid State Ionics (2011) accepted for publication.
   (Chapter 2)

6. "Interfacial Observation between $LiCoO_2$ Electrode and Li_2S–P_2S_5 Solid Electrolytes of All-Solid-State Lithium Secondary Batteries Using Transmission Electron Microscopy"
A. Sakuda, A. Hayashi, and M. Tatsumisago,
Chem. Mater., **22** (2010) 949-956.

(Chapter 3)

7. "Preparation of Highly Lithium-Ion Conductive $80Li_2S{\cdot}20P_2S_5$ Thin-Film Electrolytes Using Pulsed Laser Deposition
A. Sakuda, A. Hayashi, S. Hama, and M. Tatsumisago,
J. Am. Ceram. Soc., **93** [3] (2010) 765-768.

(Chapter 4)

8. "$LiCoO_2$ Electrode Particles Coated with Li_2S–P_2S_5 Solid Electrolyte for All-Solid-State Batteries"
A. Sakuda, A. Hayashi, T. Ohtomo, S. Hama, and M. Tatsumisago,
Electrochem. Solid-State Lett., **13** [6] (2010) A73-A75.

(Chapter 4)

9. "All-Solid-State Lithium Secondary Batteries Using $LiCoO_2$ Particles with Pulsed Laser Deposition Coatings of Li_2S–P_2S_5 Solid Electrolytes"
A. Sakuda, A. Hayashi, T. Ohtomo, S. Hama, and M. Tatsumisago,
J. Power Sources (2011) accepted for publication.

(Chapter 4)